


Spring 5-12-2022

RECEPTOR-DOPED ORGANIC TRANSISTORS: TRANSDUCING ANION BINDING FROM MIXED IONIC-ELECTRONIC TRANSPORT

Anthony Benasco
University of Southern Mississippi

Follow this and additional works at: <https://aquila.usm.edu/dissertations>

 Part of the [Electrical and Electronics Commons](#), [Polymer and Organic Materials Commons](#), and the [Polymer Science Commons](#)

Recommended Citation

Benasco, Anthony, "RECEPTOR-DOPED ORGANIC TRANSISTORS: TRANSDUCING ANION BINDING FROM MIXED IONIC-ELECTRONIC TRANSPORT" (2022). *Dissertations*. 1977.
<https://aquila.usm.edu/dissertations/1977>

This Dissertation is brought to you for free and open access by The Aquila Digital Community. It has been accepted for inclusion in Dissertations by an authorized administrator of The Aquila Digital Community. For more information, please contact aquilastaff@usm.edu.

RECEPTOR-DOPED ORGANIC TRANSISTORS: TRANSDUCING ANION
BINDING FROM MIXED IONIC-ELECTRONIC TRANSPORT

by

Anthony Benasco

A Dissertation
Submitted to the Graduate School,
the College of Arts and Sciences
and the School of Polymer Science and Engineering
at The University of Southern Mississippi
in Partial Fulfillment of the Requirements
for the Degree of Doctor of Philosophy

Approved by:

Dr. Jason D. Azoulay, Committee Chair

Dr. Xiaodan Gu

Dr. Sergei Nazarenko

Dr. Derek L. Patton

Dr. Jeffery S. Wiggins

May 2022

COPYRIGHT BY

Anthony Benasco

2022

Published by the Graduate School



ABSTRACT

Organic semiconductors based on π -conjugated polymers show remarkable properties such as high tolerance to structural defects, low processing temperature requirements, biocompatibility, ease of fabrication, and tunable properties. Conjugated polymers integrated into device arrays can exhibit collective properties sensitive to minor perturbations in the surrounding media. However, these devices rely on serendipitous sensitivity to the analyte of interest, and strategies for specific detection remain a considerable change. There remains a compelling, global need for technologies to monitor phosphate due to its prevalence in agricultural runoff, leading to fish kills and economic decline for commercial and recreational fisheries. The strong hydration energies of phosphate anions, the propensity to oligomerize, and the complexity of seawater have collectively limited the progress of chromatographic, spectrophotometric, potentiometric, and *in-situ* sensing technologies towards phosphate detection.

Despite the key challenges in the chemical recognition of anions in highly competitive aqueous environments, there have been notable strides involving supramolecular chemistries. The affinity of the receptors to their target analyte has progressed in leaps and bounds over the last two decades with new, exotic interactions involving the hydrophobic effect, metal–anion coordination complexes, electroneutral host molecules with C–H hydrogen bonding motifs, to name a few. This dissertation explores the utility of polarized C–H hydrogen-bonding recognition sites in soft condensed matter electronic materials.

Chapter I introduces a brief historical survey of conjugated polymers, the fundamental concepts and mechanisms behind optoelectronic sensing technologies, and

the intrinsic properties found in conjugated polymer semiconductors that make them excellent candidate materials for chemical sensing applications.

Chapter II establishes the experimental protocols and methods used to extract relevant device parameters to detect changes in the material properties.

Chapter III-IV explores the integration and utility of charge-neutral, shape-persistent macrocycles and how the receptor influences the charge transport, morphology, analyte sensitivity/selectivity, and storage/electrochemical stability.

Overall, a facile, label-free approach was achieved for real-time aqueous measurements. The combination of semiconducting polymers with next-generation receptors offers manifold opportunities for designing novel active layers that can be applied within emerging OFET-based diagnostic, healthcare, environmental monitoring, and bioelectronics platforms.

ACKNOWLEDGMENTS

First and foremost, I want to extend my gratitude and appreciation to my research advisor, mentor, and colleague, Dr. Jason D. Azoulay. During this program, I have grown immensely as a polymer scientist and engineer under his tutelage. Thank you for trusting me and offering the intellectual freedom to explore the many avenues offered in my discipline. It is also an honor and privilege to receive my education and training from the USM's Polymer Science and Engineering Department.

To my committee members: Dr. Xiaodan Gu, Dr. Sergei Nazarenko, Dr. Derek L. Patton, Dr. Jeffery Wiggins, and other faculty members, I am very grateful for the excellent education and mentorship over the years. Your contributions to my personal and professional growth were impactful in more ways than words can describe.

To my external academic and industrial collaborators: Dr. Amar H. Flood (the University of Indiana, Department of Chemistry), Dr. Valerie Pierre (the University of Minnesota, College of Pharmacy), Dr. Qilin Dai (Jackson State University, Department of Chemistry, Physics and Atmospheric Sciences), Dr. Santanu Kundu (Mississippi State University, Swalm School of Engineering), Dr. Tse Nga (Tina) Ng (University of California San Diego, Jacobs School of Engineering), Dr. Andrew Bernard (Sea-Bird Scientific), Yusheng Chen (Indiana University), Dr. Wei Zhao (Indiana University), Randell Wilharm (University of Minnesota), Dr. Jian Xiong (Jackson State University), Madhubhashini Lakdusinghe (Mississippi State University), Shuo Wu (University of California San Diego), thank you for allowing me the opportunity to collaborate and expand my research capabilities and domains of experience.

To my past and present colleagues at USM: Dr. Jared Bates, Logan Dugas, Cheyenne Liu, Dr. Daniel Weller, Dr. William Walker, Dr. Song Zhang, Luke Galuska, Kyle Mehringer, Guorong Ma, and Nathaniel Prine, thank you for your friendship and making this a phenomenal experience.

To the faculty and staff at USM's School of Polymer Science and Engineering: Dr. Bret Calhoun, Dr. William Jarrett, Chuck Collen, Nicky Harrison, Dana Froelich, Dr. Charles McCormick, Toni Altom, and Anna Patterson, for helping me during my time in the program and resolving technical and administrative issues. Dr. Karen S. Coates and the graduate school, thank you for the support and service.

DEDICATION

This dissertation is dedicated to my parents, Thomas G. and Joanne M. Benasco. You both have been my biggest supporters and sources of motivation at every stage in my life. Your unconditional love, care, and guidance have carried me through every obstacle I faced and conquered. To my siblings, Daniel, Tommy, and Christine Benasco thank you for your love, care, and strong bondages over the years. To my friend Tyler Hall-Clay, thank you for your friendship and always encouraging me never to stop believing in myself to achieve my dreams.

TABLE OF CONTENTS

ABSTRACT	ii
ACKNOWLEDGMENTS	iv
DEDICATION	vi
LIST OF TABLES	xi
LIST OF ILLUSTRATIONS	xii
LIST OF ABBREVIATIONS	xxvi
1.1 Motivations	1
1.2 Gulf Coast Waters: Status and Overview	1
1.3 Impacts on the Environment	2
1.4 Challenges at the Frontiers of Marine Science	3
1.5 Phosphorus Recognition and Detection	4
1.5.1 Challenges and Considerations	4
1.5.2 Environmental Indicators and Assays	4
1.6 Chemical Sensing Technologies	6
1.7 Conjugated Polymers	7
1.7.1 Status of Conjugated Polymers	7
1.7.2 Historical Survey of Conjugated Polymers	7
1.7.3 Semiconductor Electronic Band Structure	10
1.7.4 Physics of Doping	12

1.7.5 Charge Carrier Transport	19
1.7.5.1 Molecular Design Considerations	19
1.7.5.2 Dynamics of Intrachain and Interchain Transport.....	22
1.7.6 OFET Chemical Sensors	26
1.7.6.1 Operation Mechanism of OFET Chemical Sensors	27
1.7.6.2 Achieving Analyte Specificity: Receptor Integration	27
1.7.6.3 Supramolecular Interactions for Analyte Recognition.....	28
1.8 Summary	30
CHAPTER I – EXPERIMENTAL METHODS	33
2.1 Materials and Methods.....	33
2.1.1 General Remarks.....	33
2.2 General Characterizations.....	33
2.2.1 Atomic Force Microscopy (AFM)	33
2.2.2 Electrochemistry	34
2.2.3 Electron Paramagnetic Resonance (EPR) Spectroscopy	34
2.2.4 Ellipsometry	34
2.2.5 Environmental Stability Studies	35
2.2.6 Gel Permeation Chromatography (GPC)	35
2.2.7 UV-Vis-NIR Spectroscopy	35
2.3 OFET Device Operation and Parameter Extraction.....	36

2.3.1	Introduction.....	36
2.3.2	Operating Principles of OFETs.....	37
2.3.3	Common OFET Device Geometries.....	43
2.3.4	Role of Device Factors.....	44
2.3.5	Transistor Fabrication.....	46
2.3.6	Device Characterization.....	47
2.3.6.1	Two-Point Probe $I-V$: Extracting Room-Temperature Bulk Conductivity. .	47
2.3.6.2	Bottom-Gate/Bottom-Contact Devices: Extracting Mobility.	47
2.3.6.3	Water Sensing Tests and Characterization.	47
CHAPTER III – POLYMER-SUPRAMOLECULAR RECEPTOR COMPOSITES:		
ACTIVE FILMS IN TRANSISTOR ARCHITECTURES		
3.1	Research Objectives and Approaches.....	49
3.2	OFET Fabrication Protocol.....	49
3.2.1	Metal Deposition: Material Selection, Procedure, and Device Geometry	49
3.2.2	Organosilane Self-Assembled Monolayer Deposition:	50
3.3	General Characterization of Channel Materials.....	51
3.3.1	Properties of Cyanostar.....	52
3.3.2	Receptor-Induced Doping.....	54
3.3.3	Influence on Film Morphology.....	61
3.4	Conclusions.....	63

CHAPTER IV – RECEPTOR-INDUCED DOPING OF CONJUGATED POLYMER	
TRANSISTORS: A STRATEGY FOR SELECTIVE AND ULTRASENSITIVE	
PHOSPHATE DETECTION IN COMPLEX AQUEOUS ENVIRONMENTS 64	
4.1	Abstract 64
4.2	Introduction..... 65
4.3	Results and Discussion 67
4.4	Conclusion 76
APPENDIX A – SUPPORTING INFORMATION FOR CHAPTER III 78	
A.1	Supplemental Figures and Tables 78
APPENDIX B – SUPPORTING INFORMATION FOR CHAPTER IV 92	
B.1	Supplemental Figures and Tables..... 92

LIST OF TABLES

Table A.1 Optical and electrochemical properties summary.....	82
Table A.2 Tabulated conductivity, field-effect mobility, and calculated carrier density with the trap-limited regime (CS < 4 wt%) highlighted in reference to the above plot...	88
Table B.1 PDVT-CS film EPR summary.....	93
Table B.2 PDVT-IsoCS film EPR summary.	94

LIST OF ILLUSTRATIONS

Figure 1.1 NOAA map highlighting the Gulf of Mexico run-off contributions from farms (green) and cities (red). Iowa farmland agricultural run-off. TX/LA Gulf Coast, an area of hypoxic waters (“dead zone”). Unmanned undersea vehicles (UUV). Rosette sampler: used to collect deep ocean seafloor samples and has an attached sensor package, known as a CTD (conductivity, temperature, and depth) device.....	2
Figure 1.2 Current conjugated polymer-based technology sectors.....	8
Figure 1.3 Early examples of polymeric structures and synthetic protocols.	10
Figure 1.4 The band model and electrical conductivity range of insulators, semiconductors, and conductors. The electrical properties are determined by the size of the bandgap, the energy difference between the valence and conduction bands. Figure was motivated and adapted from Ref. 53.....	11
Figure 1.5 Schematic representation of chemical doping involving p-type and n-type doping processes. The mechanism is fundamentally rooted in the alignment of energy levels which electron transfer can take place. Figure was motivated and adapted from Ref 57.....	15
Figure 1.6 Schematic showing how the embedment of neutral dopant molecules influences the OSC energy levels with an emphasis on ion-pair formation (IPF). Figure was motivated and adapted from Ref 60.....	16
Figure 1.7 P-type doping of neutral dopants in a OSC matrix, emphasizing the formation of a neutral and ionized ground-state charge-transfer complex (CPX). λ is the reorganization energy, and U_1 and U_2 denote the Hubbard U of the neutral dopant and OSC. Figure was motivated and adapted from Ref 60.	18

Figure 1.8 Strategies for controlling the material bandgap. (a) Modulate the HOMO-LUMO energy gap through π -conjugation extension. Example structures include a thiophene monomer, dimer, trimer, tetramer, and polymer with their associated energy levels. (b) Other structural features that contribute to the bandgap: bond length alternation (E_{BLA}), substituents (electron-donating or -withdrawing character), intermolecular interactions between chains (E_{INT}), backbone planarity (E_{θ}), and monomer aromaticity (E_{RES}). (c) Enhancing the quinoid nondegenerate resonance states promotes double-bond delocalization and thus, narrower bandgaps. Figure was motivated and adapted from Ref 67..... 20

Figure 1.9 Donor and acceptor orbital hybridization upon coupling, possessing a narrower bandgap compared to conjugated homopolymers. Monomer library showing frequently used electron-rich donors (π_D) and acceptor (π_A) units Figure was motivated and adapted from Ref 73..... 22

Figure 1.10 Schematic illustrations of common solid-state (a) microstructures (semicrystalline, disordered aggregates, and amorphous) and (b) intra- and interchain charge transport. Figure was motivated and adapted from Ref. 74. 24

Figure 1.11 OSC energy levels. (a) HOMO and LUMO energies with respect to the vacuum level, showing the electron affinity, ionization potential, optical bandgap, and the presence of intragap trap states. (b) Another representation of the energy levels showing the density of states and the existing shallow and deep tail states that hamper transport of charges near the mobility edge. (c) Various transport barriers (trap sites and scattering centers) created by local defects and imperfections in the polymer matrix. Figure was motivated and adapted from Ref. 79..... 25

Figure 1.12 Supramolecular host chemistries: (a) timeline of discoveries and (b) the bond enthalpies of various intermolecular interactions showing their relative strengths.....	28
Figure 1.13 Traditional methods to endow ion selectivity using (a) optical and electrochemical (b) membrane-based and (c) membrane-free methodologies. Reprinted with permission from Ref. 108. Copyright 2010, Journal of the American Chemical Society. Adopted with permission from Ref. 109. Copyright 2020. Royal Society of Chemistry. Reprinted with permission from Ref. 114, Copyright 2019, American Chemical Society.	32
Figure 2.1 The device structure of an OFET which is composed of three electrodes (source, drain, and gate), a dielectric layer, and a semiconductor.	38
Figure 2.2 Schematic of band-bending and operating modes in OFETs: (a) p-type operation without (left) and with (right) an applied negative gate voltage and (b) n-type operation without (left) and with (right) an applied positive gate voltage.	40
Figure 2.3 The linear regime: I_{DS} as a function of V_{DS}	41
Figure 2.4 (a) The pinch-off point and (b) the saturation regime: I_{DS} as a function of V_{DS}	42
Figure 2.5 (a) Output and (b,c) transfer plots showing the linear (blue) and saturation regimes (orange).	43
Figure 2.6 OFET configurations: (a) bottom-gate/top-contact (BGTC), (b) bottom-gate/bottom-contact (BGBC), (c) top-gate/top-contact (TGTC), and (d) top-gate/bottom-contact (TGBC).....	44

Figure 2.7 (a) AutoCAD of fabricated devices used to performance the transmission line method (TLM). (b) TLM plot showing channel length (L) versus total resistance (R_T). Linear extrapolation is used to calculate the device contact resistance (R_C). (c) R_T and a three-resistor model equivalence ($R_T = R_C + R_{CH} = R_{C,Int} + R_{C,Bulk} + R_{CH}$)..... 45

Figure 3.1 (a) Molecular structures of the semiconducting polymer (**PDVT**) and (b) cyanostar receptor (**CS**) which can bind phosphate..... 51

Figure 3.2 CV experiment to measure the frontier orbital energy levels of **CS**. (a) **CS** can form a 2:1 sandwich complex with specific anion species ($CS_2 \cdot X^-$). (c) The three tested anion compositions tetrabutylborate (TBABPh₄), tetrakis(3,5-bis(trifluoromethyl)phenyl)borate (TBABArF), and hexafluorophosphate (PF₆⁻). (c) CV spectra of tested anions, where significant shifts in the reduction peaks were observed. 53

Figure 3.3 Thermogravimetric analysis (TGA) of a shape-persistent macrocycle, **CS**, versus common macrocycles: 18-Crown-6 (18-C-6), α -cyclodextrin (α -CD), and β -cyclodextrin (β -CD), showing the (a) chemical structures and (b) TGA curves. **CS** displayed a 5 wt% weight loss at ~421 °C..... 54

Figure 3.4 3-D rendering of the BGBC device structures used for charge transport measurements..... 54

Figure 3.5 UV-Vis-NIR absorption profile of pristine **PDVT** and **PDVT-CS** films spin-coated from chlorobenzene onto quartz substrates. The inset illustrates a pronounced low-energy absorption tail upon **CS** addition. 56

Figure 3.6 (a) Schematic illustration of a bottom-gate/bottom-contact (BGBC) device structure. **PDVT-CS** devices (**CS** loading = 0, 4, 10, and 20 wt%) were fabricated and

tested to evaluate electronic transformations, material compatibility, and storage stability.

(b) Electrical conductivities obtained from two-point probe measurements (-2 to 2 V) of **PDVT-CS** films. (c) FET transfer characteristics and (d) output curves (left) without and (right) with **CS** (20 wt%) showing enhancement in p-channel operation using source and drain electrodes ($L = 80 \mu\text{m}$, $W = 1 \text{ mm}$). (e) Monitoring of device stability for high performing **PDVT-CS** films over 60 days. Films were completely submerged in Instant Ocean sea salt electrolyte and showed minimal changes in the conductivity (black), field-effect mobility (red), and carrier concentration (blue)..... 59

Figure 3.7 FTIR spectra of neat **PDVT**, neat **CS**, and **PDVT-CS** blends with emphasis on the **CS** cyano peak (2215 cm^{-1}). 61

Figure 3.8 AFM-IR on **PDVT-CS** films: (a) Picture of a prefabricated device encapsulated with a spin-casted active layer with the corresponding (b) height, (c) phase, and (d) IR scans. (e) Picture of a prefabricated device encapsulated with a slow-dried film, causing the formation of spherulitic microstructures as viewed on the (f) optical microscope image (scale bar: $200 \mu\text{m}$) and AFM (g) height, (h) phase, and (i) IR scans. The IR pulses used in the test runs were activated at 1596 cm^{-1} , matching an absorption band found in **CS**. Red peaks correspond to **CS** while blue corresponds to **PDVT**..... 63

Figure 4.1 (a) EPR (X-band) spectra at room temperature of **PDVT-CS** demonstrating the formation of paramagnetic species, consistent with (b) doping. Upon addition of tetrabutylammonium dihydrogen phosphate (**TBAP**, 1 equiv. relative to **CS**) to **PDVT-CS** the films show predominantly diamagnetic behavior, consistent with (c) dedoping.. 68

Figure 4.2 OFET devices (BCBG configuration) based on a three-component mixture **PDVT-CS•TBA-X** salts (**X = P, N, Cl, PC, and HS**) and their associated a) two-point

probe I–V characteristics and b) OFET transfer curves. The variation in the dedoping response and the preservation of charge transport characteristics without degradation demonstrates that receptor-anion interactions dictate the magnitude of charge carrier reduction. c) Summary of carrier concentration (cm^{-3}) within the conductive channel and d) OFET on/off ratio comparing 10 independent devices with source and drain electrode geometries of $L = 80 \mu\text{m}$ and $W = 1 \text{mm}$ 69

Figure 4.3 a) Schematic illustration of the EGOFET device and b) the proposed sensing mechanism. c) Transient responses of the device towards phosphate ($\text{H}_2\text{PO}_4^-/\text{HPO}_4^{2-}$, nitrate (NO_3^-), bicarbonate (HCO_3^-), carbonate (CO_3^{2-}), and chloride (Cl^-) in HEPES buffer ($\text{pH} = 7.4$). d) Comparison of state-of-the-art phosphate sensors with **PDVT-CS**, which demonstrated a limit of detection (LOD) and quantification (LOQ) of 178 pM (17.3 parts per trillion (ppt)) and 430 pM (41.7 ppt), respectively. 71

Figure 4.4 Anion recognition control experiment. a) 2:1 sandwich complex involving a PF_6^- anion. Under a UV treatment (365 nm), the cyanostar was photoisomerized (**IsoCS**). b) Depiction of a trans-cis-trans-cis-trans conformer (one of 2^5 potential isomers) precluding host-guest complexation. This receptor configuration was integrated into the **PDVT** host matrix to conduct a series of control experiments where we do not expect any analyte binding. c) UV-vis absorption spectra of **CS** CHCl_3 solutions undergoing photoisomerization. The solutions show absorption profiles with the maxima (λ_{max}) reaching equilibrium beyond 1 h of exposure to 365 nm UV photons. 74

Figure 4.5 **PDVT-IsoCS** EGOFET transient responses of the device towards phosphate ($\text{H}_2\text{PO}_4^-/\text{HPO}_4^{2-}$, nitrate (NO_3^-), bicarbonate (HCO_3^-), carbonate (CO_3^{2-}), and chloride (Cl^-) in HEPES buffer ($\text{pH} = 7.4$). 76

Figure A.1 GPC (TCB, 160 °C) trace of PDVT	78
Figure A.2 UV-Vis-NIR absorption spectra in C ₆ H ₅ Cl solution	79
Figure A.3 UV-Vis-NIR absorption intensity ratio (A _{0-0/0-1}) versus material composition and film versus solution	80
Figure A.4 Cyclic voltammetry (CV) spectra showing the onset of oxidation and reduction.	81
Figure A.5 Kelvin probe force microscopy (KPFM) surface potential measurements of PDVT and PDVT-CS as-spun on ITO glass substrates. After film removal via scratch test, the probe was scanned over the film/ITO border. (a,b) Topography and (c,d) surface potential images between PDVT /ITO and PDVT-CS /ITO, where a clear distinction (potential drop) was found with CS admixing. (e) Plots showing the receptor-induced surface potential changes from images b and d.	83
Figure A.6 (a) OFET output (I _{DS} vs V _{DS}), (b) transfer (I _{DS} vs V _{GS}), and (c) gate leakage (I _{GS} vs V _{GS}) characteristics of pristine PDVT films using a BGBC device configuration and (d) 2-point probe room-temperature I–V plot (without a gate electrode).	84
Figure A.7 Monitoring charge transport shelf-life for high performing PDVT films. Films stored and measured under an (a) inert atmosphere and (b) ambient conditions (both in the absence of light). The latter case exhibited an onset of degradation beyond day 5 and the properties were no longer extractable beyond day 17.....	85
Figure A.8 (a) OFET output (I _{DS} vs V _{DS}), (b) transfer (I _{DS} vs V _{GS}), and (c) gate leakage (I _{GS} vs V _{GS}) characteristics of blended PDVT-CS (20 wt%) films using a BGBC device configuration and (d) 2-point probe room-temperature I–V plot (without a gate electrode).	86

Figure A.9 Composition-dependent charge transport properties showing conductivity, field-effect mobility, and hole carrier concentration versus CS loading in a PDVT host matrix.	87
Figure A.10 OFET transfer (a) I_{DS} vs V_{GS} and (b) $I_{DS}^{1/2}$ vs V_{GS} characteristics of PDVT films with 1 – 20 wt% CS loading.	89
Figure A.11 Monitoring charge transport shelf-life for high performing PDVT-CS films for 60 days. Films stored and measured under an (a) inert atmosphere and (b) ambient conditions (both in the absence of light) showed moderate change in conductivity, field-effect mobility, and hole concentration over a period of 60 days. No discernable degradation was found.	90
Figure A.12 Monitoring charge transport shelf-life for high performing PDVT-CS films for 60 days. Films stored and measured under UP DI water (in the absence of light) showed moderate change in conductivity, field-effect mobility, and hole concentration over a period of 60 days. No discernable degradation was found.	91
Figure B.1 EPR (X-band) spectra at 25 °C on a CS film.	92
Figure B.2 Composition-dependent charge transport properties showing conductivity, field-effect mobility, and hole carrier concentration versus IsoCS loading in a PDVT host matrix.	95
Table B.3 Tabulated conductivity, field-effect mobility, and calculated carrier density of PDVT-IsoCS with the trap-limited regime (< 10 wt% CS) highlighted in reference to the above plot.	96
Figure B.3 Variable temperature OFET transfer characteristics (180 – 340 K) of (a) PDVT , (b) PDVT-IsoCS and (c) PDVT-CS films. The temperature-dependent mobility	

was fitted to the multiple-trap and release model to calculate the mean energy of the trap states.⁷⁸ 97

Figure B.4 Total resistance of **PDVT-CS** and **PDVT-IsoCS** samples as a function of channel length (L), where the y-intercepts ($L \rightarrow 0$) show contact resistances (R_C) of 4.5 and 255.1 $M\Omega$, respectively. Inset plot: **PDVT-CS** zoomed-in. 98

Figure B.5 (a) OFET output (I_{DS} vs V_{DS}), (b) transfer (I_{DS} vs V_{GS}), and (c) gate leakage (I_{GS} vs V_{GS}) characteristics of blended **PDVT-CS•TBAP** (anion: 1 equiv. relative to **CS**) films using a BGBC device configuration and (d) 2-point probe room-temperature I–V plot (without a gate electrode). 99

Figure B.6 (a) OFET output (I_{DS} vs V_{DS}), (b) transfer (I_{DS} vs V_{GS}), and (c) gate leakage (I_{GS} vs V_{GS}) characteristics of blended **PDVT-CS•TBAN** (anion: 1 equiv. relative to **CS**) films using a BGBC device configuration and (d) 2-point probe room-temperature I–V plot (without a gate electrode). 100

Figure B.7 (a) OFET output (I_{DS} vs V_{DS}), (b) transfer (I_{DS} vs V_{GS}), and (c) gate leakage (I_{GS} vs V_{GS}) characteristics of blended **PDVT-CS•TBACl** (anion: 1 equiv. relative to **CS**) films using a BGBC device configuration and (d) 2-point probe room-temperature I–V plot (without a gate electrode). 101

Figure B.8 (a) OFET output (I_{DS} vs V_{DS}), (b) transfer (I_{DS} vs V_{GS}), and (c) gate leakage (I_{GS} vs V_{GS}) characteristics of blended **PDVT-CS•TBAPC** (anion: 1 equiv. relative to **CS**) films using a BGBC device configuration and (d) 2-point probe room-temperature I–V plot (without a gate electrode). 102

Figure B.9 (a) OFET output (I_{DS} vs V_{DS}), (b) transfer (I_{DS} vs V_{GS}), and (c) gate leakage (I_{GS} vs V_{GS}) characteristics of blended **PDVT-CS•TBAHS** (anion: 1 equiv. relative to

CS) films using a BCBG device configuration and (d) 2-point probe room-temperature I–V plot (without a gate electrode).	103
Table B.4 Tabulated conductivity, field-effect mobility, and calculated carrier density of PDVT-CS•TBA–X three-component films.	104
Figure B.10 (a,b) PDVT-TBAP and (c,d) PDVT-TBAN transfer characteristics to test for polymer-analyte interactions in the absence of receptors. The new profiles show significant degradation in FET performance which do not occur upon CS integration. These results suggest receptor-analyte host-guest complexation predominates in the three-component film studies.....	105
Figure B.11 (a) Two-point probe conductivity and b) transfer plots of analyte interfacial complexation and removal (aqueous wash). A pristine PDVT film was initially encapsulated by a CS•TBAP layer. After high precision cleaning to isolate adjacent device structures and testing the initial film properties (TBAP injection), TBAP was removed by submerging the device under UP (Type 1) DI water for 30 mins. Afterwards, the performance was recorded to demonstrate binding reversibility with potential reusability of field-deployed sensors.	106
Figure B.12 Interval plots of CS:phosphate extracted from B.10 I-V and OFET transfer plots showing change in (a) room-temperature conductivity, (b) field-effect mobility, (c) on-off current ratio, and (d) charge carrier density.....	107
Figure B.14 Variable-angle ellipsometry model fittings of (a) PDVT, (b) CS, (c) PDVT-CS, and (d) PDVT-CS•TBAP films. (e) Thickness profile showing PDVT-CS swelling by less than 1 nm over 1 hour of exposure to UP DI water. The concentration of CS was fitted from the dry film and held constant during the water measurement. Only 10	

variables (thickness and amplitude of **PDVT** and **CS** gaussian oscillators) were allowed to vary during the swelling experiment. (f) The uniqueness test shows that the modeled thickness gives the best fit and is reliable. These findings are relevant to distinguish the mode of operation, which we found to be based on the field-effect rather than volumetric like in organic electrochemical transistors (OECTs)..... 108

Figure B.16 Active layer responsiveness to pH fluctuation (4, 7, and 10). There were no significant changes in the tested pH range..... 110

Figure B.17 HEPES buffer analyte solution spiked with $\text{H}_2\text{PO}_4^-/\text{HPO}_4^{2-}$: pH as a function of anion concentration..... 111

Figure B.18 HEPES buffer analyte solution spiked with NO_3^- : pH as a function of anion concentration..... 112

Figure B.19 HEPES buffer analyte solution spiked with SiO_3^{2-} : pH as a function of anion concentration..... 113

Figure B.20 HEPES buffer analyte solution spiked with Br^- : pH as a function of anion concentration..... 114

Figure B.21 HEPES buffer analyte solution spiked with HCO_3^- : pH as a function of anion concentration..... 115

Figure B.22 HEPES buffer analyte solution spiked with CO_3^{2-} : pH as a function of anion concentration..... 116

Figure B.23 HEPES buffer analyte solution spiked with SO_4^{2-} : pH as a function of anion concentration..... 117

Figure B.24 HEPES buffer analyte solution spiked with Cl^- : pH as a function of anion concentration..... 118

Figure B.25 EGOFET transient responses based on sequential exposure to HEPES baseline solution. The devices displayed stable electrochemical performance with consistent I_{DS} output and I_{GS} leakage, revealing no dramatic changes to the film properties during the experimental run.	119
Figure B.26 (a) EGOFET gate leakage in response to HEPES solution spiked with $H_2PO_4^-/HPO_4^{2-}$	120
Figure B.27 PDVT-CS EGOFET (a) transient responses towards $H_2PO_4^-/HPO_4^{2-}$ and the corresponding (b) sensor calibration plot.	121
Figure B.28 PDVT-CS EGOFET (a) transient responses towards NO_3^- and the corresponding (b) sensor calibration plot.	122
Figure B.29 PDVT-CS EGOFET (a) transient responses towards SiO_3^{2-} and the corresponding (b) sensor calibration plot.	123
Figure B.30 PDVT-CS EGOFET (a) transient responses towards Br^- and the corresponding (b) sensor calibration plot.	124
Figure B.31 PDVT-CS EGOFET (a) transient responses towards HCO_3^- and the corresponding (b) sensor calibration plot.	125
Figure B.32 PDVT-CS EGOFET (a) transient responses towards CO_3^{2-} and the corresponding (b) sensor calibration plot.	126
Figure B.33 PDVT-CS EGOFET (a) transient responses towards SO_4^{2-} and the corresponding (b) sensor calibration plot.	127
Figure B.34 PDVT-CS EGOFET (a) transient responses towards Cl^- and the corresponding (b) sensor calibration plot.	128

Figure B.35 (a) **PDVT-CS** EGOFET limit of detection (LOD) versus analyte thermionic diameter for anions tested in HEPES buffer. Referencing to the **CS** cavity (teal line), the size effects towards anion recognition were exemplified. Low LOD and peak preference was found for $\text{H}_2\text{PO}_4^-/\text{HPO}_4^{2-}$, NO_3^- , SiO_3^{2-} , Br^- , and HCO_3^- ranging from 3.8 – 4.26 Å in size. Other anions such as Cl^- ($d_{\text{ion}} \approx 3.4$ Å), CO_3^{2-} ($d_{\text{ion}} \approx 3.78$ Å), and SO_4^{2-} ($d_{\text{ion}} \approx 4.36$ Å). 129

Figure B.36 **IsoCS** preparation for NMR titration experiments. 130

Figure B.37 In-situ ^1H NMR of **IsoCS**. 131

Figure B.38 In-situ ^1H NMR (6 – 9.5 ppm) of **IsoCS**. 132

Figure B.39 In-situ ^1H NMR of **IsoCS** with PF_6^- anion titration. 133

Figure B.40 In-situ ^1H NMR (6.5 – 9.5 ppm) of **IsoCS** with PF_6^- anion titration..... 134

Figure B.41 In-situ ^1H NMR (8.10 – 8.6 ppm) of **IsoCS** with PF_6^- anion titration..... 135

Figure B.42 **PDVT-IsoCS** EGOFET transient responses towards $\text{H}_2\text{PO}_4^-/\text{HPO}_4^{2-}$ 136

Figure B.43 **PDVT-IsoCS** EGOFET transient responses towards NO_3^- 137

Figure B.44 **PDVT-IsoCS** EGOFET transient responses towards SiO_3^{2-} 138

Figure B.45 **PDVT-IsoCS** EGOFET transient responses towards Br^- 139

Figure B.46 **PDVT-IsoCS** EGOFET transient responses towards HCO_3^- 140

Figure B.47 **PDVT-IsoCS** EGOFET transient responses towards CO_3^{2-} 141

Figure B.48 **PDVT-IsoCS** EGOFET transient responses towards SO_4^{2-} 142

Figure B.49 **PDVT-IsoCS** EGOFET transient responses towards Cl^- 143

Figure B.50 Instant Ocean sea salt electrolyte spiked with $\text{H}_2\text{PO}_4^-/\text{HPO}_4^{2-}$: pH as a function of anion concentration. 144

Figure B.51 **PDVT-CS** EGOFET transient responses towards (a) $\text{H}_2\text{PO}_4^-/\text{HPO}_4^{2-}$ dissolved in artificial seawater electrolyte and (b) the corresponding calibration plot for $\text{H}_2\text{PO}_4^-/\text{HPO}_4^{2-}$ detection and the standard error across 5 devices. 145

Figure B.52 Crystal structure of the 4:3:3 stack of tetrameric **CS** with a trianionic triphosphate ($\text{H}_2\text{PO}_4\cdots\text{H}_2\text{PO}_4\cdots\text{H}_2\text{PO}_4$)³⁻ and TBA^+ cations stacking around the tetrameric stack. 146

Table B.5 Crystal parameters¹⁰⁶ 147

Figure B.53 (a) OFET output (I_{DS} vs V_{DS}), (b) transfer (I_{DS} vs V_{GS}), and (c) gate leakage (I_{GS} vs V_{GS}) characteristics of **CS** films using a BGBC device configuration and (d) 2-point probe room-temperature I–V plot (without a gate electrode). 148

Figure B.54 A comparison of high performing **PDVT-CS** films benchmarked against capacitive, lap-on-chip, colorimetric, ion-selective electrodes, FETs, and commercialized phosphate sensors. **PDVT-CS** demonstrates a low LOD of 178 pM (17.3 parts per trillion) in HEPES and 65.4 nM (6.54 ppb) in Instant Ocean® Sea Salt Electrolyte. 149

Table B.6 Summary of state-of-the-art phosphate sensing platforms..... 150

LIST OF ABBREVIATIONS

<i>AFM</i>	atomic force microscopy
<i>α-CD</i>	α -cyclodextrin
<i>Au</i>	gold
<i>Avg.</i>	average
<i>β-CD</i>	β -cyclodextrin
<i>BLA</i>	bond-length alternation
<i>BGBC</i>	bottom-gate/bottom-contact
<i>BGTC</i>	bottom-gate/top-contact
<i>18-C-6</i>	18-crown-6
<i>C</i>	dielectric capacitance
<i>CAGR</i>	compound annual growth rate
<i>C₆H₅Cl</i>	chlorobenzene
<i>CHCl₃</i>	chloroform
<i>Cr</i>	chromium
<i>CS</i>	penta- <i>t</i> - butylpentacyanopentabenz[25]annulene, “cyanostar”
<i>CPX</i>	charge-transfer complex
<i>CTD</i>	conductivity, temperature, and depth
<i>CV</i>	cyclic voltammetry
<i>D</i>	polydispersity
<i>DA</i>	donor-acceptor

δ	extent of charge transfer
<i>DI</i>	deionized
<i>DOS</i>	density of electronic states
<i>DPPH</i>	2,2-diphenyl-1-picrylhydrazyl
E_F	fermi energy level
$E_{CPX,H}$	charge-transfer complex HOMO energy levels
$E_{CPX,L}$	charge-transfer complex LUMO energy levels
E_g	bandgap
E_g^{elec}	electrochemical bandgap
E_g^{opt}	optical bandgap
E_i	intrinsic energy level
E_{RES}	aromatic resonance stabilization
E_θ	mean deviation from planarity
<i>EA</i>	electron affinity
<i>EGOFET</i>	electrolyte-gated organic field-effect transistor
E_{HOMO}	onset of oxidation
E_{LUMO}	onset of reduction
<i>EPR</i>	electron paramagnetic resonance

<i>FTIR</i>	Fourier-transform infrared
<i>GPC</i>	gel permeation chromatography
<i>GS</i>	ground state
<i>GIWAXS</i>	grazing-incidence wide-angle X-ray scattering
<i>h</i>	Planck's constant
<i>HPLC</i>	high-performance liquid chromatography
<i>HOMO</i>	highest occupied molecular orbital
I_{DS}	drain-source current
<i>ICP-MS</i>	inductively-coupled plasma mass spectroscopy
I_{GS}	gate-source (leakage) current
<i>IP</i>	ionization potential
<i>IPA</i>	isopropyl alcohol
<i>IPF</i>	ion-pair formation
<i>ISEs</i>	ion-selective electrodes
<i>ITO</i>	indium tin oxide
<i>IUPAC</i>	International Union of Pure and Applied Chemistry
<i>I-V</i>	current-voltage
k_B	Boltzmann constant
<i>KPFM</i>	Kelvin probe force microscopy

<i>kT</i>	thermal energy
<i>L</i>	channel length
<i>LUMO</i>	lowest unoccupied molecular orbital
<i>M_n</i>	number-average molecular weight
<i>MOs</i>	molecular orbitals
<i>n</i>	charge carrier concentration
<i>NaCl</i>	sodium chloride
<i>NMR</i>	nuclear magnetic resonance
<i>OEET</i>	organic electrochemical transistor
<i>OFET</i>	organic field-effect transistor
<i>OLED</i>	organic light-emitting diode
<i>OSC</i>	organic semiconductor
<i>OSTP</i>	President's Office of Science and Technology Policy
<i>OTS</i>	octadecyltrichlorosilane
<i>P3HT</i>	poly(3-hexylthiophene-2,5-diyl)
<i>PAHs</i>	polycyclic aromatic hydrocarbons
<i>PDVT</i>	poly[2,5-bis(2-decyltetradecyl)pyrrolo[3,4- c]pyrrole-1,4-(2 <i>H</i> ,5 <i>H</i>)-dione- <i>alt</i> -(<i>E</i>)-1,2- di(2,2'-bithiophen-5-yl)ethene]
<i>PEDOT</i>	poly(3,4-ethylenedioxythiophene)
<i>ppb</i>	parts per billion
<i>ppt</i>	parts per trillion

<i>PSS</i>	poly(styrenesulfonate)
<i>4T</i>	quaterthiophene
R_{CH}	channel resistance
R_C	contact resistance
<i>rpm</i>	rotations per minute
R_T	total resistance
<i>SEC</i>	size-exclusion chromatography
<i>SiO₂</i>	silicon dioxide
<i>TBA–BArF</i>	tetrabutylammonium tetrakis(3,5- bis(trifluoromethyl)phenyl)borate
<i>TBABPh₄</i>	tetrabutylammonium tetraphenylborate
<i>TBABr</i>	tetrabutylammonium bromide
<i>TBACl</i>	tetrabutylammonium chloride
<i>TBAPF₆</i>	tetrabutylammonium hexafluorophosphate
<i>TBAHS</i>	tetrabutylammonium hydrogen sulfate
<i>TBAN</i>	tetrabutylammonium nitrate
<i>TBAP</i>	tetrabutylammonium phosphate
<i>TBAPC</i>	tetrabutylammonium perchlorate
<i>TCE</i>	trichloroethylene
<i>F₄-TCNQ</i>	2,3,5,6-tetrafluoro-7,7,8,8- tetracyanoquinodimethane
<i>TCB</i>	1,2,4-trichlorobenzene

T_d	decomposition temperature
TGA	thermal gravimetric analysis
$TGBC$	top-gate/bottom-contact
$TGTC$	top-gate/top-contact
TLM	transmission line method
UPS	ultraviolet photoelectron spectroscopy
$UUVs$	unmanned undersea vehicles
$UV-Vis-NIR$	ultraviolet-visible-near infrared
V_{DS}	drain-source voltage
V_{GS}	gate-source voltage
V_{Th}	threshold voltage
W	channel width
$wt\%$	weight percentage
λ	reorganization energy
λ_{max}	absorption maxima
μ_{FET}	field-effect mobility
σ_{RT}	room-temperature electrical conductivity

CHAPTER I- INTRODUCTION

1.1 Motivations

Organic conductors enable low-cost, low-temperature, large-scale, and unconventional device fabrication by their facile solution processability and printability compared to ubiquitous inorganic, silicon-based semiconductors. Over the past decades, the unabated development of multifunctional organic semiconductors (OSCs) ignited the production of deployable, robust technologies ranging from flexible electronics,¹ radio-frequency identification systems,² energy harvesting and storage devices,³⁻⁴ to various sensing platforms.⁵ The market value of conductive polymers is expected to soar from \$3.9 billion in 2018 to \$ 7.4 billion by 2026 with a compound annual growth rate (CAGR) of 8.1%. Commercially mature organic optoelectronic technologies, anticipated to reach 77.9 billion by 2027, are fast emerging with the adoption of innovative consumer electronics and the rising demands of new functionalities and devices. The competitive performances rooted in conjugated polymers combined with their tunable properties and broad applicability have cultivated an ensemble of research efforts and commercial products at the forefront of advanced sensing technologies in biomedical science, healthcare, and environmental monitoring of pollutants and biologically relevant anions.

1.2 Gulf Coast Waters: Status and Overview

The Mississippi Sound and Gulf Coast represent a critically important nexus of food-water-energy for the area and the greater United States, as a major source of seafood and aquaculture, oil and gas production, and trading ports.⁶ For example, the Gulf of Mexico shrimp harvesting industry is an essential commercial sector of the entire seafood industry in the U.S.⁷ The region hosts two of the top twenty trading ports in the nation, in

Mobile, AL and Pascagoula, MS, and is a primary zone for oil and gas exploration and production. This marine ecosystem, like most worldwide, is experiencing significant anthropogenic-driven change.⁸ The same technologies that allow for economic exploitation of the region’s abundant resources, such as fisheries, aquaculture, agriculture with associated runoff, and off-shore drilling, present environmental risk and had an estimated near-term negative economic impact over \$1.6b to the Gulf Coast economy.



Figure 1.1 NOAA map highlighting the Gulf of Mexico run-off contributions from farms (green) and cities (red). Iowa farmland agricultural run-off. TX/LA Gulf Coast, an area of hypoxic waters (“dead zone”). Unmanned undersea vehicles (UUV). Rosette sampler: used to collect deep ocean seafloor samples and has an attached sensor package, known as a CTD (conductivity, temperature, and depth) device.

1.3 Impacts on the Environment

Anthropogenic and natural activity at the Gulf of Mexico (Figure 1.1) and its surrounding river inflows have resulted in the concentration of toxins, chemicals, and perturbing agents that have been shown to accumulate in or disturb the lifecycle of microscopic organisms, fish, and marine mammals. These events also present threats to

the sustainability of the seafood and fishing industries. Of particular concern are rising carbon dioxide levels resulting in ocean acidification,⁹ agricultural run-offs,¹⁰ and organic matter, though related to hypoxia and “dead zones,”¹¹⁻¹² and polycyclic aromatic hydrocarbons (PAHs) resulting from oil spills.¹³ Collectively, these contaminants represent a major technological hurdle in developing robust, rapid sensing platforms for water quality monitoring with global implications.

Nutrient pollution involving excess nitrogen and phosphorus is one of the nation’s most challenging environmental challenges.¹⁴⁻¹⁶ Sixty-five percent of assessed estuaries and coastal areas have moderate to high water quality impacts from nutrient pollution, and freshwater nutrient pollution alone costs the nation billions per year.¹⁷ Drinking water violations have more than doubled in the last decade, aquatic environments have been altered, and measurable impacts on human health and the economy are evident. A consortium of Federal Agencies, led by the President’s Office of Science and Technology Policy (OSTP), has challenged the community to: (1) develop simple, robust sensors for nitrates and phosphates; (2) reduce capital expenditure and involvedness of collecting data; and (3) produce a more comprehensive representation of how nutrients exist in space and time within ecosystems. *While the use of nutrient measurement tools has increased in recent years, the high cost of acquisition and use has limited their ability to supply affordable nutrient measurement data.*

1.4 Challenges at the Frontiers of Marine Science

Current marine research primarily depends on heavy and invasive sensory equipment, ship-based sampling, and a telemetric network to understand the marine environment (Figure 1.1). Sampling has always been a fundamental problem in

oceanography. While ship-based sampling has been the mainstay of oceanographic research, the wide variety of spatial and temporal scales on which ocean processes operate requires a broader approach. Increasingly, systems of moorings, floats, and gliders work in tandem with ship-based sampling to provide data on a variety of spatial-temporal scales. *In turn, it has spurred the desire for the continued development of sensing systems that are robust in the marine environment, compact, require low power, and determine key oceanographic parameters at sufficient resolution and accuracy.*

1.5 Phosphorus Recognition and Detection

1.5.1 Challenges and Considerations

As the eleventh most abundant element on earth, phosphorus occurs naturally in soil and plays a critical role as an essential nutrient for animals and plants; in the structural integrity of cell components, gene regulation, energy storage, and signal transduction.¹⁸⁻²² Phosphorus is commonly found in the chemical form of phosphates which displays cross-interference with other common nutrients, possesses high hydration enthalpy²³⁻²⁴ and structural dependence on pH,²⁵ existing as $\text{H}_3\text{PO}_4/\text{H}_2\text{PO}_4^-$ in acidic environments and $\text{HPO}_4^{2-}/\text{PO}_4^{3-}$ in more alkaline environments. Lastly, various temporal scale processes act upon the ocean phosphorus cycle, phosphorus diffusion across the lithosphere, hydrosphere, and biosphere.²⁶⁻²⁷ *Thus, it requires oceanographers to make accurate and precise temporal and spatial measurements while needing access to reliable and robust in-situ techniques.*

1.5.2 Environmental Indicators and Assays

A significant challenge in marine science has been delivering inexpensive, robust, and portable sensor devices to measure phosphate nutrient levels with high sensitivity and

selectivity. The modern science of color vision (colorimetry) powerfully shaped identifying and quantifying anion composition. Colorimetry was commonplace in laboratories before wide accessibility to commercialized spectrophotometry and chromatography instrumentation. Performing colorimetric experiments enabled the detection of anions by the perception of color changes. As a prime example, the molybdenum blue phosphorus method is a wet-chemical technique performed with a single solution reagent composed of ammonium molybdate, ascorbic acid, and antimony. In the presence of orthophosphate, a rapid reaction occurs and yields a blue-purple compound corresponding to the self-assembly of phosphomolybdate complexes (structural form: β -keggin ions).²⁸ The β -keggin ion colorant can be optically monitored for chemical analysis.

Advancements in analytical instrumentation, such as inductively coupled plasma mass spectroscopy (ICP-MS) and high-performance liquid chromatography (HPLC), have recently enabled the detection of chemical analytes for water quality assessment.²⁹⁻³⁰ ICP-MS can achieve low detection limit measurements as low as parts per billion (ppb, $\mu\text{g/l}$) to parts per trillion (ppt, ng/l) with remarkable speed, precision, and analyte sensitivity. A plasma source is heated to vaporize the sample into individual atoms or ions, separating the ions based on their mass-to-charge ratio. However, compared to other MS techniques, ICP-MS with argon plasma introduces interfering polyatomic species and is susceptible to orifice leakages introducing constituent gases of air and contamination of instrument apparatuses. HPLC is an analytical technique for separating, identifying, and quantifying trace organic compounds. The significant drawbacks of ICP-MS and HPLC are due to the intrinsic time-sensitive nature of pollutant collection and analysis. Like

most laboratory-based instrumentation, the operation is costly, labor-intensive, and cannot achieve rapid deployment for direct field use.

1.6 Chemical Sensing Technologies

According to the International Union of Pure and Applied Chemistry (IUPAC), a chemical sensor is a technology capable of transducing chemical information (concentration and composition) into an analytical signal in the form of optical, fluorescence, electrical, etc. The chemical sensor platform comprises several core elements: a receptor and signal transducer. The receptor may include a natural or synthetic molecule that preferentially interacts with a target species. At the same time, a transducer may consist of benchtop laboratory instruments or miniaturized devices that monitor property-induced changes when subjected to an analyte of interest. There are two general categories of aquatic nutrient sensors: optical and electrochemical. Among all the published work on optical sensors, fluorescence detection is the method of choice for numerous diagnostic and research applications.³¹ Fluorescence offers the most straightforward route to multiplex analysis, which can significantly increase material throughput testing and reduce expenses. However, conventional fluorescent reagents limit assay sensitivity or require complex and expensive instrumentation to deliver the required performance. Electrochemical sensors are emerging analytical tools that transduce electrochemical reactions into an applicable signal. These sensors offer low-cost fabrication, diverse functionalities, lightweight and portable frameworks, and modular properties to tune the device affinities toward chemical and biological analytes.

1.7 Conjugated Polymers

1.7.1 Status of Conjugated Polymers

New emerging markets are enabled by solution-processable electronic materials and their harmonious assimilation into novel systems. Molecule-based semiconductors, ranging from small molecules to conjugated polymers, afford functional and highly receptive properties towards a variety of external stimulants. Of the major device platforms, organic field-effect transistors (OFETs) possess one of the highest market potentials but still have not reached commercialization performance. Yet, significant efforts and improvements have been made over the past few decades due to our progressive understanding of charge transport in amorphous and semi-crystalline conjugated polymers, strong foundations in structure-property relationships, and design-driven computational methods to lead experimental efforts.

1.7.2 Historical Survey of Conjugated Polymers

Conjugated polymers encompass a diverse set of organic macromolecules structurally characterized as a delocalized π -electron system, yielding optical signatures and electronic behaviors suitable for a wide array of new-generation electronic materials (Figure 1.2).³²⁻⁴⁵ Since the initial discovery and characterization of highly conductive polymers in halogen-doped polyacetylene (1976),⁴⁶ organic electronic materials with structural variants ranging from small molecules and polymers have been realized and enabled far-reaching fundamental science and distinct manufacturing paradigms. As such, the scientific community recognized the impact and potential of conductive polymers by awarding the 2000 Nobel Prize in Chemistry jointly to Alan J. Heeger, Alan G. MacDiarmid, and Hideki Shirakawa. Each laureate made their seminal findings during

the late 1970s and developed conjugated polymers into a primary research domain. From polyacetylene, the simplest linear conjugated polymer in terms of molecular design, a diverse portfolio of monomers and conjugated polymers were successfully created due to the pioneering works of Richard F. Heck, Ei-ichi Negishi, and Akira Suzuki, all of whom were jointly awarded the Nobel Prize in Chemistry 2010 based on palladium catalysts.

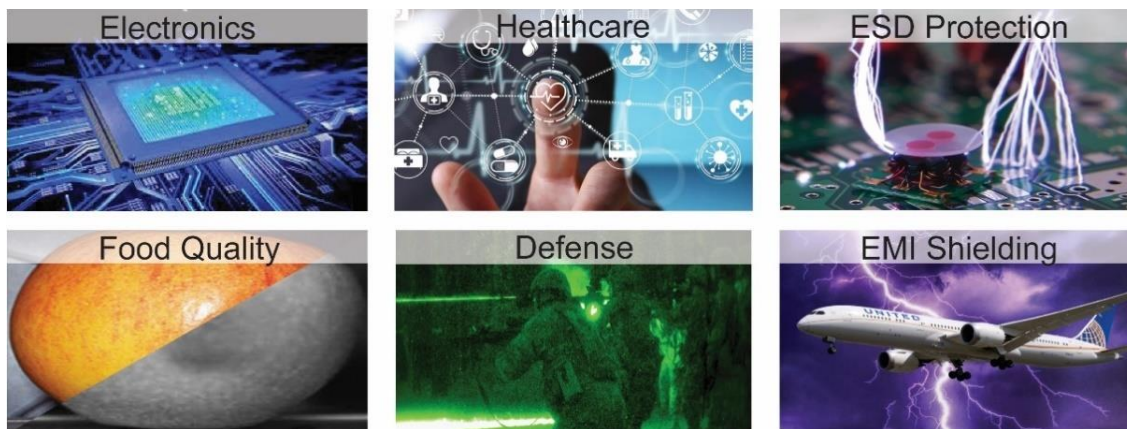


Figure 1.2 *Current conjugated polymer-based technology sectors.*

The early history behind conjugated polymers predates both the ability to characterize the molecular structure of materials and the Hermann Staudinger macromolecular theory of polymers (the 1920s). Scientists have argued that the first fully synthetic polymer was also the earliest known example of conjugated polymers. Polyaniline, known as emeraldine or aniline black, displayed practical use in its most primitive form and became widely recognized as the first synthetic dye created, commercialized, and electropolymerized (Figure 1.3).⁴⁷ Polypyrrole gave a new outlook to organic polymers being the first conjugated polymer to exhibit significant conductivity and to be prepared as a plastic film. Afterward, vast improvements in synthetic approaches and characterization tools resulted in establishing conjugated polymer constructs that are uncross-linked and not polymerized via oxidation. Linear

polyacetylene was first generated in 1955 using novel catalytic systems based on organometallic compounds. It later garnered the scientific community's attention following the inadvertent formation of a silvery film (product from a Ziegler-Natta catalyst overload). The film resulted in remarkably high electrical conductivity and achieved values competitive to graphite. Following this century of studying these materials in a sporadic and isolated fashion, the chemical processes and properties were analyzed intensely in the 1970s after the ground-breaking work on conducting polymers. Specifically, in 1977 significant milestones were reached by Alan J. Heeger, Alan G. MacDiarmid, and Hideki Shirakawa, producing crystalline polyacetylene with metallic properties ($> 500 \text{ S cm}^{-1}$) following exposure to halogen vapor.^{46, 48} These seminal findings revolutionized the field, accelerated the burgeoning development of conjugated polymer chemistry, and provided new avenues to enhance the film properties via chemical doping. At this point, the most challenging obstacles to the applicability of conjugated polymers involve the solution-processability issues in water and organic solvents and the unstable nature to oxidative degradation, all of which hinder its commercial viability. The main objective was to structurally modify the polymers to alter the optoelectronic properties, electrochemical/environmental stability, and solution-processability using new synthetic tools. The introduction of poly(3,4-ethylenedioxythiophene) doped with polystyrene sulfonate (PEDOT:PSS) solved the solution processability issues. PEDOT:PSS is an aqueous dispersion of two ionomers and possesses a unique combination of transparency, conductivity, and flexibility.⁴⁹⁻⁵⁰ Since then, a diversity of conjugated polymer materials has been produced at the industrial scale and plays an integral role in modern electronics.⁵¹⁻⁵² *Nevertheless, for the field to*

progress, further elucidation on essential aspects of the role of chemical structure towards the final device properties is needed to enable the desired functionality.

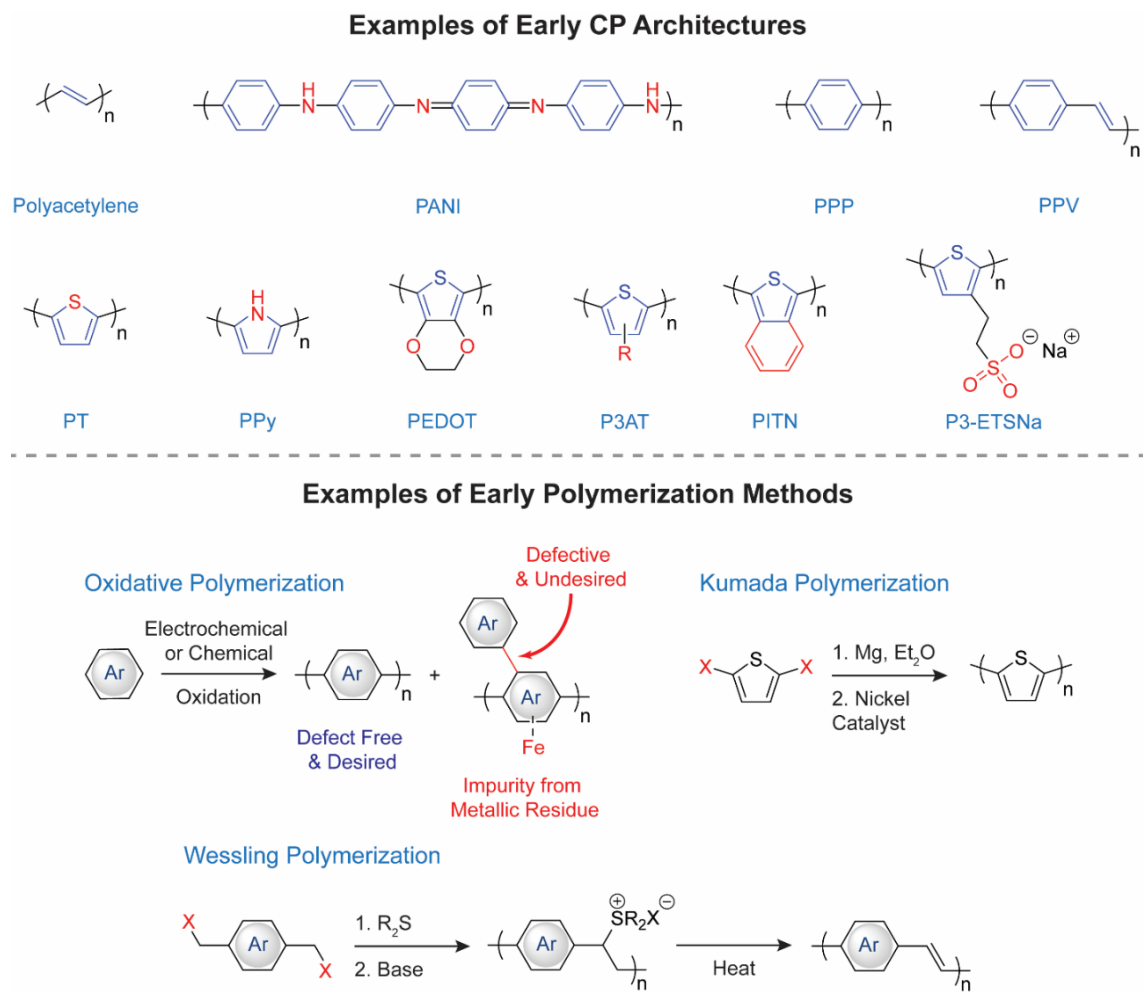


Figure 1.3 Early examples of polymeric structures and synthetic protocols.

1.7.3 Semiconductor Electronic Band Structure

The band theory of solids (Figure 1.4), developed by Felix Bloch in 1928, is a valuable model that describes the electronic states within solid materials.⁵³ This framework conceptualizes the relationship between the availability of free electrons in a system – the energetic gap (bandgap, E_g) between the valence and conduction bands – and the material classification as an insulator, a semiconductor, or a conductor.⁵⁴ The

discrete energy levels of atoms mix and form electronic bands, in which the width is characterized by a density of electronic states (DOS). The DOS tells us the number of available (existing) states at any given energy, E . In conjugated systems, the valence and conduction bands are analogous to the highest occupied molecular orbitals (HOMO, π -band) and lowest unoccupied molecular orbitals (LUMO, π^* -band) of molecules, respectively. The magnitude of the energy gap separating these frontier molecular orbitals relates to the behavior of the electrons (their ability to transfer to excited energetic states).

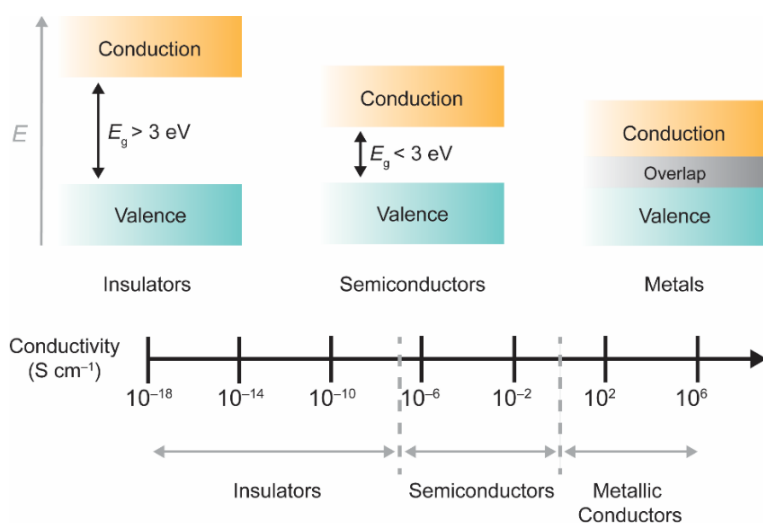


Figure 1.4 *The band model and electrical conductivity range of insulators, semiconductors, and conductors. The electrical properties are determined by the size of the bandgap, the energy difference between the valence and conduction bands. Figure was motivated and adapted from Ref. 53.*

Insulators possess high electrical resistance due to the tightly-bound nature of the outer electrons. According to the band theory of solids, the bandgap, composed of forbidden energies (where electrons cannot occupy), is too large ($E_g > 3 \text{ eV}$) to overcome, and electrons cannot reach the conduction band to yield free charge carriers in the system. Metals are conductors of electricity and can readily transport free charge carriers from the overlapping valence and conduction bands. Semiconductors, including

small molecules and conjugated polymers, possess a narrower bandgap than insulators ($E_g < 3$ eV). When the gap between the frontier orbitals is narrow enough, a finite number of electrons ($e^{E_g/kT}$) can access the conduction band via thermal excitation. The frontier orbital energetics dictate the electrical properties and can be modulated by doping techniques that generate free charge carriers. Frequently adopted strategies for doping include chemical, electrochemical, photo, and interfacial. Chemical and electrochemical doping are unique because the effects are permanent until charge compensation or the removal of carriers occur. Photo-induced doping is well-known in the application of photoconductors, and while the properties are transient, the intensity of the light-radiant energy controls the level of channel conduction. The excitonic processes persist until the carrier is trapped or quenched via recombination. Interfacial doping involves charge injection and extraction in the absence of counter-ions. The electrons and holes reside in the π^* -band and π -band, respectively, only under appropriate voltage bias conditions. It's worth noting that charge injection onto conjugated macromolecular chains, denoted as "doping", is mechanistically distinct from the doping processes of epitaxially grown inorganic semiconductors (silicon, germanium). *The material properties (molecular, electronic, morphology, and permittivity) significantly influence the conductivity and the associated loss mechanisms.*

1.7.4 Physics of Doping

Processes that result in doped semiconductors decrease the bandgap further by altering the electron population of intragap states. Doping in inorganic semiconductors involves the substitutional insertion of atomic impurities into a regular crystal lattice structure. It can be classified based on the majority carriers within a closed system:

predominantly holes (p-type) or electrons (n-type). The majority carrier type is controlled by the insertion of atoms that have higher valence (pentavalent, n-type impurity) or lower valence (trivalent, p-type impurity) compared to the host atom (silicon). Charge neutrality is maintained despite the mechanism of action and the underlying microscopic details.⁵⁵ In a uniformly doped semiconductor, the sum of charges associated with the carriers must equal zero; the negative charge of an electron (n_o) or ionized acceptor (N_A) cancels out the positive charge of a hole (p_o) or ionized donor (N_D), where $p_o + n_o + N_D + N_A = 0$. This concept is also applied to conjugated, macromolecular chains.

Nevertheless, the chemical doping phenomenology of conjugated polymers is unique compared to inorganic semiconductors. Doping conjugated polymer semiconductors involves the oxidation (p-type) or reduction (n-type) of the π -electron system and the anisotropic chemistry of the host material.⁵⁶ *The underlying physics of doping and the systematic control of structure and morphology are paramount to the progress of material science and multifunctional macromolecular materials with tunable electronic configurations.*

The most intuitive way to understand the physical processes behind molecular doping of organic semiconductors is by using models and representations showing the transferability of electrons between the host and dopant species. The simplest case involves “an integer number of electrons transferred from the polymer to the dopant molecule (p-doping) or the dopant molecule to the polymer (n-doping)” (Figure 1.5).⁵⁷ The ease of transferability is controlled by the energetic offset between the dopant electron affinity (EA) and the polymer ionization potential (IP) for p-doping and the energetic difference between the polymer EA and the dopant IP for n-doping.

Unfortunately, this model does not capture every relevant process and relationship and fails to explain why specific systems deviate from this concept. Many host/dopant systems possess significant activation energies compared to their theoretical amount. The low permittivity, formation of hybridized host/dopant complexes, and effects on the nano-/microstructure, while not an exhaustive list, are notable explanations to describe the origins of the activation energy and the disparity between theoretical and experimental data.⁵⁸ Also, dopants are generally processed into organic films through co-evaporation, wet-chemical techniques, or gas-phase exposure.⁵⁹ The mere existence of different polymorphs and the positioning of dopant molecules in the host matrix introduces unique doping mechanisms. *While the film processability can be achieved with ease, an improved understanding of the doping-processing-nanostructure relationships is required and remains an elusive concept due to the intricate processes behind OSC-dopant interactions.*

Molecular doping in polymers is linked to many convoluted processes, of which electron transfer alters the polymer charge carrier density and transport. Two widely recognized electron transfer processes are ion-pair formation (IPF) and ground-state charge-transfer complex (GS-CPX) formation.⁵⁹⁻⁶⁰ While there's more to the design rules than just the alignment of the EA and IP, their energetic values play a major part in understanding how electron transfer occurs between the host and dopant and why specific systems favor p-type over n-type doping and vice versa. The key notion behind IPF is the energetic difference between the EA and IP. Since the energy of an electron increases moving upwards in the energy diagram (due to lower binding energy), an electron is transferred to the acceptor molecule, which possesses a lower energy state for the

electron to reside. The electron-rich or -poor character of the polymer defines if the process is p-type or n-type doping, respectively, because the mobile charge carriers are governed by the intrachain and interchain transport of the polymer. For example, in p-type doping, the OSC EA must be higher or equal in energy than the dopant IP, in which the electron transfers from the OSC HOMO to the dopant LUMO. The electron transfer to the LUMO results in the formation of dopant anion and OSC cation (the ion-pair) (Figure 1.6), which is exemplified in copious amounts of prototypical polymer-dopant systems.

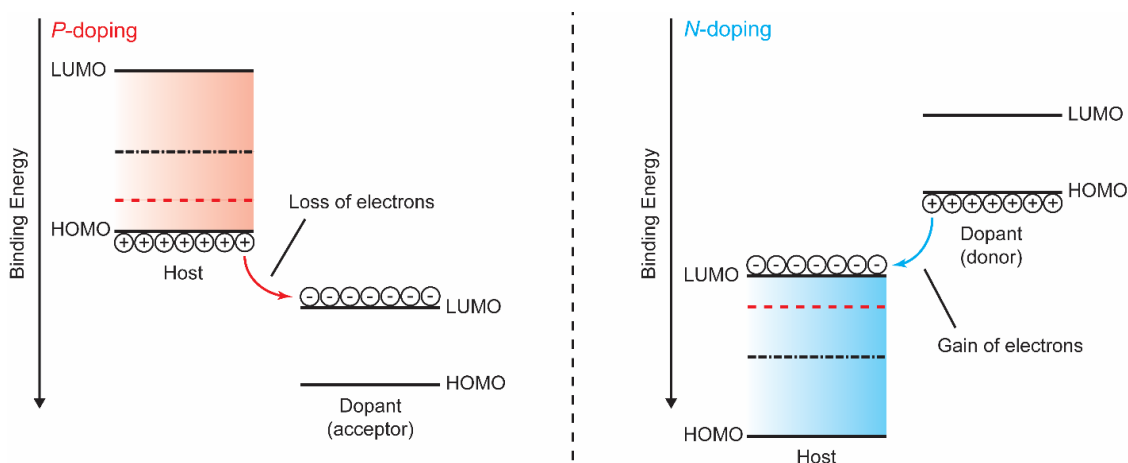


Figure 1.5 Schematic representation of chemical doping involving p-type and n-type doping processes. The mechanism is fundamentally rooted in the alignment of energy levels which electron transfer can take place. Figure was motivated and adapted from Ref 57.

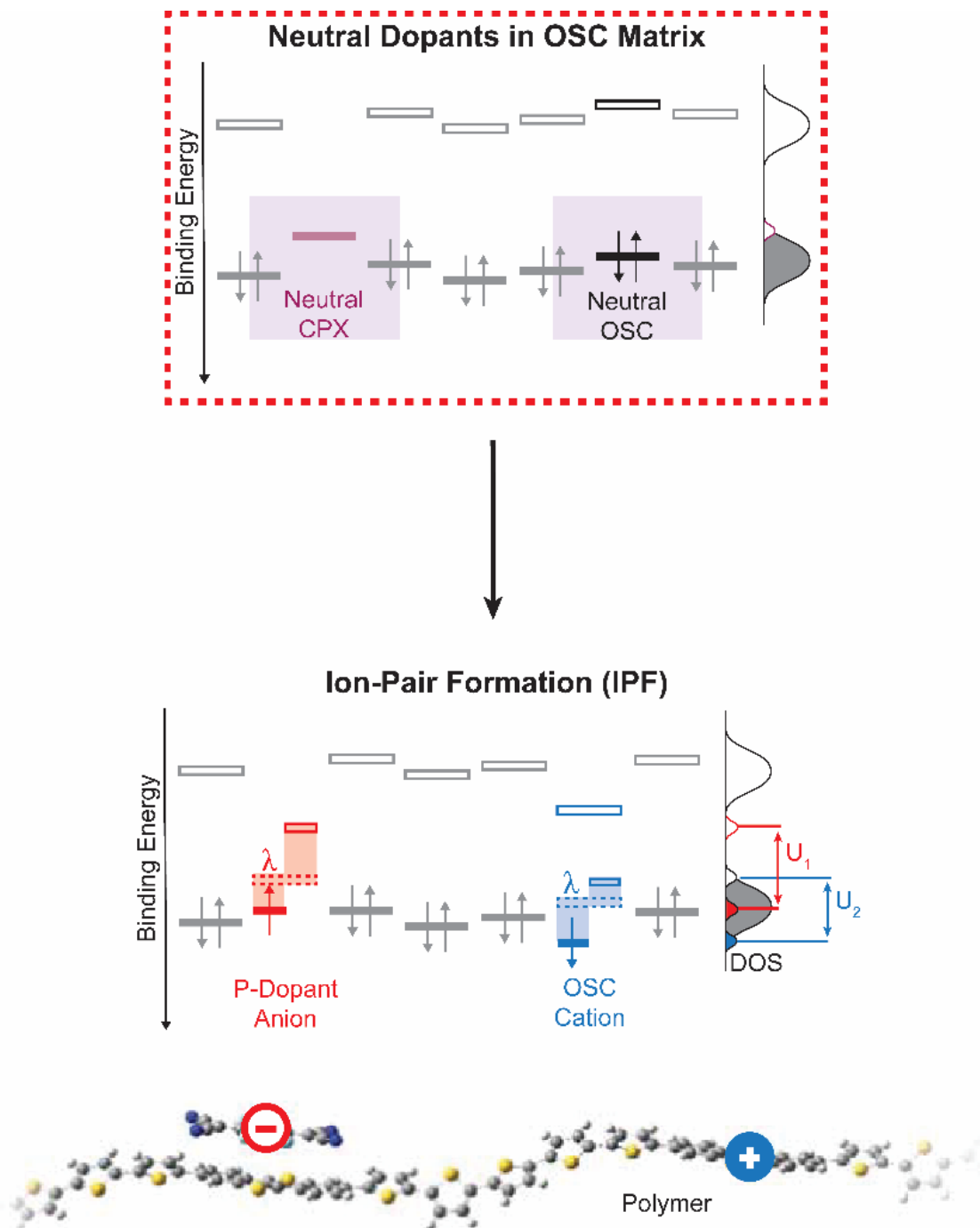


Figure 1.6 Schematic showing how the embedment of neutral dopant molecules influences the OSC energy levels with an emphasis on ion-pair formation (IPF). Figure was motivated and adapted from Ref 60.

In contrast to ion-pair formation, a GS-CPX formation is another known doping mechanism that involves the supramolecular hybridization of frontier orbitals between conjugated polymer and dopant species. This process generates a new set of frontier orbitals (modified DOS) whose occupied bonding ($E_{CPX,H}$) and antibonding orbital energies ($E_{CPX,L}$) as given by in a Hückel-type model (Equation 1.1):

$$E_{CPX,H/L} = \frac{H_{OSC} + L_{dop}}{2} \pm \sqrt{(H_{OSC} - L_{dop})^2 + 4\beta^2} \quad (1.1)$$

where β is the resonance integral and describes the force binding two neighboring molecules.⁶⁰ The unique nature of GS-CPX permits the interactions between molecules where the H_{OSC} and L_{dop} are not in resonance (Figure 1.7). The probability of occurrence for hybridization is equal regardless of the L_{dop} energy being higher or lower than the H_{OSC} .⁵⁹ Newly formed frontier orbitals are generated from the hybridization, but their relative amplitudes govern the extent of charge transfer (δ). Both IPF and CPX can form simultaneously where only partial charge transfer is observed. CPX formation has been detected in numerous conjugated molecules⁶¹⁻⁶⁴ and polymers.⁶⁵ Fourier transform infrared spectroscopy (FTIR) is commonly employed to investigate the doping mechanism, in which the CPX exhibits diagnostic electronic absorption bands. For example, studies have been conducted on the doping of poly(3-hexylthiophene-2,5-diyl) (P3HT) and quaterthiophene (4T), a thiophene oligomer, using a 2,3,5,6-tetrafluoro-7,7,8,8-tetracyanoquinodimethane (F₄-TCNQ) p-dopant. Vastly different phenomenology was observed using the diagnostic cyano-vibrations (C≡N) and energy levels of F₄-TCNQ. Under the effect of IPF, the lateral conductivity of P3HT was improved by

several orders of magnitude compared to 4T since the latter case only translated into partial charge transfer ($\delta = 0.21$). These supramolecular hybrid energy levels can be quantitatively determined using ultraviolet photoelectron (UPS) and inverse photoemission spectroscopy (IPES), commonly employed surface science techniques that measure the occupied and unoccupied electronic structure of molecules. Many fundamental challenges must be addressed to rationalize the molecular doping processes in OSCs fully. *Our understanding of intermolecular coupling, phenomenologically intermediate cases between IPF and CPX formation, and Coulombic interactions of ionized species and charge carriers (trapping mobile carriers) are several areas that need to be addressed to construct a unifying picture of doping and the associated charge transport properties.*

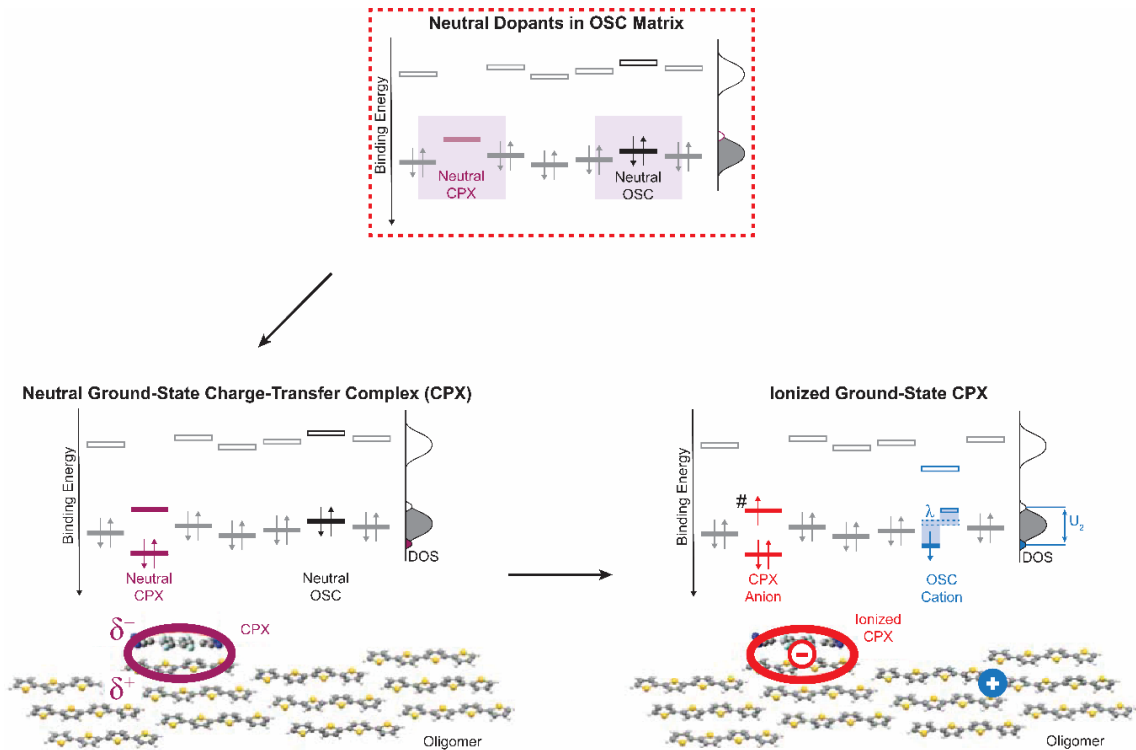


Figure 1.7 *P*-type doping of neutral dopants in a OSC matrix, emphasizing the formation of a neutral and ionized ground-state charge-transfer complex (CPX). λ is the

reorganization energy, and U_1 and U_2 denote the Hubbard U of the neutral dopant and OSC. Figure was motivated and adapted from Ref 60.

1.7.5 Charge Carrier Transport

1.7.5.1 Molecular Design Considerations

While inorganic technologies still outperform many doped conjugated polymers, it was apparent to researchers back in the 1990s that the electrical conductivity, charge carrier mobility, environmental and electrochemical stability, and charge storage capacity were lagging far behind to breakthrough to the marketplace. Of the major device platforms, field-effect transistors have the highest market potential outlook because they constitute the basic building blocks of integrated circuits and displays. However, the efficiency of an electron to move through an OSC (electron mobility) is not sufficient for current-driven OLED displays.⁶⁶ The key focus was centered around the molecular and process engineering of conjugated polymers to meet the ever-growing demands of the consumer market, as device operation and efficacy are bound to the material properties and process engineering conditions.

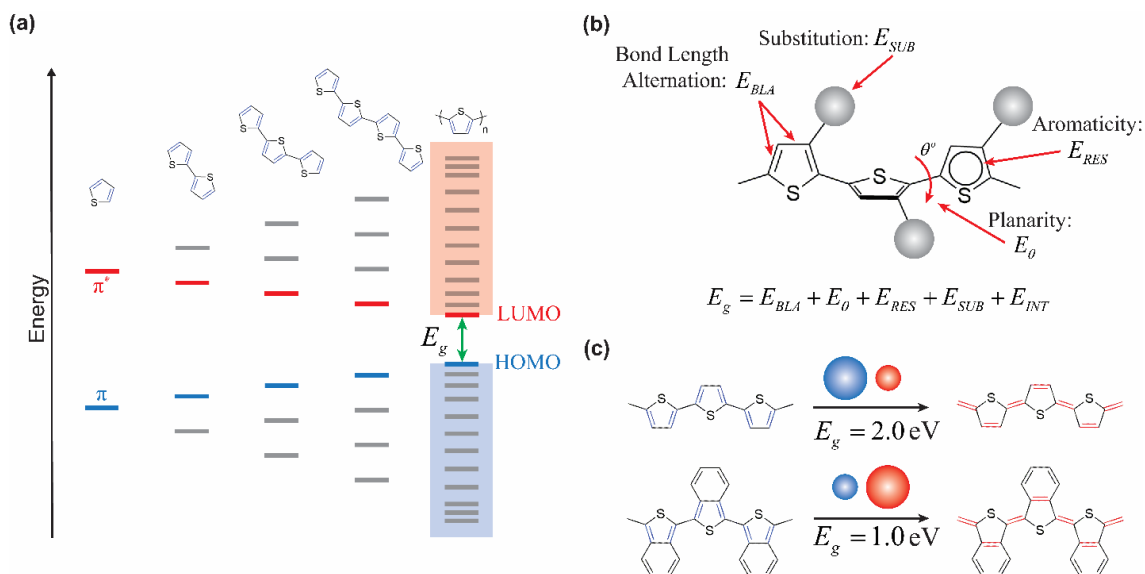


Figure 1.8 *Strategies for controlling the material bandgap. (a) Modulate the HOMO-LUMO energy gap through π -conjugation extension. Example structures include a thiophene monomer, dimer, trimer, tetramer, and polymer with their associated energy levels. (b) Other structural features that contribute to the bandgap: bond length alternation (E_{BLA}), substituents (electron-donating or -withdrawing character), intermolecular interactions between chains (E_{INT}), backbone planarity (E_{Θ}), and monomer aromaticity (E_{RES}). (c) Enhancing the quinoid nondegenerate resonance states promotes double-bond delocalization and thus, narrower bandgaps. Figure was motivated and adapted from Ref 67.*

The bandgap and the positioning of the HOMO and LUMO bands versus vacuum are essential parameters constrained to the molecular chemical design.⁶⁷ Several chemical design strategies produce high-performing, narrow bandgap materials based on straightforward principles. For electron transport is fastest along the backbone axis, one can vision a hypothetical scenario in which complete electron delocalization is achieved along a planar, conjugated chain. This particular structure would acquire a backbone structure composed of all carbon-carbon bonds with the same bond length, known as the bond-length alternation (BLA).⁶⁸ Reduced BLA can be expected to enhance the optoelectronic properties due to a narrower bandgap. Extending the π -electron system by covalent attachment of conjugated monomer units while increasing the molecular weight extends the conjugation length and effectively narrows the bandgap. Except for a few conjugated polymers (e.g., polyacetylene), most aromatic systems such as polythiophene and other heterocyclic conjugated polymers have a non-degenerate ground state, in which two existing mesomeric structures (aromatic and quinoidal) are not energetically equivalent.⁶⁹ The population distribution between aromatic and quinoid is limited to its energetic stability. For example, while offering stability, the aromatic form is typically the dominant structure. Still, it is not effective in delocalizing electrons along the chain because of the inherent confinement of its π -electrons. The quinoid form possesses a

higher energetic state and a narrower energy gap to promote electrons for transport means. An energetic penalty is associated with the aromatic-quinoid transition, which determines the aromatic stabilization resonance (E_{RES}).⁷⁰ The donor-acceptor approach is now the most conventional route to control the bandgap (Figure 1.9).^{67, 71} It introduces alternating electron-rich (donor) and electron-deficient (acceptor) units along the backbone length. The bandgap and ensuing properties are governed by the hybridization of the corresponding donor and acceptor frontier orbitals and gave rise to narrower bandgaps due to quinoid stabilization and more π -electron delocalization. The backbone rotational disorder, or the mean deviation from planarity (E_θ), can negatively affect the bandgap, limiting the π -electron delocalization.⁷² Strategic insertion of electron-withdrawing and -donating functionalities on the monomer units can directly alter the HOMO and LUMO energy levels. Strong electron-withdrawing (-donating) groups can affect the HOMO levels by shifting them further away from the vacuum level.^{67, 73}

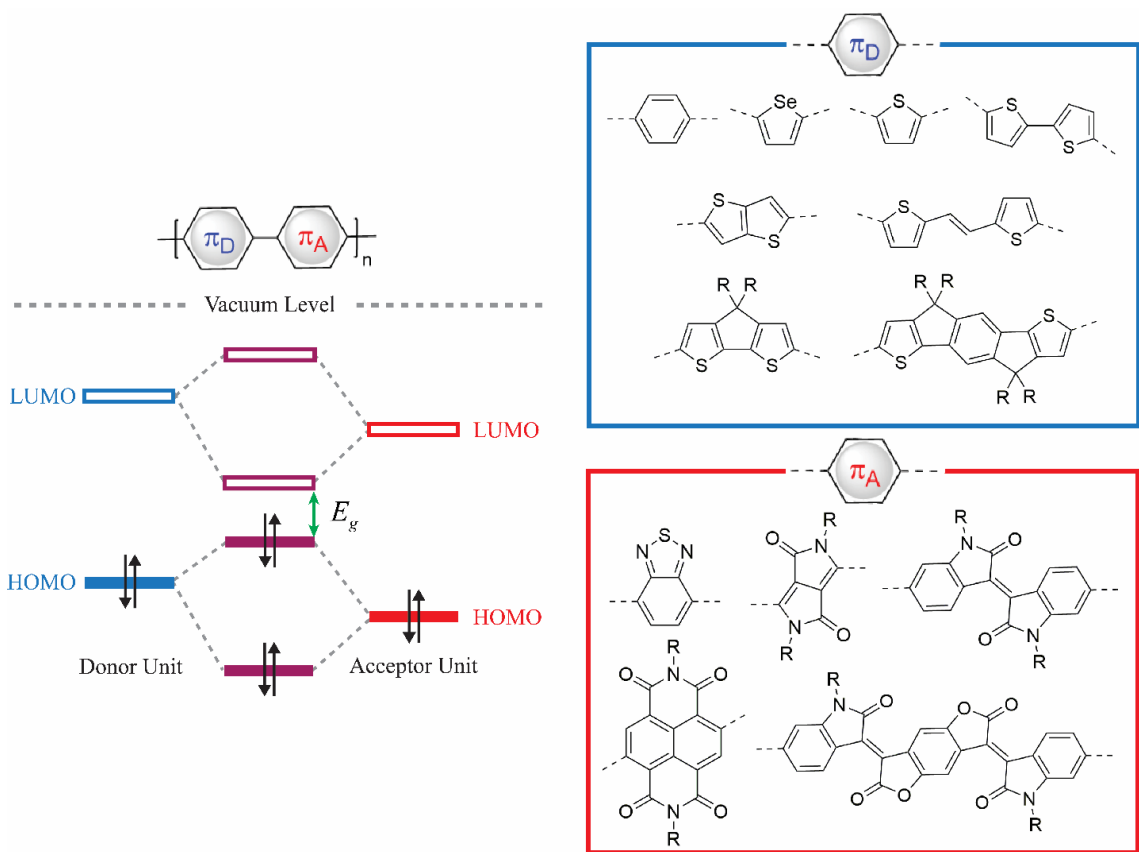


Figure 1.9 Donor and acceptor orbital hybridization upon coupling, possessing a narrower bandgap compared to conjugated homopolymers. Monomer library showing frequently used electron-rich donors (π_D) and acceptor (π_A) units Figure was motivated and adapted from Ref 73.

1.7.5.2 Dynamics of Intrachain and Interchain Transport

Conjugated polymer chains, due to their torsional disorder, have many spatial configurations or conformational freedom. The physical properties are highly dependent on chain conformation, intermolecular interactions, and multiscale microstructures varying from entirely amorphous to crystalline.⁷⁴ The structural disorder is inherent in many conjugated polymer systems and has shown evidence of electron localization and trap sites that limit carrier mobility.⁷⁵ The intermediate semicrystalline structures, while poorly understood, exhibits semi-ordered and disordered domains and are displayed in

numerous molecular systems. The co-existence of ordered regions made of co-facially stacked molecules and lattice disordered regions produces a range of length scales dictating how the charge carriers effectively travel within the OSC (Figure 1.10).^{74, 76}

Intrachain transport involves the delocalization of the electron across the backbone. While intrachain processes are faster than interchain, the wavefunction overlap (electron coupling between monomer units) is essential to attaining high carrier mobility and is done through careful molecular design (Figure 1.8).⁷⁷ Conjugated polymers are typically hampered by molecular defects caused by twisted bonds and steric effects, reducing the π -conjugation length and mobility. Extensive chain alignment between neighboring conjugated sections can deliver fast charge motion *via* charge hopping.⁷⁸ It is well-known that poorly ordered or nearly amorphous microstructures decrease carrier mobility. Recent observations have linked electronic localization to the rise of trap-limited transport and are reflected in the Gaussian distribution in the frontier orbital energies (Figure 1.11).⁷⁹ The extended tail, or band tail states, possess a DOS projecting into the material bandgap with a continuous distribution in energy and can disrupt the charge carrier transport acting as hole/electron trap sites.⁸⁰ Deeper traps in the bandgap can be created as more structural defects/disorders are introduced to the system.

Molecular-scale features such as molecular weight, dispersity (\mathcal{D}), solubilizing groups, backbone rigidity, chain π - π stacking, and substrate compatibility influence the domain size, polymer phase segregation, and interchain transport processes.

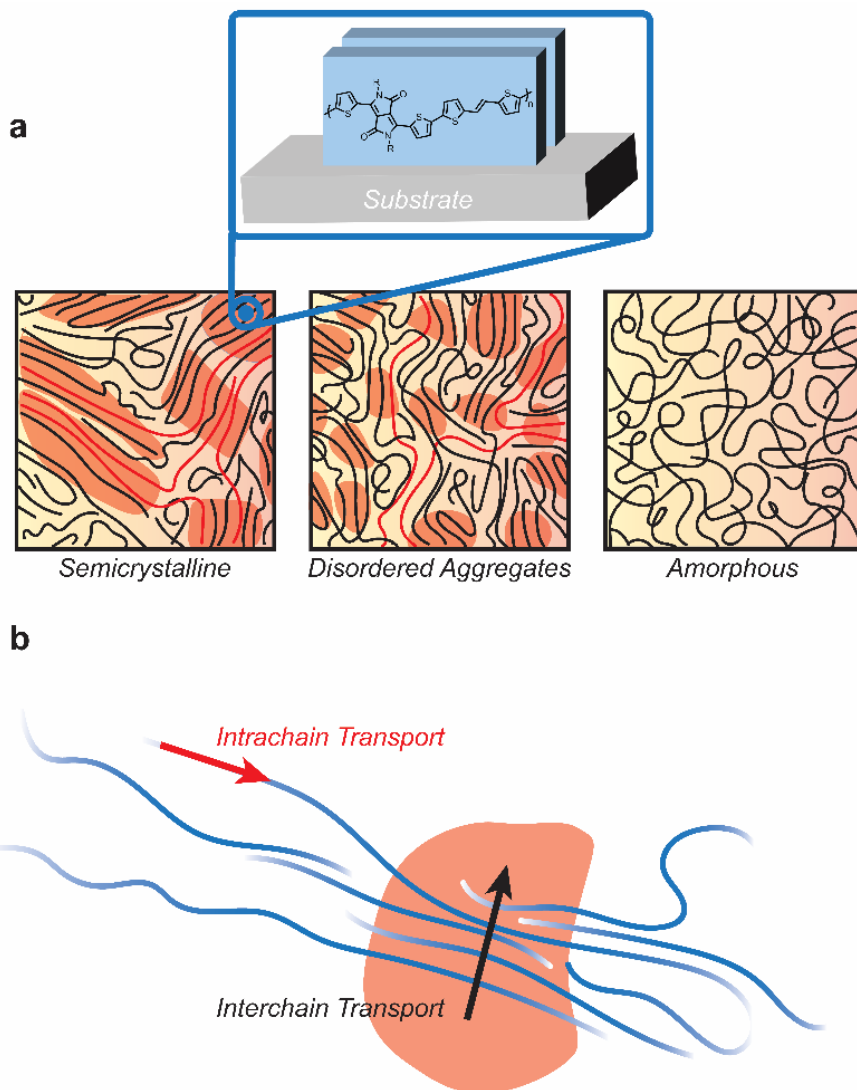


Figure 1.10 Schematic illustrations of common solid-state (a) microstructures (semicrystalline, disordered aggregates, and amorphous) and (b) intra- and interchain charge transport. Figure was motivated and adapted from Ref. 74.

The rate-limiting step in macroscopic transport is the interchain charge transport. The anisotropic chemistry of conjugated polymers affords unique properties that control macroscopic charge transport and even offers advantages to enhance chemical doping. The electronic structures remain intact due to the strong intrachain bonds. At the same time, the chain packing is composed of weak forces (e.g., van der Waals) that are easily disturbed, giving rise to a number and variety of defects that complicate transport.⁵⁶ π -

cloud overlap between adjacent chains is associated with ordered domains and contributes to the reduction of interchain distance and activation barrier for transport following a phonon-assisted hopping mechanism.⁸¹ Phonon-assisted tunneling is a quantum mechanical process that occurs between two neighboring sites on separate chains, where the electron tunnels through an energetic barrier for activation hopping, producing two-dimensional transport. The mechanism is highly sensitive to the π - π stacking mode (face-on, edge-on, and end-on).⁸² *Due to the hypersensitivity of microstructures to the deposition conditions, it is imperative to discern the relationships between process-dependent π -aggregate formation and connectivity towards macroscopic charge transport.*

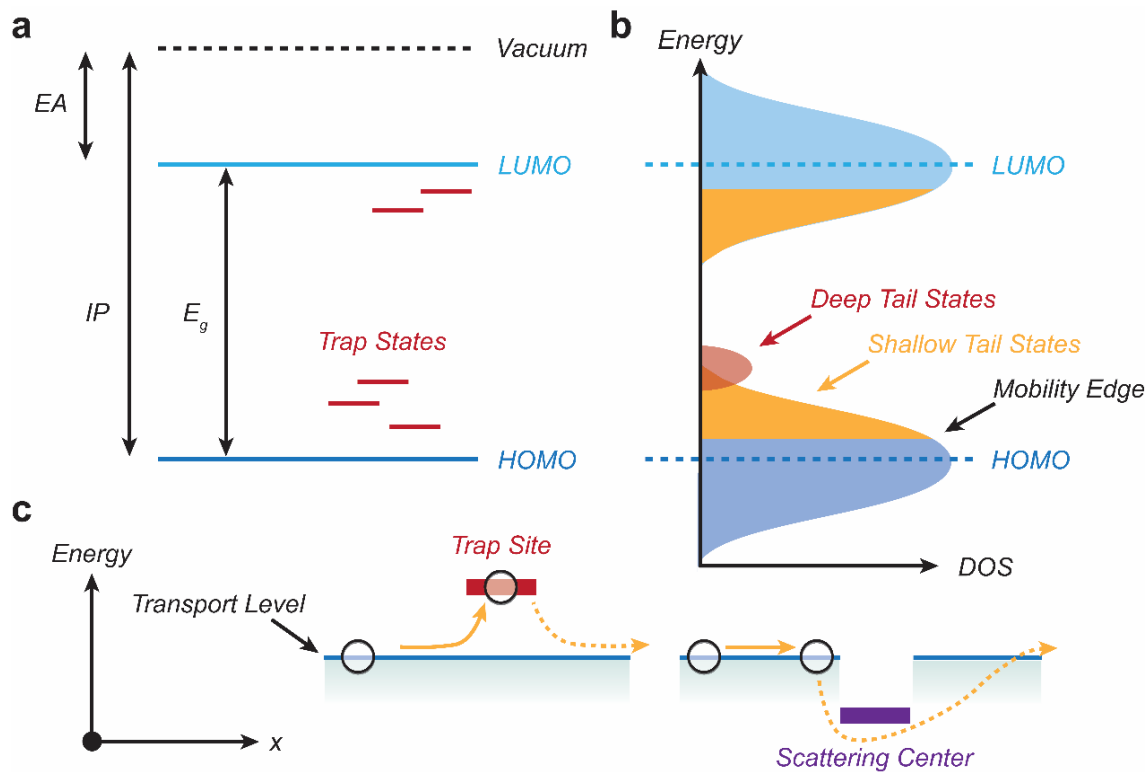


Figure 1.11 OSC energy levels. (a) HOMO and LUMO energies with respect to the vacuum level, showing the electron affinity, ionization potential, optical bandgap, and the presence of intragap trap states. (b) Another representation of the energy levels showing the density of states and the existing shall and deep tail states that hamper transport of

charges near the mobility edge. (c) Various transport barriers (trap sites and scattering centers) created by local defects and imperfections in the polymer matrix. Figure was motivated and adapted from Ref. 79.

1.7.6 OFET Chemical Sensors

OFETs have demonstrated utility in many consumer technologies and show unparalleled modularity in sensing a wide variety of biological, chemical, and physical analytes.^{5, 83} OFETs operating in aqueous environments and applying in chemical and biological detection are emerging technology anticipated to have profound effects on biomedical science, healthcare, and sensing platforms.⁸⁴⁻⁸⁹ These materials can be fabricated onto microarrays using diverse, low-cost manufacturing paradigms, affording the capability to integrate various sensors within a small area, precluding the need for expensive labeling and detection equipment, and offering real-time diagnostic tools that can be used in the field. Donor-acceptor conjugated polymers endow a unique set of optoelectronic properties as compared to their homopolymer analogues with improvements in chemical stability, tunable electronic structures, excitonic processes, and charge carrier transport. Analyte binding changes the surface potential and alters the OFET conductive channel. Of significant interest is that detection in the μM range could be achieved at a relatively low receptor density on the surface.

The limiting characteristics of this technology include the lack of available materials for the specific detection of other analytes, lack of specific/tailored interactions between the receptor and analyte, low number of conjugated polymers that demonstrate stability in aqueous environments, limited understanding of the features that account for this stability, the multistep nature of incorporating functionalized nanoparticle chemistries, and the non-specific interaction found in complex aqueous environments.

Furthermore, the detection limits necessary for reliable operation are typically in the nM range. It is straightforward to anticipate that an increase in sensitivity can be accomplished through approaches such as higher receptor density, interactions leading to more dramatic changes, and modification of the polymer and device structure.

1.7.6.1 Operation Mechanism of OFET Chemical Sensors

While various device architectures have been intensively researched and tested, OFET sensors embody some of the highest performing electronic detection platforms due to their inherent signal amplification properties originating from a three-terminal configuration. The device generates a tunable, internal electric field that induces the formation of mobile charge carriers. Unlike inorganics, these charge carriers adhere to the polymer backbone structure and are highly responsive to the surrounding environment changes. Conjugated polymer-based sensors can exhibit collective properties sensitive to minor perturbations and tailor analyte responses through straightforward synthetic means. Photo, pressure, and temperature sensors are a few other applications that have been explored.⁹⁰⁻⁹⁴ When exposed to these different external stimuli, the possible mechanism routes include change of the charge carrier density, conductivity, capacitance, and transport pathways.

1.7.6.2 Achieving Analyte Specificity: Receptor Integration

For chemical sensing, these devices usually rely on the serendipitous sensitivity of the material to the analyte of interest, and strategies for specific detection remain a challenge. Various conjugated polymer materials that utilize covalently bound recognition probes for binding to analytes have been studied as valuable platforms for facilitating chemical and biological fluorescence sensors. Due to rapid exciton migration

in conjugated polymers, a single analyte binding event can quench many fluorescent sites within the polymer leading to significant enhancements in sensitivity. Receptor integration in OFET devices is also necessary to achieve analyte specificity and enhance the binding signal in opposition to the background noise production.

Knopmacher *et al.* reported state-of-the-art OFET sensors stable in seawater over extended periods based on a high-performing isoindigo-based polymer.⁹⁵ To achieve detection Hg^{2+} induces a conformational change upon binding to DNA, causing an accumulation of negative charge near the OFET surface (*p*-channel enhancement). The binding events change the surface potential and alter the channel conduction with the magnitude of change based on the analyte concentration.

1.7.6.3 Supramolecular Interactions for Analyte Recognition

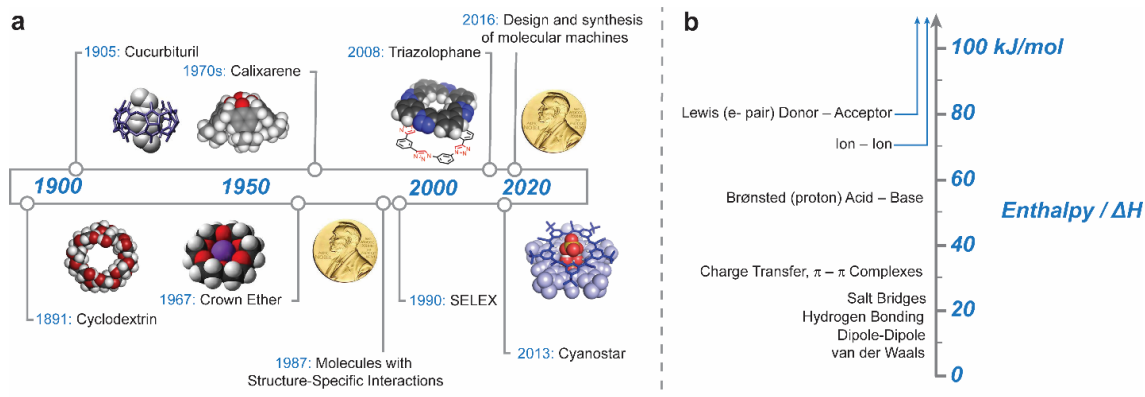


Figure 1.12 *Supramolecular host chemistries: (a) timeline of discoveries and (b) the bond enthalpies of various intermolecular interactions showing their relative strengths.*

The molecular recognition of anions has established roots in the late 1960s and later became fundamental pillars to modern supramolecular chemistry due to their prevalence in biological and environmental processes.^{23, 96-97} Computationally-driven design of anion receptors has led to remarkable progress in sensing, extraction, and membrane transport. Most of which were studied intensively in nonpolar media due to

poor receptor solubility in water and electrostatic screening of charges; the strength of the hydration layer is higher in anions than analogous cations. More elaborate design and tailored affinity are still necessary for proper utility in biological, medical, and environmental applications, predominantly in aqueous media. Acyclic systems have been proposed as a probable solution. For example, a series of guanidinium-based receptors have recently demonstrated the selective binding of phosphate and pyrophosphate in aqueous media in the presence of counter ions such as Cl^- , Br^- , NO_3^- , CO_3^{2-} , SO_4^{2-} , and ClO_4^{2-} .⁹⁸ The receptor has demonstrated phosphate binding with an affinity of 10^5 M^{-1} with negligible interactions in the presence of other anions. However, *acyclic receptors require aqueous solubility since the binding affinity demands of their collapsible structures (high conformational freedom) to generate the binding pocket.* Several macrocyclic systems made headway over the years as “host/guest” chemistries from shaped cavitands (cyclodextrins, calix[n]arenes, and cucurbiturils), bicyclic/polycyclic multidentate ligands (cryptands), crown ethers, and mechanically-interlocked molecular architectures (rotaxanes and catenanes).⁹⁹ Macrocyclic structures enable tunable binding properties based on physical (complementary shape and size) and chemical attributes (modes of intermolecular interactions) (Figure 1.12). *However, many macrocyclic structures are not designed for anionic species but rather towards electron-poor molecules.* The binding pockets of macrocycles, such as cyclodextrins and calix[n]arenes form inclusion complexes with polycyclic aromatic hydrocarbons of various shapes and sizes and was demonstrated for adsorption onto nanoparticle surfaces.¹⁰⁰⁻¹⁰² For cyclophanes, π -electron poor organic compounds are incorporated into their ring structures with binding affinities resulting from a combination of non-covalent bonding

interactions, including “face-to-face [$\pi\cdots\pi$] stacking and orthogonal [C–H $\cdots\pi$] interactions.”¹⁰³⁻¹⁰⁴ *In the quest for anion recognition, developing suitable receptor systems and compatible device materials and architectures remains a substantial challenge for operating in real-world conditions.*

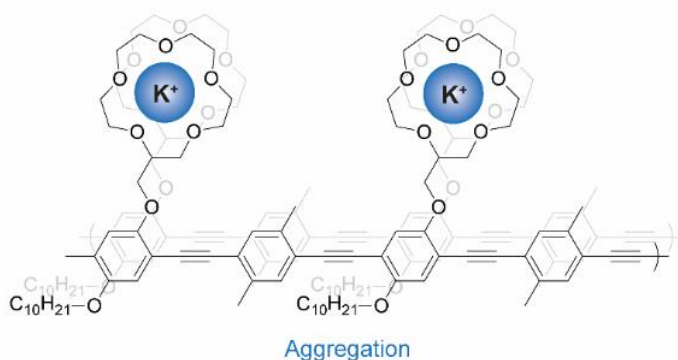
A recent form of hydrogen bonding centered around exotic interactions based on polarized C–H hydrogen-bonding motifs designed for binding weakly-coordinating anion species. “Cyanostar” (CS) (Figure 1.12) are promising charge-neutral, shape-persistent macrocycles that offer a subset of properties favorable for the sequestering, remediation, and detection of phosphate anions.¹⁰⁵⁻¹⁰⁷ However, they have never been incorporated into an OFET device architecture as a molecular recognition probe for chemical sensing, and there is lack of understanding how supramolecular systems can affect the charge transport properties of OSCs.

1.8 Summary

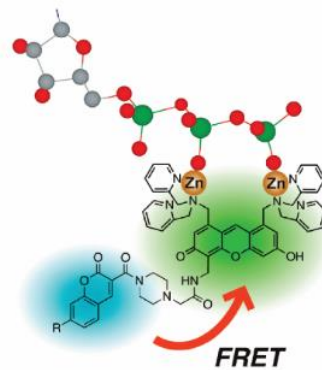
In particular, due to its inherent responsiveness to minor perturbations and structural tunability, conjugated polymers have shown to be promising candidates for developing novel chemical sensing platforms. Specifically, conjugated polymers can operate as signal translators for surface binding events or redox chemical reactions when electronically coupled to a media of interest. Alterations in the channel material electrical current can correspond to the nature of the surrounding environment—representing a physiological or environmental state. Thus, an electrical transduction platform can be realized to sense, record, and monitor surface activities in real-time. While a pristine form of the active layer would rely on serendipitous interactions towards an analyte of interest, specific detection can be achieved with the integration of suitable recognition probes to

facilitate binding events in proximity to the device surface. While optical detection¹⁰⁸⁻¹⁰⁹ has been the preferred method, most electrochemical systems are not designed to trace the presence of anionic species and range from membrane-based¹¹⁰⁻¹¹² to membrane-free (functionalized molecules, blended systems, and modified electrodes)¹¹³⁻¹¹⁶ (Figure 1.13). *A major contribution to the progress of chemical sensors is to further develop and exploit the sensitivity and selectivity of novel recognition probes for phosphate detection and expand the utility to other weakly coordinating analytes.*

a) Optical Detection



Angew. Chem. Int. Ed. **2000**, 39, 3868

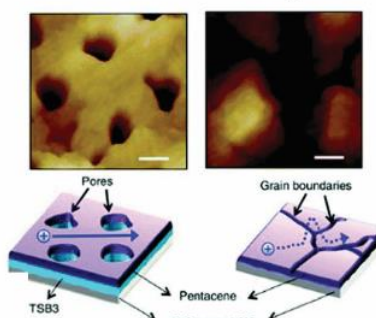


Förster Resonance Energy Transfer

J. Am. Chem. Soc. **2010**, 132, 38

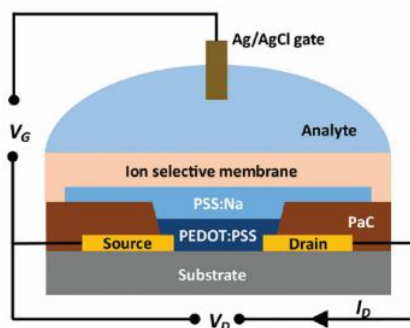
Electronic Detection Platforms

b) Membrane-Based Selectivity



Nanoporous Films

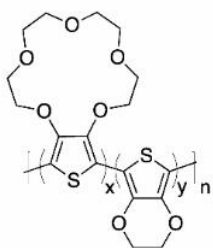
Mater. Chem. Front. **2020**, 4, 3505-3520



Ion-Selective Membranes

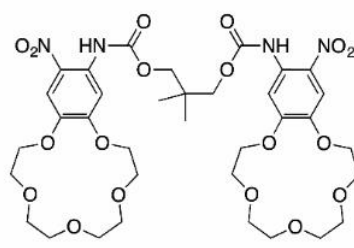
Adv. Mater. **2020**, 32, 2004790

c) Membrane-Free Selectivity



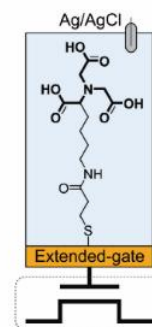
Functionalized

Adv. Funct. Mater. **2019**, 29, 194403



Blended

Adv. Electron. Mater. **2022**, 2100853



Modified Gate

ACS Sens. **2019**, 4, 2571

Figure 1.13 Traditional methods to endow ion selectivity using (a) optical and electrochemical (b) membrane-based and (c) membrane-free methodologies. Reprinted with permission from Ref. 108. Copyright 2010, Journal of the American Chemical Society. Adopted with permission from Ref. 109. Copyright 2020. Royal Society of Chemistry. Reprinted with permission from Ref. 114, Copyright 2019, American Chemical Society.

CHAPTER II – EXPERIMENTAL METHODS

2.1 Materials and Methods

2.1.1 General Remarks

All manipulations of air- and moisture sensitive compounds were performed under an inert atmosphere using standard glovebox and Schlenk techniques. Reagents, unless otherwise specified, were purchased from Sigma Aldrich, and used without further purification. Chlorobenzene (C₆H₅Cl) was degassed and dried over 4 Å molecular sieves prior to use. Tris(dibenzylideneacetone)dipalladium(0) was purchased from Strem Chemicals and used as received. 1,2-(*E*)-Bis(5'-trimethylstannanyl-2'-*C*-thienyl)ethene, 3,6-bis-(5-bromo-thiophen-2-yl)-*N,N'*-bis(2-decyltetradecyl)-1,4-dioxo-pyrrolo[3,4-*c*]pyrrole, poly[2,5-bis(2-decyltetradecyl)pyrrolo[3,4-*c*]pyrrole-1,4-(2*H*,5*H*)-dione-*alt*-(*E*)-1,2-di(2,2'-bithiophen-5-yl)ethene] (**PDVT**), and penta-*t*-butylpentacyanopentabenz[25]annulene (cyanostar, **CS**) were prepared according to literature procedures.

2.2 General Characterizations

2.2.1 Atomic Force Microscopy (AFM)

The surface potential and topography data were recorded with a Bruker Dimension Icon scanning probe microscope. Kelvin probe force microscopy (KPFM) measurements were performed with MESP-V2 (tip radius: 35 nm) probes using a two-pass procedure. AFM-IR data were collected in tapping mode at a 45° angle using a gold-coated AFM probe (spring constant 40 N/m and resonant frequency 300 kHz). Through FTIR characterization, the mid-IR laser is optimized to frequencies correlating to each component (IR laser power of 15.78%). Images were flattened in Analysis Studio

software and then smoothing was done in Gwyddion open-source software using the Gaussian filter.

2.2.2 Electrochemistry

The electrochemical reduction and oxidation onsets were measured by cyclic voltammetry (CV) at a scan rate of 50 mV s^{-1} . Scans were carried out drop-cast polymer films in degassed anhydrous acetonitrile with tetrabutylammonium hexafluorophosphate (0.1 M) as the supporting electrolyte. The CV apparatus consists of platinum wires (working and counter electrodes) and Ag/AgCl (reference) electrode.⁴ The reference electrode was calibrated to ferrocene (internal standard) with the potential axis corrected to the standard hydrogen electrode (SHE: -4.75 eV). The bandgap was calculated from the difference of the onset of oxidation (E_{HOMO}) and reduction (E_{LUMO}).

2.2.3 Electron Paramagnetic Resonance (EPR) Spectroscopy

Room-temperature continuous-wave EPR spectra were recorded on a Bruker EMXmicro EPR spectrometer (X-band) microwave bridge. The solution sample was dissolved in chloroform, evaporated inside a 4 mm quartz tube, and sealed in a N_2 -filled glovebox. Spin concentration was obtained by comparing against a 2,2-diphenyl-1-picrylhydrazyl (DPPH) standard with a known spin concentration.¹¹⁷ The thin film samples were prepared in anhydrous chloroform (8 mg mL^{-1}), and the solvent was subsequently removed via a rotary evaporator.

2.2.4 Ellipsometry

To investigate the water uptake (film swelling behavior) of the films during measurements, we employed ellipsometry on a J.A. Woollam M-2000® UI Ellipsometer with a 500 μL variable temperature liquid cell accessory (incident angle at 70° and held at

23 °C). The results were modeled on the CompleteEase software. Each sample was scanned using 5 angles (55°, 60°, 65°, 70°, and 75°) over the range of 245 – 1700 nm at 2 s scan intervals. Data was first fit using an anisotropic B-spline, which establishes an initial absorption profile using 103 varying parameters. B-spline model was then converted to a series of gaussian general oscillators as an optimized model with variables reduced to 20 or less per material.¹¹⁸

2.2.5 Environmental Stability Studies

Long-term electrical measurements were conducted to assess material storage stability. Over a sixty-day period, pristine and composite films were stored in inert (N₂ glovebox), ambient, ultrapure deionized (DI) water (MilliQ > 18.0 MΩ-cm, Millipore), and high nutrient Instant Ocean Sea Salt solution, all in the absence of light.

2.2.6 Gel Permeation Chromatography (GPC)

The number average molecular weight (M_n), weight average molecular weight (M_w), and dispersity (D) were determined by gel permeation chromatography (GPC) at 160 °C in 1,2,4-trichlorobenzene (TCB), stabilized with 125 ppm of BHT in an Agilent PL-GPC 220 High Temperature GPC/SEC system using a set of three PLgel Olexis columns. Polymers were pre-dissolved at a concentration of 1.00 – 2.00 mg mL⁻¹ in TCB with stirring at 160 °C for 12 h.

2.2.7 UV-Vis-NIR Spectroscopy

The optical absorption spectra were recorded from 0.250 to 3.30 μm on a Cary 5000 UV-Vis-NIR spectrophotometer. Dilute sample solutions were made by dissolving the polymer and receptor in chlorobenzene solution, and thin films were prepared by spin-coating a chlorobenzene solution (10 mg mL⁻¹) onto quartz substrates.¹¹⁷ The optical

bandgaps were calculated based on the absorption onset from thin film absorption spectra following (Equation 2.1):

$$E_g^{opt} = \frac{hc}{\lambda_{onset}} \quad (2.1)$$

where h is Planck's constant, c is the speed of light, and λ_{onset} is the absorption onset.

2.3 OFET Device Operation and Parameter Extraction

2.3.1 Introduction

Research in organic electronics is driven by opportunities to develop novel technologies and garner a deep fundamental understanding of charge transport and soft condensed matter physics. Proper design and material integration of conjugated polymers can afford precise control over the optoelectronic properties via tailoring chemical syntheses and solution-processing techniques, higher tolerance to structural defects, ease of fabrication, and transparency. While most conjugated polymers do not meet the performance requirements critical for applications (e.g., current-driven flexible OLED displays), the role of the device structure, processing techniques, transport properties, morphology, polymer energetics, and doping are indispensable elements to enable far-reaching advancements. State-of-the-art metrics have been achieved thus far from our improved understanding of the role of polymeric structures – from atomic to microstructural and mesoscopic scales – on material functionality. However, the bottleneck of the charge transport in OSCs can be further alleviated by proper engineering at the metal-OSC interface, where charge injection and extraction occur. *Careful considerations of device geometry, architecture, material selection, and parasitic*

*loss mechanisms are instrumental to understanding the functioning principles and to push OFETs closer to commercialization.*¹¹⁹

2.3.2 Operating Principles of OFETs

An OFET is a three-terminal device (Figure 2.1) composed of a source, drain, and gate electrode, mutually acting as an electronic “relay.” Electrical charges flow across the semiconductor between the source and drain contacts (I_{DS}) and function based on the applied voltage between the two contacts (V_{DS}). The electrical conductivity is then amplified by an external electric field, generated by an applied gate voltage (V_{GS}), and is known as the “field effect.” The gate voltage facilitates control between off- and on-state and enables the transistor to function as the switching element of microprocessor circuits in modern devices. When operating in the on-state, the OFET behaves similar to a capacitor with mobile charges. Applying voltages at the three metal contacts creates an equipotential surface at the dielectric/OSC interface and induces a charge accumulation layer (< 10 nm in thickness). The dielectric is made of organic or inorganic insulating material that is polarizable (shift in the molecule’s equilibrium position) under an applied electric field and is sandwiched between the gate contact and the OSC. Electric charges are not exchanged between the gate and OSC because the dielectric does not have loosely bound or free electrons capable of drifting across the material. OFET devices usually operate in enhancement mode, where the OSC is intrinsically in an undoped state and is intentionally doped under appropriate gate biasing. A second device operation involves depletion-mode, where the device is in the on-state at zero gate voltage, and channel conduction reduces under gate biasing. A plethora of OFET devices with p-type and n-type operations have now reached the performance of polycrystalline silicon FETs,

exhibiting field-effect mobilities (μ_{FET}) higher than $1 \text{ cm}^2 \text{ V}^{-1} \text{ s}^{-1}$. In principle, these two carrier types can be operated based on the charge injection barrier at the source and drain contacts and the material electrochemical stability.

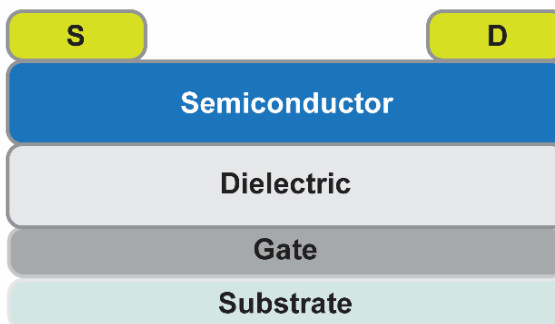


Figure 2.1 *The device structure of an OFET which is composed of three electrodes (source, drain, and gate), a dielectric layer, and a semiconductor.*

The operating principle and modes of OFETs are illustrated in Figure 2.2, which shows a series of band diagrams. The focal point of the figure is the band-bending in the OSC near the dielectric surface, as it determines if the device will operate under enhancement or depletion mode. For a p-type semiconductor (Figure 2.2a), the Fermi level (E_F) lies below the intrinsic energy (E_i , the halfway point between the frontier orbital energy levels). In equilibrium, when the gate voltage bias is zero, the Fermi levels of the polymer and metal are aligned, and band-bending does not occur (flat band condition). P-channel operation (accumulation of holes) occurs under a negative gate bias. The gate electrode Fermi level is raised to higher energy (closer to the vacuum level) and generates an electric field across the dielectric layer. The electric field is responsible for the polymer HOMO and LUMO band bending in the direction of the gate electrode Fermi level. Under the “field-effect”, the HOMO energy level approaches the OSC Fermi level near the dielectric interface and accumulates of holes. The energy

difference between the HOMO and Fermi levels controls the carrier density of holes and follows an exponential relationship. The charges that accumulate at the OSC/dielectric interface move along the channel length (L) direction towards the source/drain electrodes, where charge carrier injection and extraction occur. For an n-type semiconductor (Figure 2.2b), the Fermi level is situated above E_i . Applying a positive gate bias causes band-bending in the opposite direction to lower energy (away from the vacuum level) and results in the accumulation of electrons. This is due to the LUMO level approaching the OSC Fermi level near the dielectric interface. The material selection of the source and drain electrodes are essential to the OFET operation mode and efficiency. The metal work function alignment of the OSC HOMO and LUMO is necessary to enable p-channel and n-channel operation, respectively, and efficient charge carrier injection and extraction.

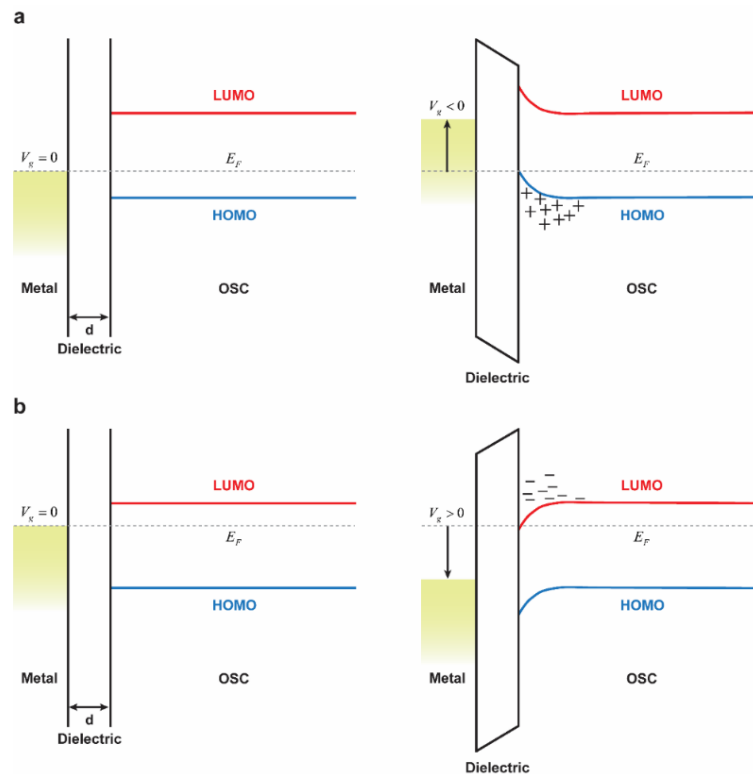


Figure 2.2 *Schematic of band-bending and operating modes in OFETs: (a) p-type operation without (left) and with (right) an applied negative gate voltage and (b) n-type operation without (left) and with (right) an applied positive gate voltage.*

OFETs have been constructed through a variety of device architectures and fabrication processes, such as vacuum evaporation, single-crystal-growth, and solution-processing, of which solution-based printing processes are the most desirable manufacturing approach.⁸³ In general, OFETs enable control of the channel current between the source and drain contacts by modulating gate-terminal bias and giving rise to three OFET operation regimes: linear, pinch-off, and saturation regime. Current-voltage (I - V) characteristics are used to extract the device figures-of-merit and are calculated in either the linear or saturation regime. The OFET channel is activated when the gate bias exceeds the threshold voltage ($V_{GS} > V_{Th}$). While under a constant gate bias, the drain-to-source bias is tuned to control the channel response. When $V_{DS} \ll V_{GS}$ the conductive channel is characterized as having a uniform distribution of mobile carriers, performing like an Ohmic resistor (current increases linearly with voltage). It is known as the linear regime, and the output current is approximated from the following (Equation 2.2):

$$I_{DS}^{lin} = \frac{1}{2} \mu_{FET} C \frac{W}{L} (V_{GS} - V_{Th}) V_{DS} \quad (2.2)$$

where W is the channel width, L is the channel length, and C is the capacitance per unit area.

The field-effect mobility (μ_{FET} , units: [$\text{cm}^2 \text{V}^{-1} \text{s}^{-1}$]) is an important figure of merit and probes how fast (efficient) the charge carriers move across the OSC channel within an electric field and can be measured by the transconductance (g_m) (Equation 2.3):¹²⁰

$$g_m = \left. \frac{\partial I_{DS}}{\partial V_{GS}} \right|_{V_{DS}} = \mu_{FET} C \frac{W}{L} V_{DS} \quad (2.3)$$

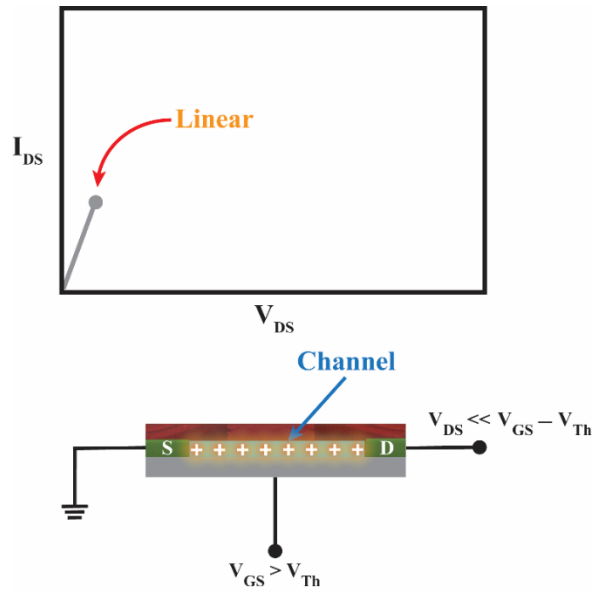


Figure 2.3 The linear regime: I_{DS} as a function of V_{DS} .

The mobile carriers across the channel is no longer uniformly distributed when V_{DS} is increased beyond a certain magnitude. The I - V curve becomes sublinear as a depletion region is formed in the conductive channel, and results in high resistance on the drain electrode side. The mobile carrier density near the drain is small and only a space charge limited saturation current is permitted to flow across the depletion region. The I - V characteristics becomes quadratic ($I \propto V^2$), so the output current adopts the following relationship (Equation 2.4):

$$I_{DS}^{sat} = \frac{1}{2} \mu_{FET} C \frac{W}{L} (V_{GS} - V_{Th})^2 \quad (2.4)$$

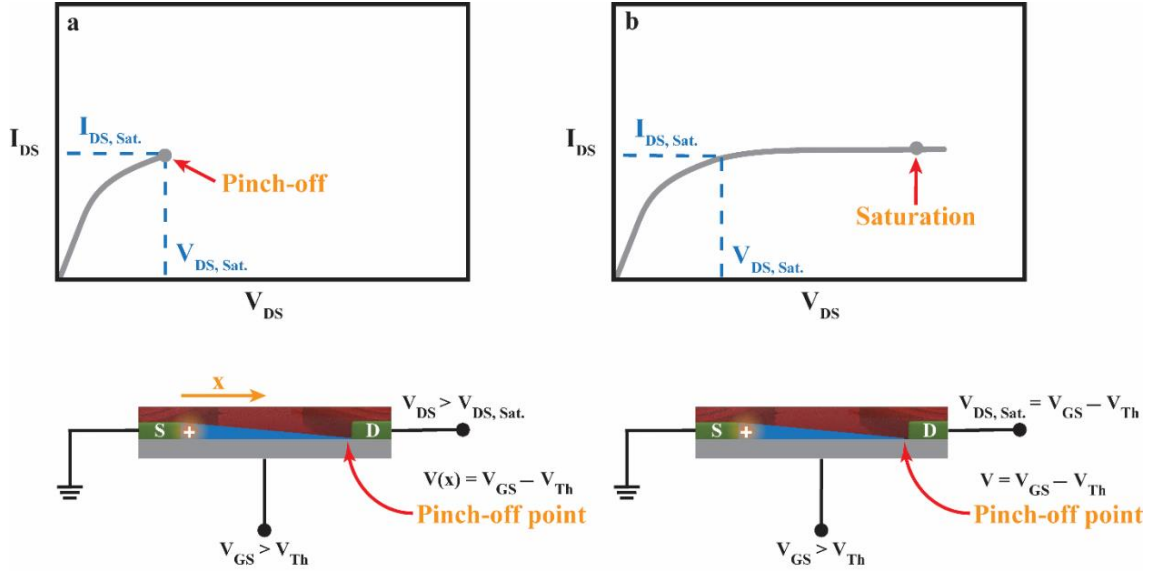


Figure 2.4 (a) The pinch-off point and (b) the saturation regime: I_{DS} as a function of V_{DS} .

Output and transfer characteristic plots (Figure 2.5) are used to extrapolate the OFET parameters such as μ_{FET} , V_{Th} , on-off current ratio (I_{ON} / I_{OFF} , unitless), and subthreshold swing (S , units: [V decade⁻¹]). The on-off ratio (ratio of the drain current in the on- and off-state) is an important device metric, as it measures the quality of the device as an electronic switch and the purity of the OSC. For clean switching behavior, higher values are excellent, with state-of-the-art devices achieving $>10^6$. Collectively, to achieve high-performance OFET devices, the off-state current can be reduced by limiting parasitic gate leakage current (I_{GS}) and minimizing residual dopant species while enhancing the on-state current by increasing the OSC mobility. The subthreshold swing measures the switching ability between the off- and on-state. High subthreshold swing values generally imply the enlargement of shallow trap states and is given as:

$$S = \frac{dV_{GS}}{d(\log I_{DS})} \quad (2.5)$$

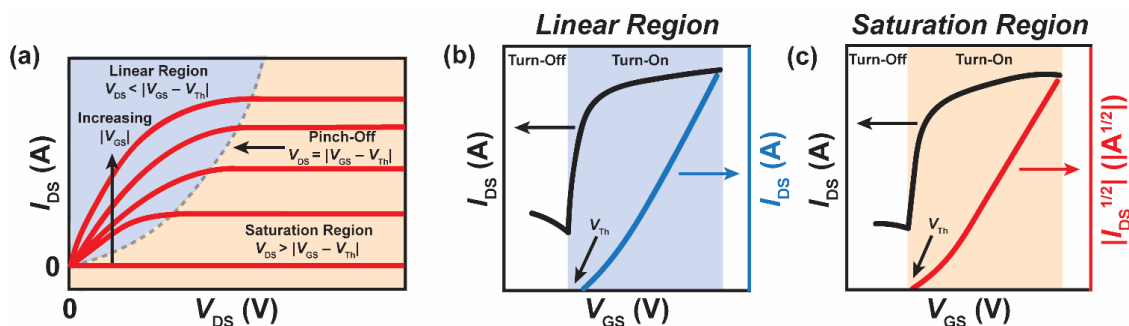


Figure 2.5 (a) Output and (b,c) transfer plots showing the linear (blue) and saturation regimes (orange).

2.3.3 Common OFET Device Geometries

The assortment of device geometries (Figure 2.6) is rooted in the solution-processability of polymers and small-molecule systems with electrical properties ranging from insulating to semiconducting. As such, there are four common device geometries are constructed according to the positioning of the source/drain and gate electrode in reference to the OSC layer: bottom-gate/top-contact (BGTC), bottom-gate/bottom-gate (BGBC), top-gate/top-contact (TGTC), and top-gate/bottom-contact (TGBC). BGBC and TGTC are coplanar geometries, while BGTC and TGBC are staggered geometries. Coplanar devices are characterized by having all three electrodes on the same side of the OSC, and staggered devices have the source/drain and gate electrodes on opposite sides of the OSC. For specific materials, it may be advantageous to encapsulate the OSC layer and source-drain contacts underneath the dielectric layer for protection against environmental degradation. However, for chemical sensing, it may be beneficial to directly expose the OSC surface to the environment where an analyte is introduced and offers the potential to achieve higher signal amplification. In the next section, parasitic resistance pathways will be discussed since they are highly sensitive to geometric factors (coplanar vs staggered) and material processing.

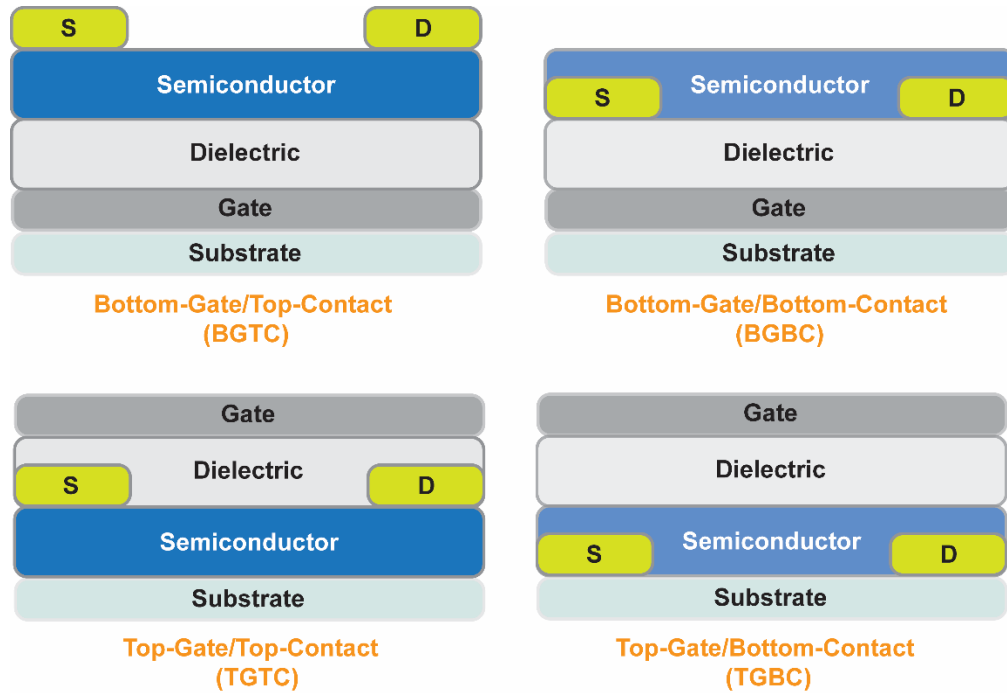


Figure 2.6 OFET configurations: (a) bottom-gate/top-contact (BGTC), (b) bottom-gate/bottom-contact (BGBC), (c) top-gate/top-contact (TGTC), and (d) top-gate/bottom-contact (TGBC).

2.3.4 Role of Device Factors

Contemporary organic semiconductors typically suffer from poor contact injection properties since the electrode-OSC junction is composed of heterogenous materials, resulting in high contact resistance (OSC FETs: $R_c \geq 100 \Omega \text{ cm}$ versus silicon metal-oxide-semiconductor FETs: $R_c < 0.1 \Omega \text{ cm}$).¹²¹ Small enhancements in the charge injection and extraction can extend the device functionality and efficiency. The total resistance (R_T) can be described as the sum of the channel resistance (R_{CH}) and contact resistance – composed of interfacial ($R_{C,Int}$) and adjacent domains extending towards the channel ($R_{C,Bulk}$) (Figure 2.7).¹²¹ The contact resistance is particularly sensitive to the doping concentration, band alignment between the CP and electrode, and the hopping

mechanism of charge carriers in OSCs. However, the $R_{C,Bulk}$ is especially affected by the device structure and charge carrier mobility. Staggered geometries are generally beneficial in lowering the $R_{C,Bulk}$ because there is an extended injection area above the metal contact contributing to the carrier diffusion. Intensive research efforts discovered ways to alter the contact injection barrier by changing the metal work function, controlling the metal surface states, and the OSC morphology. Lastly, the processing conditions, specifically spin-coating, can produce non-interactive interfaces due to disordered, kinetically quenched morphologies. *The effects of contact resistance on the conjugated polymer charge transport properties will be elucidated using the transmission line method.*

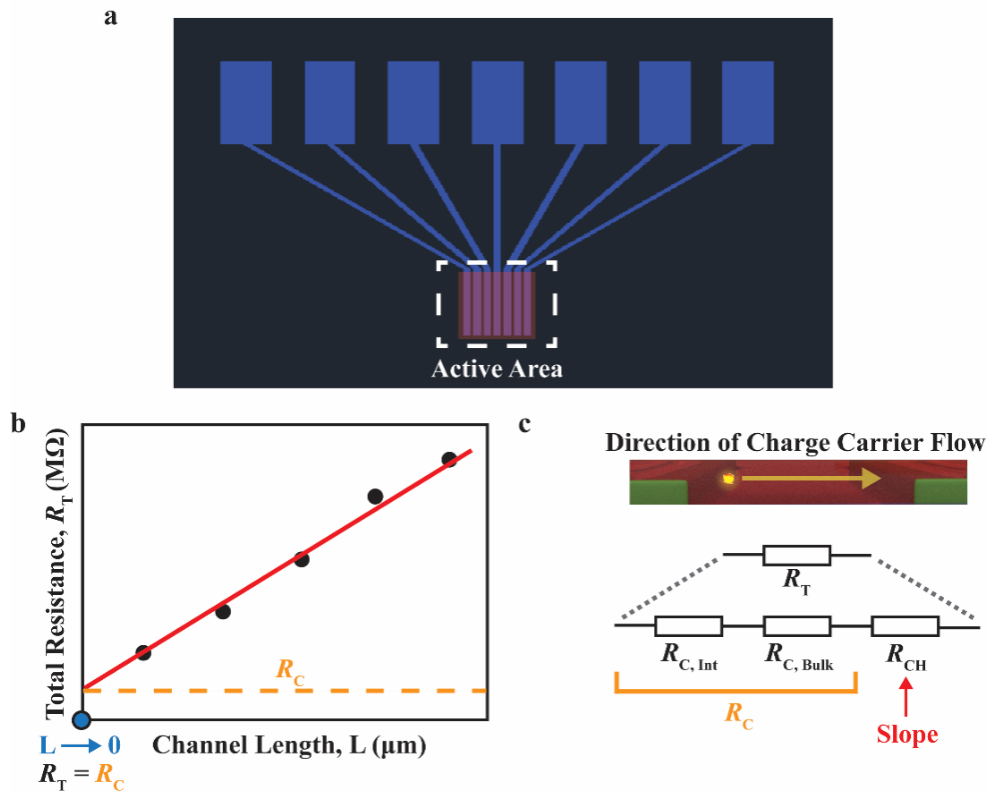


Figure 2.7 (a) AutoCAD of fabricated devices used to perform the transmission line method (TLM). (b) TLM plot showing channel length (L) versus total resistance (R_T).

Linear extrapolation is used to calculate the device contact resistance (R_C). (c) R_T and a three-resistor model equivalence ($R_T = R_C + R_{CH} = R_{C,Int} + R_{C,Bulk} + R_{CH}$).

2.3.5 Transistor Fabrication

Si/SiO₂ substrates (20 mm × 15 mm) were sequentially submerged into 2% (by volume) Hellmanex detergent in deionized (DI) water, DI water, acetone, and isopropyl alcohol (IPA) for 10 mins using sonication, followed by drying in an oven. The substrates were then treated in a UV–O₃ cleaner for 20 mins.¹¹⁷ Gold electrodes (60 nm) were thermally evaporated onto a chromium adhesion layer (5 nm) at 1×10^{-7} torr using a shadow mask. The electrodes were separated by an 80 μm x 1 mm spacing and acts as the sensor active area with a transmission line leading from each electrode as shown in **Fig. 2A**. The devices were then submerged in 3 mM octadecyltrichlorosilane (OTS) in trichloroethylene solvent for 20 s, followed by spin-coating at 3000 rpm for 10 s. The substrates were placed in a desiccator and exposed to ammonium hydroxide (28–30% in water) overnight, followed by sequential washing in toluene, acetone, and IPA.¹²² The polymer and receptor were dissolved in chlorobenzene at 90 °C to make a solution of 8 mg ml⁻¹ and 2 mg ml⁻¹, respectively, in a nitrogen atmosphere. The polymer solution was spin-coated onto the substrate at 1000 rpm for 60 s, resulting in a 91 nm thick film, creating a bottom-gate/bottom contact device. Host-guest complexation studies were initially done by physically mixing tetrabutylammonium organic salts into the polymer/receptor solution.

2.3.6 Device Characterization

2.3.6.1 Two-Point Probe I - V : Extracting Room-Temperature Bulk Conductivity.

The sensor chips were mounted on a Signatone 1160 Series probe station using a standard X-Y stage.¹²³ Semiconductor figures of merit were evaluated inside a nitrogen filled glovebox and recorded on a Keithley 4200 semiconductor characterization system (SCS). Room temperature conductivity was measured using a two-point probe method (source and drain, without gate) by sweeping the voltage from -2 to 2 V, determined by the following relationship (Equation 2.6):^{117, 124}

$$\sigma_{RT} = \frac{I}{V} \times \frac{L}{WT} \quad (2.6)$$

where I , V , L , W , and T represent current, voltage, channel length, channel width, and active layer thickness (measured by AFM), respectively.

2.3.6.2 Bottom-Gate/Bottom-Contact Devices: Extracting Mobility.

The field-effect mobility was extracted from the transfer curve (linear regime) (2.7):¹²⁴

$$\mu = \frac{L}{WC_i V_{DS}} \times \frac{\Delta I_{DS}}{\Delta V_{GS}} \quad (2.7)$$

where C_i , V_{DS} , V_{GS} , and I_{DS} represent the dielectric capacitance, source-drain voltage, gate-source voltage, and source-drain current, respectively.

2.3.6.3 Water Sensing Tests and Characterization.

The EGOFETs experiments were carried out in ambient conditions and used HEPES buffer (100 mM, pH = 7.4) in DI water or Instant Ocean sea salt solution as the electrolyte and a Ag/AgCl pellet as the gate electrode.¹²⁵ The transient responses were measured using a Keithley 4200 SCS with a 4200-source meter unit (SMU) that was used

to bias the source, drain, and gate electrodes. **PDVT-CS** and **PDVT-IsoCS** EGFET sensors were exposed to a baseline and analyte solution (spiked with either dihydrogen phosphate, nitrate, metasilicate, bromide, chloride, sulfate, bicarbonate, or carbonate) of various concentrations mixed into another batch of baseline solution. This protocol was used to minimize pH-dependent channel conduction responses. The sensor performance and transient responses were measured using a Keithley 4200A-SCS Parameter Analyzer. The sensor sensitivity is defined by the relative change of the drain current under applied voltage ($V_{GS} = -0.7$ V and $V_{DS} = -1.0$ V in our case) following equation (2.8):¹²⁶⁻¹²⁷

$$S = \frac{|I_{DS}(analyte) - I_{DS}(baseline)|}{I_{DS}(baseline)} \times 100 \quad (2.8)$$

CHAPTER III – POLYMER-SUPRAMOLECULAR RECEPTOR COMPOSITES:
ACTIVE FILMS IN TRANSISTOR ARCHITECTURES

3.1 Research Objectives and Approaches

This section systematically incorporates receptors into polymeric systems and lays the groundwork for broadly applicable electronic detection platforms for sensing contaminants in water (Chapter IV). Using an integrated approach combining synthetic chemistry, polymer science, and device fabrication and engineering, we seek to gain a fundamental understanding of receptor-induced transformations on the transistor device metrics, material energetics, and film morphology. Our approach to chemical sensing is governed by coordinated π -orbital hybridization between a conjugated polymer and a shape-persistent macrocyclic receptor (preferentially binds to weakly-coordinating anions), forming a favorable complex towards charge transport enhancement. To evaluate the utility of our approach, OFET devices were primarily utilized as a characterization tool to quantify measurable changes in the polymer properties while precisely controlling additive loading, solution-processing conditions, and polymer compatibility.

3.2 OFET Fabrication Protocol

3.2.1 Metal Deposition: Material Selection, Procedure, and Device Geometry

An EvoVac Physical Vapor Deposition system from Angstrom Engineering was used to thermally deposit gold (Au) source, drain, and gate contacts. Au as a noble metal offers heightened resistance to corrosion, more prolonged survival in saline conditions of the marine environment, readily modifiable surfaces for self-assembled monolayers (SAMs), and energetic compatibility to most p-type transport materials. In the latter case, Au possesses a work function from 5.10 – 5.47 eV (dependent on the surface atomic

configurations or crystal faces) and closely aligns with the HOMO of p-type polymers, enabling effective hole transport. Silicon substrates (Wafer Pro, 3000 Å dry thermal oxide dielectric), after solvent and UV-O₃ cleaning, were placed in an evaporation stack and covered with a shadow mask outlining the source-drain contacts (linear geometries). Since Au has poor adhesion to all oxide substrates, an adhesion layer is necessary for electrode stability. 5 nm layer of chromium (Cr) was deposited first to promote high binding strength with the dielectric's native hydroxyl groups. Therefore, an interconnecting bridge between the substrate and Au layer (60 nm) is established. Variable channel lengths ($L = 30, 40, 50, 60,$ and $80 \mu\text{m}$ and constant channel widths ($W = 1000 \mu\text{m}$) were chosen during the device optimization phase.

3.2.2 Organosilane Self-Assembled Monolayer Deposition:

One of the critical steps in device fabrication and processing is the precise tuning of crystalline self-assembled monolayers (SAMs) composed of organosilane compounds. Octadecyltrichlorosilane (OTS) SAM deposition is employed because it tunes the dielectric surface energy and roughness. OTS also increases the charge carrier mobility by removing dielectric traps (physisorbed “trapped” water and native hydroxyl groups) and improves the nucleation and growth behavior for vacuum-deposited and solution-cast OSCs. Exceptional quality OTS SAMs have been previously achieved using the Langmuir-Blodgett technique, solution immersion, vapor deposition, and spin-coating. In this section, we assess the OTS SAM processing conditions and their relation to device figures-of-merit.

Before applying a trichlorosilane layer, the substrate was cleaned via UV-O₃ and examined using a contact angle goniometer. When placing a droplet of deionized (DI)

water on the silicon oxide substrate, there should be no measurable contact angle. A 3 mM solution of OTS in trichloroethylene (TCE) was devised and spin-casted in a glove box. Depending on the OTS concentration, the reaction time can take up to 10 to 15 minutes. OTS was deposited *via* spin-coating by covering the entire surface and allowing the OTS to partially assemble for 15 s. The substrate was spun at 3000 rpm for 10 s and placed inside a desiccator next to a vial filled with ammonium hydroxide (28–30% water) overnight. The substrates were then first rinsed with toluene, as nucleophilic solvents (e.g., 2-isopropanol (IPA), acetone, methanol) will cause the residual trichlorosilane solution to polymerize. Lastly, acetone rinse is used as a quality checkup and should dewet completely with proper OTS SAM coverage.

3.3 General Characterization of Channel Materials

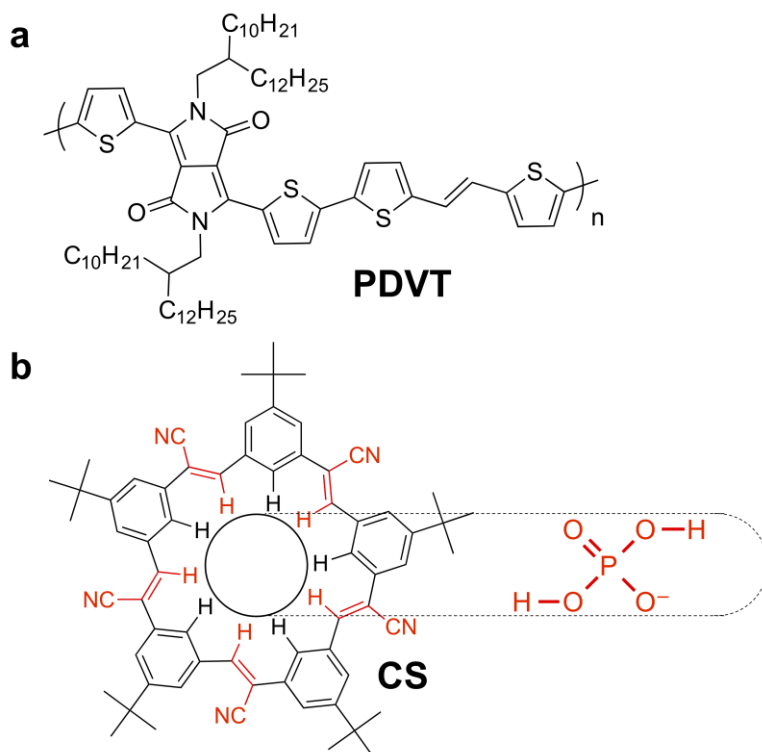


Figure 3.1 (a) Molecular structures of the semiconducting polymer (**PDVT**) and (b) cyanostar receptor (**CS**) which can bind phosphate.

3.3.1 Properties of Cyanostar

The high solubility of penta-*t*-butylpentacyanopentabenz[25]annulene “cyanostar” (CS) (Figure 3.1) in common halogenated organic solvents enables solution processing, and thin films were prepared by spin-coating a chlorobenzene solution (10 mg ml⁻¹) on quartz for UV-Vis spectroscopy and on prefabricated device substrates for charge transport measurements. The CS thin films demonstrate an absorption profile with an absorption maximum (λ_{\max}) of 318 nm and an optical bandgap (E_g^{opt}) of 3.45 eV; the latter is estimated by the absorption onset. The electrochemical bandgaps of CS with anion (X^-) complexation ($\text{CS}_2 \cdot X^-$) and without (empty cavity) were measured by cyclic voltammetry (CV) with CS dissolved in dichloromethane (CH_2Cl_2) electrolyte solution (Figure 3.2). The reduction (LUMO level) of cyanostar species is measured directly by CV. In contrast, the oxidation (HOMO level) is based on the optical bandgap since the onset shifting only occurred during the reduction processes.

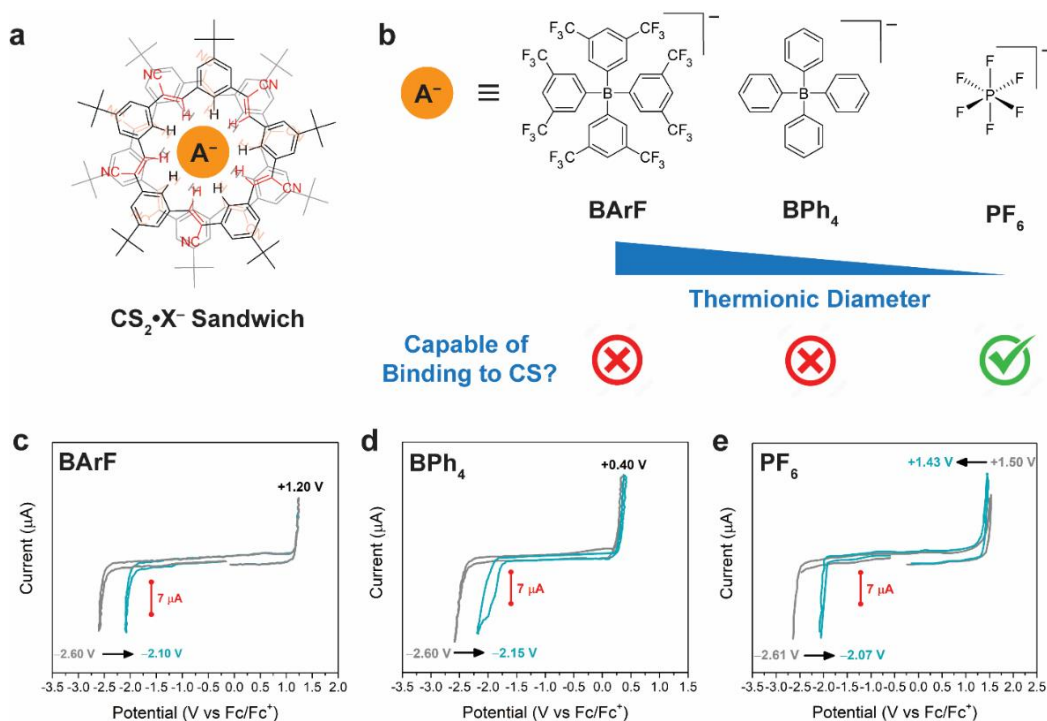


Figure 3.2 CV experiment to measure the frontier orbital energy levels of CS. (a) CS can form a 2:1 sandwich complex with specific anion species ($\text{CS}_2 \cdot \text{X}^-$). (c) The three tested anion compositions tetrabutylammonium tetraphenylborate (TBABPh_4), tetrakis(3,5-bis(trifluoromethyl)phenyl)borate (TBABArF), and hexafluorophosphate (PF_6^-). (c) CV spectra of tested anions, where significant shifts in the reduction peaks were observed.

Using CS's size-selective nature, the empty CS frontier orbitals can only be measured if the proper electrolyte is selected, where the ionic diameter of the anion exceeds the cavity size (macrocycle: $\sim 4.5 \text{ \AA}$). Tetrabutylammonium tetraphenylborate (TBABPh_4) and tetrabutylammonium tetrakis(3,5-bis(trifluoromethyl)phenyl)borate (TBABArF) were chosen due to their bulky aryl groups, which do not permit the anions to bind with CS. Since CS has shown to have a high binding affinity and produces a sandwich structure with hexafluorophosphate (PF_6^-), TBAPF_6 was used to determine the anion-bound CS ($\text{CS}_2 \cdot \text{X}^-$) frontier orbitals. CVs show that the HOMO is positioned at -3.05 eV (-3.21 eV), and the LUMO is positioned at -6.50 eV (-6.66 eV) for CS ($\text{CS}_2 \cdot \text{X}^-$). These results suggest that CS is an electrical insulator and could not operate solely as a channel material and must be coupled to a semiconductor. The π -conjugation of the CS macrocycle, while not enabling electrical conductivity, is still an attractive feature for "molecular recognition and hierarchical self-assembly,"¹²⁸ as their structures are geometrically well-defined and possess low conformational flexibility. The rigid structure translated to high thermal stability with a 5% weight loss around $421 \text{ }^\circ\text{C}$, unlike its predecessor molecules 18-Crown-6 (18-C-6), α -cyclodextrin (α -CD), and β -cyclodextrin (β -CD) where degradation occurs $< 350 \text{ }^\circ\text{C}$ (Figure 3.3)

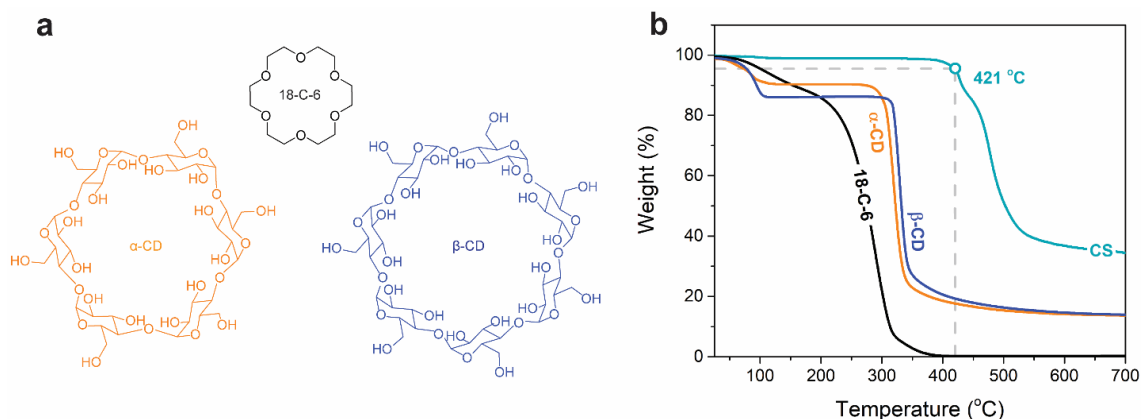


Figure 3.3 Thermogravimetric analysis (TGA) of a shape-persistent macrocycle, CS, versus common macrocycles: 18-Crown-6 (18-C-6), α -cyclodextrin (α -CD), and β -cyclodextrin (β -CD), showing the (a) chemical structures and (b) TGA curves. CS displayed a 5 wt% weight loss at ~ 421 $^{\circ}\text{C}$.

3.3.2 Receptor-Induced Doping

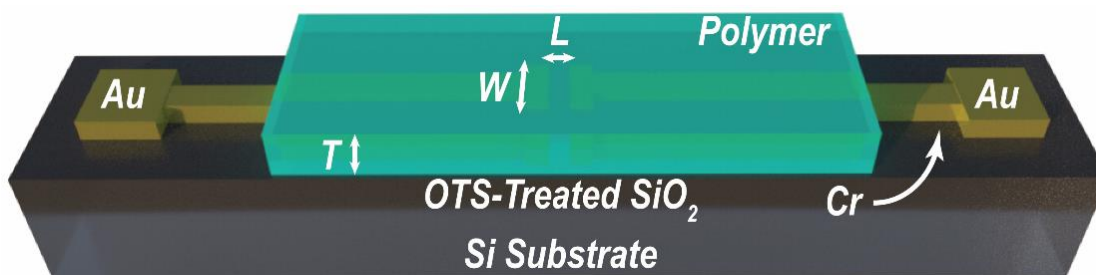


Figure 3.4 3-D rendering of the BGBC device structures used for charge transport measurements.

The conjugated polymer poly[2,5-bis(2-decyltetradecyl)pyrrolo[3,4-*c*]pyrrole-1,4-(2*H*,5*H*)-dione-*alt*-(*E*)-1,2-di(2,2'-bithiophen-5-yl)ethene] (**PDVT**) was chosen on the basis of its high field-effect mobility (μ), excellent film-forming properties, and environmental stability.¹²⁹⁻¹³⁰ Both **PDVT** and **CS** feature rigid extended π -systems that promote strong intermolecular and solid-state interactions, indicative of their potential for electronic coupling. The polymer was synthesized using a microwave-assisted Stille cross-coupling copolymerization resulting in a number average molecular weight (M_n) of 43.7 kg mol^{-1} and dispersity (\mathcal{D}) of 2.14 (Figure A.1). Mixtures of the polymer and

receptor were initially examined using UV-Vis-NIR and electron paramagnetic resonance (EPR) spectroscopies. Thin films for UV-Vis-NIR studies were prepared by spin-coating chlorobenzene mixtures of the polymer (10 mg mL⁻¹) and CS (1:1 w/w% relative to polymer) onto quartz substrates. An absorption maximum (λ_{max}) at 804 nm in the pristine PDVT is consistent with aggregation from π - π stacking. The solid-state absorption of PDVT-CS displayed a modest blue shift of 11 and 6 nm at the 0-0 and 0-1 vibronic peaks, a concomitant lowering of the relative intensity of these transitions (PDVT-CS: $I_{0-0}/I_{0-1} = 1.07$, PDVT: $I_{0-0}/I_{0-1} = 1.24$), and the presence of a low energy absorption tail (Figure 3.5). The decrease of intensity of the π - π stacking peak can be associated with a partial disruption of polymer chain interactions and solid-state ordering.¹³¹ These data further suggest the formation of a ground-state charge-transfer complex (GS-CPX) from the electronic coupling between the PDVT and CS.¹³² Further details regarding optical and electrochemical characterization can be found in Figures A.2–A.5 and Table A.1.

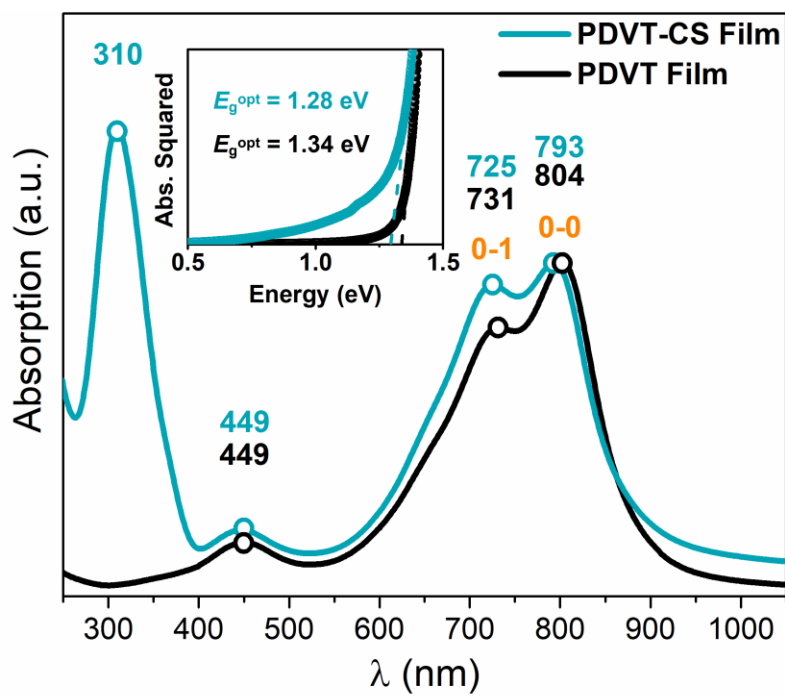


Figure 3.5 *UV-Vis-NIR absorption profile of pristine PDVT and PDVT-CS films spin-coated from chlorobenzene onto quartz substrates. The inset illustrates a pronounced low-energy absorption tail upon CS addition.*

OFETs have demonstrated utility in a large number of consumer technologies and show unparalleled modularity in sensing a wide variety of biological, chemical, and physical analytes.^{84, 133} Thus, **PDVT** and **CS** were combined and utilized as the active layer within the channel of an OFET in order to investigate whether the previously observed doping phenomena could be translated into a signal transduction mechanism and applied for anion sensing. **PDVT-CS** films (**CS** loading = 0, 4, 10, 20 wt%) were spin-coated onto *n*-octadecyltrichlorosilane (OTS)-treated SiO₂/Si substrates (electrodes: Cr ≈ 5 nm, Au ≈ 60 nm, length (*L*) = 80 μm and channel width (*W*) = 1 mm) to construct bottom-gate, bottom-contact (BGBC) devices (Figure 3.6). Figure 3.6b-d shows the room-temperature conductivities (σ_{RT}) obtained using two-point probe measurements and OFET transfer and output characteristics for neat **PDVT** and **PDVT-CS** (20 wt%) composite films. Further details on the fabrication, solution processing, and testing parameters are discussed in the Supporting Information.

All devices demonstrated *p*-type FET behavior. The neat **PDVT** films displayed an average hole mobility of $2.95 \times 10^{-2} \text{ cm}^2 \text{ V}^{-1} \text{ s}^{-1}$ and on/off current ratio (I_{on}/I_{off}) of $\sim 10^6$. Low loadings of 1–2 wt% **CS** are pinned to a trap-limited doping regime,^{5, 58} while a critical threshold of 4 wt% **CS** was found to produce linear *I-V* characteristics consistent with Ohmic transport. A concomitant increase in σ_{RT} was evident upon increasing the **CS** concentration. Loadings of 4, 10, and 20 wt% **CS** result in σ_{RT} of 1.17×10^{-5} , 1.75×10^{-4} , and $8.20 \times 10^{-3} \text{ S cm}^{-1}$, respectively. The **PDVT-CS** transfer curves do not exhibit a well-defined off-state (Figure 3.6c), indicating the manifestation of

mobile carriers, consistent with EPR studies and a lowering of the gate-dependent channel conduction. There was a concomitant increase in μ up to $3.43 \times 10^{-2} \text{ cm}^2 \text{ V}^{-1} \text{ s}^{-1}$ for the 20 wt% **CS** devices. The enhancement of carrier mobility, with increasing **CS** loading, is unique and emanates from doping since all prior reports generally demonstrate deleterious effects on mobility upon the incorporation of receptor chemistries into organic semiconductors.¹³⁴ The carrier concentration (n) was calculated from the mobility using the equation $\sigma = nq\mu$, where q is the elementary charge (Figure A.10 and Table A.2). The addition of **CS** correlates with a proportional increase in σ_{RT} with n increasing from 10^{15} cm^{-3} (neat **PDVT**) to greater than 10^{18} cm^{-3} at 20 wt% **CS**.

The Ohmic transport of the composite systems can be associated with the presence of free carriers introduced by doping and the modified injection barrier at the electrode-semiconductor junction.¹²⁴ As such, variable temperature (180 – 340 K) mobility and transmission line method (TLM) measurements were performed to extract the activation energy (E_a) and the contact resistance (R_C), respectively. The temperature-dependence of μ originates from a thermally activated process described by the relation $\mu(T) = \mu_0 \exp(-E_a / k_B T)$, where μ_0 is a pre-exponential factor, k_B is the Boltzmann constant, and T denotes the temperature.¹²⁴ The values for E_a of 78 meV (**PDVT-CS**) < $E_a = 113 \text{ meV}$ (**PDVT**) ($\Delta E_a \approx 35 \text{ meV}$) are consistent with a reduced energetic barrier for charge transport. The TLM results suggest a reduction of the contact resistance ($R_C = 4.5 \text{ M}\Omega$) consistent with doping and change in surface potential observed by KPFM (Figure A.6).¹³⁵ Therefore, despite producing kinetically quenched morphologies from spin-coating, the composite systems do not appear to be hampered by non-interactive

interfaces formed at the electrode-OSC junction.¹²¹ To investigate the electrical stability of the **PDVT-CS** transistors, devices were monitored under an atmosphere of nitrogen in the dark, in ambient conditions, in ultrapure DI water, and in Instant Ocean Sea Salt electrolyte. In all cases, the devices exhibit excellent storage stability over a 60-day testing period, even when completely submerged into Instant Ocean Sea Salt electrolyte (Figure 3.6e), a rare demonstration that is essential for practical translation to field use.^{95,}

136-137

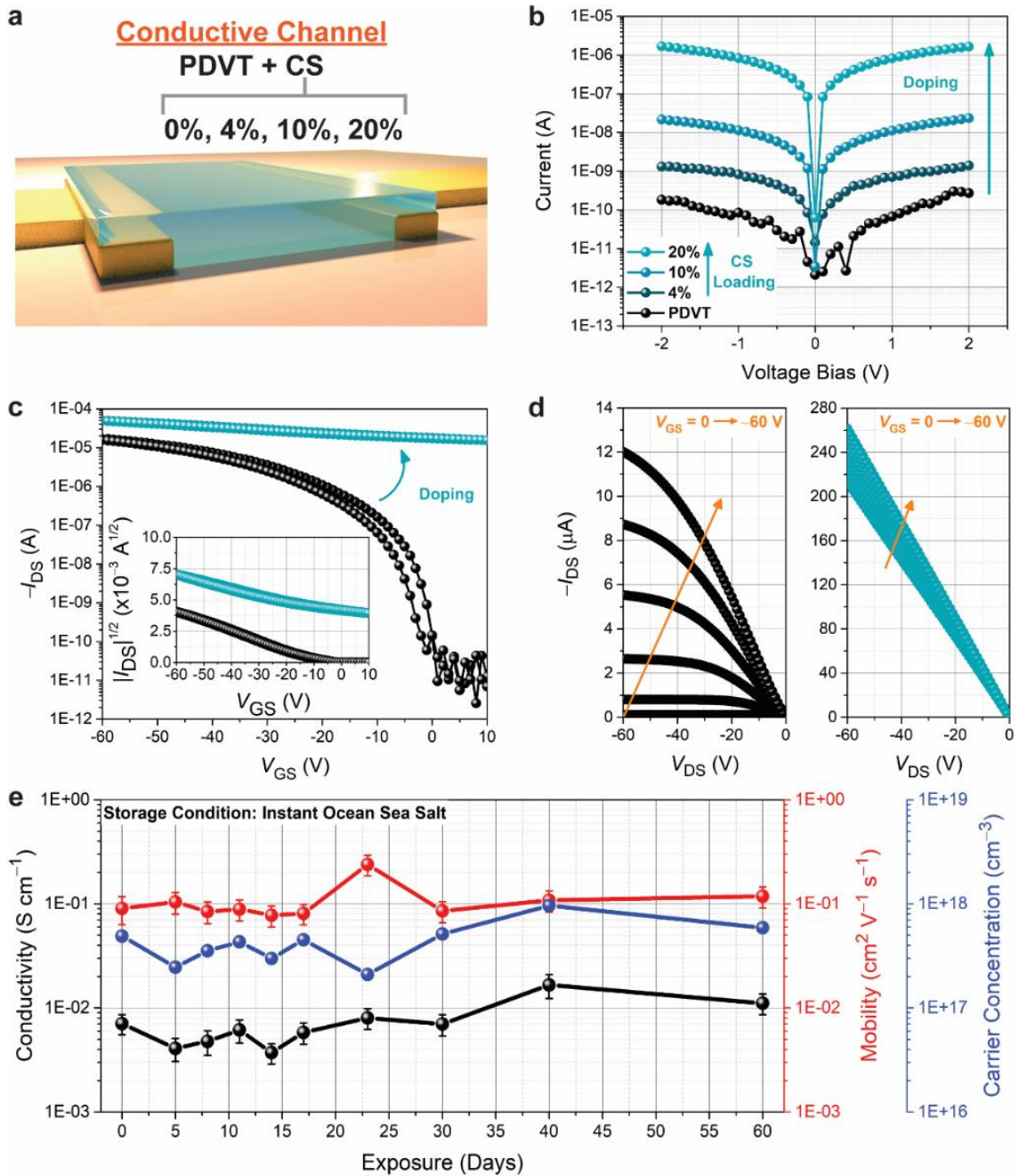


Figure 3.6 (a) Schematic illustration of a bottom-gate/bottom-contact (BGBC) device structure. PDVT-CS devices (CS loading = 0, 4, 10, and 20 wt%) were fabricated and tested to evaluate electronic transformations, material compatibility, and storage stability. (b) Electrical conductivities obtained from two-point probe measurements (-2 to 2 V) of PDVT-CS films. (c) FET transfer characteristics and (d) output curves (left) without and (right) with CS (20 wt%) showing enhancement in p-channel operation using source and drain electrodes ($L = 80 \mu\text{m}$, $W = 1 \text{ mm}$). (e) Monitoring of device stability for high performing PDVT-CS films over 60 days. Films were completely submerged in

Instant Ocean sea salt electrolyte and showed minimal changes in the conductivity (black), field-effect mobility (red), and carrier concentration (blue).

In terms of doping efficiency, based on the ratio of free charge carriers to dopant molecules, the polymer-dopant mixture in our system possesses low efficiency,⁵⁸ a threshold receptor loading (~4 wt%) is needed to achieve the slightest enhancement in conductivity and performance saturation ensues beyond 20 wt%. These findings, coupled to the ones found in UV-Vis-NIR and EPR, suggest there is a reasonable probability that the underlying mechanism is based on orbital hybridization, giving rise to a GS-CPX. FTIR was employed to measure shifts in the **CS** cyano group ($C\equiv N$, 2215 cm^{-1}) diagnostic peaks to investigate this potential mechanism route. Since p-type doping is the most viable option, shifts in the cyano-vibrational bands in FTIR are held to indicate a negatively charged state of **CS**.⁶⁵ In this case, the degree of charge transfer (δ) can be quantified based on the observed frequency shift ($\Delta\nu$), following:

$$\delta = \frac{2\Delta\nu}{\nu_0} \left[1 - \frac{\nu_1^2}{\nu_0^2} \right]^{-1}$$

where the ν_0 and ν_1 are the neutral dopant and radical anion vibrational frequencies, respectively. The **CS** dopant strength is weak and translates to only partial charge transfer ($\delta = 0.02$) from the small red-shift to 2214 cm^{-1} (in **PDVT-CS**). An extremely small portion of **CS** is ionized in the mixture and supports the GS-CPX mechanism.

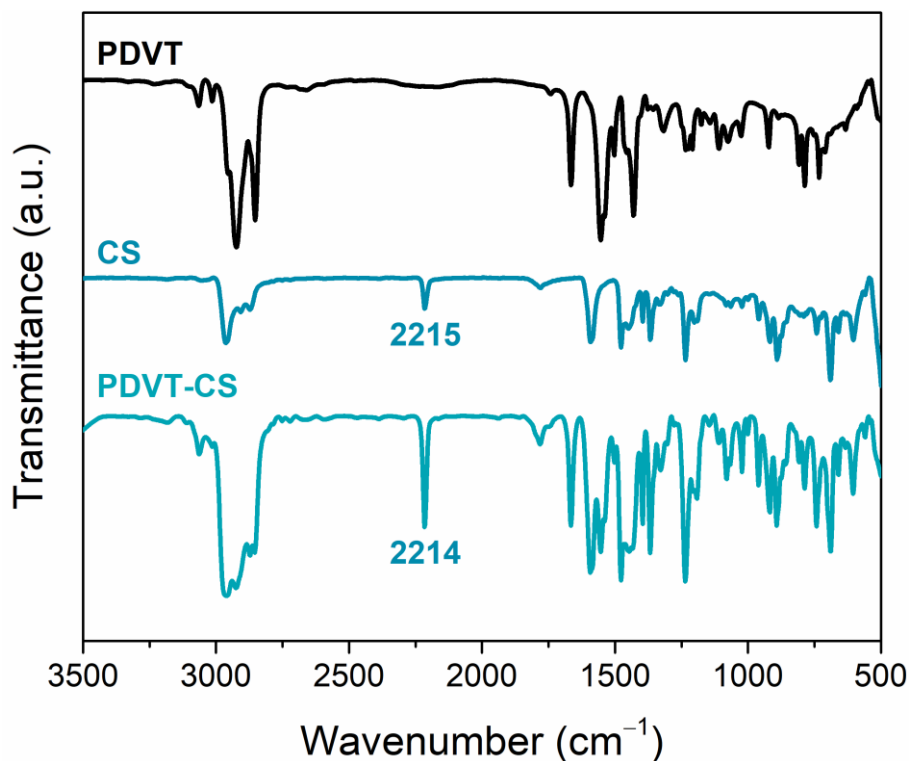


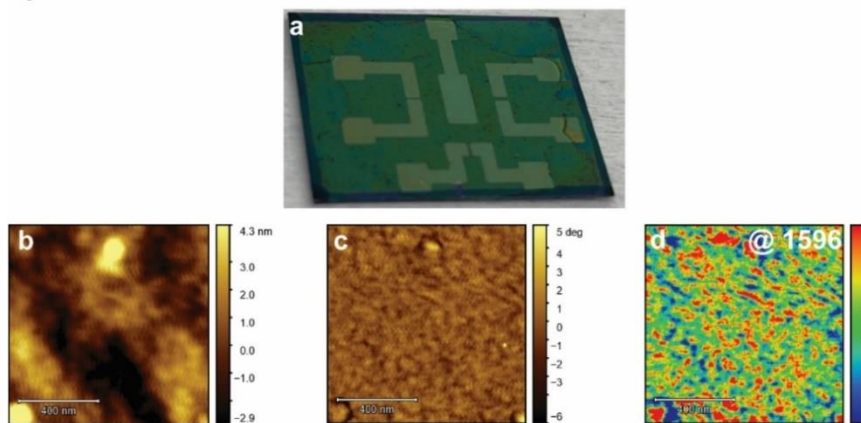
Figure 3.7 FTIR spectra of neat *PDVT*, neat *CS*, and *PDVT-CS* blends with emphasis on the *CS* cyano peak (2215 cm^{-1}).

3.3.3 Influence on Film Morphology

Nanoscale chemical composition mapping was facilitated through atomic force microscope infrared spectroscopy (AFM-IR). It is a technique that merges the chemical analysis power of IR spectroscopy and the surface probing capabilities of high-resolution scanning probe microscopy. A high-speed and tunable pulsed IR laser is focused on the position below the AFM tip. After tuning the laser pulse rates to the characteristics of the AFM cantilever, the AFM tip (gold-coated, spring constant: 40 N/m) oscillates at a resonance frequency of 300 kHz in tapping mode and makes intermittent contact with the sample surface. When a pulsed IR wavelength matches the absorption band of the molecule, a thermal expansion occurs and increases the amplitude of oscillation, and alters the response of the cantilever. Chemical composition mapping is then generated by

measuring the AFM cantilever oscillation amplitude as a function of surface position at a fixed excitation wave number (1596 cm^{-1} , CS C=C stretching). The AFM images show that spin-coated films display a reasonably smooth surface and a homogeneous distribution of CS (red regions) (Figure 3.8d). Slow drying the film improves chain alignment and small-molecule self-assembly. These two concepts are evident in Figure 3.8e-i; the CS macrocycles behave as microscopic templates for controlling the directional crystallization of PDVT chains. CS can undergo self-association and create an extended tube-like space that comprises the highly ordered lamellae. In contrast, the PDVT chains (blue regions) align with the tubular structures and takes part as the amorphous region.

Spin-Cast



Slow Drying

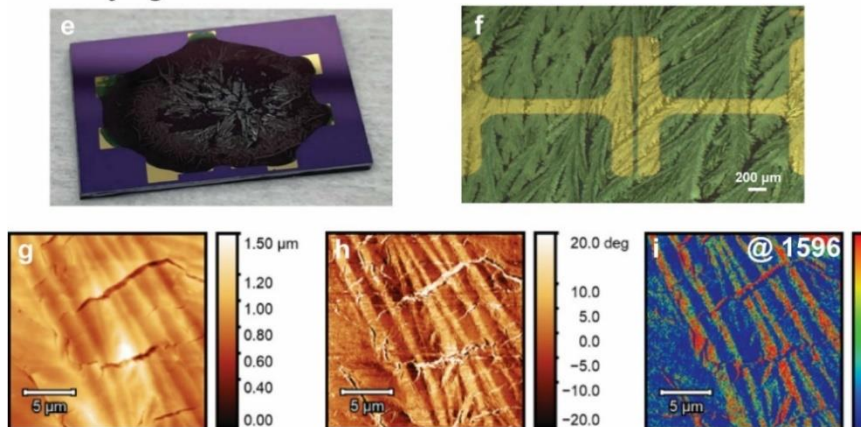


Figure 3.8 AFM-IR on **PDVT-CS** films: (a) Picture of a prefabricated device encapsulated with a spin-casted active layer with the corresponding (b) height, (c) phase, and (d) IR scans. (e) Picture of a prefabricated device encapsulated with a slow-dried film, causing the formation of spherulitic microstructures as viewed on the (f) optical microscope image (scale bar: 200 μm) and AFM (g) height, (h) phase, and (i) IR scans. The IR pulses used in the test runs were activated at 1596 cm^{-1} , matching an absorption band found in **CS**. Red peaks correspond to **CS** while blue corresponds to **PDVT**.

3.4 Conclusions

PDVT as a host matrix offers excellent compatibility with **CS**, enabling a polymer dopant system based on the weak intermolecular coupling that could potentially augment the signal transduction mechanism for anion binding studies. The shape-persistent structure of **CS** appears to improve the film microstructure ordering, especially when the films are not kinetically quenched by spin-coating. This combination of materials offers various opportunities to tune important device figures of merits and new mechanisms that could be explored for sensing applications.

CHAPTER IV – RECEPTOR-INDUCED DOPING OF CONJUGATED POLYMER TRANSISTORS: A STRATEGY FOR SELECTIVE AND ULTRASENSITIVE PHOSPHATE DETECTION IN COMPLEX AQUEOUS ENVIRONMENTS

4.1 Abstract

Phosphate oxyanions play central roles in biological, agricultural, industrial, and ecological processes. Their high hydration energies and dynamic properties present a number of critical challenges limiting the development of sensing technologies that are cost-effective, selective, sensitive, field-deployable, and which operate in real-time within complex aqueous environments. Here, we demonstrate a strategy that enables the fabrication of an electrolyte-gated organic field-effect transistor (EGOFET) that overcomes these challenges and enables sensitive phosphate quantification in challenging aqueous environments such as seawater. The device channel comprises a composite layer incorporating a diketopyrrolopyrrole-based semiconducting polymer and a π -conjugated penta-*t*-butylpentacyanopentabenz[25]annulene “cyanostar” receptor capable of oxyanion recognition and embodies a new concept, where the receptor synergistically enhances the stability and transport characteristics via doping. Upon exposure of the device to phosphate, a current reduction was observed, consistent with dedoping upon analyte binding. Sensing studies demonstrate ultrasensitive and selective phosphate detection within remarkably low limits of detection of 178 pM (17.3 parts per trillion) in buffered samples and stable operation in seawater. This receptor-based doping strategy, in conjunction with the versatility of EGOFETs for miniaturization and monolithic integration, enables manifold opportunities in diagnostics, healthcare, and environmental monitoring.

4.2 Introduction

Phosphate oxyanions play central roles in biological, agricultural, industrial, and ecological processes.¹³⁸⁻¹⁴⁰ As a principal constituent of biological systems, phosphate is industrially relevant in the production of medicinal drugs, pharmaceuticals, therapies, and is crucial to the growth of plants and animals.¹⁴¹⁻¹⁴² Phosphate oxyanions also serve as potent environmental pollutants “responsible for the eutrophication of natural water sources” leading to hypoxia, fish kills, and “dead zones”.¹⁴³⁻¹⁴⁶ The development of low-cost, selective, and real-time sensors that operate in complex aqueous environments remains a considerable task, precluding the development of critical sensing technologies such as those related to biomedicine, environmental monitoring, and point-of-need testing.^{31, 147-151} Current methods of nutrient quantification necessitate sample collection, extraction, and enrichment followed by colorimetric analyses or laboratory-based spectrophotometric, fluorescent, and chromatographic methods.¹⁵²⁻¹⁵⁴ Portable ion-selective electrodes (ISEs) offer the opportunity for real-time monitoring, however, the hydrated nature and dynamic properties of these anions result in cross-interference,¹⁵⁵⁻¹⁵⁶ limiting their accurate quantification at relevant concentrations (0.02 – 2 μM) in freshwater and seawater.¹⁵² The need for improved analytical performance, miniaturization, *in-situ* operation, and access to spatially and temporally representative data has driven the development of solid-state potentiometric, chemiresistive, amperometric, capacitive, and field-effect transistor sensor platforms.¹⁵⁷⁻¹⁵⁹ In these devices, specificity is derived from molecular recognition elements such as ion-selective membranes, molecularly imprinted polymers, biomacromolecules, and small-molecule receptors.^{5, 95, 160-161} Despite the exploration of a vast chemical space and advancements in

device design, the specificity and sensitivity required for trace detection of these anions have yet to be achieved.

Label-free organic electronic sensors based on organic field-effect transistor (OFET) architectures offer novel attributes that match the needs of emerging sensor platforms.^{5, 162-163} These include low-cost fabrication on diverse substrates, synthetic tunability, mechanical compliance, and direct integration with existing signal processing electronics, enabling monolithic sensing systems.¹¹⁰ Furthermore, OFET-based sensors offer improved sensitivity resulting from amplification endowed by the field-effect, the integration of chemical probes at the surface, channel, or electrodes of the device, and high diversity in device architecture. These attributes have advanced OFET-based sensors to the forefront of environmental, biomedical, and wearable diagnostics platforms. Among these, electrolyte-gated OFETs (EGOFETs) are promising for *in-situ* monitoring since they directly transduce interfacial phenomena such as molecular recognition events into electrical signals with ultra-high sensitivity.¹⁶³ While these transistors can be endowed with selectivity through various functionalization strategies, it remains a challenge to electronically couple such receptor chemistries to the active materials of these devices.¹¹⁰ Furthermore, the integration of many host-guest chemistries into transistors comes at the cost of reduced device performance and a loss of both stability and selectivity in complex aqueous environments.

Over the past two decades, there have been remarkable breakthroughs in the design and synthesis of supramolecular receptors capable of host-guest oxyanion complexation.^{107, 164-166} In particular, penta-*t*-butylpentacyanopentabenz[25]annulene “cyanostar” (CS) demonstrates high-fidelity binding of larger anions such as H_2PO_4^-

within its electropositive, size-selective cavity by virtue of aromatic CH bonding interactions.^{105, 167} **CS** has been utilized as an ionophore¹⁶⁸⁻¹⁶⁹ but has not been leveraged in an OFET architecture to endow selectivity. Here, we describe the development of an EGOFET comprised of a composite layer of a semiconducting polymer poly[2,5-bis(2-decyltetradecyl)pyrrolo[3,4-*c*]pyrrole-1,4-(2*H*,5*H*)-dione-*alt*-(E)-1,2-di(2,2'-bithiophen-5-yl)ethene] (**PDVT**) and **CS** that enables the detection of oxyanions within complex aqueous environments. Crucial aspects of the sensor, such as high environmental stability and oxyanion recognition, are achieved using a new strategy in which **CS** dopes the semiconducting polymer. In the presence of analytes, **CS** preferentially binds phosphate, resulting in dedoping and large changes to the electrical properties that are compatible with digital readout methods. The robust nature of the electronic doping-dedoping phenomena is demonstrated in complex aqueous environments such as seawater and is therefore amenable for the real-time selective detection of phosphate oxyanions.

4.3 Results and Discussion

Electron paramagnetic resonance (EPR) spectroscopy was used to investigate the doping phenomena. Films were prepared by evaporating chloroform solutions of **PDVT** and **PDVT-CS** in 4 mm quartz EPR tubes using the same **CS** loading as the UV-Vis-NIR films. While **PDVT** films and **CS** showed no signal (Figure 4.1 and Figure B.1), **PDVT-CS** films displayed a broad, single line at a *g*-factor (*g*) of 2.0034, indicating the formation of paramagnetic species (Figure 4.1a,b and Table B.1) by doping. Doping was also supported by Kelvin force microscopy (KPFM) measurements, which demonstrate a considerable shift in the **PDVT** Fermi level upon the addition of **CS** (Figure A.6).¹⁷⁰ **CS** macrocycles offer novel anion recognition capabilities on account of their propensity to

bind and stabilize anions.¹⁰⁶ As such, organic-soluble tetrabutylammonium dihydrogen phosphate (**TBAP**, 1 equiv. relative to **CS**) was mixed with **PDVT-CS**, which resulted in a dramatic reduction in the EPR signal and predominantly diamagnetic behavior (Figure 4.1a,c). Taken together, the **PDVT-CS** combination demonstrates an anion-induced electronic transition which presents itself as a design paradigm for the chemical sensing of phosphate.

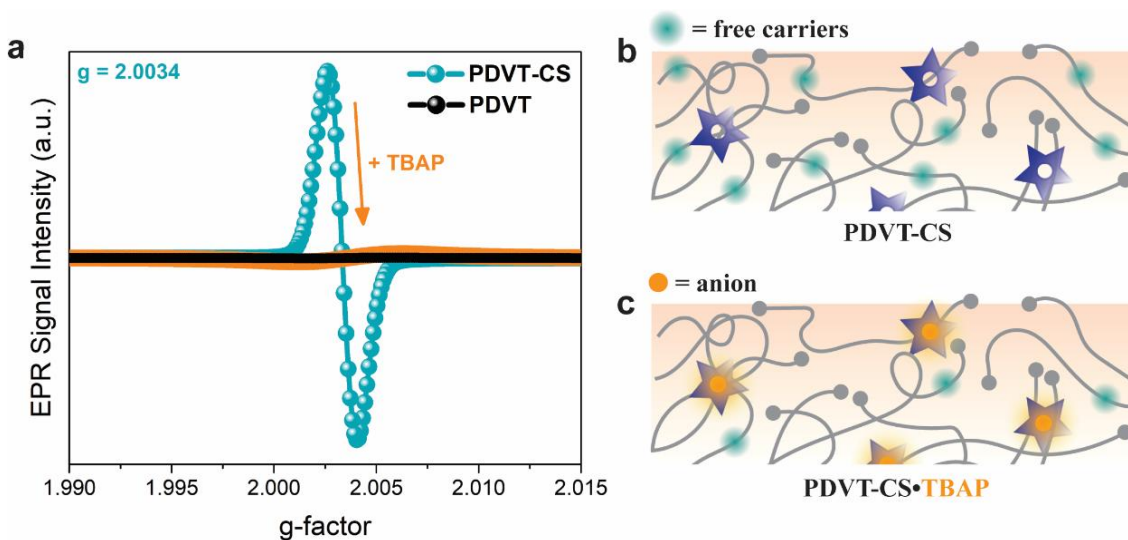


Figure 4.1 (a) EPR (X-band) spectra at room temperature of **PDVT-CS** demonstrating the formation of paramagnetic species, consistent with (b) doping. Upon addition of tetrabutylammonium dihydrogen phosphate (**TBAP**, 1 equiv. relative to **CS**) to **PDVT-CS** the films show predominantly diamagnetic behavior, consistent with (c) dedoping.

We sought to translate the electronic behavior observed for **PDVT-CS** mixtures exposed to **TBAP** from Figure 4.1 by incorporating the composite into an OFET architecture. Anions were directly embedded into the **PDVT-CS** composite matrix to investigate anion-induced electronic perturbations. Adopting the original protocols for device fabrication and testing, organic-soluble tetrabutylammonium salts (**TBAX**, where **X** = dihydrogen phosphate (**P**), nitrate (**N**), chloride (**Cl**), perchlorate (**PC**), and hydrogen

sulfate (**HS**)) were added to **PDVT-CS** chlorobenzene solutions (1 equiv. relative to **CS**) for competitive binding measurements. The anions listed were selected based on their vital role and prevalence in ecosystems and agriculture.¹⁷¹⁻¹⁷³ The binding of anions by **CS** in low dielectric solvents is an electrostatically driven process, which takes place inside the central cavity and arises from activated C–H hydrogen-bonding units.¹⁰⁵ The solvent choice (chlorobenzene, $\epsilon = 5.62$) and the sequential film casting into an OFET architecture introduces the appropriate conditions to monitor the analyte's preferential interactions, whether towards the receptor or polymer chain.

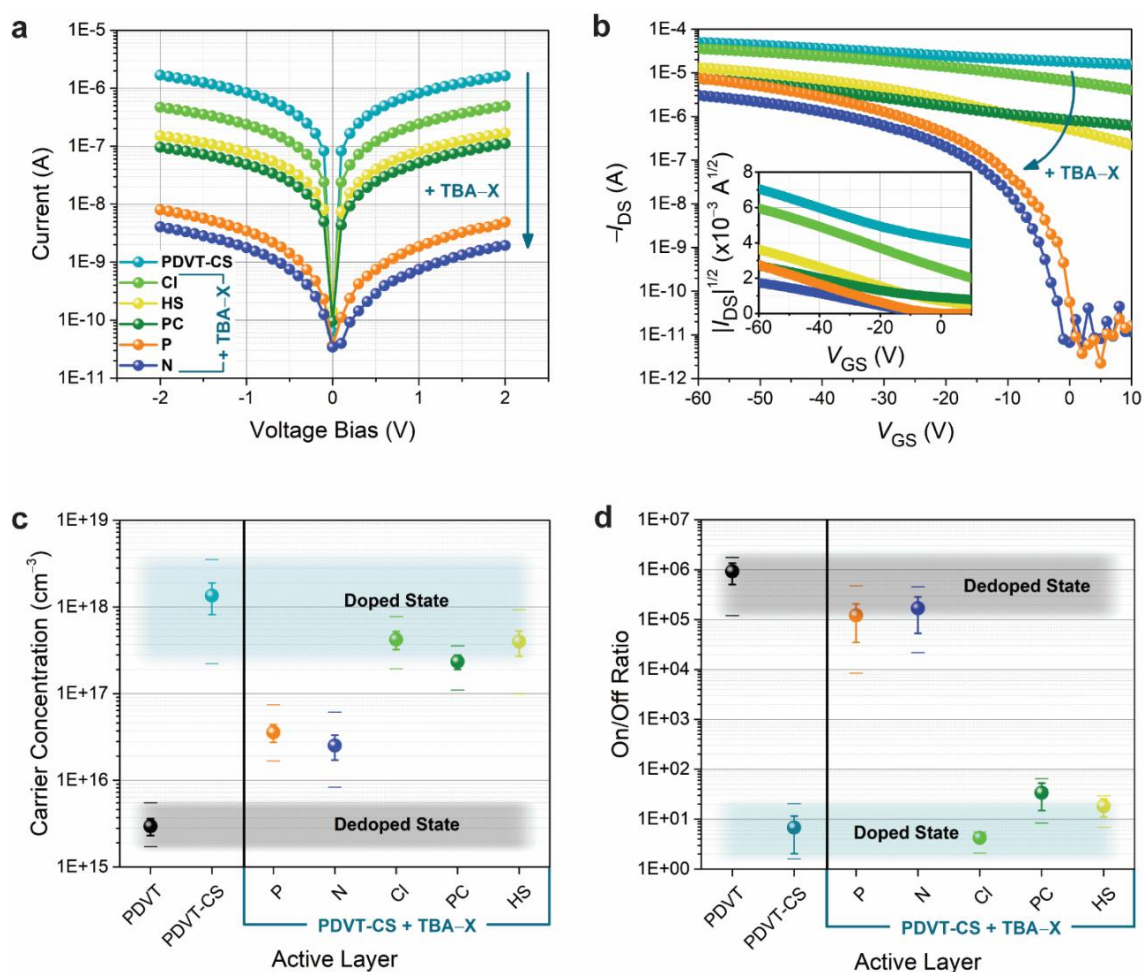


Figure 4.2 OFET devices (BCBG configuration) based on a three-component mixture **PDVT-CS•TBA-X** salts ($X = P, N, Cl, PC,$ and **HS**) and their associated a) two-point

probe I–V characteristics and b) OFET transfer curves. The variation in the dedoping response and the preservation of charge transport characteristics without degradation demonstrates that receptor-anion interactions dictate the magnitude of charge carrier reduction. c) Summary of carrier concentration (cm^{-3}) within the conductive channel and d) OFET on/off ratio comparing 10 independent devices with source and drain electrode geometries of $L = 80 \mu\text{m}$ and $W = 1 \text{mm}$.

Both σ_{RT} and μ measurements reveal anion composition-dependent channel conduction and offsets from the original **PDVT-CS** film properties (dedoping) (Figure 4.2). The **TBAP** and **TBAN** films, in particular, displayed the highest reduction (> 2 orders of magnitude) in bulk channel conduction with $\sigma_{\text{RT}} = 3.55 \times 10^{-5}$ and $5.28 \times 10^{-5} \text{ S cm}^{-1}$ and in carrier density with $n = 5.24 \times 10^{16}$ and $2.49 \times 10^{16} \text{ cm}^{-3}$, respectively (Figure 4.2a,c). These characteristics coincide with the high on-off current ratios ($I_{\text{on}}/I_{\text{off}} > 10^5$) (Figure 4.2b,d) and closely mirror the native **PDVT** profile (Figure 3.6c). On the other hand, σ_{RT} values only moderately decreased to $3.09 \times 10^{-3} \text{ S cm}^{-1}$ (**TBACl**), $4.86 \times 10^{-4} \text{ S cm}^{-1}$ (**TBAPC**), and $6.40 \times 10^{-4} \text{ S cm}^{-1}$ (**TBAHS**) and similar carrier concentrations were obtained with $n = 4.59 \times 10^{17}$, 2.40×10^{17} , and $1.54 \times 10^{17} \text{ cm}^{-3}$, respectively. To ensure these anion interactions are preferential to the receptor, **TBAP** and **TBAN** were separately added to **PDVT** (without **CS**) to assess how it alters the transfer profile. Both conditions degraded the **PDVT** *p*-channel operation once introduced (Figure B.10) and support the notion of receptor-anion host-guest complexation as the dominant factor in the dedoping responses. Collectively, the electrical characterization techniques correlate to the diamagnetic behavior found in EPR studies (Figure 4.1a,c). Due to the weak nature of intermolecular interactions, the host-guest complexation of **CS** resulted in a perturbation of the electronic structure or

diminished steric interactions with the π -system. This robust phenomenon manifests as a dramatic change in electrical properties only in the presence of specific anions.

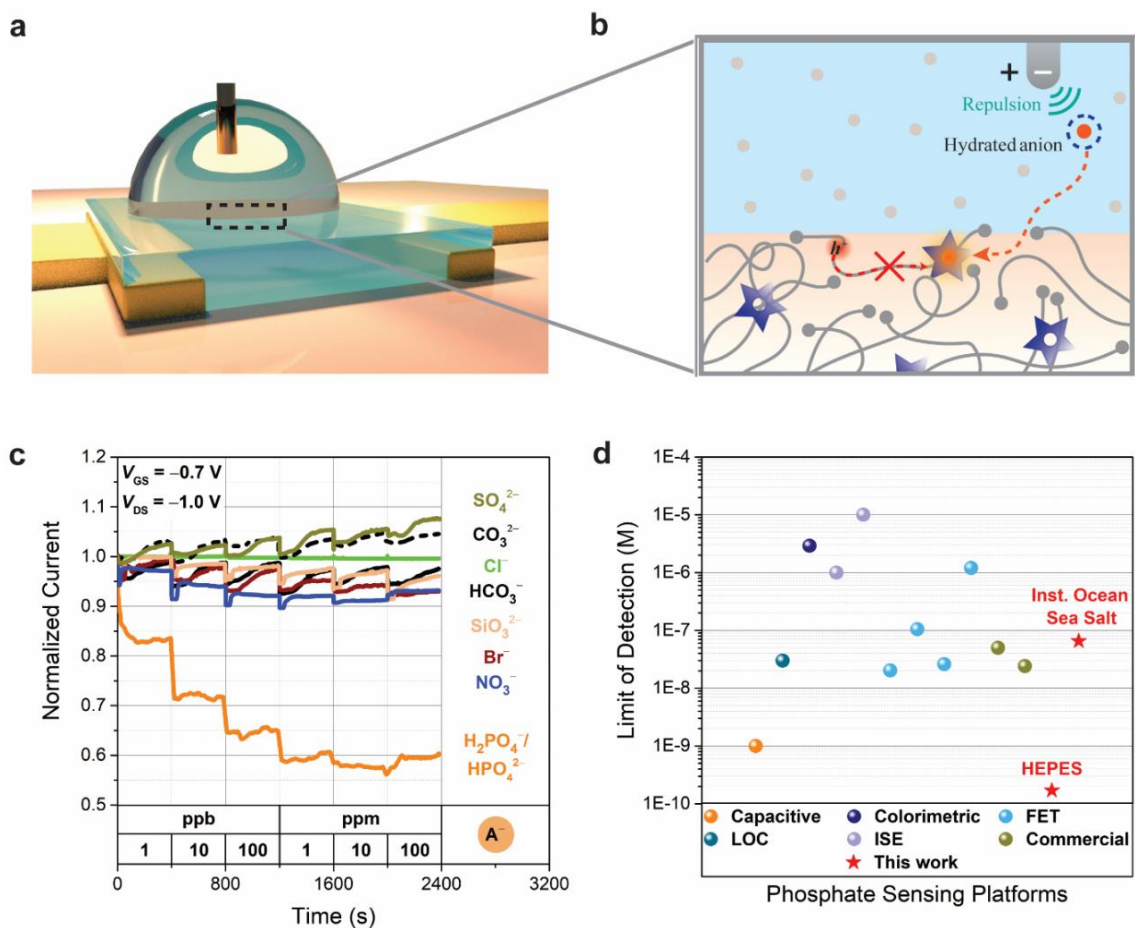


Figure 4.3 a) Schematic illustration of the EGOFET device and b) the proposed sensing mechanism. c) Transient responses of the device towards phosphate ($H_2PO_4^-/HPO_4^{2-}$), nitrate (NO_3^-), bicarbonate (HCO_3^-), carbonate (CO_3^{2-}), and chloride (Cl^-) in HEPES buffer (pH = 7.4). d) Comparison of state-of-the-art phosphate sensors with PDVT-CS, which demonstrated a limit of detection (LOD) and quantification (LOQ) of 178 pM (17.3 parts per trillion (ppt)) and 430 pM (41.7 ppt), respectively.

To investigate whether the observed anion selectivity in the OFET configuration could be translated to a real-time aqueous sensor, water-soluble sodium salts of the previously tested anions were introduced to the PDVT-CS film within an aqueous

electrolyte (HEPES, pH = 7.4), (Figure 4.3a). In this EGOFET configuration, the Ag/AgCl gate was electrically coupled to the composite film via the electrolyte solution, which was then spiked with the anion salt of interest. The gate electrode bias facilitates ion migration towards the channel interface with no bulk volumetric response due to the hydrophobic nature of the film (Figure B.14). Further details regarding EGOFET fabrication can be found in the Supporting Information. While **PDVT-CS** films remained stable when tested under various pH conditions (4 – 10, Figure B.16), HEPES buffer (baseline) solution showed consistent output responses (Figure B.25) and was used to maintain consistent sensing environments between each analyte (Figures B.17–B.24). Baseline measurements were first conducted by monitoring the drain current (I_{DS}) drift upon continuous exposure to an aqueous solution with no target analyte present. Next, the transient responses toward dissolved sodium salts of phosphate ($H_2PO_4^-$), nitrate (NO_3^-), bicarbonate (HCO_3^-), carbonate (CO_3^{2-}), and chloride Cl^- at various concentrations (nM – mM) were measured and compared to the baseline trend so as to determine the channel current offset and the resultant chemical sensing performance (Figures B.27a–B.34a). The sensitivity (S) is defined by the relative change of the drain current under the same voltage conditions ($V_{GS} = -0.7$ V and $V_{DS} = -1.0$ V) following the equation:¹⁷⁴

$$S = \frac{|I_{DS}(analyte) - I_{DS}(baseline)|}{I_{DS}(baseline)} \times 100$$

Upon analyte introduction, the electrical response to phosphate anions emanates from migration to the film interface (< 1 nm film swelling exposed to DI water, Figure B.14), leading to physical adsorption and channel conduction changes. In this case, receptor-analyte complexation generated a dedoping response as a function of anion concentration,

which matches the results from the three-component films (Figures 4.1–4.2). The limit of detection (LOD) and quantification (LOQ) were calculated from the noise of each sensor as previously reported.¹⁷⁵⁻¹⁷⁶ From the calibration plot for phosphate, the LOD and LOQ were calculated to be 178 pM (17.3 ppt) and 430 pM (41.7 ppt), respectively. The observed sensitivity is competitive with diverse classes of state-of-the-art phosphate sensors including capacitive,¹⁷⁷ colorimetric,¹⁷⁸ lab-on-chip (LOC),¹⁷⁹ ion-selective electrodes (ISE),¹⁸⁰⁻¹⁸¹ FETs,^{175, 182-184} and commercialized products (Figure 4.3d and Table B.6).

The selectivity was investigated by individually challenging the device with other mono- and divalent anions comprising NO_3^- , SiO_3^{2-} , Br^- , HCO_3^- , CO_3^{2-} , SO_4^{2-} , and Cl^- (Figure 4.3c). Overall, the transient responses revealed a more pronounced reduction in the bulk channel conduction upon exposure to phosphate when compared to the other anions tested. Calibration and sensitivity metrics for each anion can be found in the Figures B.27b–B.34b.

To demonstrate the potential for real-time phosphate oxyanion detection in the marine environment, we tested the **PDVT-CS** EGOFETs in high ionic strength, artificial seawater solution (Instant Ocean Sea Salt electrolyte). This mixture gives a typical salinity of 35 parts per thousand and contains appreciable concentrations of ions prevalent in seawater (>1 ppm): Na^+ , K^+ , Mg^{2+} , Ca^{2+} , and Sr^{2+} , Br^- , Cl^- , CO_3^{2-} , HCO_3^- , and SO_4^{2-} . The transient responses toward the dissolved sodium salt of phosphate at various concentrations (nM – mM) were measured using the same conditions employed for measurements in HEPES buffer. The LOD and LOQ in artificial seawater were 65.4 nM (6.54 parts per billion (ppb)) and 940 nM (91.2 ppb), respectively (Figure B.51b). The

measured sensitivity and seawater stability (Figure 3.6e) are competitive with current technologies (Figure 4.3d, Table B.6), demonstrating the utility of our approach for the real-time selective detection of phosphate oxyanions.

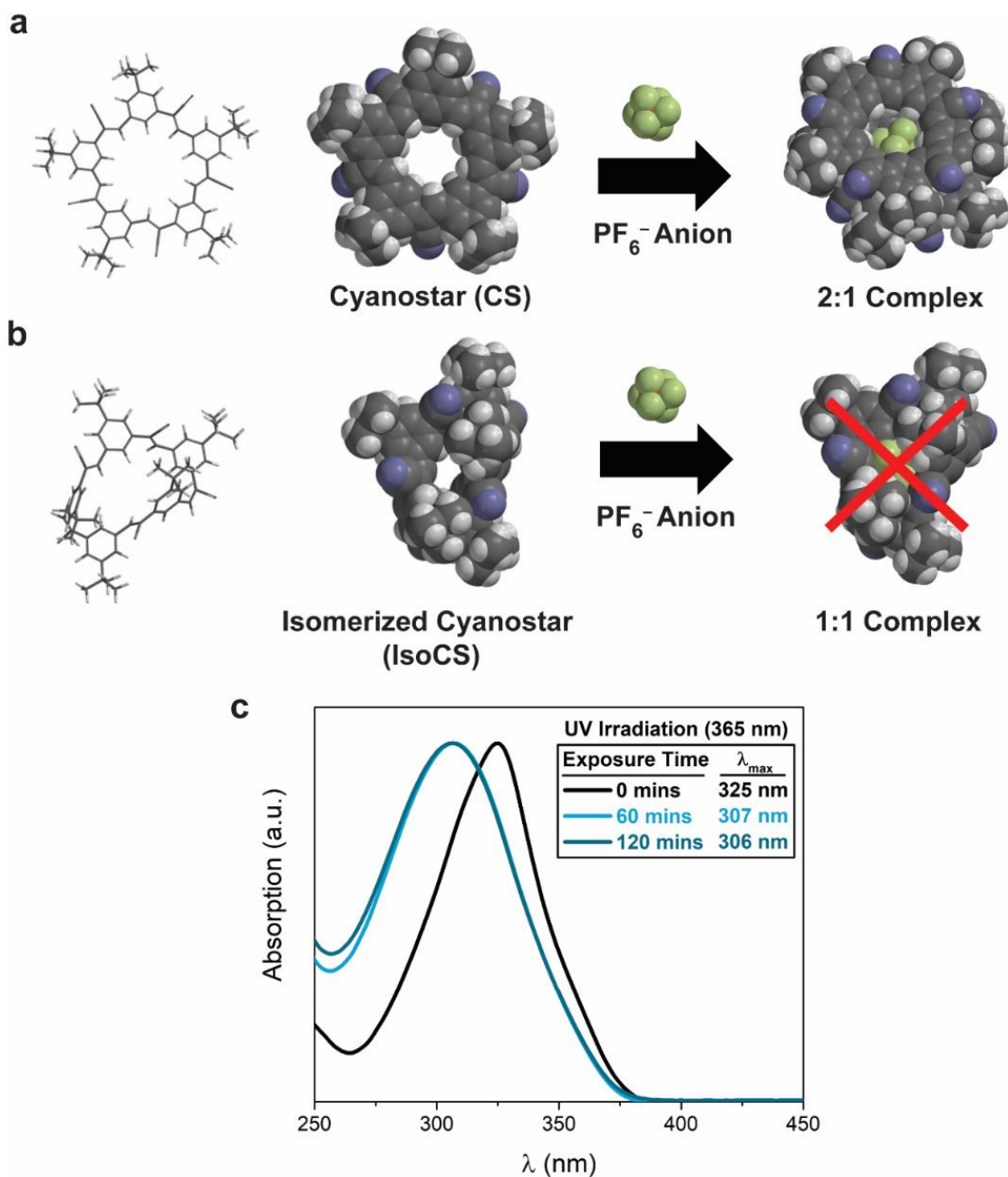


Figure 4.4 Anion recognition control experiment. a) 2:1 sandwich complex involving a PF_6^- anion. Under a UV treatment (365 nm), the cyanostar was photoisomerized (*IsoCS*). b) Depiction of a *trans-cis-trans-cis-trans* conformer (one of 2^5 potential isomers) precluding host-guest complexation. This receptor configuration was integrated

into the **PDVT** host matrix to conduct a series of control experiments where we do not expect any analyte binding. c) UV-vis absorption spectra of **CS** CHCl_3 solutions undergoing photoisomerization. The solutions show absorption profiles with the maxima (λ_{max}) reaching equilibrium beyond 1 h of exposure to 365 nm UV photons.

To further support the **CS**-dependent selective dedoping of the real-time sensor, EGFETs were fabricated and tested with photoisomerized **IsoCS** (Figure 4.4, Figure B.2 and Table B.3), rather than **CS**. The solution NMR of **IsoCS** (Figures B.36–38) and sequential PF_6^- anion titration experiments (Figures S39-41) suggested a lack of anion affinity. Moreover, aqueous sensors using **PDVT-IsoCS** active layers were electrochemically unstable and no statistically significant electrical responses were observed upon anion addition (Figure 4.5 and Figures B.42–49). Taken together, the anion-selective dedoping response of the device was dependent on the shape-persistent electropositive cavity of the **CS**, rather than other possible interactions with **PDVT**.

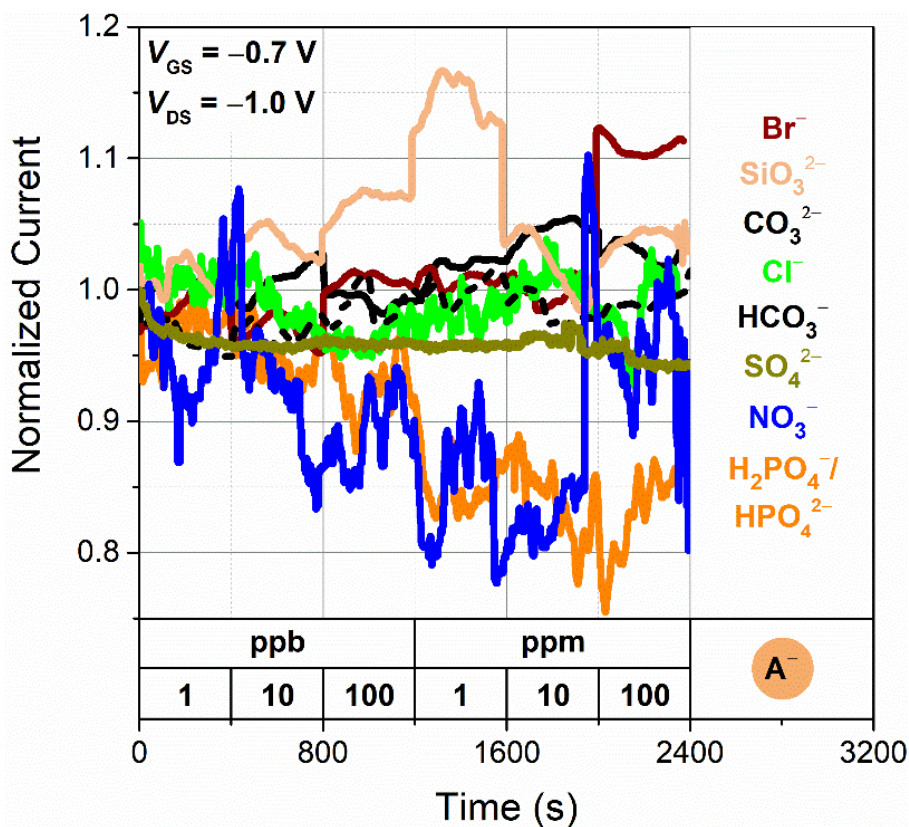


Figure 4.5 *PDVT-IsoCS EGOFET transient responses of the device towards phosphate ($H_2PO_4^-/HPO_4^{2-}$), nitrate (NO_3^-), bicarbonate (HCO_3^-), carbonate (CO_3^{2-}), and chloride (Cl^-) in HEPES buffer (pH = 7.4).*

4.4 Conclusion

In summary, we have demonstrated a new strategy for the selective detection of phosphate, an anion with central roles in biological, agricultural, industrial, and ecological processes. This was enabled by the combination of the semiconducting polymer **PDVT** with **CS**. This synergistic combination offered engineered electronic interactions that result in doping and unparalleled stability in water, selective phosphate complexation by the receptor in the presence of competing anions, and a significant dedoping of the polymer in the presence of phosphate. Spectroscopic analysis suggests the doping was promoted by weak orbital mixing of **PDVT** and **CS**, forming a ground state CTC sensitive to electronic and structural perturbations induced by analyte binding. When the active layer was mixed with TBA salts of various anions, the device transfer and *I-V* characteristics demonstrate a selective and strong dedoping response toward phosphate. This selectivity was then translated to an EGOFET for real-time experiments, which demonstrated ultrasensitive phosphate detection with a LOD of 178 pM (17.3 ppt) in buffered samples, well within the U.S. Environmental Protection Agency specifications. The device also demonstrated the stable, selective, and sensitive detection of phosphate in artificial seawater, a rare demonstration and critical step towards practical field deployment. The unmatched performance of this sensor and new strategy for analyte detection overcome significant challenges and offer a novel approach for phosphate detection within complex aqueous environments. In a broader context, the combination of semiconducting polymers with next-generation receptors offers manifold opportunities

for designing novel composite films that can be applied within emerging OFET-based diagnostic, healthcare, environmental monitoring, and bioelectronics platforms.

A.1 Supplemental Figures and Tables

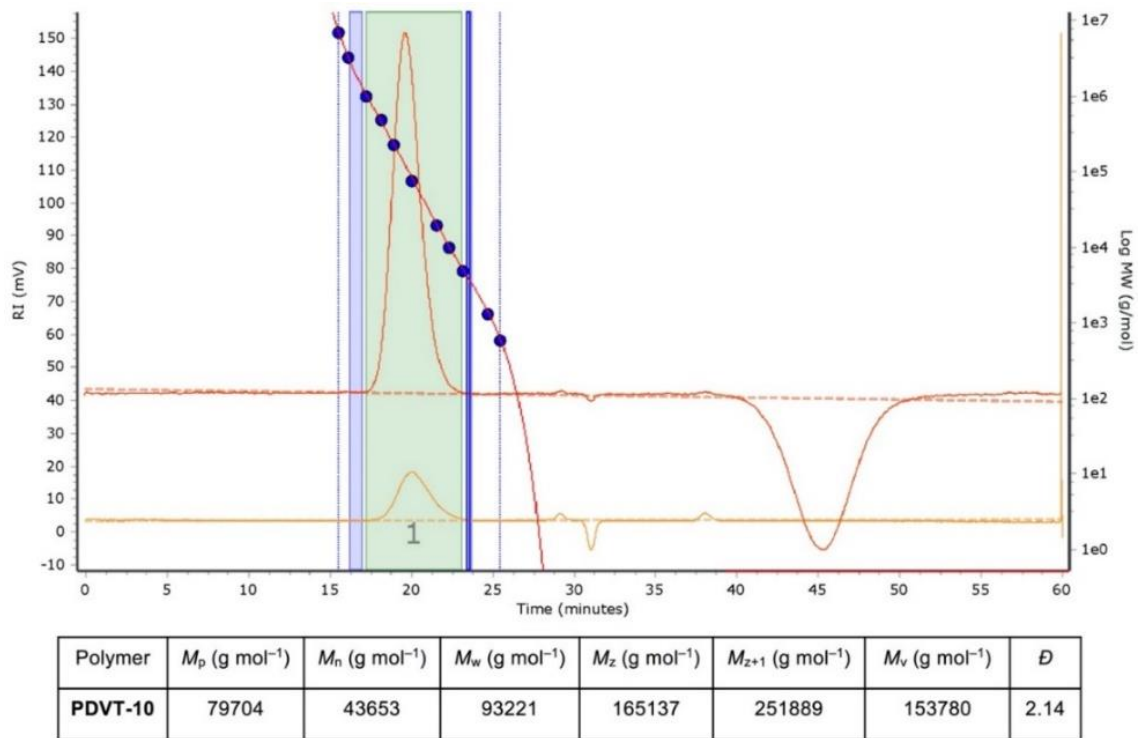


Figure A.1 GPC (TCB, 160 °C) trace of **PDVT**.

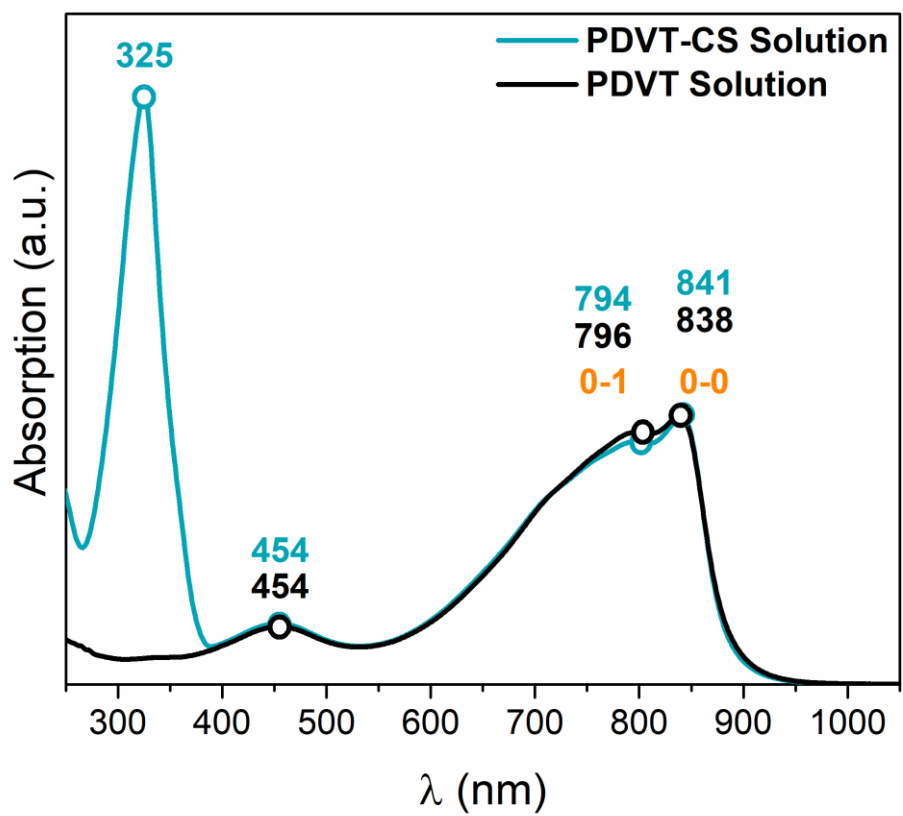


Figure A.2 UV-Vis-NIR absorption spectra in C_6H_5Cl solution

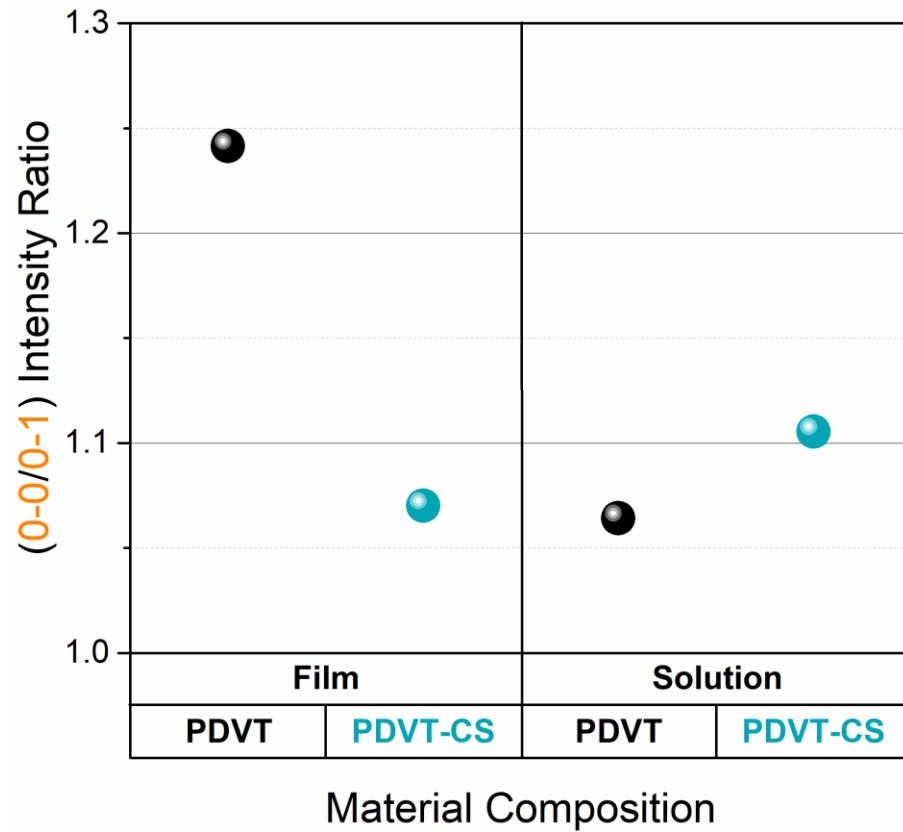


Figure A.3 UV-Vis-NIR absorption intensity ratio ($A_{0-0/0-1}$) versus material composition and film versus solution .

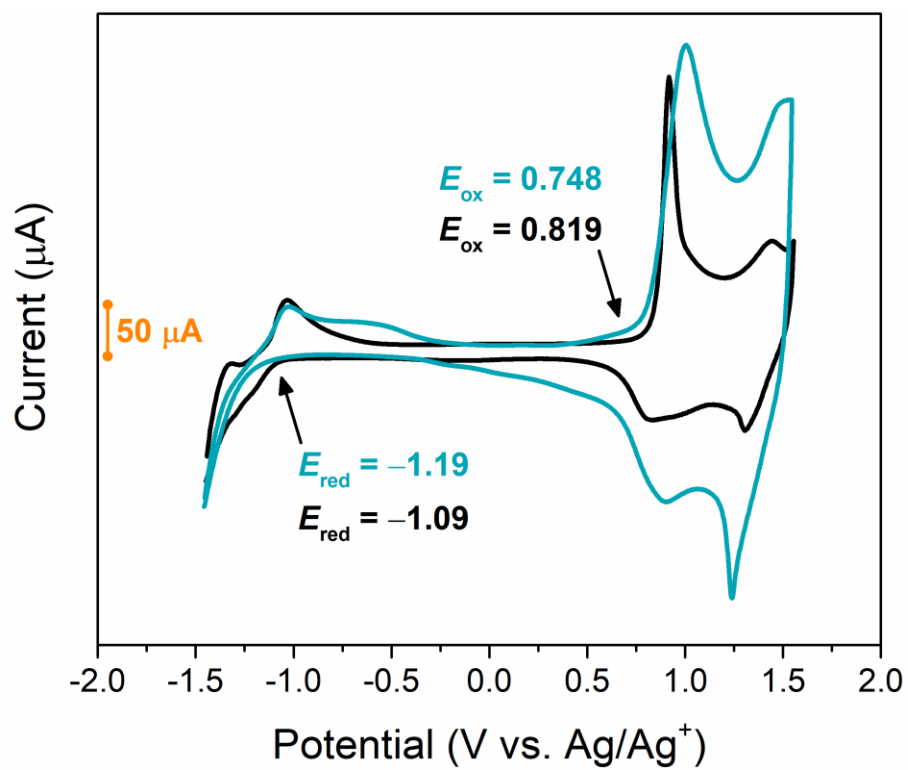


Figure A.4 Cyclic voltammetry (CV) spectra showing the onset of oxidation and reduction.

Table A.1 *Optical and electrochemical properties summary.*

Polymer	Solution λ_{\max}^a (nm)	Film λ_{\max}^b (nm)	$E_g^{\text{opt } c}$ (eV)	E_{HOMO}^d (eV)	E_{LUMO}^e (eV)	$E_g^{\text{elec } f}$ (eV)
PDVT	838, 796, 454	804, 731, 449	1.34	-5.57	-3.66	1.91
PDVT- CS	841, 794, 454, 325	793, 725, 449, 310	1.28	-5.50	-3.56	1.94

^a Dilute solution made from C_6H_5Cl . ^b Thin films spin-coated from C_6H_5Cl (10 mg mL^{-1}). ^c

E_g^{opt} estimated from the film absorption onset. ^d E_{HOMO} and ^e E_{LUMO} calculated from the CV onset of oxidation and reduction, respectively. ^f E_g^{elec} calculated from the difference between E_{HOMO} and E_{LUMO} .

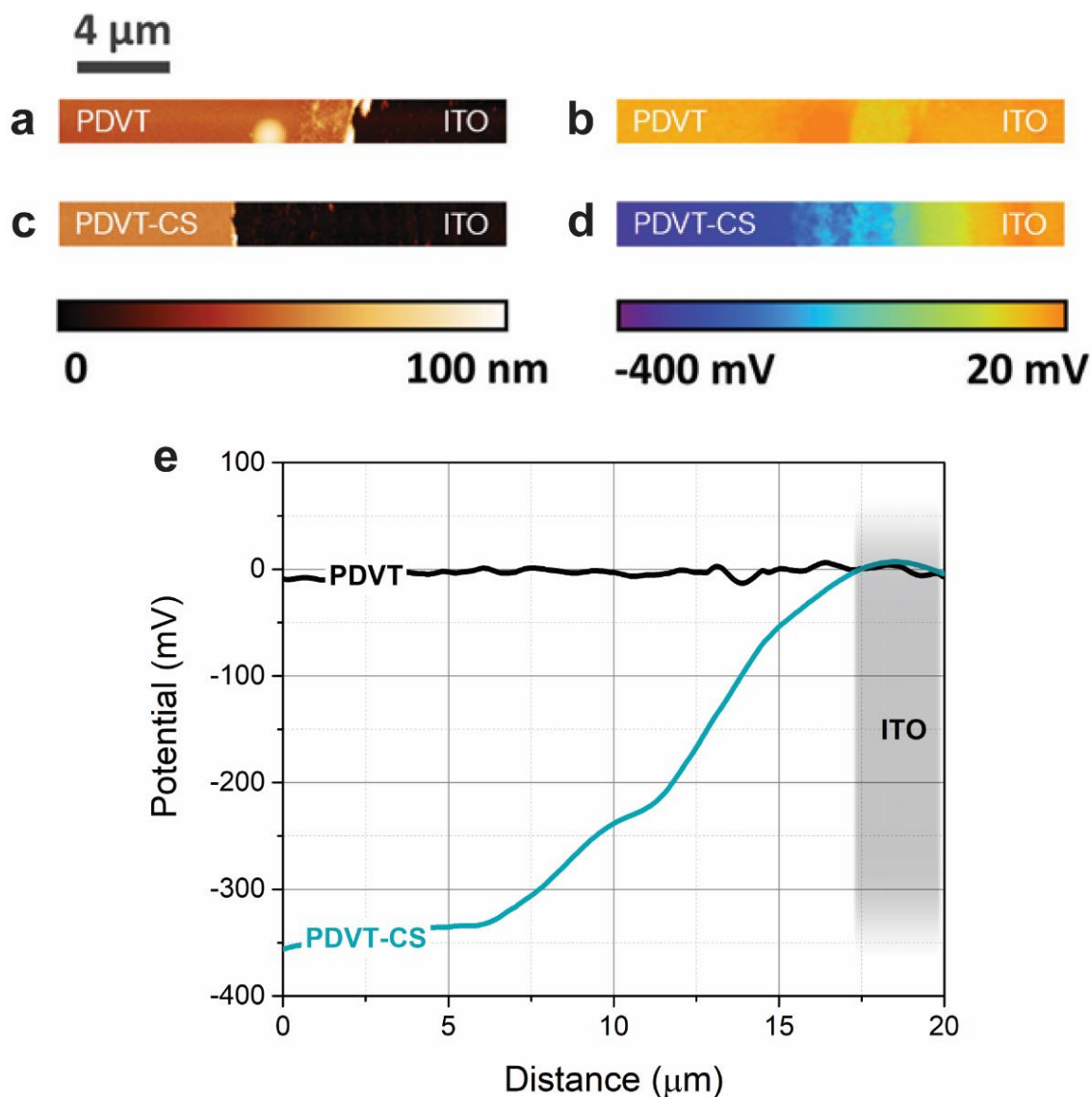


Figure A.5 Kelvin probe force microscopy (KPFM) surface potential measurements of **PDVT** and **PDVT-CS** as-spun on ITO glass substrates. After film removal via scratch test, the probe was scanned over the film/ITO border. (a,b) Topography and (c,d) surface potential images between **PDVT/ITO** and **PDVT-CS/ITO**, where a clear distinction (potential drop) was found with **CS** admixing. (e) Plots showing the receptor-induced surface potential changes from images b and d.

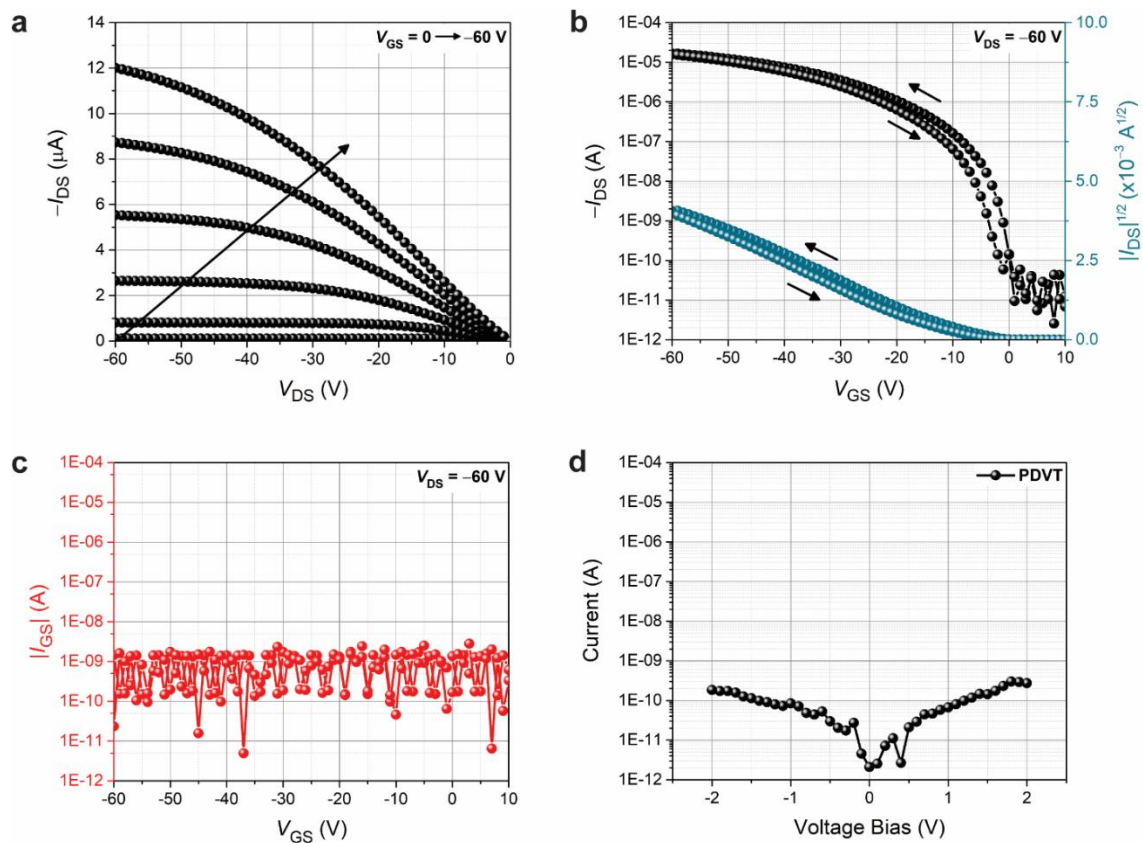


Figure A.6 (a) OFET output (I_{DS} vs V_{DS}), (b) transfer (I_{DS} vs V_{GS}), and (c) gate leakage (I_{GS} vs V_{GS}) characteristics of pristine PDVT films using a BGBC device configuration and (d) 2-point probe room-temperature I - V plot (without a gate electrode).

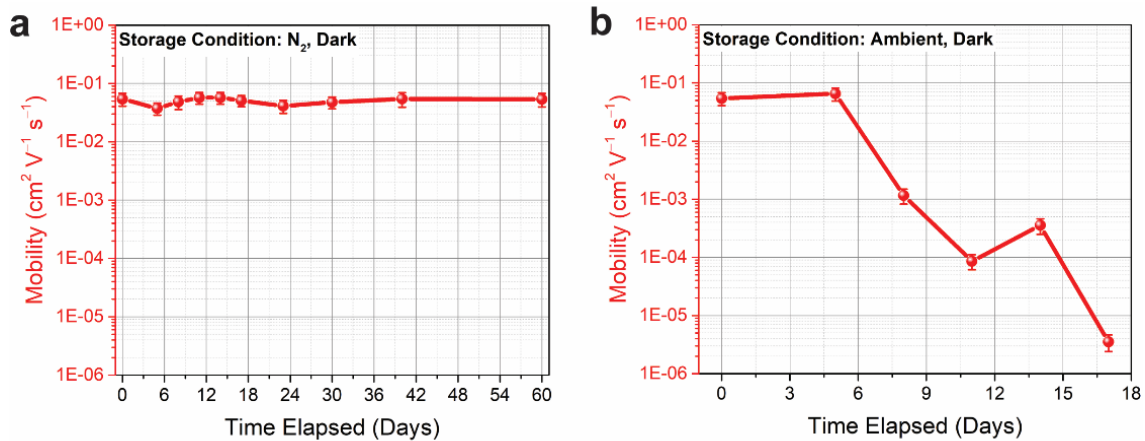


Figure A.7 Monitoring charge transport shelf-life for high performing **PDVT** films. Films stored and measured under an (a) inert atmosphere and (b) ambient conditions (both in the absence of light). The latter case exhibited an onset of degradation beyond day 5 and the properties were no longer extractable beyond day 17.

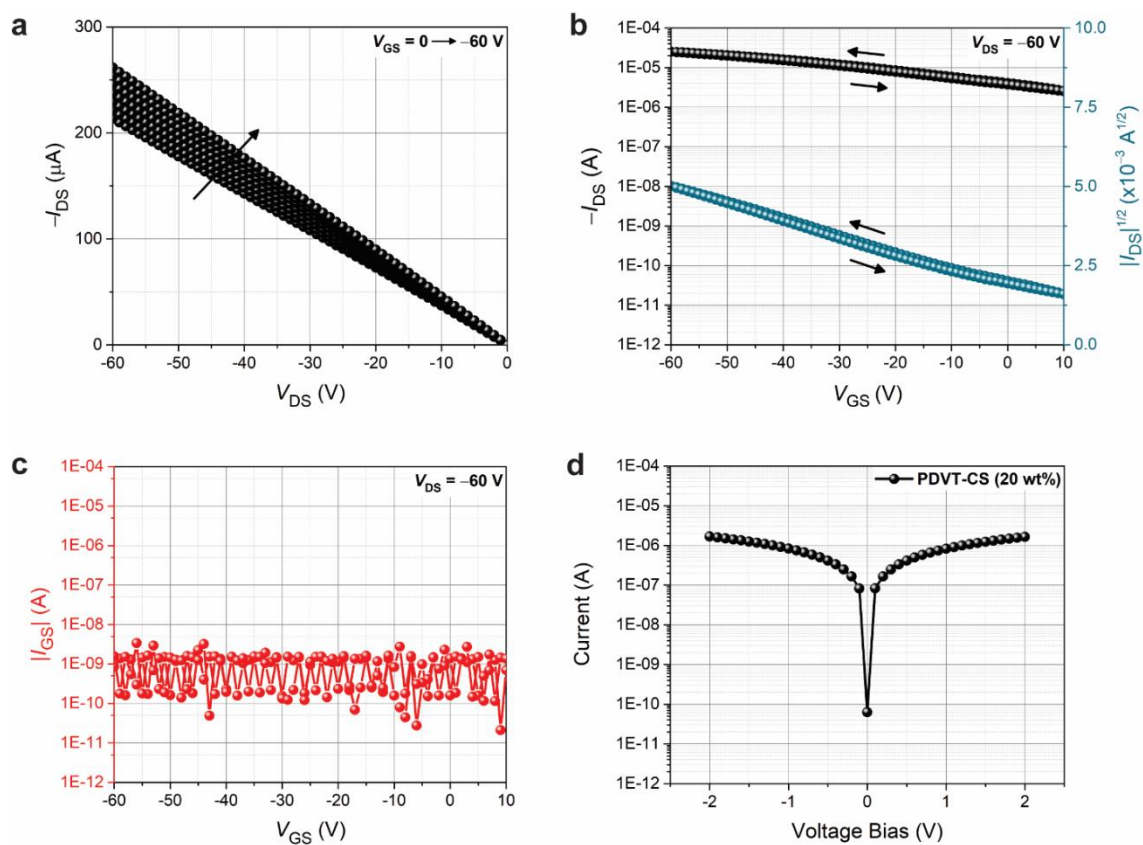


Figure A.8 (a) OFET output (I_{DS} vs V_{DS}), (b) transfer (I_{DS} vs V_{GS}), and (c) gate leakage (I_{GS} vs V_{GS}) characteristics of blended **PDVT-CS** (20 wt%) films using a BGBC device configuration and (d) 2-point probe room-temperature I - V plot (without a gate electrode).

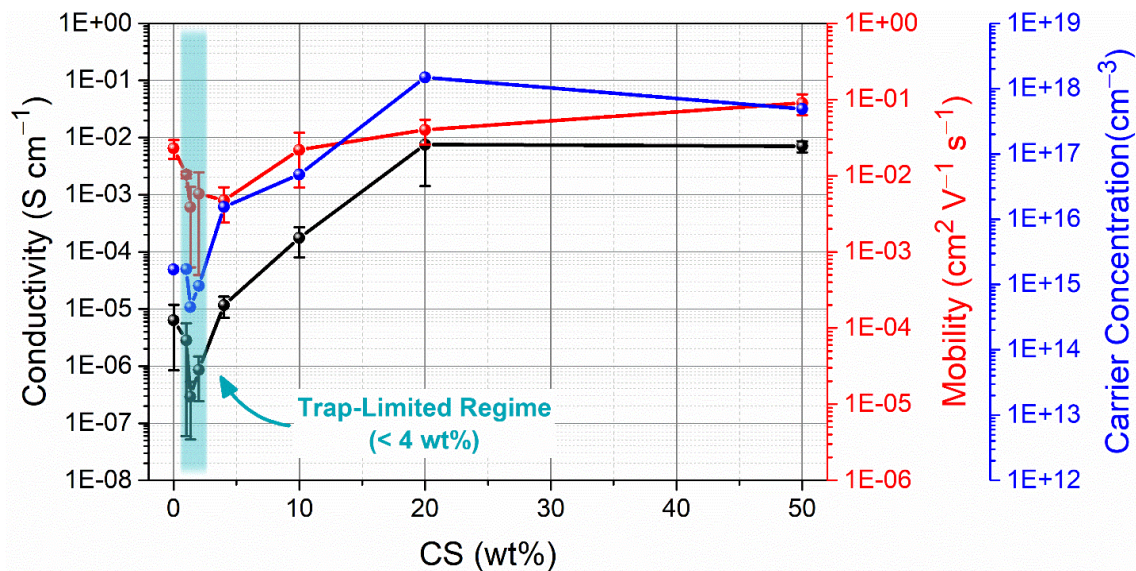


Figure A.9 Composition-dependent charge transport properties showing conductivity, field-effect mobility, and hole carrier concentration versus CS loading in a PDVT host matrix.

Table A.2 Tabulated conductivity, field-effect mobility, and calculated carrier density with the trap-limited regime ($CS < 4$ wt%) highlighted in reference to the above plot.

Material System	Composition	Conductivity ($S\ cm^{-1}$)		Mobility ($cm^2\ V^{-1}\ s^{-1}$)		Calculated carrier density (cm^{-3})
		Average	Max	Average	Max	
PDVT^a	Pristine	6.30×10^{-6}	1.36×10^{-5}	2.29×10^{-2}	2.95×10^{-2}	1.70×10^{15}
PDVT-CS^b	1%	2.83×10^{-6}	5.00×10^{-6}	1.02×10^{-2}	3.07×10^{-2}	1.71×10^{15}
	1.33%	2.80×10^{-7}	8.58×10^{-7}	3.87×10^{-3}	1.26×10^{-2}	4.52×10^{14}
	2%	8.80×10^{-7}	4.53×10^{-6}	5.78×10^{-3}	1.37×10^{-2}	9.50×10^{14}
	4%	1.17×10^{-5}	1.90×10^{-5}	4.75×10^{-3}	1.00×10^{-2}	1.54×10^{16}
	10%	1.75×10^{-4}	3.36×10^{-4}	2.25×10^{-2}	4.01×10^{-2}	4.85×10^{16}
	20%	8.20×10^{-3}	1.67×10^{-2}	3.43×10^{-2}	6.00×10^{-2}	1.49×10^{18}
	50%	7.07×10^{-2}	1.10×10^{-2}	9.01×10^{-2}	1.44×10^{-1}	4.90×10^{17}

^{a,b} All processed films were prepared in C_6H_5Cl at 110° overnight and spin-coated at 1000 rpm for 1 min, and the film thicknesses (50 – 100 nm) were measured via profilometry. ^b Binary composite films with variation in CS content (1–50 wt%).

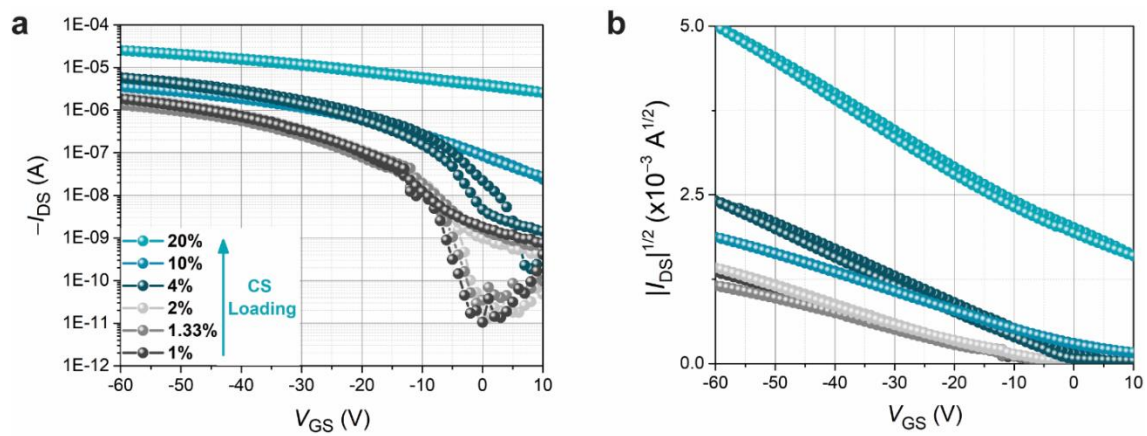


Figure A.10 OFET transfer (a) I_{DS} vs V_{GS} and (b) $I_{DS}^{1/2}$ vs V_{GS} characteristics of **PDVT** films with 1 – 20 wt% CS loading.

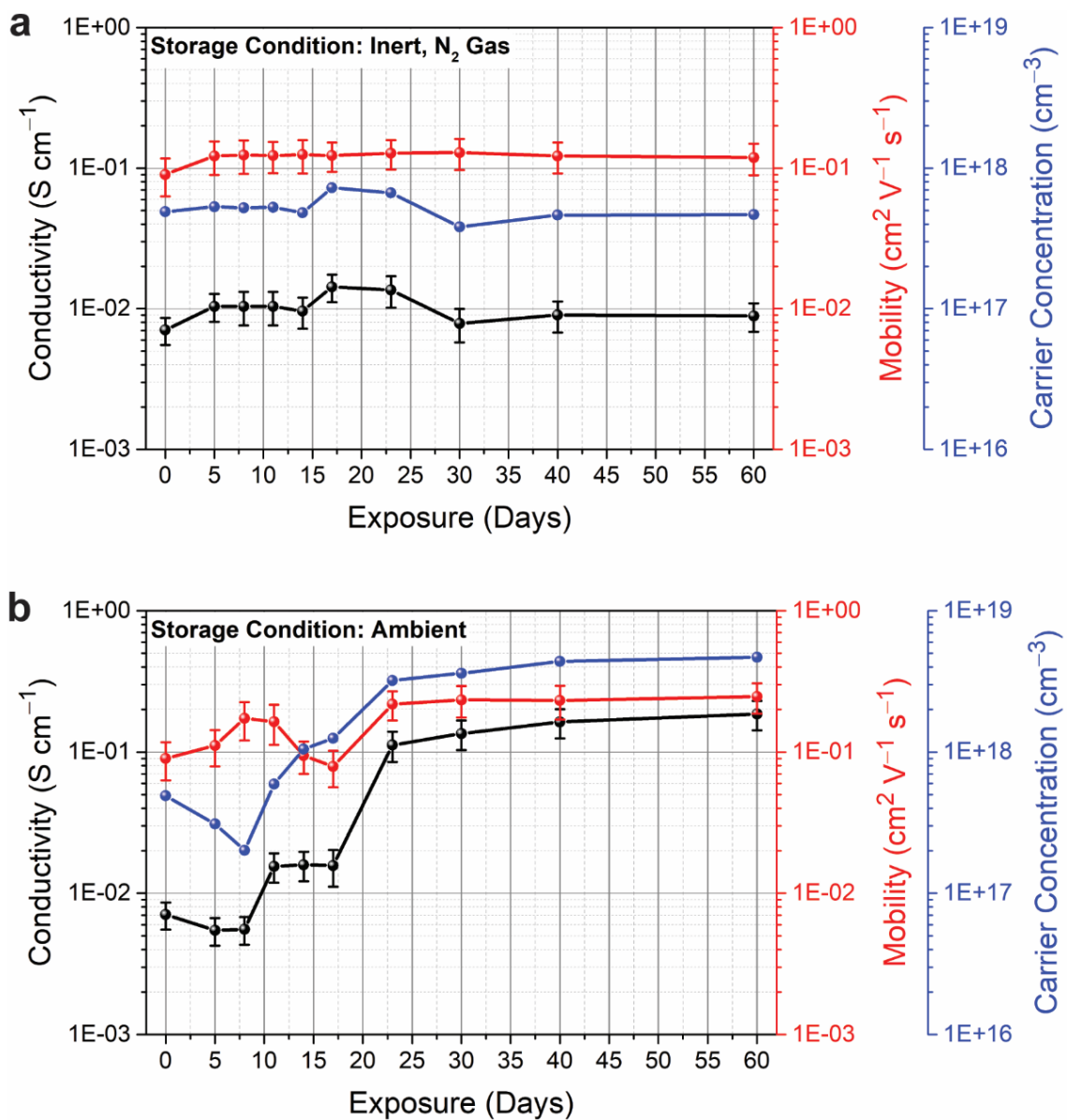


Figure A.11 Monitoring charge transport shelf-life for high performing *PDVT-CS* films for 60 days. Films stored and measured under an (a) inert atmosphere and (b) ambient conditions (both in the absence of light) showed moderate change in conductivity, field-effect mobility, and hole concentration over a period of 60 days. No discernible degradation was found.

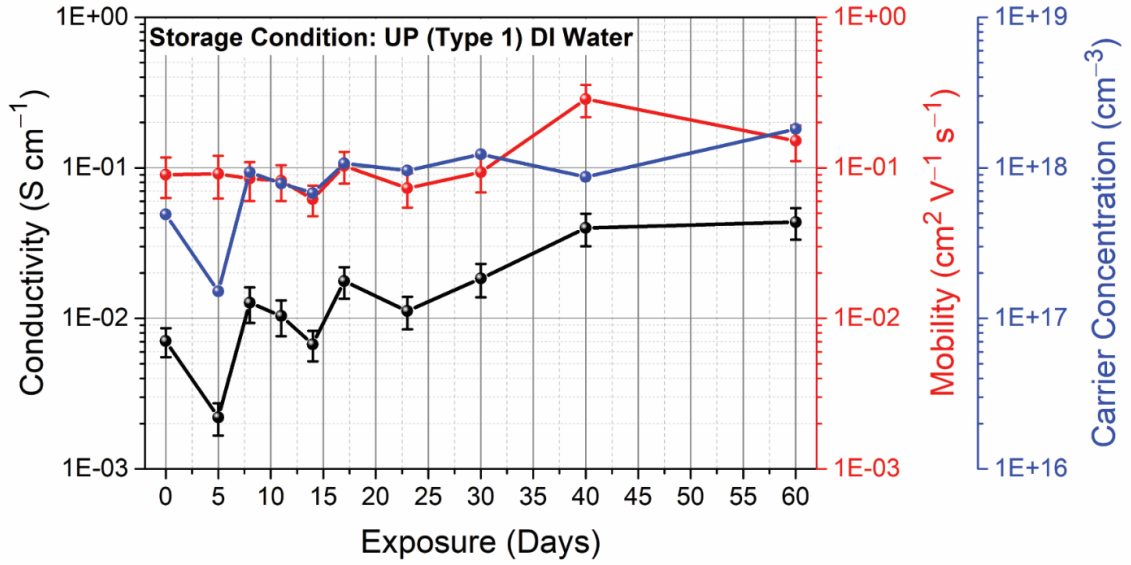


Figure A.12 *Monitoring charge transport shelf-life for high performing PDVT-CS films for 60 days. Films stored and measured under UP DI water (in the absence of light) showed moderate change in conductivity, field-effect mobility, and hole concentration over a period of 60 days. No discernable degradation was found.*

B.1 Supplemental Figures and Tables

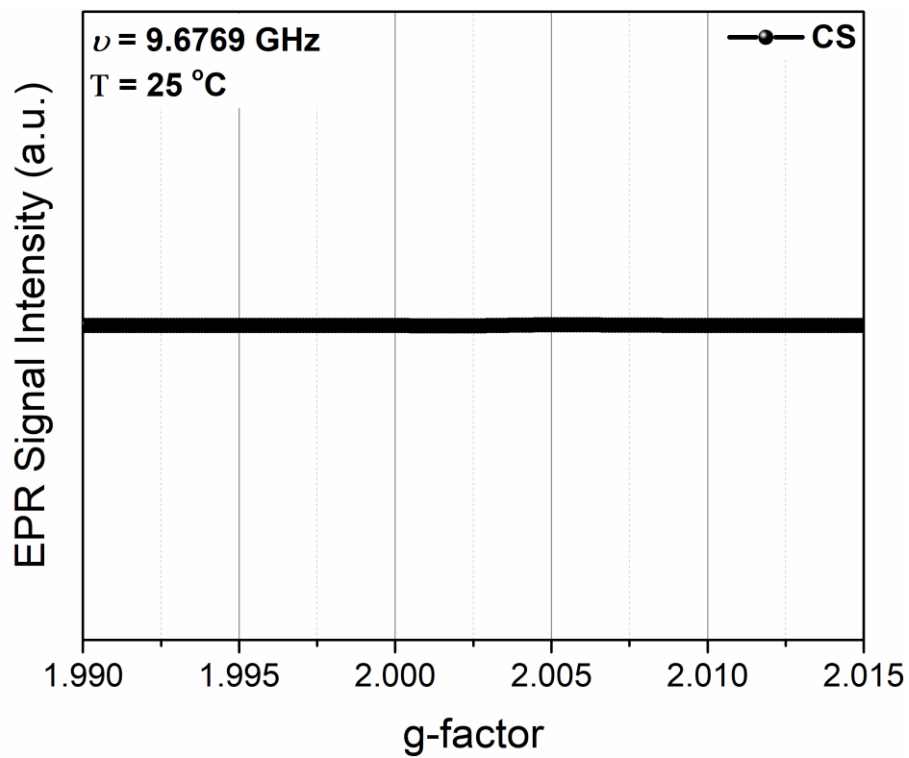


Figure B.1 EPR (X-band) spectra at 25 °C on a CS film.

Table B.1 *PDVT-CS film EPR summary.*

#spins/g	#spins/mol repeat unit	#spins/mol	#spins/chain	mol of spins	singlet spin/repeat unit	singlet spin/chain
7.1×10^{14}	8.5×10^{17}	3.1×10^{19}	5.1×10^{-5}	9.4×10^{-9}	7.0×10^{-7}	2.6×10^{-5}

Table B.2 *PDVT-IsoCS film EPR summary.*

#spins/g	#spins/mol repeat unit	#spins/mol	#spins/chain	mol of spins	singlet spin/repeat unit	singlet spin/chain
5.0×10^{14}	6.0×10^{17}	2.2×10^{19}	3.6×10^{-5}	6.7×10^{-9}	5.0×10^{-7}	1.8×10^{-5}

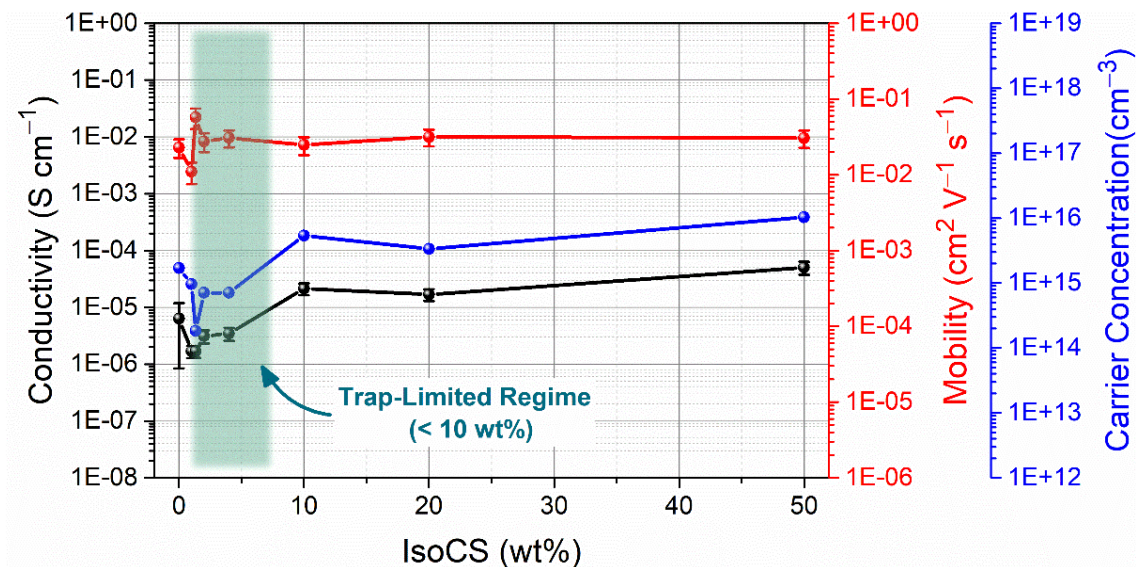


Figure B.2 *Composition-dependent charge transport properties showing conductivity, field-effect mobility, and hole carrier concentration versus IsoCS loading in a PDVT host matrix.*

Table B.3 *Tabulated conductivity, field-effect mobility, and calculated carrier density of PDVT-IsoCS with the trap-limited regime (< 10 wt% CS) highlighted in reference to the above plot.*

Material System	Composition	Conductivity (S cm ⁻¹)		Mobility (cm ² V ⁻¹ s ⁻¹)		Calculated carrier density (cm ⁻³)
		Average	Max	Average	Max	
PDVT^a	Pristine	6.30×10^{-6}	1.36×10^{-5}	2.29×10^{-2}	2.95×10^{-2}	1.70×10^{15}
PDVT-IsoCS^b	1%	1.69×10^{-6}	4.11×10^{-6}	1.10×10^{-2}	3.26×10^{-2}	9.60×10^{14}
	1.33%	1.69×10^{-6}	1.38×10^{-5}	5.73×10^{-2}	8.40×10^{-2}	1.84×10^{14}
	2%	3.12×10^{-6}	8.48×10^{-6}	2.76×10^{-2}	7.58×10^{-2}	7.06×10^{14}
	4%	3.47×10^{-6}	8.32×10^{-6}	3.07×10^{-2}	6.93×10^{-2}	7.06×10^{14}
	10%	2.14×10^{-5}	6.01×10^{-5}	2.48×10^{-2}	5.75×10^{-2}	5.40×10^{15}
	20%	1.69×10^{-5}	5.89×10^{-5}	3.16×10^{-2}	5.88×10^{-2}	3.34×10^{15}
	50%	5.02×10^{-5}	1.01×10^{-4}	3.05×10^{-2}	4.59×10^{-2}	1.03×10^{16}

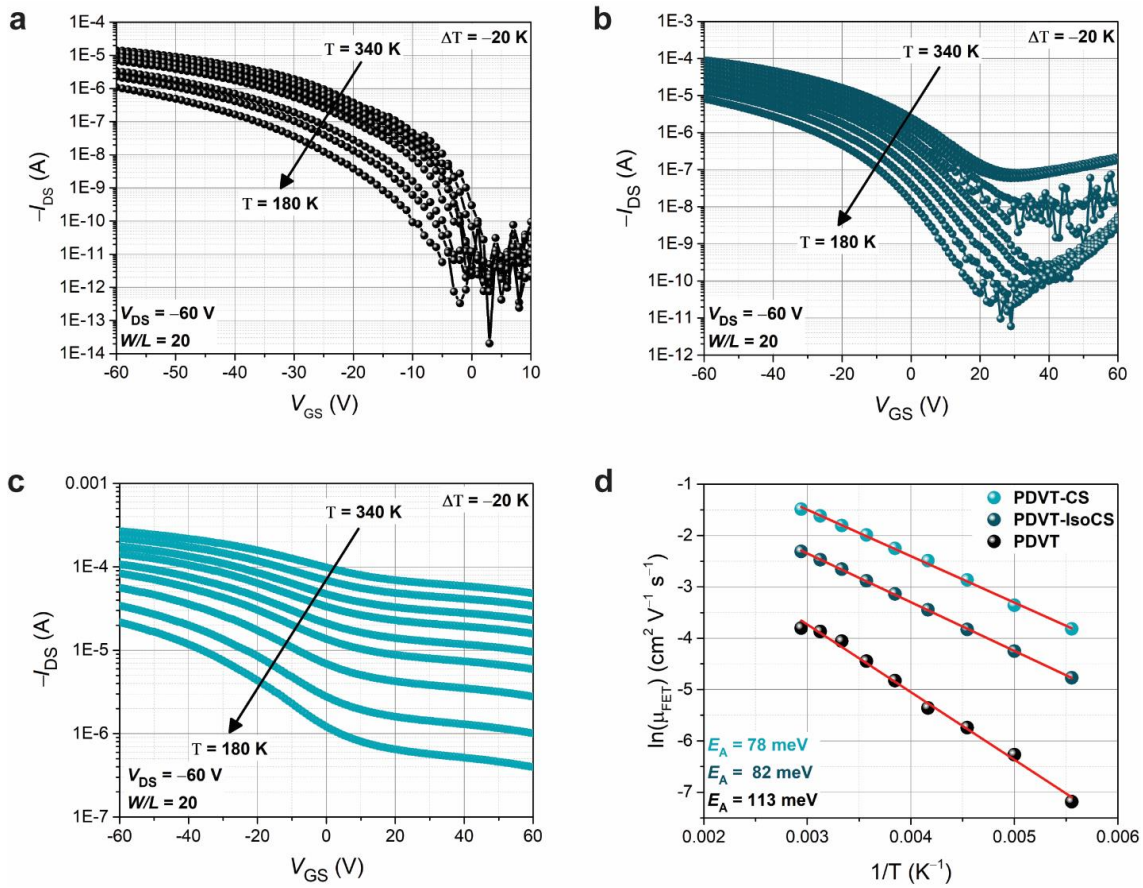


Figure B.3 Variable temperature OFET transfer characteristics (180 – 340 K) of (a) PDVT, (b) PDVT-IsoCS and (c) PDVT-CS films. The temperature-dependent mobility was fitted to the multiple-trap and release model to calculate the mean energy of the trap states.⁷⁸

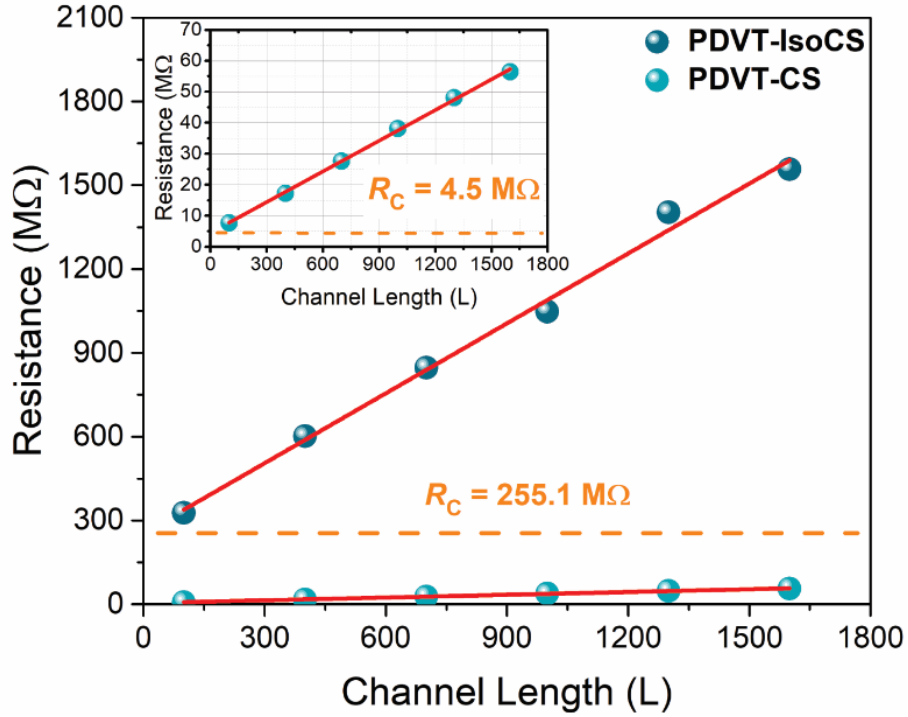


Figure B.4 Total resistance of *PDVT-CS* and *PDVT-IsoCS* samples as a function of channel length (L), where the y-intercepts ($L \rightarrow 0$) show contact resistances (R_C) of 4.5 and 255.1 MΩ, respectively. Inset plot: *PDVT-CS* zoomed-in.

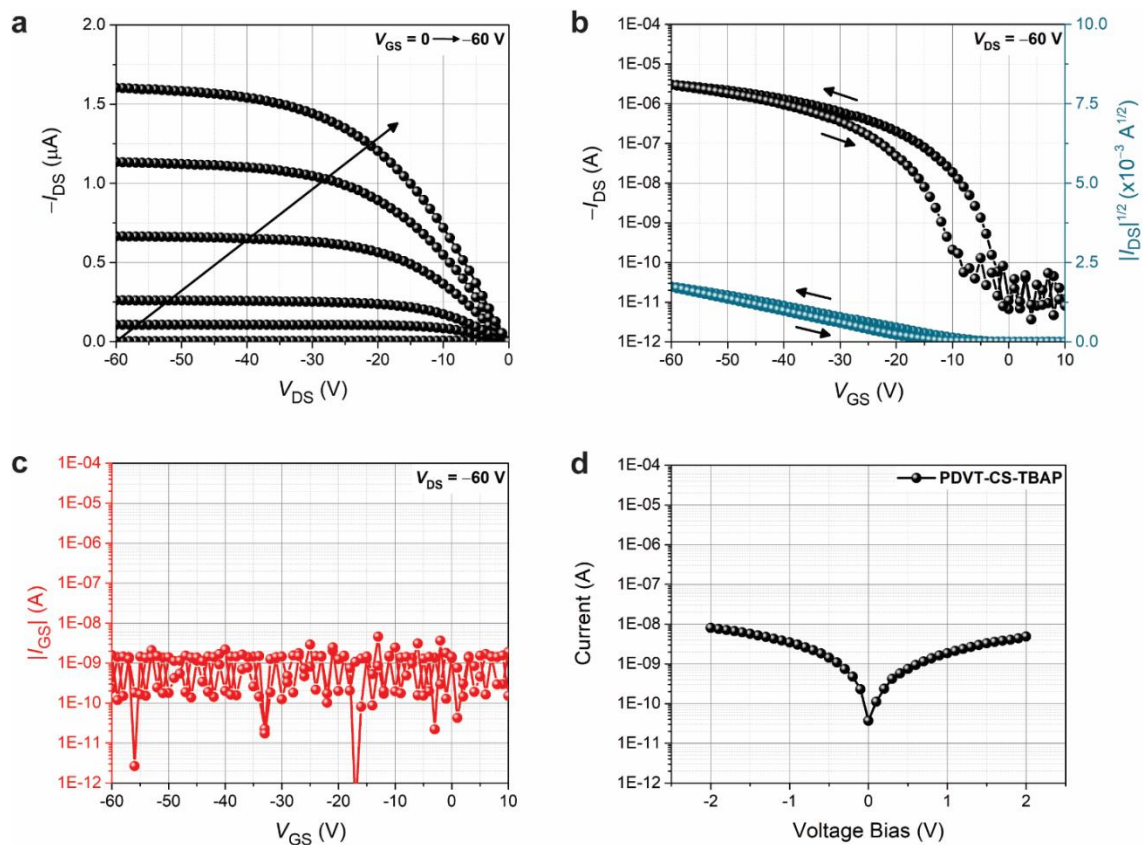


Figure B.5 (a) OFET output (I_{DS} vs V_{DS}), (b) transfer (I_{DS} vs V_{GS}), and (c) gate leakage (I_{GS} vs V_{GS}) characteristics of blended **PDVT-CS-TBAP** (anion: 1 equiv. relative to CS) films using a BGBC device configuration and (d) 2-point probe room-temperature I - V plot (without a gate electrode).

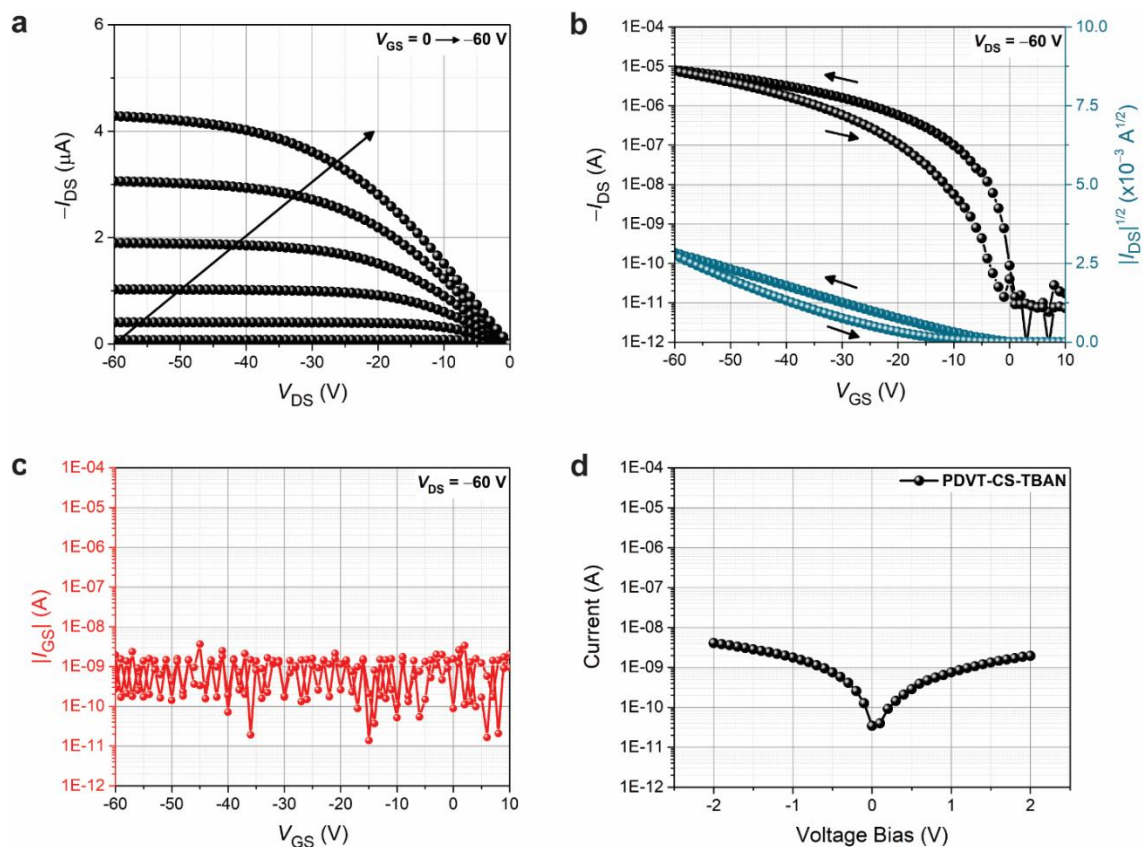


Figure B.6 (a) OFET output (I_{DS} vs V_{DS}), (b) transfer (I_{DS} vs V_{GS}), and (c) gate leakage (I_{GS} vs V_{GS}) characteristics of blended PDVT-CS-TBAN (anion: 1 equiv. relative to CS) films using a BGBC device configuration and (d) 2-point probe room-temperature I-V plot (without a gate electrode).

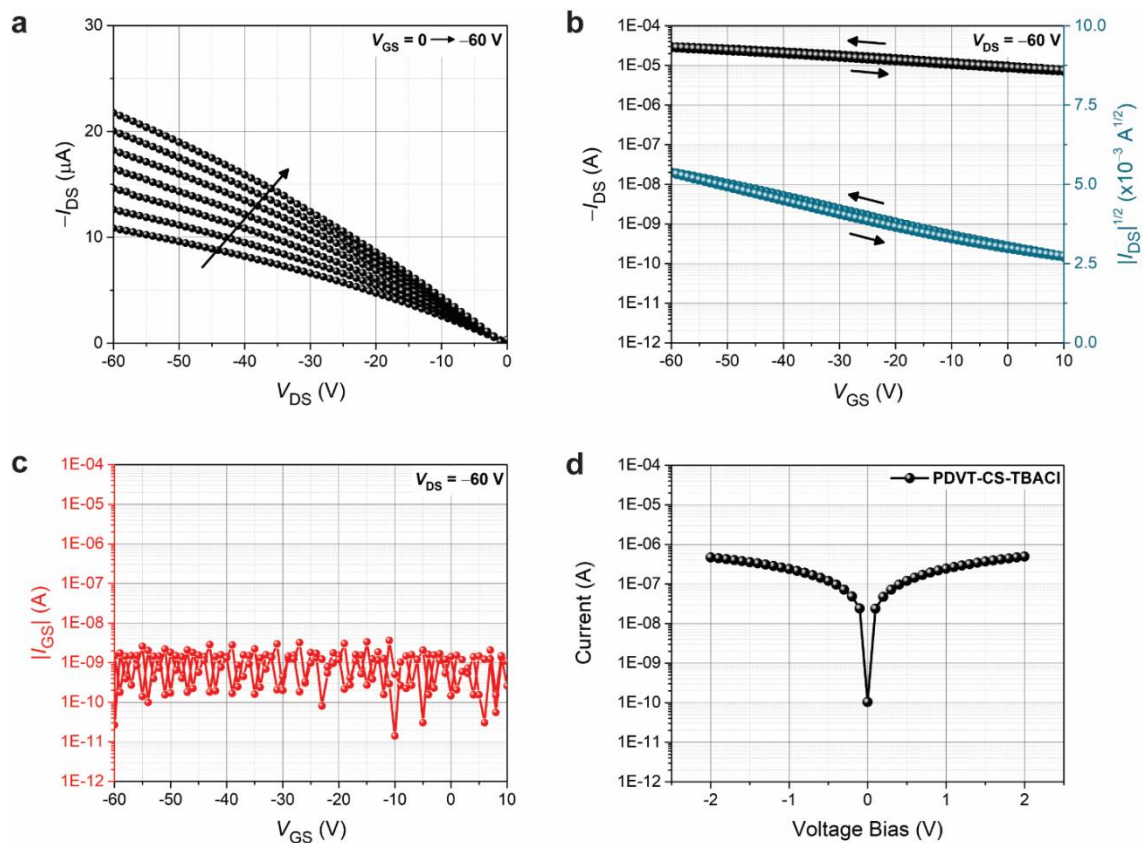


Figure B.7 (a) OFET output (I_{DS} vs V_{DS}), (b) transfer (I_{DS} vs V_{GS}), and (c) gate leakage (I_{GS} vs V_{GS}) characteristics of blended **PDVT-CS-TBACl** (anion: 1 equiv. relative to CS) films using a BGBC device configuration and (d) 2-point probe room-temperature $I-V$ plot (without a gate electrode).

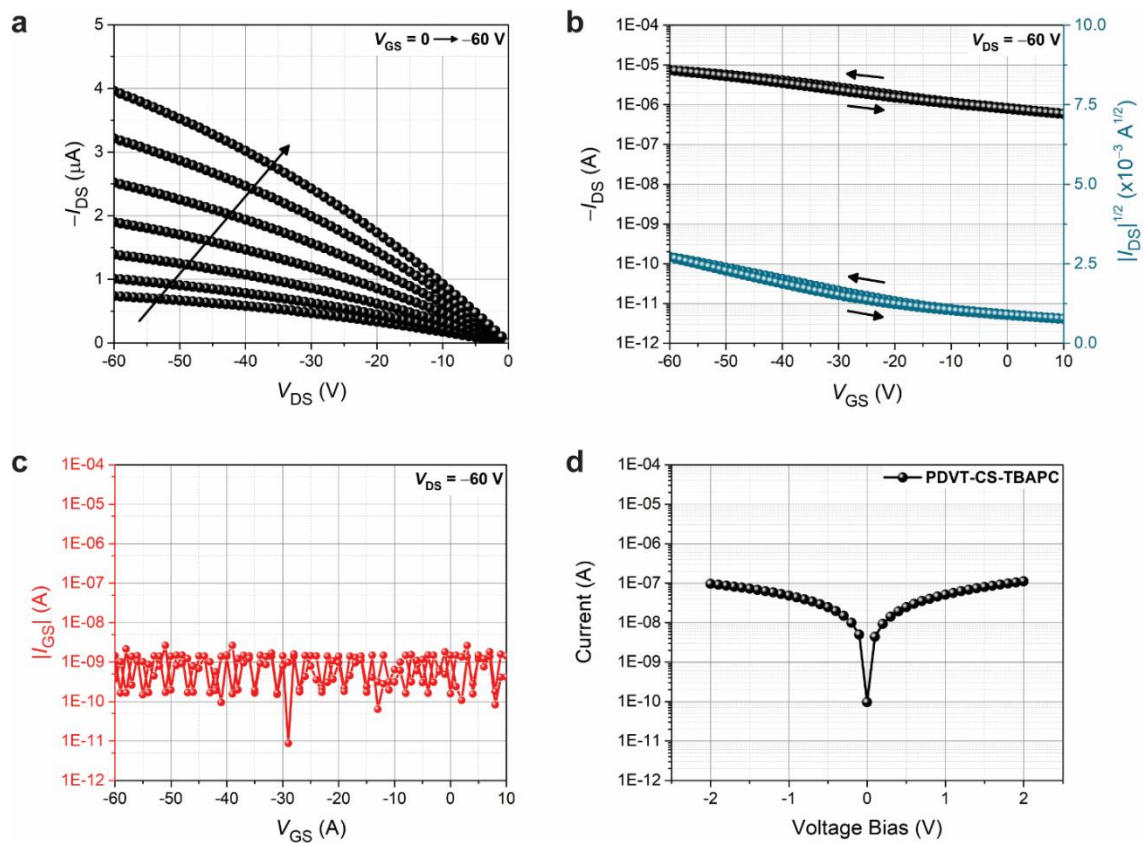


Figure B.8 (a) OFET output (I_{DS} vs V_{DS}), (b) transfer (I_{DS} vs V_{GS}), and (c) gate leakage (I_{GS} vs V_{GS}) characteristics of blended PDVT-CS•TBAPC (anion: 1 equiv. relative to CS) films using a BGBC device configuration and (d) 2-point probe room-temperature I-V plot (without a gate electrode).

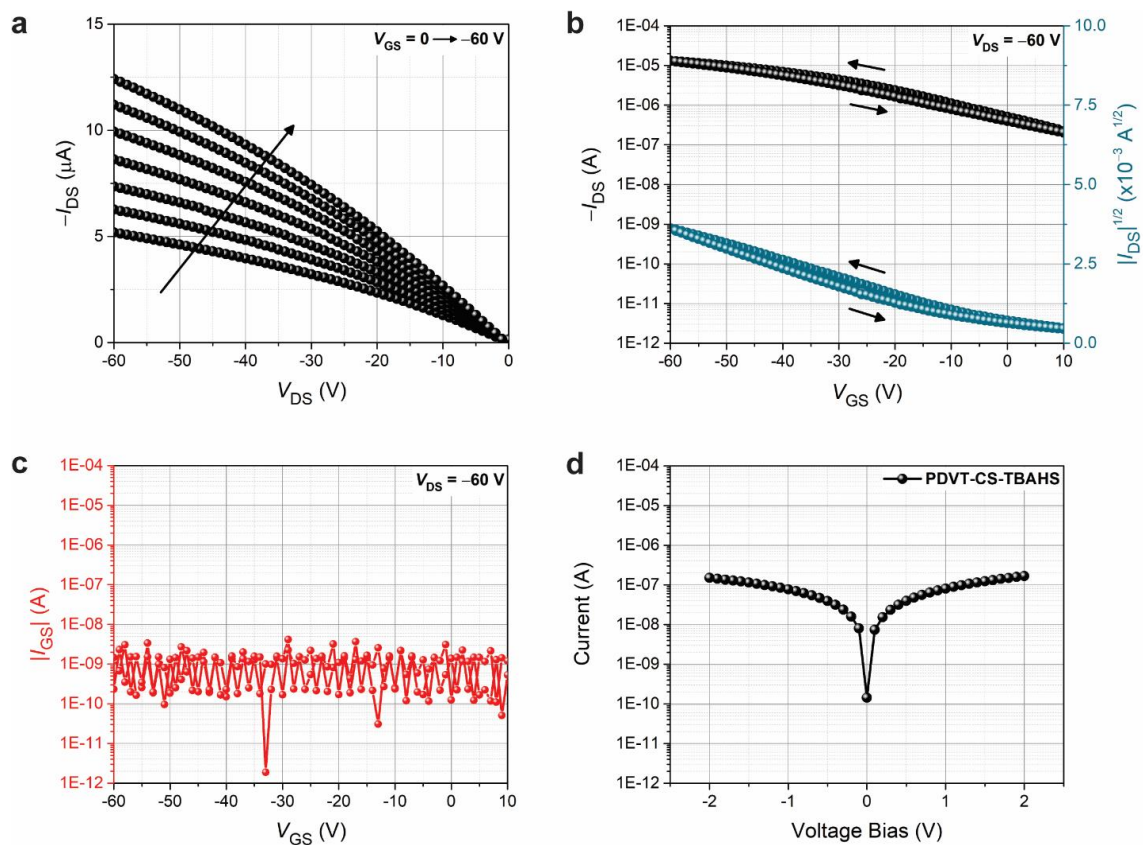


Figure B.9 (a) OFET output (I_{DS} vs V_{DS}), (b) transfer (I_{DS} vs V_{GS}), and (c) gate leakage (I_{GS} vs V_{GS}) characteristics of blended PDVT-CS-TBAHS (anion: 1 equiv. relative to CS) films using a BCBG device configuration and (d) 2-point probe room-temperature I - V plot (without a gate electrode).

Table B.4 *Tabulated conductivity, field-effect mobility, and calculated carrier density of PDVT-CS•TBA–X three-component films.*

Material System	Composition	Conductivity (S cm ⁻¹)		Mobility (cm ² V ⁻¹ s ⁻¹)		Calculated carrier density (cm ⁻³)
		Average	Max	Average	Max	
PDVT^a	Pristine	6.30×10^{-6}	1.36×10^{-5}	2.29×10^{-2}	2.95×10^{-2}	1.70×10^{15}
PDVT-CS•TBA–X^b	P	3.55×10^{-5}	8.79×10^{-5}	4.23×10^{-3}	1.09×10^{-2}	5.24×10^{16}
	N	5.28×10^{-5}	1.01×10^{-4}	1.33×10^{-2}	1.78×10^{-2}	2.49×10^{16}
	Cl	3.09×10^{-3}	5.13×10^{-3}	4.20×10^{-2}	5.56×10^{-2}	4.59×10^{17}
	PC	4.86×10^{-4}	6.10×10^{-4}	1.27×10^{-2}	1.52×10^{-2}	2.40×10^{17}
	HS	6.40×10^{-4}	9.59×10^{-4}	2.60×10^{-2}	2.91×10^{-2}	1.54×10^{17}

^{a,b} All processed films were prepared in C₆H₅Cl at 110° overnight and spin-coated at 1000 rpm for 1 min, and the film thicknesses (50 – 100 nm) were measured via profilometry. ^b Multicomponent films: direct mixing of organic-soluble tetrabutylammonium (TBA–X) salt analogues (1 equiv. relative to CS) with PDVT-CS (20 wt%) solution formulations.

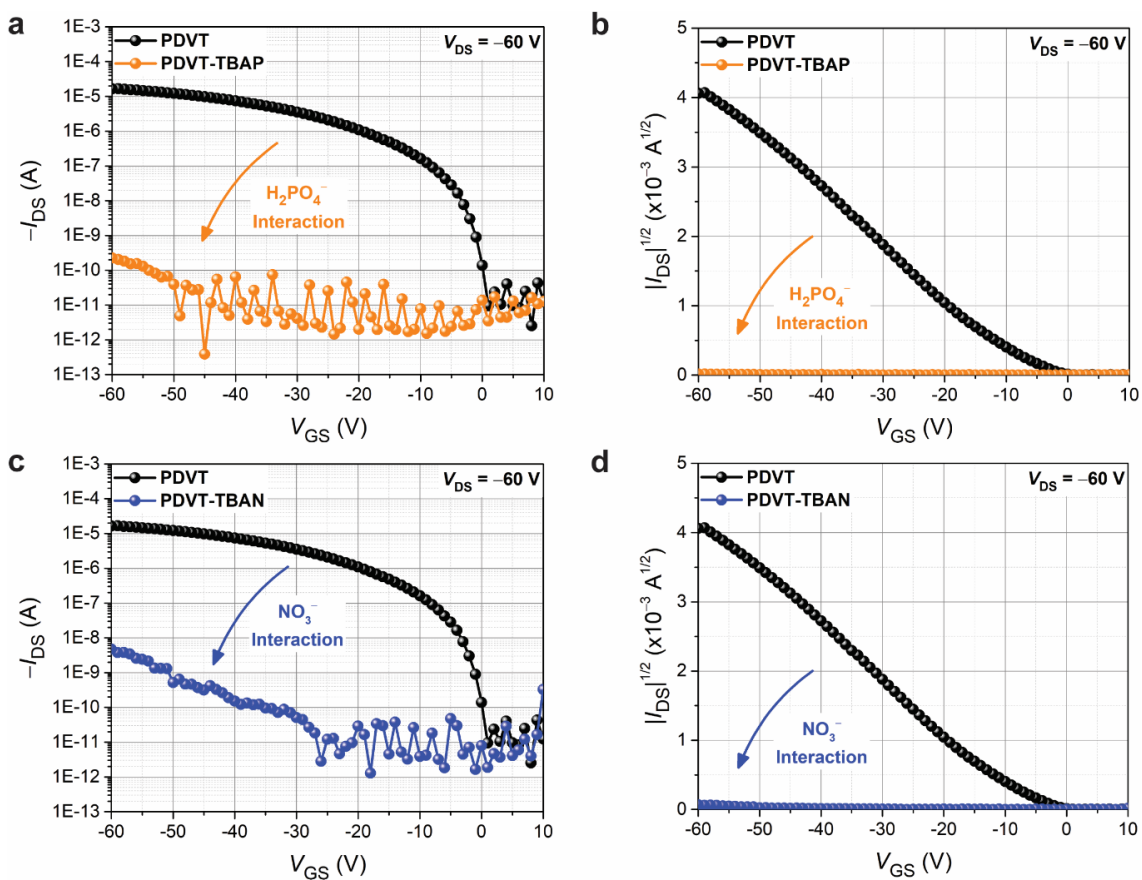


Figure B.10 (a,b) *PDVT-TBAP* and (c,d) *PDVT-TBAN* transfer characteristics to test for polymer-analyte interactions in the absence of receptors. The new profiles show significant degradation in FET performance which do not occur upon CS integration. These results suggest receptor-analyte host-guest complexation predominates in the three-component film studies.

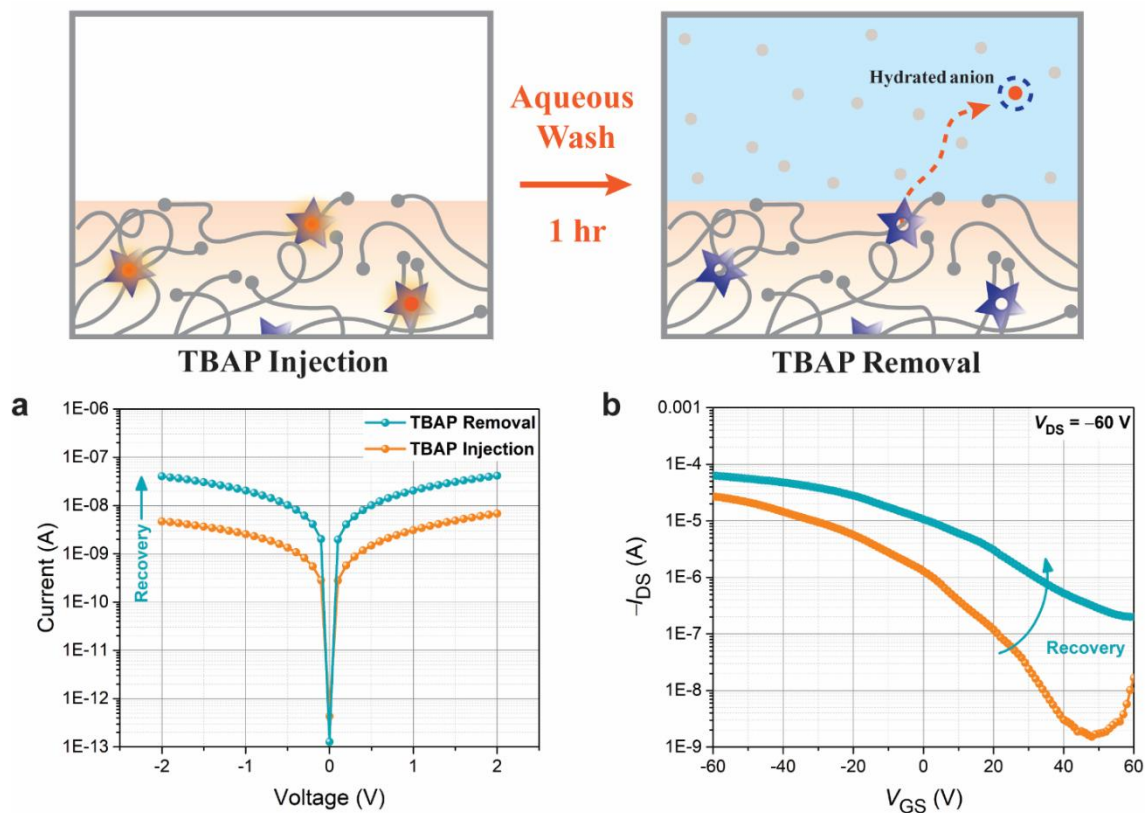


Figure B.11 (a) Two-point probe conductivity and (b) transfer plots of analyte interfacial complexation and removal (aqueous wash). A pristine *PDVT* film was initially encapsulated by a *CS*•*TBAP* layer. After high precision cleaning to isolate adjacent device structures and testing the initial film properties (*TBAP* injection), *TBAP* was removed by submerging the device under UP (Type 1) DI water for 30 mins. Afterwards, the performance was recorded to demonstrate binding reversibility with potential reusability of field-deployed sensors.

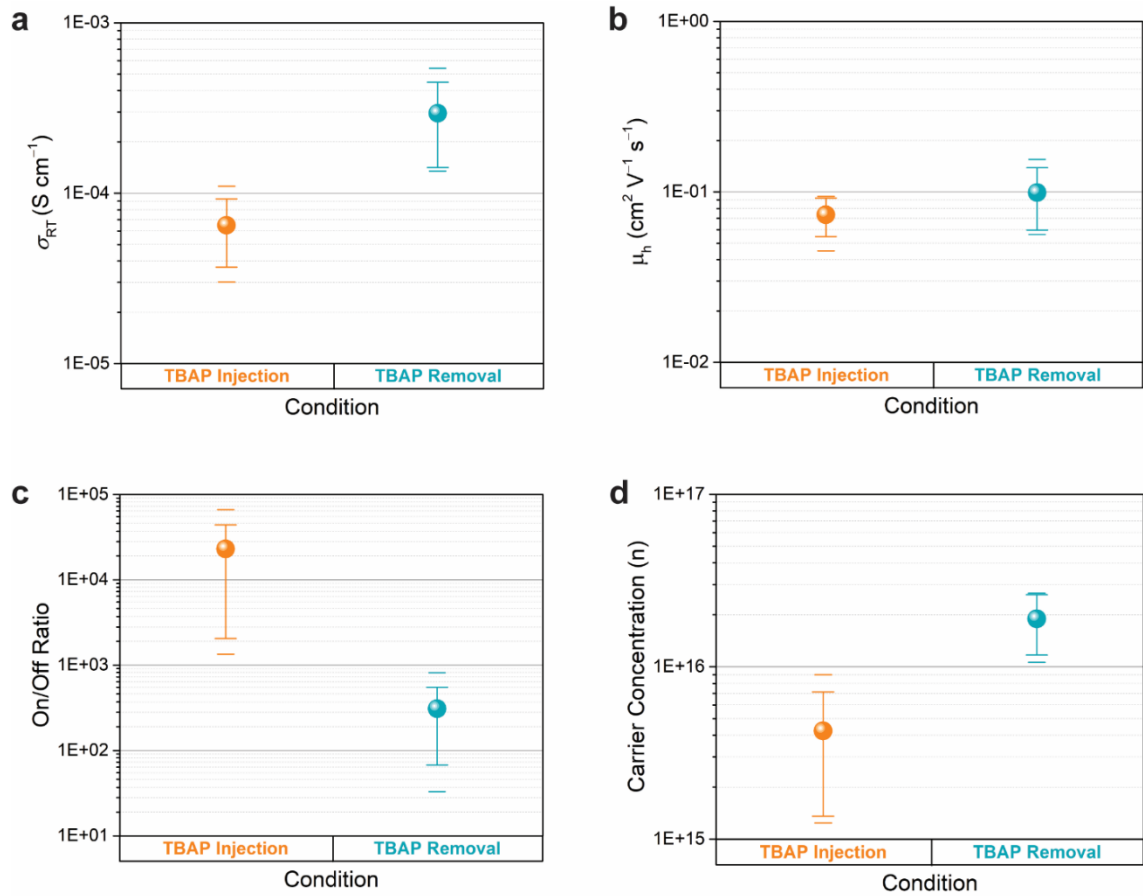


Figure B.12 Interval plots of CS:phosphate extracted from B.10 I-V and OFET transfer plots showing change in (a) room-temperature conductivity, (b) field-effect mobility, (c) on-off current ratio, and (d) charge carrier density.

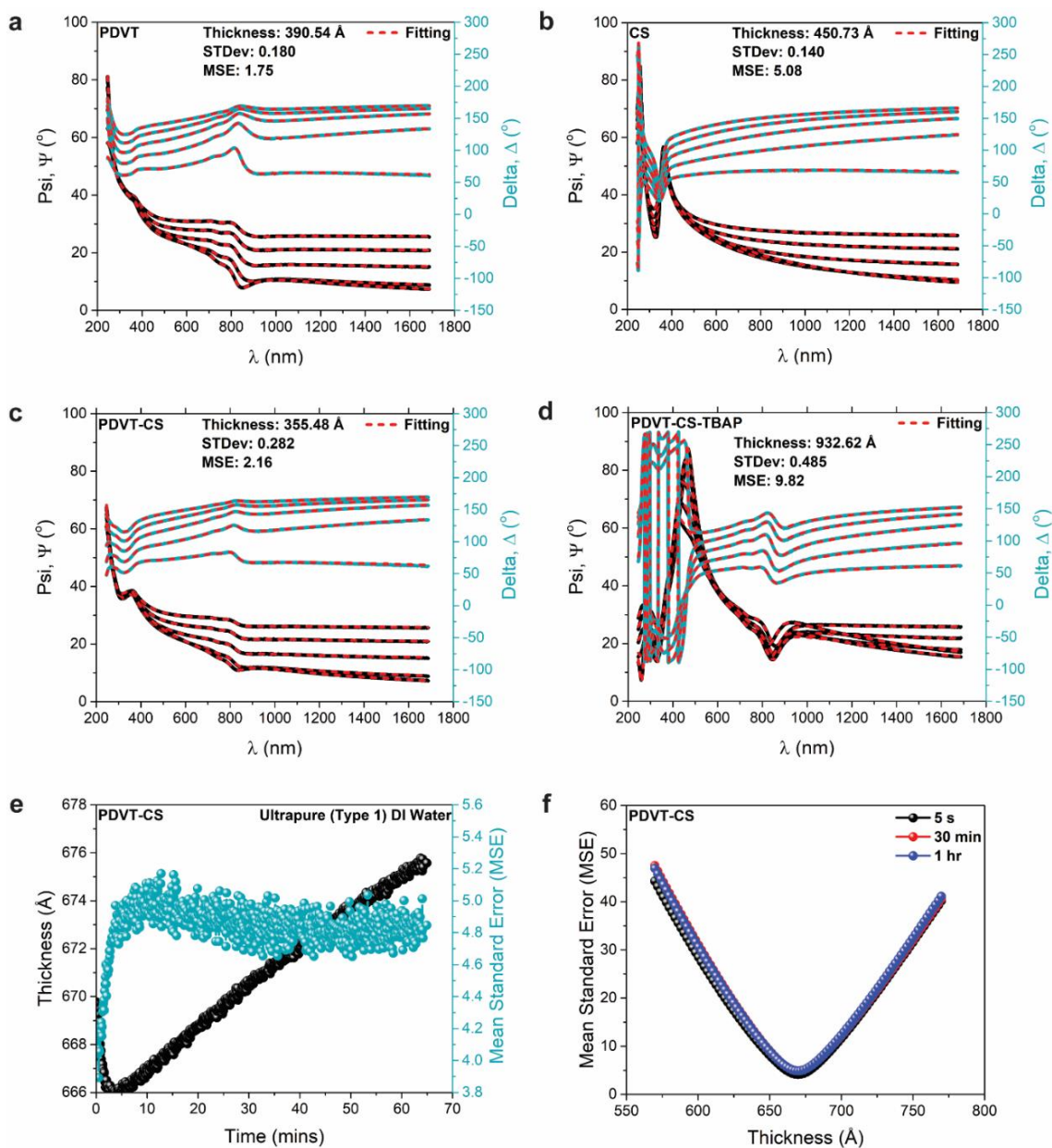


Figure B.14 Variable-angle ellipsometry model fittings of (a) **PDVT**, (b) **CS**, (c) **PDVT-CS**, and (d) **PDVT-CS•TBAP** films. (e) Thickness profile showing **PDVT-CS** swelling by less than 1 nm over 1 hour of exposure to UP DI water. The concentration of **CS** was fitted from the dry film and held constant during the water measurement. Only 10 variables (thickness and amplitude of **PDVT** and **CS** gaussian oscillators) were allowed to vary during the swelling experiment. (f) The uniqueness test shows that the modeled thickness

gives the best fit and is reliable. These findings are relevant to distinguish the mode of operation, which we found to be based on the field-effect rather than volumetric like in organic electrochemical transistors (OECTs).

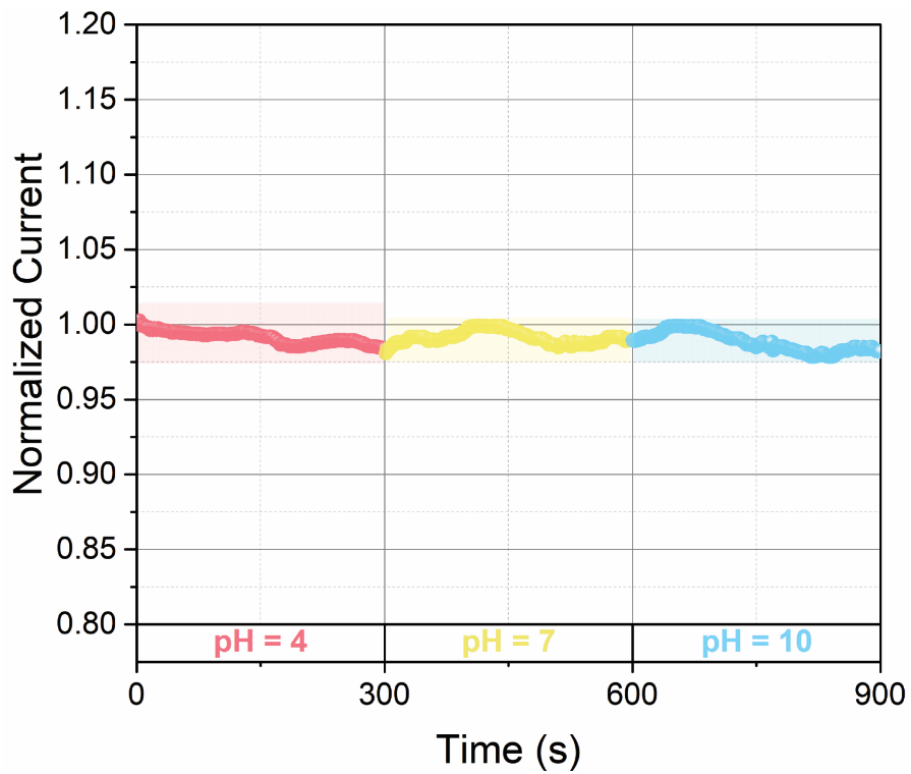


Figure B.16 Active layer responsiveness to pH fluctuation (4, 7, and 10). There were no significant changes in the tested pH range.

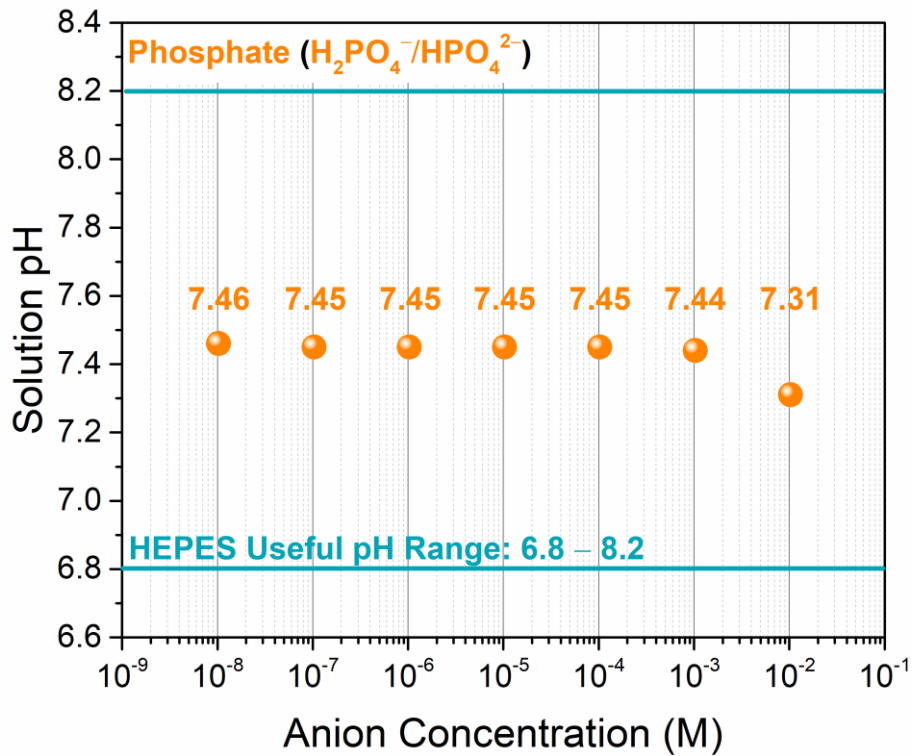


Figure B.17 HEPES buffer analyte solution spiked with $H_2PO_4^-/HPO_4^{2-}$: pH as a function of anion concentration.

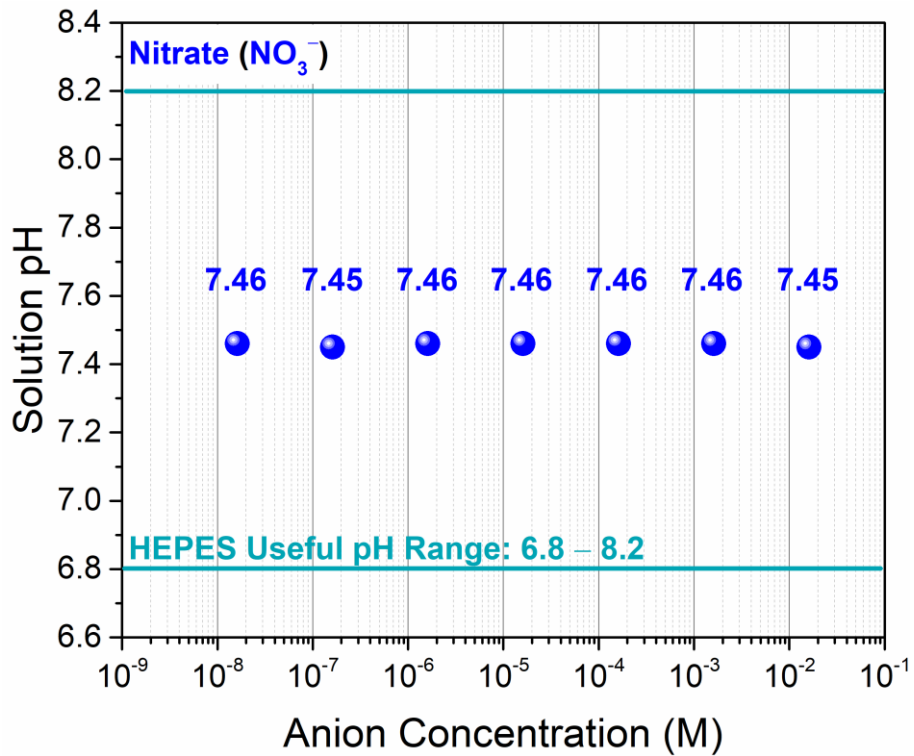


Figure B.18 HEPES buffer analyte solution spiked with NO_3^- : pH as a function of anion concentration.

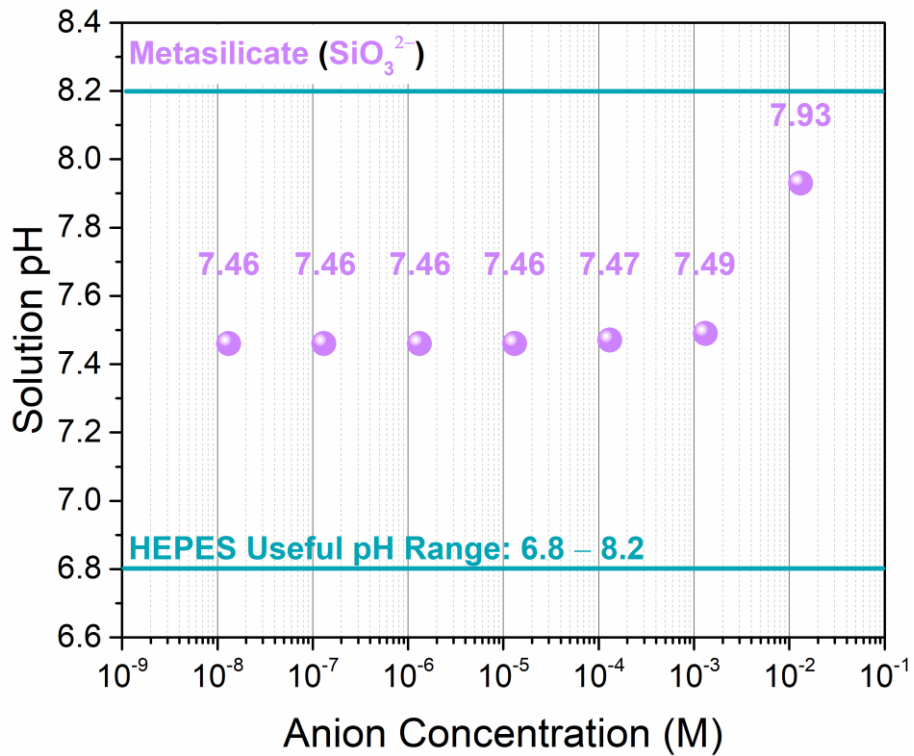


Figure B.19 HEPES buffer analyte solution spiked with SiO_3^{2-} : pH as a function of anion concentration.

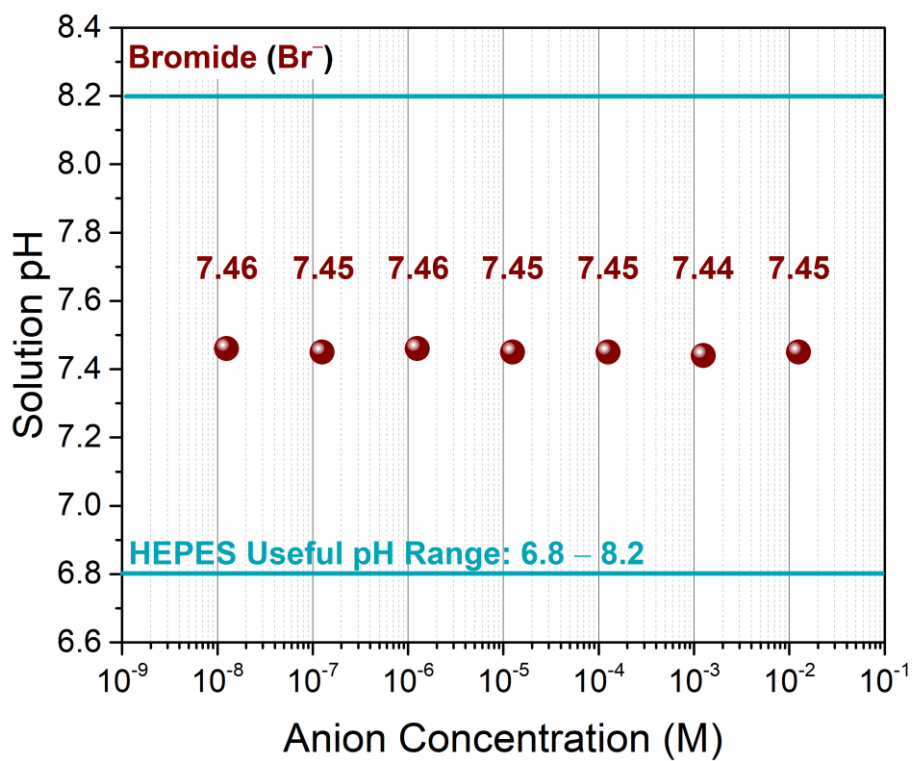


Figure B.20 HEPES buffer analyte solution spiked with Br^- : pH as a function of anion concentration.

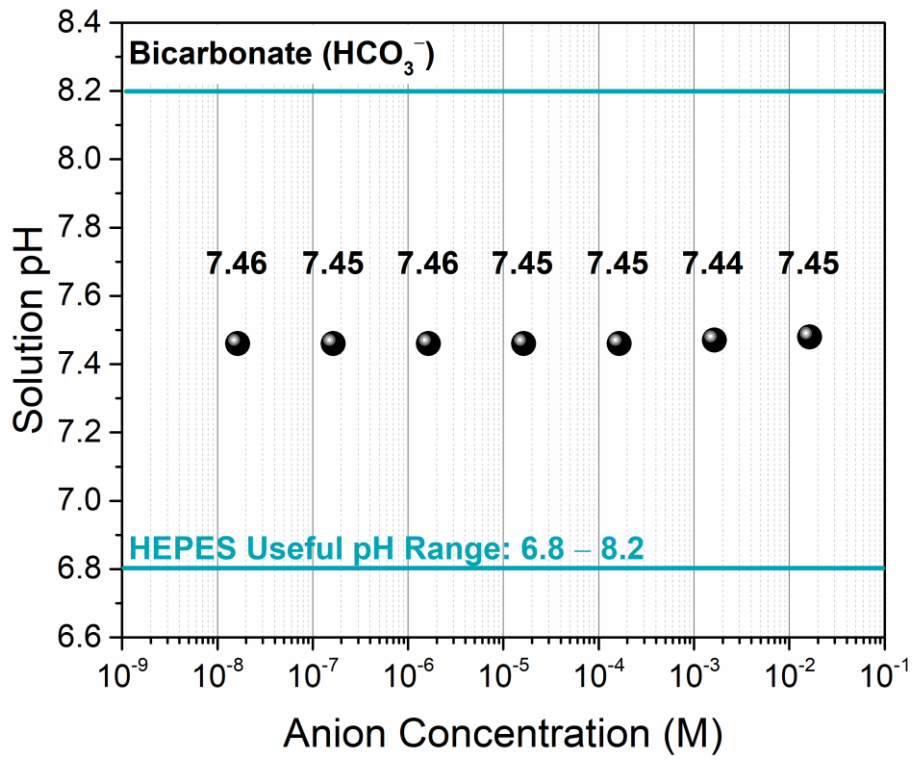


Figure B.21 HEPES buffer analyte solution spiked with HCO_3^- : pH as a function of anion concentration.

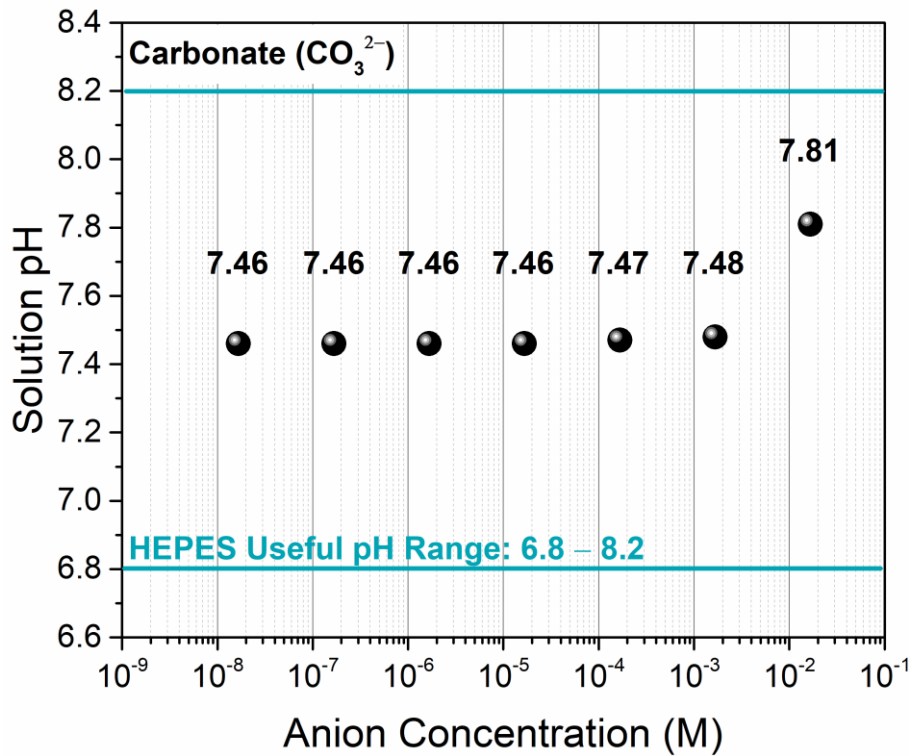


Figure B.22 HEPES buffer analyte solution spiked with CO_3^{2-} : pH as a function of anion concentration.

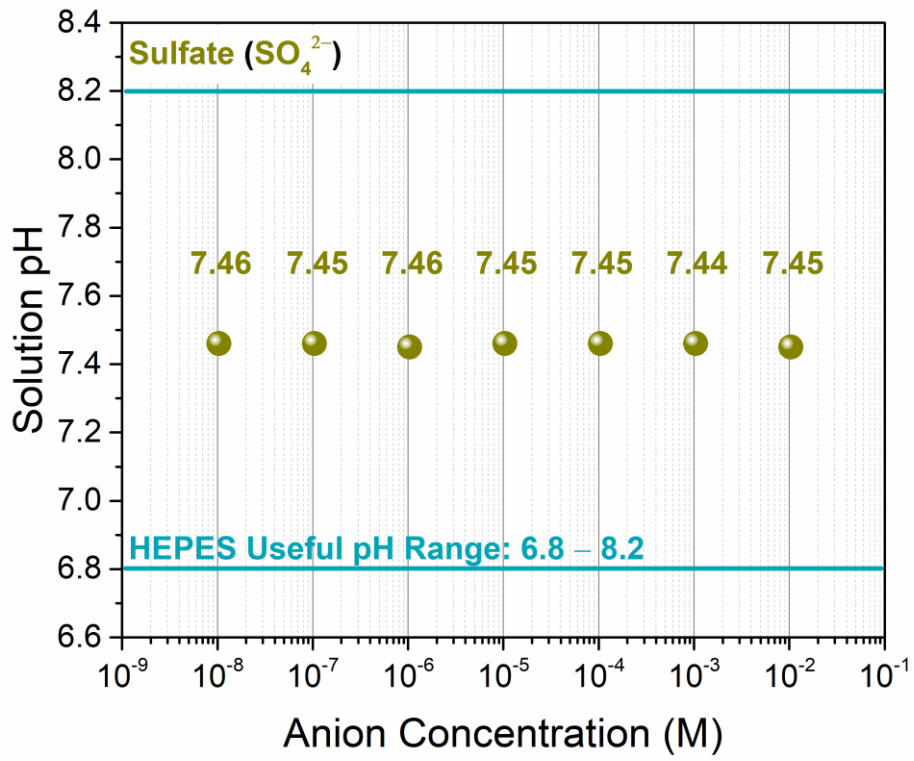


Figure B.23 HEPES buffer analyte solution spiked with SO_4^{2-} : pH as a function of anion concentration.

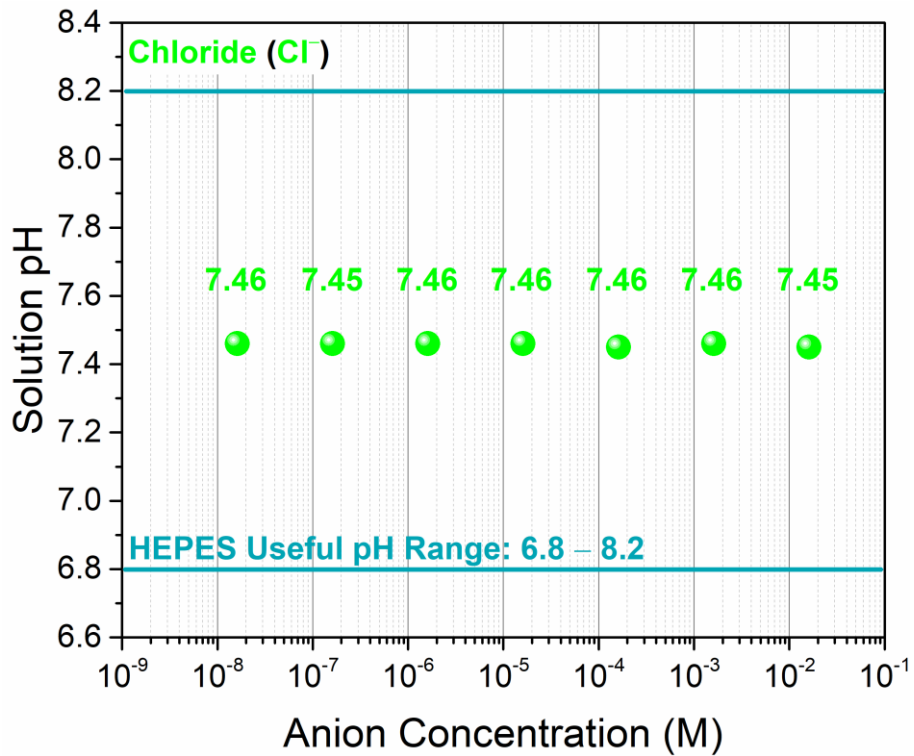


Figure B.24 HEPES buffer analyte solution spiked with Cl^- : pH as a function of anion concentration.

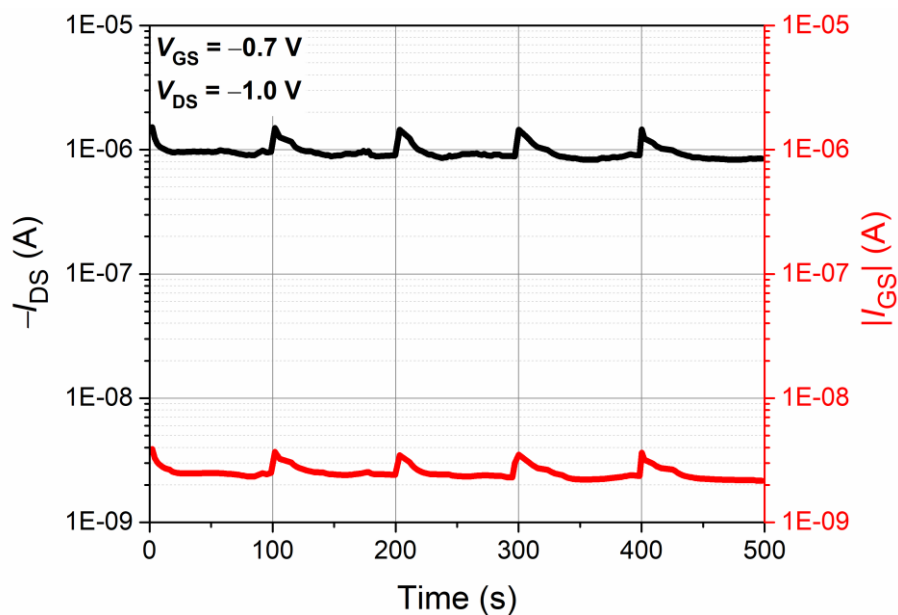


Figure B.25 EGO-FET transient responses based on sequential exposure to HEPES baseline solution. The devices displayed stable electrochemical performance with consistent I_{DS} output and I_{GS} leakage, revealing no dramatic changes to the film properties during the experimental run.

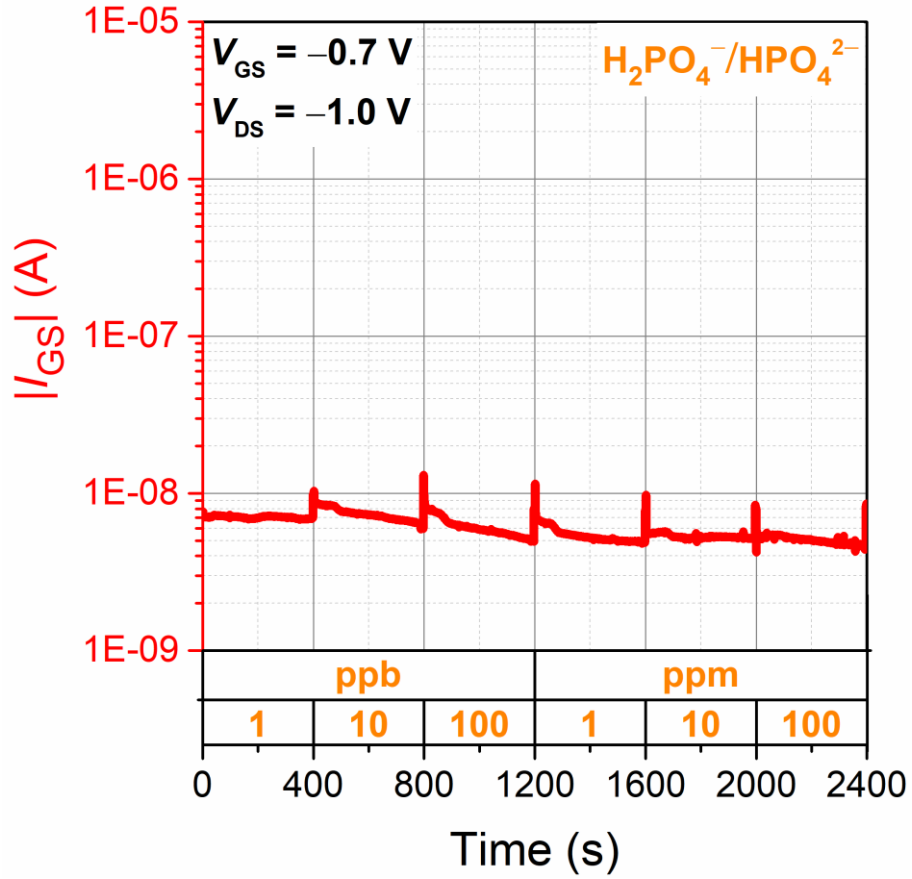


Figure B.26 (a) EGO-FET gate leakage in response to HEPES solution spiked with $\text{H}_2\text{PO}_4^- / \text{HPO}_4^{2-}$.

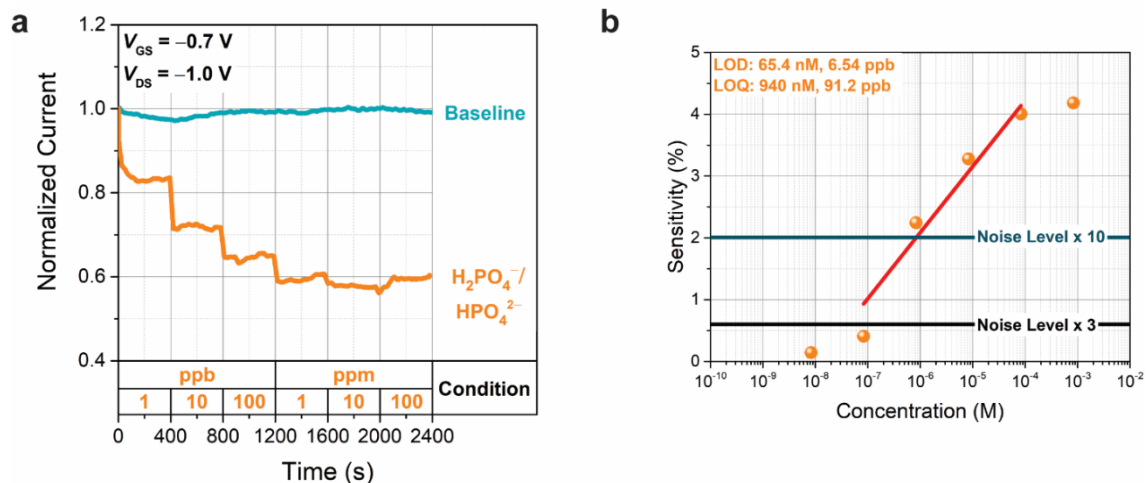


Figure B.27 *PDVT-CS EGFET (a) transient responses towards $\text{H}_2\text{PO}_4^-/\text{HPO}_4^{2-}$ and the corresponding (b) sensor calibration plot.*

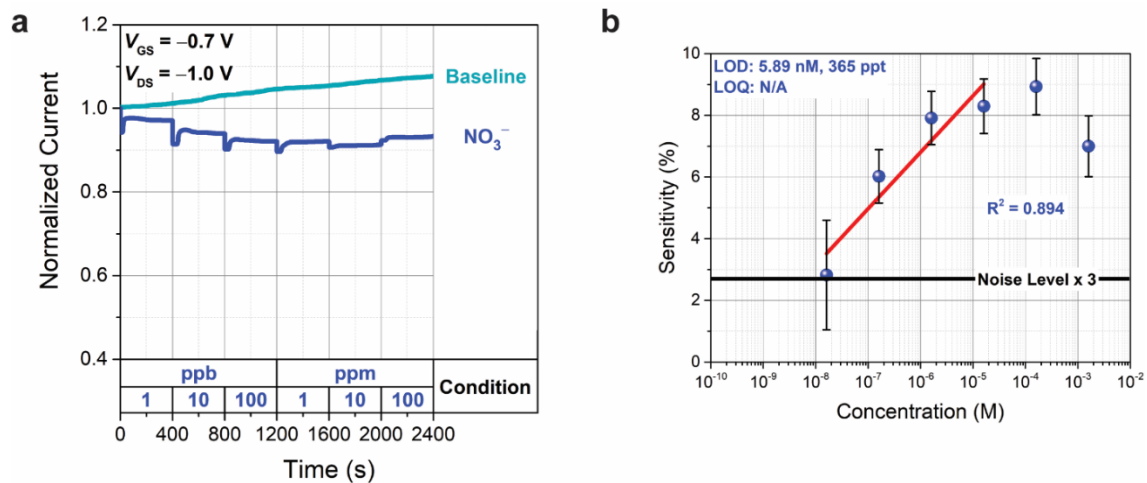


Figure B.28 *PDVT-CS EGFET* (a) transient responses towards NO_3^- and the corresponding (b) sensor calibration plot.

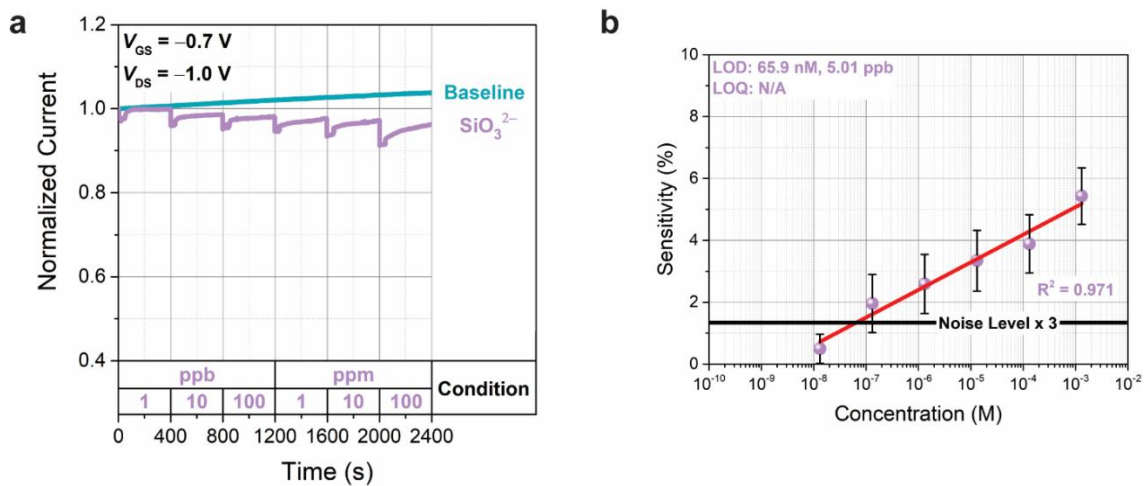


Figure B.29 *PDVT-CS EGOFET* (a) transient responses towards SiO_3^{2-} and the corresponding (b) sensor calibration plot.

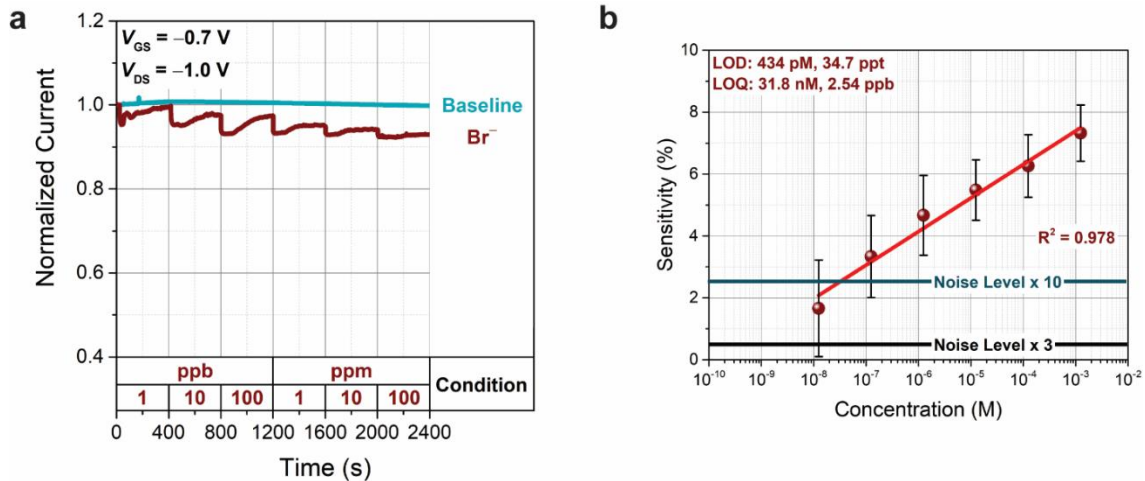


Figure B.30 *PDVT-CS EGOFET* (a) transient responses towards Br^- and the corresponding (b) sensor calibration plot.

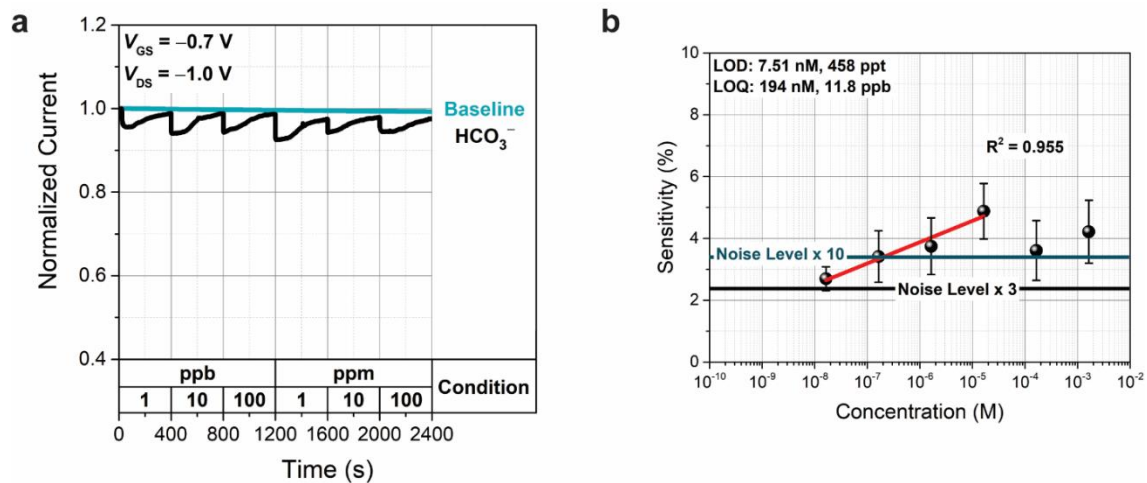


Figure B.31 *PDVT-CS EGOFET* (a) transient responses towards HCO_3^- and the corresponding (b) sensor calibration plot.

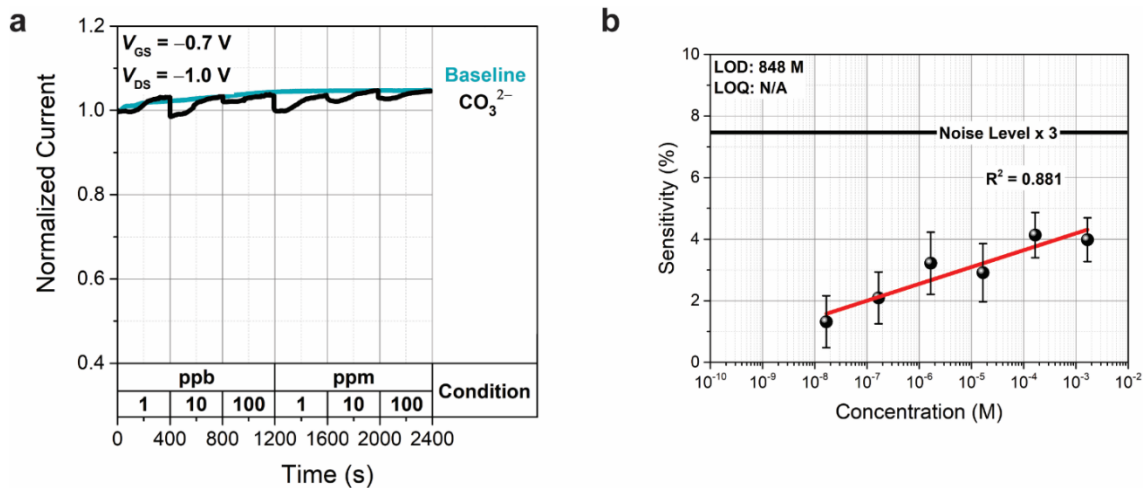


Figure B.32 *PDVT-CS EGOFET* (a) transient responses towards CO_3^{2-} and the corresponding (b) sensor calibration plot.

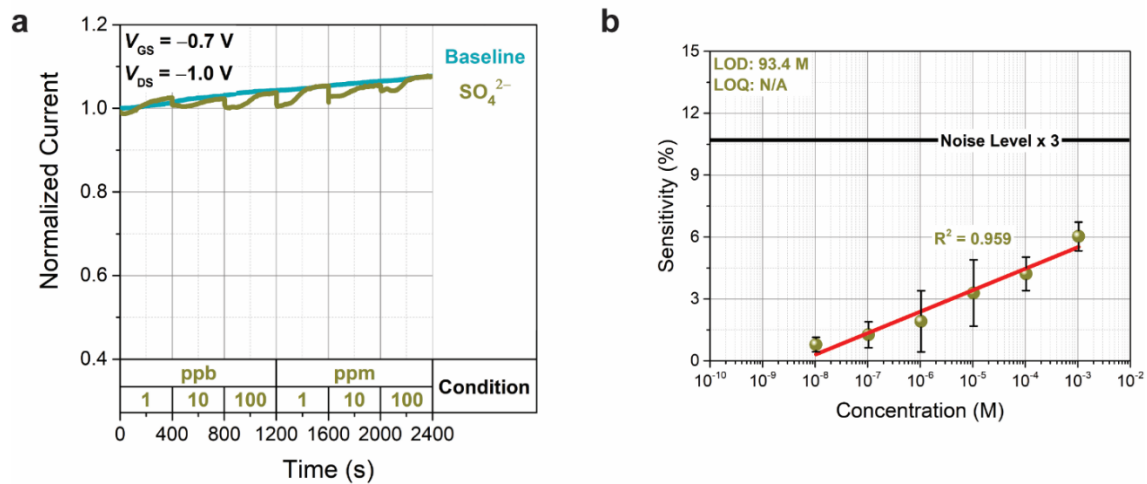


Figure B.33 *PDVT-CS EGOFET* (a) transient responses towards SO_4^{2-} and the corresponding (b) sensor calibration plot.

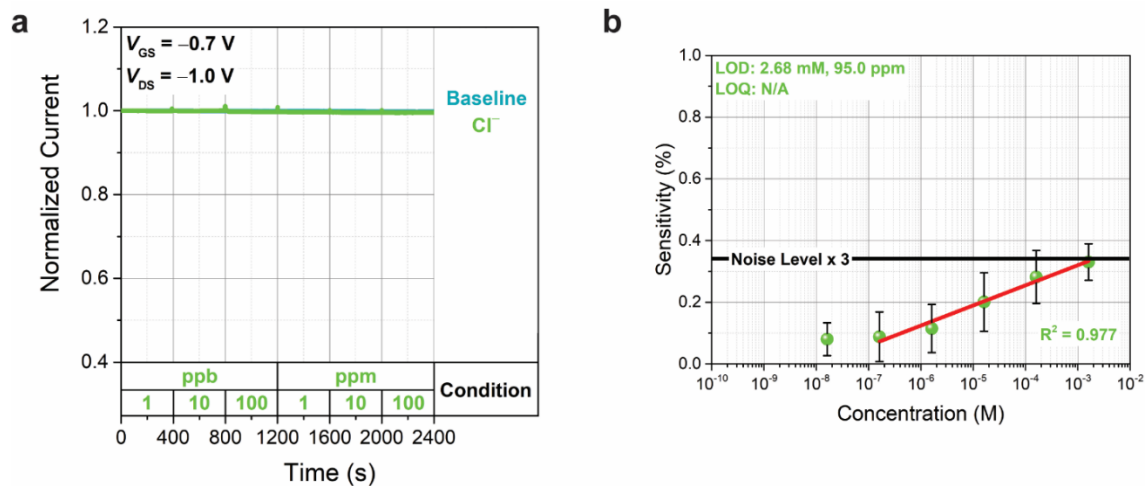


Figure B.34 *PDVT-CS EGOFET* (a) transient responses towards Cl^- and the corresponding (b) sensor calibration plot.

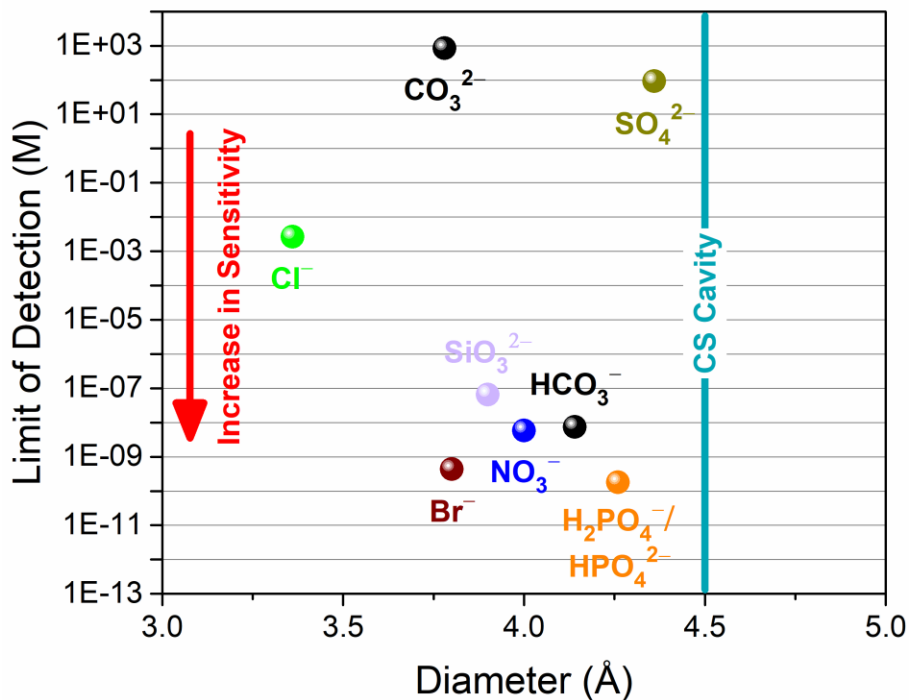


Figure B.35 (a) *PDVT-CS EGOFET* limit of detection (LOD) versus analyte thermionic diameter for anions tested in HEPES buffer. Referencing to the CS cavity (teal line), the size effects towards anion recognition were exemplified. Low LOD and peak preference was found for $\text{H}_2\text{PO}_4^-/\text{HPO}_4^{2-}$, NO_3^- , SiO_3^{2-} , Br^- , and HCO_3^- ranging from 3.8 – 4.26 Å in size. Other anions such as Cl^- ($d_{\text{ion}} \approx 3.4$ Å), CO_3^{2-} ($d_{\text{ion}} \approx 3.78$ Å), and SO_4^{2-} ($d_{\text{ion}} \approx 4.36$ Å).

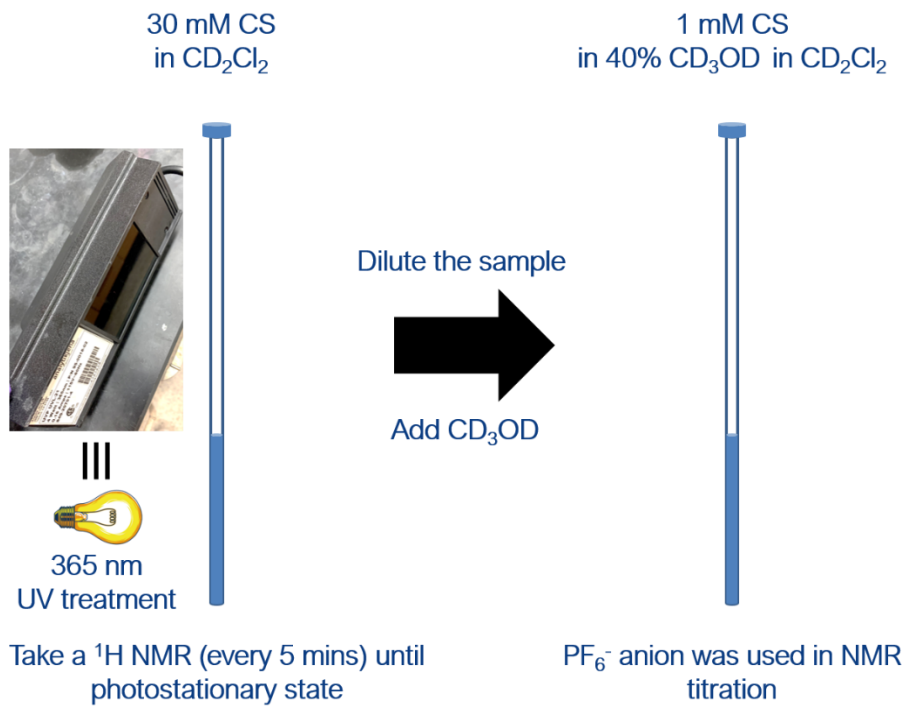


Figure B.36 *IsoCS* preparation for NMR titration experiments.

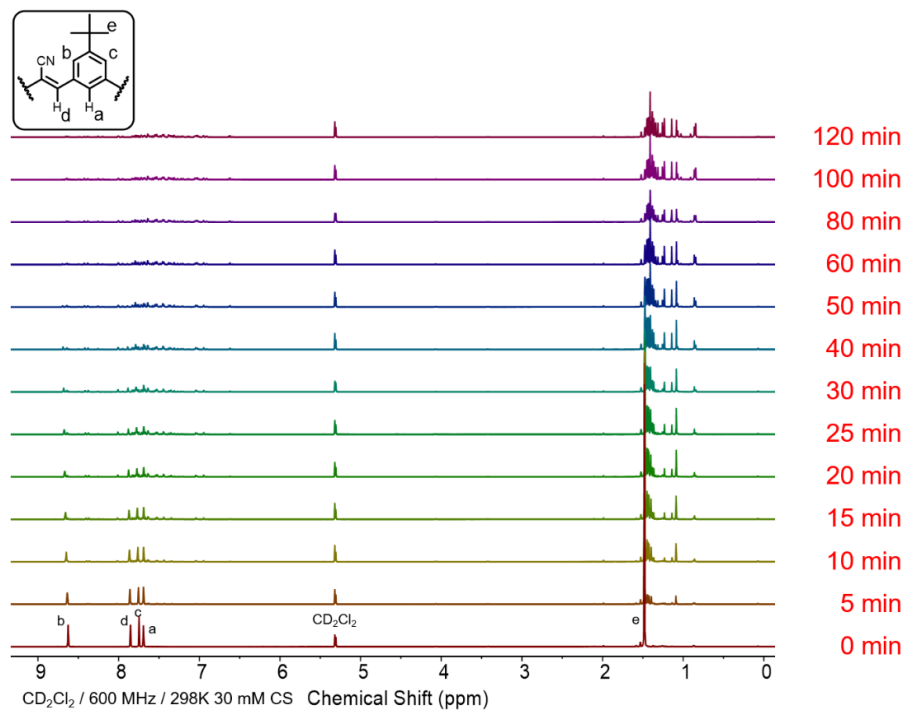


Figure B.37 *In-situ* ¹H NMR of *IsoCS*.

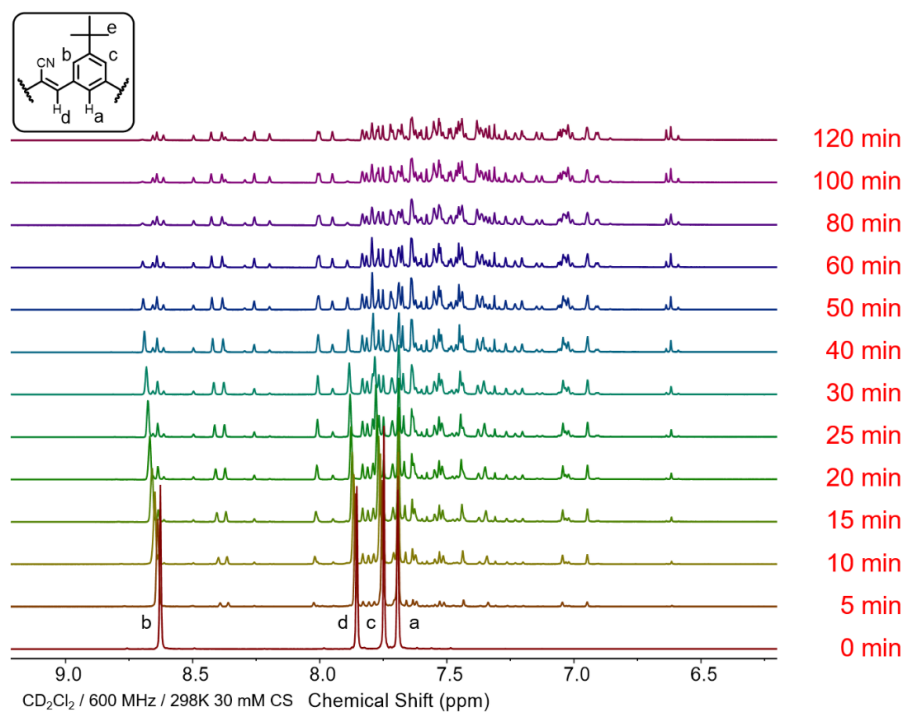


Figure B.38 *In-situ* ¹H NMR (6 – 9.5 ppm) of **IsoCS**.

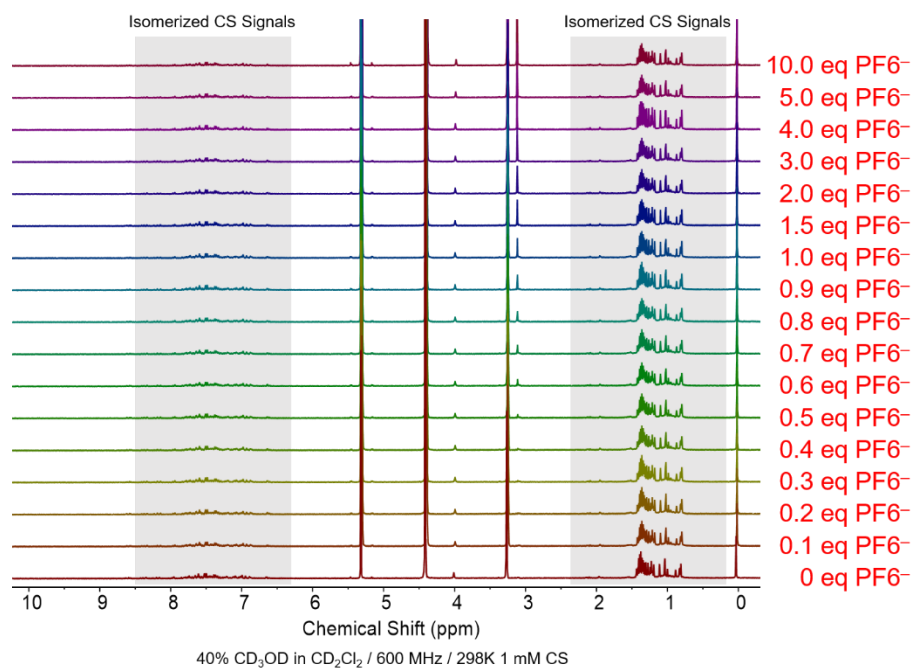


Figure B.39 *In-situ* ¹H NMR of *IsoCS* with PF₆⁻ anion titration.

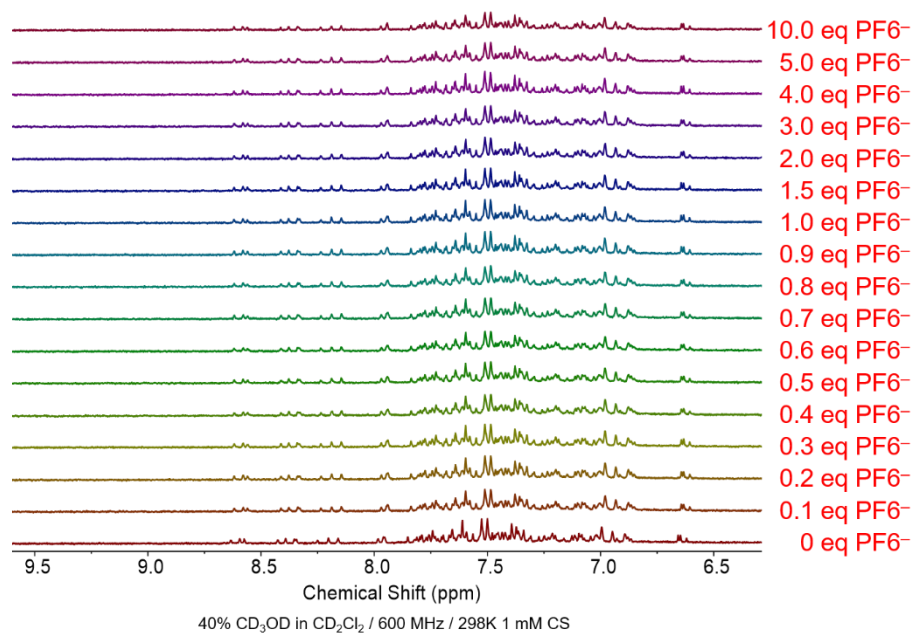


Figure B.40 *In-situ* ¹H NMR (6.5 – 9.5 ppm) of *IsoCS* with PF₆⁻ anion titration.

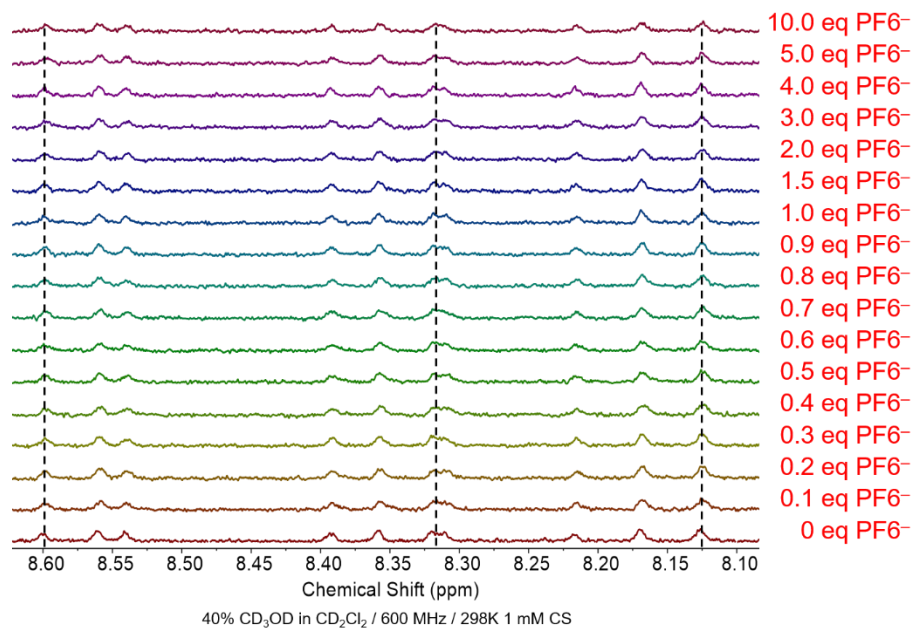


Figure B.41 *In-situ* ^1H NMR (8.10 – 8.6 ppm) of **IsoCS** with PF_6^- anion titration.

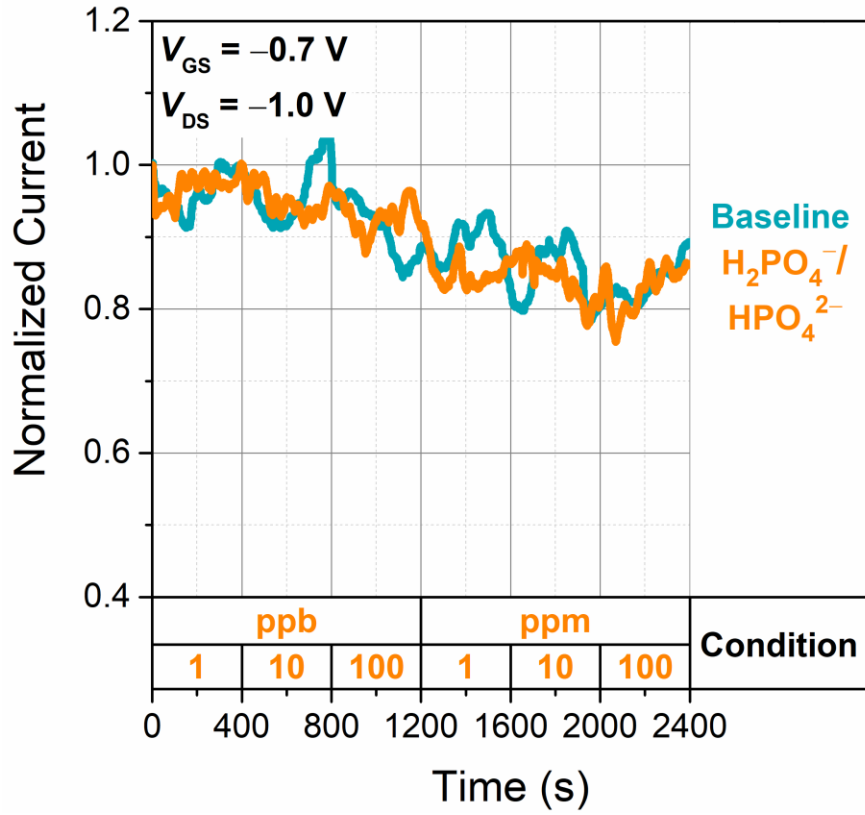


Figure B.42 *PDVT-IsoCS EGFET transient responses towards $\text{H}_2\text{PO}_4^-/\text{HPO}_4^{2-}$.*

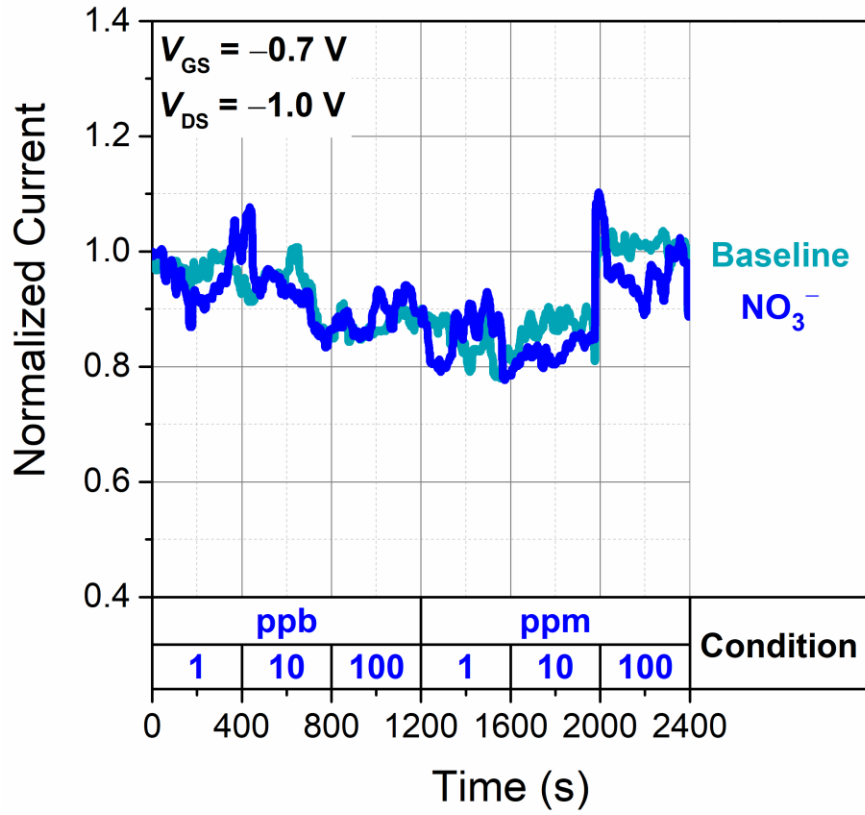


Figure B.43 *PDVT-IsoCS EGFET transient responses towards NO_3^- .*

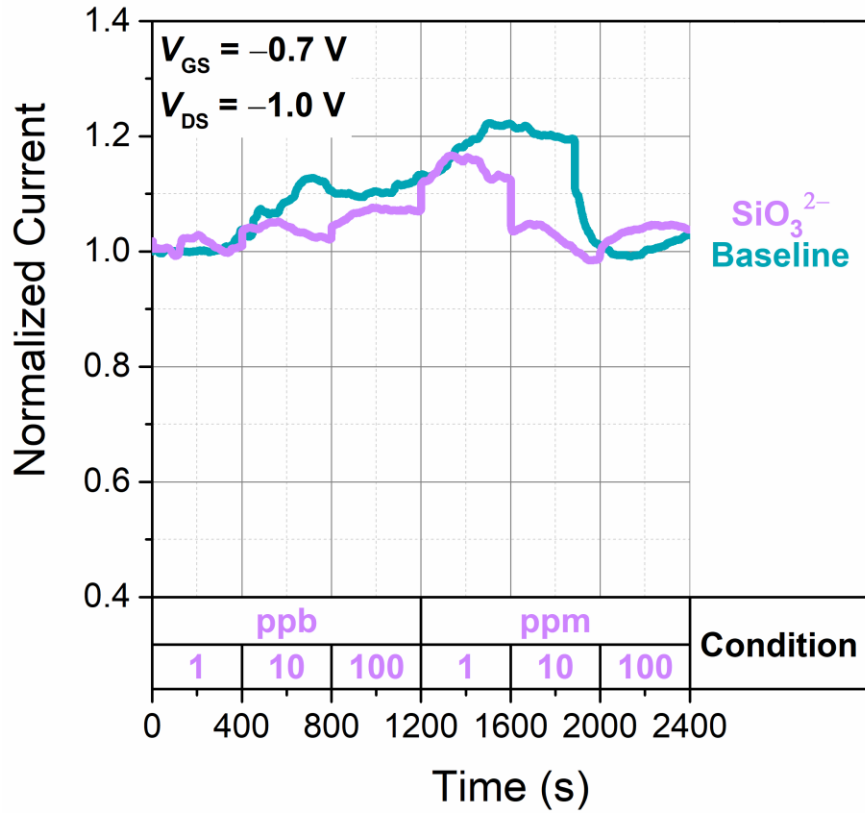


Figure B.44 *PDVT-IsoCS EGFET transient responses towards SiO_3^{2-} .*

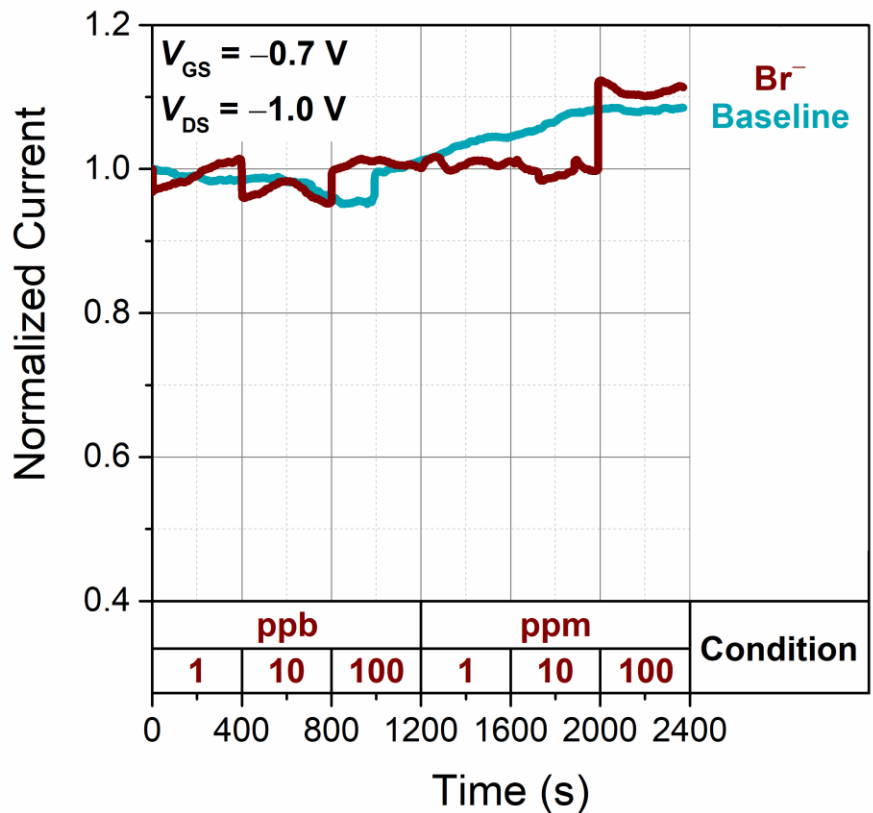


Figure B.45 *PDVT-IsoCS EGFET transient responses towards Br⁻*.

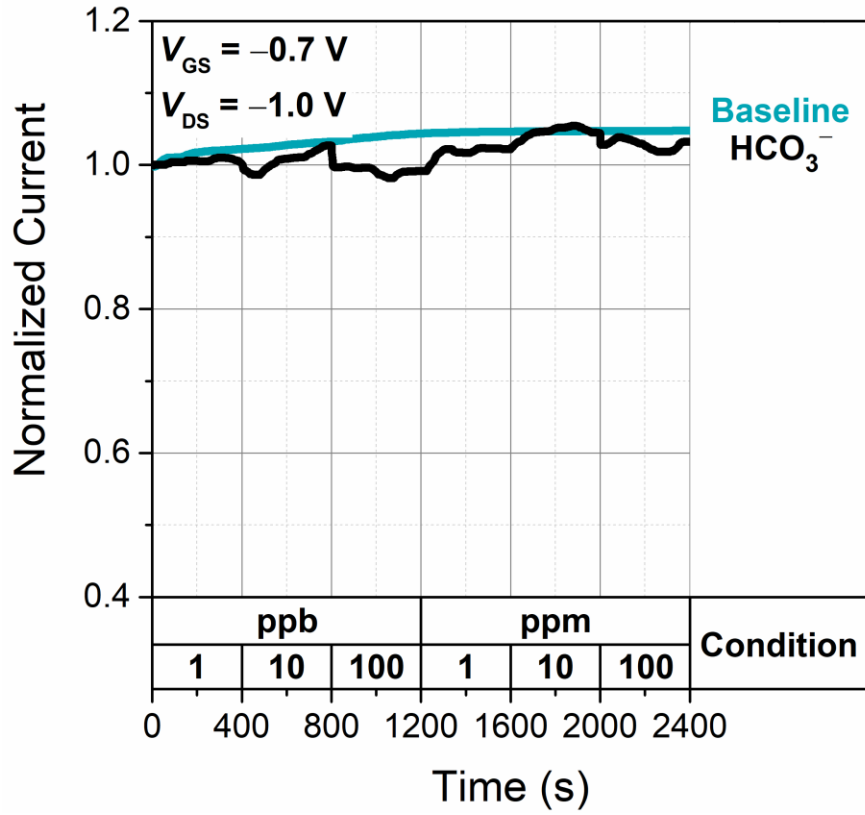


Figure B.46 *PDVT-IsoCS EGO FET transient responses towards HCO_3^- .*

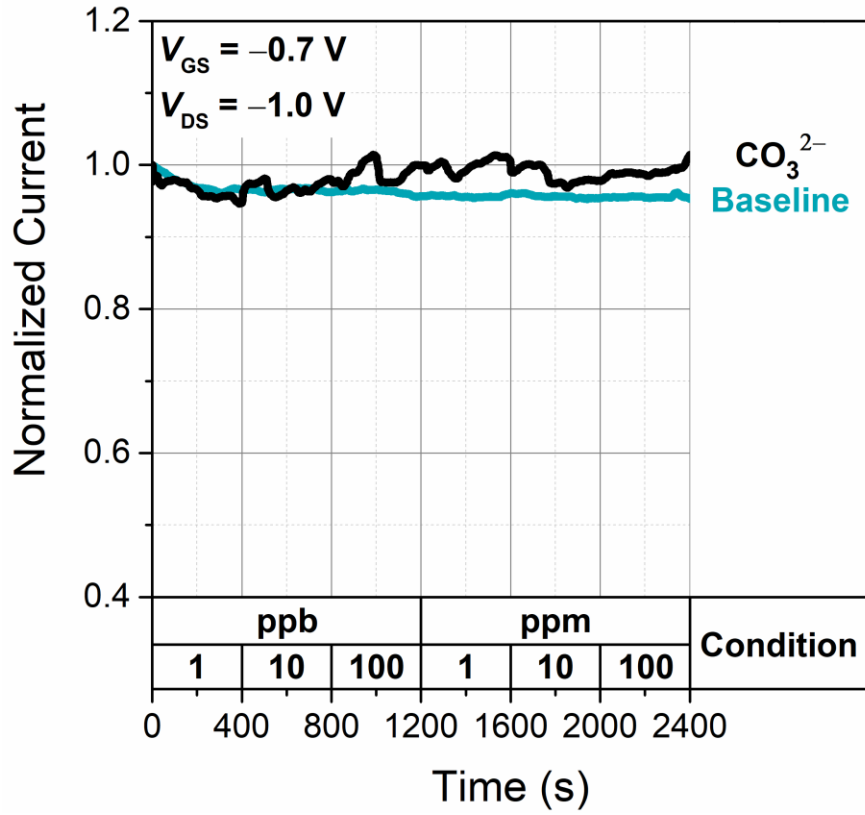


Figure B.47 *PDVT-IsoCS EGOFET transient responses towards CO_3^{2-} .*

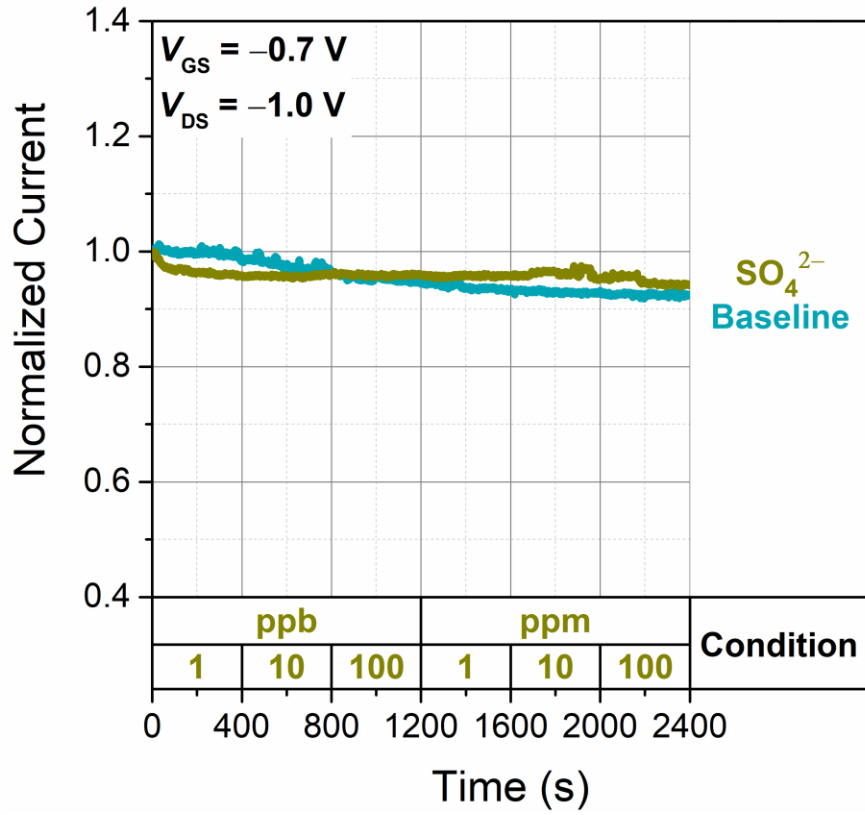


Figure B.48 *PDVT-IsoCS EGOFET transient responses towards SO₄²⁻.*

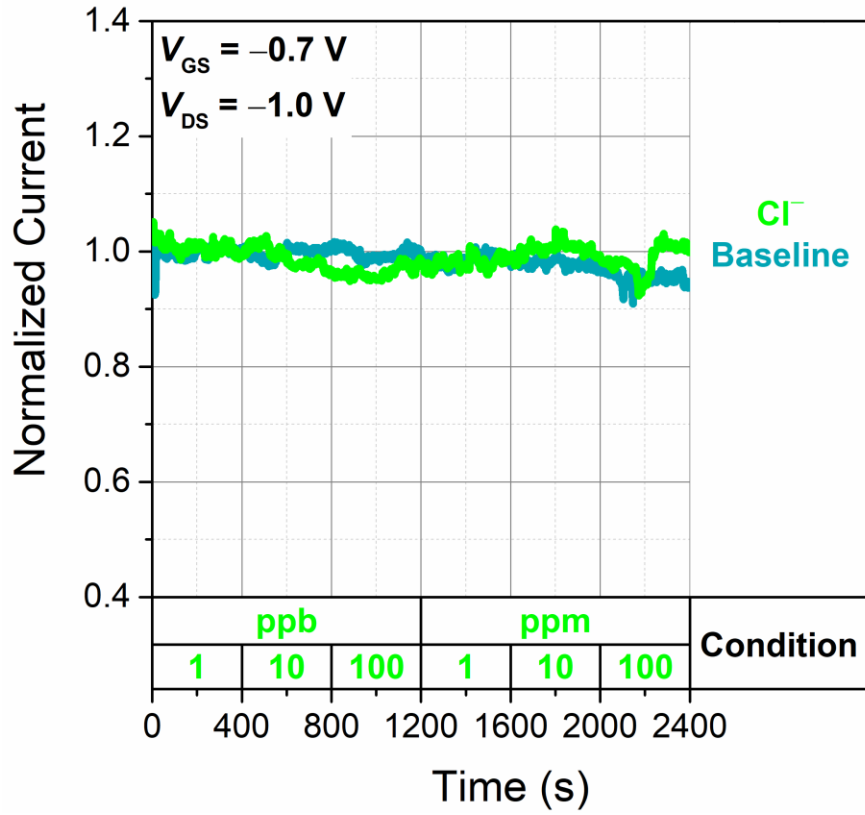


Figure B.49 *PDVT-IsoCS EGO FET transient responses towards Cl⁻.*

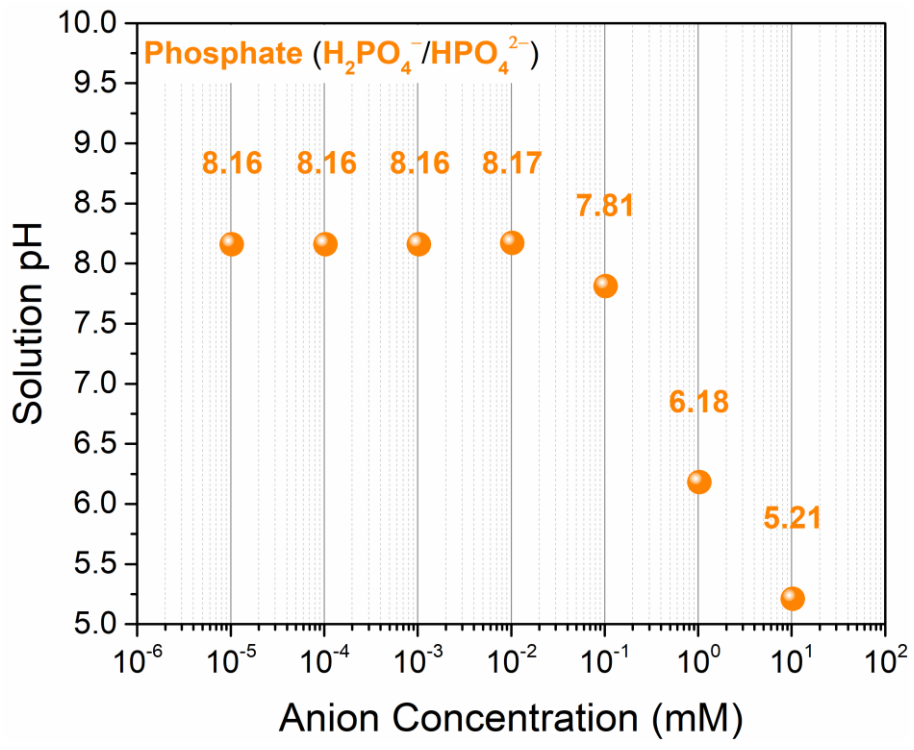


Figure B.50 Instant Ocean sea salt electrolyte spiked with $\text{H}_2\text{PO}_4^-/\text{HPO}_4^{2-}$: pH as a function of anion concentration.

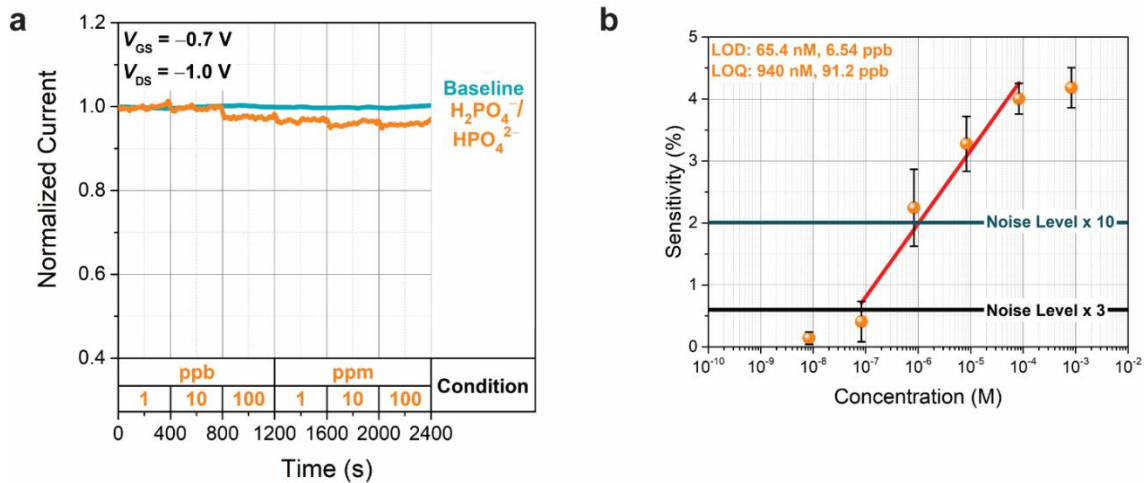


Figure B.51 *PDVT-CS EGFET transient responses towards (a) $\text{H}_2\text{PO}_4^-/\text{HPO}_4^{2-}$ dissolved in artificial seawater electrolyte and (b) the corresponding calibration plot for $\text{H}_2\text{PO}_4^-/\text{HPO}_4^{2-}$ detection and the standard error across 5 devices.*

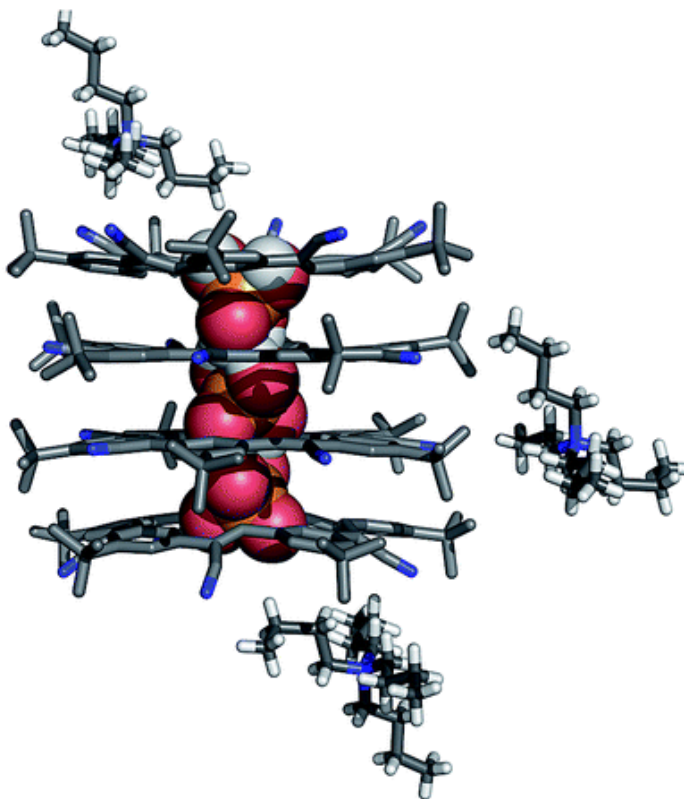


Figure B.52 *Crystal structure of the 4:3:3 stack of tetrameric CS with a trianionic triphosphate ($H_2PO_4 \cdots H_2PO_4 \cdots H_2PO_4$)³⁻ and TBA⁺ cations stacking around the tetrameric stack.*

Table B.5 *Crystal parameters*¹⁰⁶

Parameter	Crystal Structure [CS ₄ (H ₂ PO ₄) ₃ (TBA) ₃] CCDC 1588590
Formula	C ₃₀₈ H ₃₇₄ N ₂₃ O ₁₂ P ₃
M / g mol ⁻¹	4683.19
Temperature / K	230(2)
λ / Å	0.71073
Crystal System	Triclinic
Space Group	<i>P</i> -1
Crystal Color	Colorless
Crystal Size / mm	0.21×0.19×0.16 mm ³
<i>a</i>	21.138(2)
<i>b</i>	21.616(2)
<i>c</i>	21.948(2)
α	118.123(5)
β	106.659(6)
γ	99.169(6)
V/Å ³	7942.5(14)
F ₀₀₀	2524
<i>Z</i>	1
Calculated Density / g cm ⁻³	0.979
Absorption Coefficient (mm)	0.074
Reflections Collected	27892
Reflections Observed	9529
Data/Restraints/Parameters	27892/5061/1898
GOOF	1.343
Final R Indices / %	13.99
R Indices (all data) / %	43.07
Largest Diff Peak and Hole e Å ⁻³	0.556/-0.364

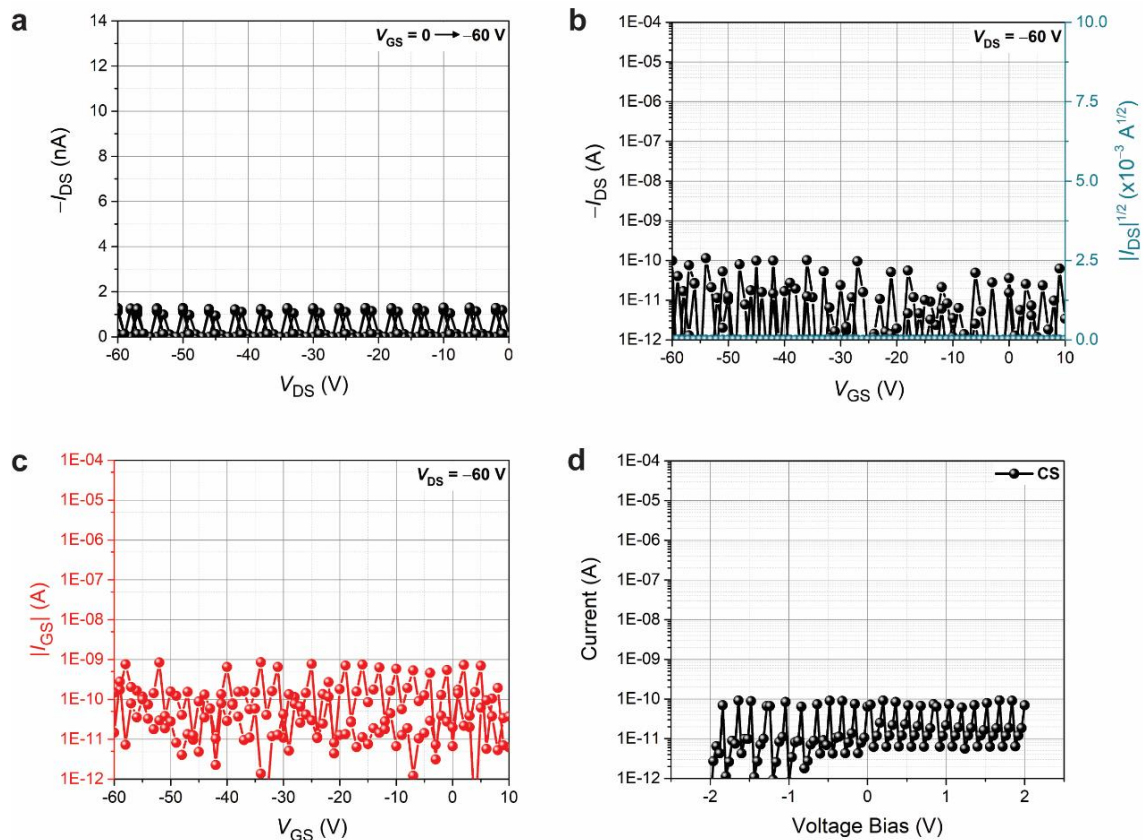
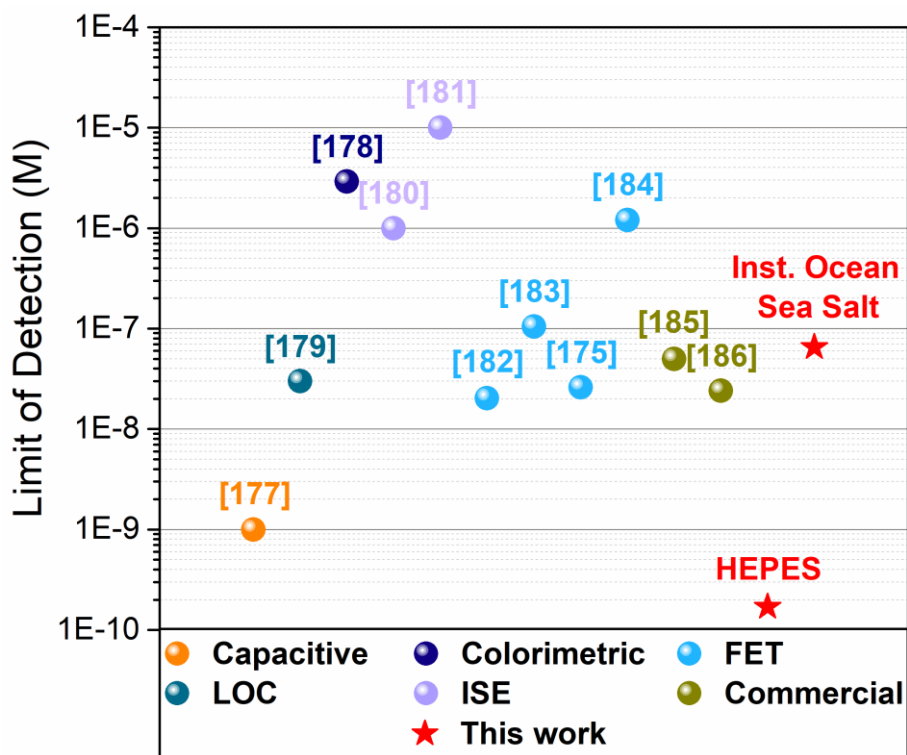


Figure B.53 (a) OFET output (I_{DS} vs V_{DS}), (b) transfer (I_{DS} vs V_{GS}), and (c) gate leakage (I_{GS} vs V_{GS}) characteristics of CS films using a BGBC device configuration and (d) 2-point probe room-temperature $I-V$ plot (without a gate electrode).



Phosphate Sensing Platforms

Figure B.54 A comparison of high performing *PDVT-CS* films benchmarked against capacitive, lap-on-chip, colorimetric, ion-selective electrodes, FETs, and commercialized phosphate sensors. *PDVT-CS* demonstrates a low LOD of 178 pM (17.3 parts per trillion) in HEPES and 65.4 nM (6.54 ppb) in Instant Ocean® Sea Salt Electrolyte.

Table B.6 Summary of state-of-the-art phosphate sensing platforms.

Receptor	Platform	LOD (M)	Chemical Interferants	Year	Ref
Cu(II)Pc-PAA	C-V	1×10^{-9}	Cl^- , SO_4^{2-} , CO_3^{2-} , ClO_4^-	2017	177
Molybdenum Blue	Lab-On-Chip	3×10^{-8}	Si(OH)_4	2017	179
Molybdenum Blue	Colorimetric	2.9×10^{-6}	–	2020	178
Silver Salt-Based Membranes	ISE	1×10^{-6}	–	2018	180
Cobalt Electrodes	ISE	1×10^{-5}	HCO_3^- , Cl^- , Br^- , NO_3^- , Ac^- , F^-	2007	181
MIP	FET	2.0×10^{-8}	SO_4^{2-} , MnO_4^-	2016	182
Ferritin/Graphene Oxide	FET	1.1×10^{-7}	SO_4^{2-} , CO_3^{2-} , NO_3^-	2020	183
Ferritin/Graphene Oxide	FET	2.6×10^{-8}	SO_4^{2-} , CO_3^{2-} , Cl^-	2017	175
Ag Graphene Oxide	FET	1.2×10^{-6}	SO_4^{2-} , Mg^{2+} , K^+ , HCO_3^- , Ca^{2+} , TPP	2019	184
Receptor	Platform	LOD (M)	Link	Ref	
Cycle – PO_4	Optics	5.0×10^{-8}	https://www.planet-ocean.co.uk/PDF/CYC-LE-PO4.pdf	185	
HydroCycle PO_4 (Sea-Bird Scientific)	Wet-Chemistry Sensor	2.4×10^{-8}	https://www.seabird.com/hydrocycle-po/product?id=54721314201	186	

References

1. Forrest, S. R., The path to ubiquitous and low-cost organic electronic appliances on plastic. *Nature* **2004**, *428*, 911.
2. Steudel, S.; Myny, K.; Arkhipov, V.; Deibel, C.; De Vusser, S.; Genoe, J.; Heremans, P., 50 MHz rectifier based on an organic diode. *Nat. Mater.* **2005**, *4*, 597.
3. Russ, B.; Glauddell, A.; Urban, J. J.; Chabiny, M. L.; Segalman, R. A., Organic thermoelectric materials for energy harvesting and temperature control. *Nat. Rev. Mater.* **2016**, *1*.
4. Joo, Y.; Huang, L.; Eedugurala, N.; London, A. E.; Kumar, A.; Wong, B. M.; Boudouris, B. W.; Azoulay, J. D., Thermoelectric Performance of an Open-Shell Donor–Acceptor Conjugated Polymer Doped with a Radical-Containing Small Molecule. *Macromolecules* **2018**, *51*, 3886.
5. Li, H.; Shi, W.; Song, J.; Jang, H.-J.; Dailey, J.; Yu, J.; Katz, H. E., Chemical and biomolecule sensing with organic field-effect transistors. *Chem. Rev.* **2019**, *119* (1), 3-35.
6. Kulat, M. I.; Mohtar, R. H.; Olivera, F., Holistic Water-Energy-Food Nexus for Guiding Water Resources Planning: Matagorda County, Texas Case. *Front. Environ. Sci.* **2019**, *7*.
7. Gallaway, B. J.; Raborn, S. W.; Picariello, L.; Putman, N. F., Changes in Shrimping Effort in the Gulf of Mexico and the Impacts to Red Snapper. *iScience* **2020**, *23* (5), 101111.
8. Lin, Q.; Mendelssohn, I. A., Impacts and Recovery of the Deepwater Horizon Oil Spill on Vegetation Structure and Function of Coastal Salt Marshes in the Northern Gulf of Mexico. *Environ. Sci Technol.* **2012**, *46* (7), 3737-3743.
9. Doney, S. C.; Fabry, V. J.; Feely, R. A.; Kleypas, J. A., Ocean Acidification: The Other CO₂ Problem. *Annu. Rev. Mar. Sci.* **2009**, *1* (1), 169-192.
10. Xia, Y.; Zhang, M.; Tsang, D. C. W.; Geng, N.; Lu, D.; Zhu, L.; Igalavithana, A. D.; Dissanayake, P. D.; Rinklebe, J.; Yang, X.; Ok, Y. S., Recent advances in control technologies for non-point source pollution with nitrogen and phosphorous from agricultural runoff: current practices and future prospects. *Appl. Biol. Chem.* **2020**, *63* (1), 8.
11. Rabalais, N. N.; Turner, R. E.; Dortch, Q.; Justic, D.; Bierman, V. J.; Wiseman, W. J., Nutrient-enhanced productivity in the northern Gulf of Mexico: past, present and future. *Hydrobiologia* **2002**, *475*, 39-63.
12. Bianchi, T. S.; DiMarco, S. F.; Cowan, J. H., Jr.; Hetland, R. D.; Chapman, P.; Day, J. W.; Allison, M. A., The science of hypoxia in the Northern Gulf of Mexico: a review. *Sci. Total Environ.* **2010**, *408* (7), 1471-84.
13. Allan, S. E.; Smith, B. W.; Anderson, K. A., Impact of the deepwater horizon oil spill on bioavailable polycyclic aromatic hydrocarbons in Gulf of Mexico coastal waters. *Environ. Sci Technol.* **2012**, *46* (4), 2033-9.
14. Klimeski, A.; Chardon, W. J.; Turtola, E.; Uusitalo, R., Potential and limitations of phosphate retention media in water protection: a process-based review of laboratory and field-scale tests. *Agric. Food Sci.* **2012**, *21*, 206-223.

15. Howarth, R. W.; Anderson, D. B.; Cloern, J. E.; Elfring, C.; Hopkinson, C. S.; Lapointe, B.; Malone, T.; Marcus, N.; McGlathery, K.; Sharpley, A. N.; Walker, D., Nutrient pollution of coastal rivers, bays, and seas. *Issues Ecol.* **2000**, (7), 1-16.
16. Howarth, R. W.; Sharpley, A.; Walker, D., Sources of nutrient pollution to coastal waters in the United States: Implications for achieving coastal water quality goals. *Estuaries* **2002**, 25 (4), 656-676.
17. Bricker, S. B.; Longstaff, B.; Dennison, W.; Jones, A.; Boicourt, K.; Wicks, C.; Woerner, J., Effects of nutrient enrichment in the nation's estuaries: A decade of change. *Harmful Algae* **2008**, 8 (1), 21-32.
18. Braasch, D. A.; Corey, D. R., Locked nucleic acid (LNA): fine-tuning the recognition of DNA and RNA. *Chem. Biol.* **2001**, 8 (1), 1-7.
19. Greengard, P.; Valtorta, F.; Czernik, A. J.; Benfenati, F., Synaptic Vesicle Phosphoproteins and Regulation of Synaptic Function. *Science* **1993**, 259 (5096), 780-785.
20. Ohvo-Rekilä, H.; Ramstedt, B.; Leppimäki, P.; Peter Slotte, J., Cholesterol interactions with phospholipids in membranes. *Prog. Lipid. Res.* **2002**, 41 (1), 66-97.
21. Adams, R. L. P. K. J. T. L. D. P., *The biochemistry of the nucleic acids*. Chapman and Hall: London, **1986**.
22. Saenger, W., *Principles of nucleic acid structure*. Springer-Verlag: New York, **1984**.
23. Busschaert, N.; Caltagirone, C.; Van Rossom, W.; Gale, P. A., Applications of Supramolecular Anion Recognition. *Chem. Rev.* **2015**, 115 (15), 8038-8155.
24. Marcus, Y., A simple empirical model describing the thermodynamics of hydration of ions of widely varying charges, sizes, and shapes. *Biophys. Chem.* **1994**, 51 (2), 111-127.
25. Bian, Y.; Chen, X.; Ren, Z. J., pH Dependence of Phosphorus Speciation and Transport in Flow-Electrode Capacitive Deionization. *Environ. Sci Technol.* **2020**, 54 (14), 9116-9123.
26. Filippelli, G. M., The Global Phosphorus Cycle: Past, Present, and Future. *Elements* **2008**, 4 (2), 89-95.
27. Paytan, A.; McLaughlin, K., The Oceanic Phosphorus Cycle. *Chem. Rev.* **2007**, 107 (2), 563-576.
28. Nagul, E. A.; McKelvie, I. D.; Worsfold, P.; Kolev, S. D., The molybdenum blue reaction for the determination of orthophosphate revisited: Opening the black box. *Anal. Chim. Acta* **2015**, 890, 60-82.
29. Madrid, Y.; Zayas, Z. P., Water sampling : Traditional methods and new approaches in water sampling strategy. *Trends Anal. Chem.* **2007**, 26, 293-299.
30. Islam, M. S.; Ahmed, M. K.; Raknuzzaman, M.; Habibullah -Al- Mamun, M.; Islam, M. K., Heavy metal pollution in surface water and sediment: A preliminary assessment of an urban river in a developing country. *Ecol. Indic.* **2015**, 48, 282-291.
31. Williams, A. K.; Tropp, J.; Crater, E. R.; Eedugurala, N.; Azoulay, J. D., Thiol–ene click post-polymerization modification of a fluorescent conjugated polymer for parts-per-billion pyrophosphate detection in seawater. *ACS Appl. Polym. Mater.* **2019**, 1 (3), 309-314.

32. Arias, A. C.; MacKenzie, J. D.; McCulloch, I.; Rivnay, J.; Salleo, A., Materials and applications for large area electronics: solution-based approaches. *Chem. Rev.* **2010**, *110* (1), 3-24.
33. Chen, S.; Deng, L.; Xie, J.; Peng, L.; Xie, L.; Fan, Q.; Huang, W., Recent developments in top-emitting organic light-emitting diodes *Adv. Mater.* **2010**, *22* (46), 5227-5239.
34. Gelinck, G.; Heremans, P.; Nomoto, K.; Anthopoulos, T. D., Organic transistors in optical displays and microelectronic applications. *Adv. Mater.* **2010**, *22* (34), 3778-3798.
35. Baran, D.; Balan, A.; Celebi, S.; Meana Esteban, B.; Neugebauer, H.; Sariciftci, N. S.; Toppare, L., Processable Multipurpose Conjugated Polymer for Electrochromic and Photovoltaic Applications. *Chem. Mater.* **2010**, *22* (9), 2978-2987.
36. Krebs, F. C., Fabrication and processing of polymer solar cells: A review of printing and coating techniques. *Sol. Energy Mater. Sol. Cells* **2009**, *93* (4), 394-412.
37. Geffroy, B.; le Roy, P.; Prat, C., Organic light-emitting diode (OLED) technology: materials, devices and display technologies. *Polym. Int.* **2006**, *55* (6), 572-582.
38. Guo, Y.; Yu, G.; Liu, Y., Functional Organic Field-Effect Transistors. *Adv. Mater.* **2010**, *22* (40), 4427-4447.
39. Usta, H.; Facchetti, A.; Marks, T. J., n-Channel Semiconductor Materials Design for Organic Complementary Circuits. *Acc. Chem. Res.* **2011**, *44* (7), 501-510.
40. Dong, H.; Zhu, H.; Meng, Q.; Gong, X.; Hu, W., Organic photoresponse materials and devices. *Chem. Soc. Rev.* **2012**, *41* (5), 1754-1808.
41. Li, G.; Zhu, R.; Yang, Y., Polymer solar cells. *Nat. Photonics* **2012**, *6*, 153-161.
42. Nelson, J., Polymer:fullerene bulk heterojunction solar cells. *Mater. Today* **2011**, *14* (10), 462-470.
43. He, F.; Yu, L., How Far Can Polymer Solar Cells Go? In Need of a Synergistic Approach. *J. Phys. Chem. Lett.* **2011**, *2* (24), 3102-3113.
44. Azzellino, G.; Grimoldi, A.; Binda, M.; Caironi, M.; Natali, D.; Sampietro, M., Fully inkjet-printed organic photodetectors with high quantum yield *Adv. Mater.* **2013**, *25* (47), 6829-33.
45. Baeg, K. J.; Binda, M.; Natali, D.; Caironi, M.; Noh, Y. Y., Organic light detectors: photodiodes and phototransistors. *Adv. Mater.* **2013**, *25*, 4267-95.
46. Chiang, C. K.; Fincher, C. R.; Park, Y. W.; Heeger, A. J.; Shirakawa, H.; Louis, E. J.; Gau, S. C.; MacDiarmid, A. G., Electrical Conductivity in Doped Polyacetylene. *Phys. Rev. Lett.* **1977**, *39* (17), 1098-1101.
47. Rasmussen, S. C., Conjugated and Conducting Organic Polymers: The First 150 Years. *Chempluschem* **2020**, *85* (7), 1412-1429.
48. Shirakawa, H.; Louis, E. J.; MacDiarmid, A. G.; Chiang, C. K.; Heeger, A. J., Synthesis of electrically conducting organic polymers: halogen derivatives of polyacetylene, (CH). *J. Chem. Soc., Chem. Commun.* **1977**, (16), 578-580.
49. Kayser, L. V.; Lipomi, D. J., Stretchable Conductive Polymers and Composites Based on PEDOT and PEDOT:PSS. *Adv. Mater.* **2019**, *31* (10), 1806133.
50. Shi, H.; Liu, C.; Jiang, Q.; Xu, J., Effective Approaches to Improve the Electrical Conductivity of PEDOT:PSS: A Review. *Adv. Electron. Mater.* **2015**, *1* (4), 1500017.

51. Kim, M.; Ryu, S. U.; Park, S. A.; Choi, K.; Kim, T.; Chung, D.; Park, T., Donor–Acceptor-Conjugated Polymer for High-Performance Organic Field-Effect Transistors: A Progress Report. *Adv. Funct. Mater.* **2020**, *30* (20), 1904545.
52. Wu, J.-S.; Cheng, S.-W.; Cheng, Y.-J.; Hsu, C.-S., Donor–acceptor conjugated polymers based on multifused ladder-type arenes for organic solar cells. *Chem. Soc. Rev.* **2015**, *44* (5), 1113-1154.
53. Singleton, J., *Band theory and electronic properties of solids*. Oxford University Press: **2001**; Vol. 2.
54. Kaur, G.; Adhikari, R.; Cass, P.; Bown, M.; Gunatillake, P., Electrically conductive polymers and composites for biomedical applications. *RSC Adv.* **2015**, *5* (47), 37553-37567.
55. Arkhipov, V. I.; Heremans, P.; Emelianova, E. V.; Bäessler, H., Effect of doping on the density-of-states distribution and carrier hopping in disordered organic semiconductors. *Phys. Rev. B* **2005**, *71* (4), 045214.
56. Heeger, A. J., Semiconducting and metallic polymers: the fourth generation of polymeric materials. ACS Publications: **2001**; Vol. 105, pp 8475-8491.
57. Xu, Y.; Sun, H.; Liu, A.; Zhu, H.-H.; Li, W.; Lin, Y.-F.; Noh, Y.-Y., Doping: A Key Enabler for Organic Transistors. *Adv. Mater.* **2018**, *30* (46), 1801830.
58. Lussem, B.; Keum, C. M.; Kasemann, D.; Naab, B.; Bao, Z.; Leo, K., Doped organic transistors. *Chem. Rev.* **2016**, *116* (22), 13714-13751.
59. Scaccabarozzi, A. D.; Basu, A.; Aniés, F.; Liu, J.; Zapata-Arteaga, O.; Warren, R.; Firdaus, Y.; Nugraha, M. I.; Lin, Y.; Campoy-Quiles, M.; Koch, N.; Müller, C.; Tsetseris, L.; Heeney, M.; Anthopoulos, T. D., Doping Approaches for Organic Semiconductors. *Chem Rev.* **2022**, *122* (4), 4420-4492.
60. Salzmänn, I.; Heimel, G.; Oehzelt, M.; Winkler, S.; Koch, N., Molecular Electrical Doping of Organic Semiconductors: Fundamental Mechanisms and Emerging Dopant Design Rules. *Acc. Chem. Res.* **2016**, *49* (3), 370-378.
61. Salzmänn, I.; Heimel, G., Toward a comprehensive understanding of molecular doping organic semiconductors (review). *J. Electron Spectros. Relat. Phenomena* **2015**, *204* (PartA), 208-222.
62. Salzmänn, I.; Heimel, G.; Duhm, S.; Oehzelt, M.; Pingel, P.; George, B. M.; Schnegg, A.; Lips, K.; Blum, R.-P.; Vollmer, A.; Koch, N., Intermolecular Hybridization Governs Molecular Electrical Doping. *Phys. Rev. Lett.* **2012**, *108* (3), 035502.
63. Méndez, H.; Heimel, G.; Opitz, A.; Sauer, K.; Barkowski, P.; Oehzelt, M.; Soeda, J.; Okamoto, T.; Takeya, J.; Arlin, J.-B.; Balandier, J.-Y.; Geerts, Y.; Koch, N.; Salzmänn, I., Doping of Organic Semiconductors: Impact of Dopant Strength and Electronic Coupling. *Angew. Chem. Int. Ed.* **2013**, *52* (30), 7751-7755.
64. Yang, J.; Li, Y.; Duhm, S.; Tang, J.; Kera, S.; Ueno, N., Molecular Structure-Dependent Charge Injection and Doping Efficiencies of Organic Semiconductors: Impact of Side Chain Substitution. *Adv. Mater. Interfaces* **2014**, *1* (3), 1300128.
65. Méndez, H.; Heimel, G.; Winkler, S.; Frisch, J.; Opitz, A.; Sauer, K.; Wegner, B.; Oehzelt, M.; Röthel, C.; Duhm, S.; Töbrens, D.; Koch, N.; Salzmänn, I., Charge-transfer crystallites as molecular electrical dopants. *Nat. Commun.* **2015**, *6* (1), 8560.
66. Sirringhaus, H., 25th Anniversary Article: Organic Field-Effect Transistors: The Path Beyond Amorphous Silicon. *Adv. Mater.* **2014**, *26*, 1319.

67. Scharber, M. C.; Sariciftci, N. S., Low Band Gap Conjugated Semiconducting Polymers. *Adv. Mater. Technol.* **2021**, *6* (4), 2000857.
68. Bourhill, G.; Bredas, J.-L.; Cheng, L.-T.; Marder, S. R.; Meyers, F.; Perry, J. W.; Tiemann, B. G., Experimental Demonstration of the Dependence of the First Hyperpolarizability of Donor-Acceptor-Substituted Polyenes on the Ground-State Polarization and Bond Length Alternation. *J. Am. Chem. Soc.* **1994**, *116* (6), 2619-2620.
69. Moliton, A.; Hiorns, R. C., Review of electronic and optical properties of semiconducting π -conjugated polymers: applications in optoelectronics. *Polym. Int.* **2004**, *53* (10), 1397-1412.
70. Savagian, L. R.; Österholm, A. M.; Shen, D. E.; Christiansen, D. T.; Kuepfert, M.; Reynolds, J. R., Conjugated Polymer Blends for High Contrast Black-to-Transmissive Electrochromism. *Adv. Opt. Mater.* **2018**, *6* (19), 1800594.
71. Beaujuge, P. M.; Ellinger, S.; Reynolds, J. R., The donor-acceptor approach allows a black-to-transmissive switching polymeric electrochrome. *Nat. Mater.* **2008**, *7* (10), 795-799.
72. Zhang, J.; Tan, C.-H.; Zhang, K.; Jia, T.; Cui, Y.; Deng, W.; Liao, X.; Wu, H.; Xu, Q.; Huang, F.; Cao, Y., π -Extended Conjugated Polymer Acceptor Containing Thienylene-Vinylene-Thienylene Unit for High-Performance Thick-Film All-Polymer Solar Cells with Superior Long-Term Stability. *Adv. Energy Mater.* **2021**, *11* (48), 2102559.
73. Brus, V. V.; Lee, J.; Luginbuhl, B. R.; Ko, S.-J.; Bazan, G. C.; Nguyen, T.-Q., Solution-Processed Semitransparent Organic Photovoltaics: From Molecular Design to Device Performance. *Adv. Mater.* **2019**, *31* (30), 1900904.
74. Noriega, R.; Rivnay, J.; Vandewal, K.; Koch, F. P.; Stingelin, N.; Smith, P.; Toney, M. F.; Salleo, A., A general relationship between disorder, aggregation and charge transport in conjugated polymers. *Nat. Mater.* **2013**, *12* (11), 1038-44.
75. Dykstra, T. E.; Hennebicq, E.; Beljonne, D.; Gierschner, J.; Claudio, G.; Bittner, E. R.; Knoester, J.; Scholes, G. D., Conformational Disorder and Ultrafast Exciton Relaxation in PPV-family Conjugated Polymers. *J. Phys. Chem. B* **2009**, *113* (3), 656-667.
76. Salleo, A.; Kline, R. J.; DeLongchamp, D. M.; Chabinyc, M. L., Microstructural Characterization and Charge Transport in Thin Films of Conjugated Polymers. *Adv. Mater.* **2010**, *22* (34), 3812-3838.
77. Gu, K.; Loo, Y.-L., The Polymer Physics of Multiscale Charge Transport in Conjugated Systems. *J. Polym. Sci. B Polym. Phys.* **2019**, *57* (23), 1559-1571.
78. Liu, C.; Huang, K.; Park, W.-T.; Li, M.; Yang, T.; Liu, X.; Liang, L.; Minari, T.; Noh, Y.-Y., A unified understanding of charge transport in organic semiconductors: the importance of attenuated delocalization for the carriers. *Mater. Horiz.* **2017**, *4* (4), 608-618.
79. Rivnay, J.; Mannsfeld, S. C. B.; Miller, C. E.; Salleo, A.; Toney, M. F., Quantitative Determination of Organic Semiconductor Microstructure from the Molecular to Device Scale. *Chem. Rev.* **2012**, *112* (10), 5488-5519.
80. Venkateshvaran, D.; Nikolka, M.; Sadhanala, A.; Lemaur, V.; Zelazny, M.; Kepa, M.; Hurhangee, M.; Kronemeijer, A. J.; Pecunia, V.; Nasrallah, I.; Romanov, I.; Broch, K.; McCulloch, I.; Emin, D.; Olivier, Y.; Cornil, J.; Beljonne, D.; Sirringhaus, H., Approaching disorder-free transport in high-mobility conjugated polymers. *Nature* **2014**, *515* (7527), 384-388.

81. Cataldo, S.; Pignataro, B., Polymeric Thin Films for Organic Electronics: Properties and Adaptive Structures. *Materials* **2013**, *6* (3), 1159-1190.
82. Osaka, I.; Takimiya, K., Backbone orientation in semiconducting polymers. *Polymer* **2015**, *59*, A1-A15.
83. Lee, Y. H.; Jang, M.; Lee, M. Y.; Kweon, O. Y.; Oh, J. H., Flexible Field-Effect Transistor-Type Sensors Based on Conjugated Molecules. *Chem.* **2017**, *3*, 724-763.
84. Irimia-Vladu, M., "Green" electronics: biodegradable and biocompatible materials and devices for sustainable future. *Chem. Soc. Rev.* **2014**, *43* (2), 588-610.
85. Lin, P.; Yan, F., Organic thin-film transistors for chemical and biological sensing. *Adv Mater* **2012**, *24* (1), 34-51.
86. Elkington, D.; Cooling, N.; Belcher, W.; Dastoor, P. C.; Zhou, X., Organic Thin-Film Transistor (OTFT)-Based Sensors. *Electronics* **2014**, *3* (2), 234-254.
87. Mulla, M. Y.; Tuccori, E.; Magliulo, M.; Lattanzi, G.; Palazzo, G.; Persaud, K.; Torsi, L., Capacitance-modulated transistor detects odorant binding protein chiral interactions. *Nat. Commun.* **2015**, *6* (1), 6010.
88. Palazzo, G.; De Tullio, D.; Magliulo, M.; Mallardi, A.; Intranuovo, F.; Mulla, M. Y.; Favia, P.; Vikholm-Lundin, I.; Torsi, L., Detection Beyond Debye's Length with an Electrolyte-Gated Organic Field-Effect Transistor. *Adv. Mater.* **2015**, *27* (5), 911-916.
89. Torsi, L.; Magliulo, M.; Manoli, K.; Palazzo, G., Organic field-effect transistor sensors: a tutorial review. *Chem. Soc. Rev.* **2013**, *42*, 8612.
90. Mannsfeld, S. C. B.; Tee, B. C. K.; Stoltenberg, R. M.; Chen, C. V. H. H.; Barman, S.; Muir, B. V. O.; Sokolov, A. N.; Reese, C.; Bao, Z., Highly sensitive flexible pressure sensors with microstructured rubber dielectric layers. *Nat. Mater.* **2010**, *9* (10), 859-864.
91. Schwartz, G.; Tee, B. C. K.; Mei, J.; Appleton, A. L.; Kim, D. H.; Wang, H.; Bao, Z., Flexible polymer transistors with high pressure sensitivity for application in electronic skin and health monitoring. *Nat. Commun.* **2013**, *4* (1), 1859.
92. Yokota, T.; Inoue, Y.; Terakawa, Y.; Reeder, J.; Kaltenbrunner, M.; Ware, T.; Yang, K.; Mabuchi, K.; Murakawa, T.; Sekino, M.; Voit, W.; Sekitani, T.; Someya, T., Ultraflexible, large-area, physiological temperature sensors for multipoint measurements. *Proc. Natl. Acad. Sci. U. S. A.* **2015**, *112* (47), 14533-8.
93. Ren, X.; Pei, K.; Peng, B.; Zhang, Z.; Wang, Z.; Wang, X.; Chan, P. K. L., A Low-Operating-Power and Flexible Active-Matrix Organic-Transistor Temperature-Sensor Array. *Adv. Mater.* **2016**, *28* (24), 4832-4838.
94. Zhao, D.; Fabiano, S.; Berggren, M.; Crispin, X., Ionic thermoelectric gating organic transistors. *Nat. Commun.* **2017**, *8* (1), 14214.
95. Knopfmacher, O.; Hammock, M. L.; Appleton, A. L.; Schwartz, G.; Mei, J.; Lei, T.; Pei, J.; Bao, Z., Highly stable organic polymer field-effect transistor sensor for selective detection in the marine environment. *Nat. Commun.* **2014**, *5*, 2954.
96. Molina, P.; Zapata, F.; Caballero, A., Anion Recognition Strategies Based on Combined Noncovalent Interactions. *Chem. Rev.* **2017**, *117* (15), 9907-9972.
97. Langton, M. J.; Serpell, C. J.; Beer, P. D., Anion recognition in water: recent advances from a supramolecular and macromolecular perspective. *Angew. Chem.* **2016**, *55* (6), 1974-1987.

98. Kataev, E.; Müller, C.; Kolesnikov, G.; Khrustalev, V., Guanidinium-Based Artificial Receptors for Binding Orthophosphate in Aqueous Solution. *Eur. J. Org. Chem.* **2014**, *2014*.
99. Steed, J. W. A. J. L., *Supramolecular chemistry*. Wiley: Chichester, UK, **2009**.
100. Leyton, P.; Sanchez-Cortes, S.; Garcia-Ramos, J. V.; Domingo, C.; Campos-Vallette, M.; Saitz, C.; Clavijo, R. E., Selective Molecular Recognition of Polycyclic Aromatic Hydrocarbons (PAHs) on Calix[4]arene-Functionalized Ag Nanoparticles by Surface-Enhanced Raman Scattering. *J. Phys. Chem. B* **2004**, *108* (45), 17484-17490.
101. Joseph, R.; Rao, C. P., Ion and Molecular Recognition by Lower Rim 1,3-Di-conjugates of Calix[4]arene as Receptors. *Chem. Rev.* **2011**, *111* (8), 4658-4702.
102. Xie, Y.; Wang, X.; Han, X.; Xue, X.; Ji, W.; Qi, Z.; Liu, J.; Zhao, B.; Ozaki, Y., Sensing of polycyclic aromatic hydrocarbons with cyclodextrin inclusion complexes on silver nanoparticles by surface-enhanced Raman scattering. *Analyst* **2010**, *135* (6), 1389-1394.
103. Barnes, J. C.; Juríček, M.; Strutt, N. L.; Frascioni, M.; Sampath, S.; Giesener, M. A.; McGrier, P. L.; Bruns, C. J.; Stern, C. L.; Sarjeant, A. A.; Stoddart, J. F., ExBox: A Polycyclic Aromatic Hydrocarbon Scavenger. *J. Am. Chem. Soc.* **2013**, *135* (1), 183-192.
104. Bachrach, S. M.; Nickle, Z. O. M., Designing a “Flatter” ExBox4+ Analogue. *J. Phys. Chem. A* **2015**, *119* (42), 10613-10619.
105. Lee, S.; Chen, C.-H.; Flood, A. H., A pentagonal cyanostar macrocycle with cyanostilbene CH donors binds anions and forms dialkylphosphate [3]rotaxanes. *Nat. Chem.* **2013**, *5* (8), 704-710.
106. Fatila, E. M.; Pink, M.; Twum, E. B.; Karty, J. A.; Flood, A. H., Phosphate–phosphate oligomerization drives higher order co-assemblies with stacks of cyanostar macrocycles. *Chem. Sci.* **2018**, *9* (11), 2863-2872.
107. Zhao, W.; Qiao, B.; Chen, C.-H.; Flood, A. H., High-fidelity multistate switching with anion–anion and acid–anion dimers of organophosphates in cyanostar complexes. *Angew. Chem. Int. Ed.* **2017**, *56* (42), 13083-13087.
108. Kim, J.; McQuade, D. T.; McHugh, S. K.; Swager, T. M., Ion-Specific Aggregation in Conjugated Polymers: Highly Sensitive and Selective Fluorescent Ion Chemosensors. *Angew. Chem. Int. Ed.* **2000**, *39* (21), 3868-3872.
109. Kurishita, Y.; Kohira, T.; Ojida, A.; Hamachi, I., Rational Design of FRET-Based Ratiometric Chemosensors for in Vitro and in Cell Fluorescence Analyses of Nucleoside Polyphosphates. *J. Am. Chem. Soc.* **2010**, *132* (38), 13290-13299.
110. Wang, Y.; Gong, Q.; Miao, Q., Structured and functionalized organic semiconductors for chemical and biological sensors based on organic field effect transistors. *Mater. Chem. Front.* **2020**, *4* (12), 3505-3520.
111. Sessolo, M.; Rivnay, J.; Bandiello, E.; Malliaras, G. G.; Bolink, H. J., Ion-selective organic electrochemical transistors. *Adv. Mater.* **2014**, *26* (28), 4803-4807.
112. Han, S.; Yamamoto, S.; Polyravas, A. G.; Malliaras, G. G., Microfabricated Ion-Selective Transistors with Fast and Super-Nernstian Response. *Adv. Mater.* **2020**, *32* (48), 2004790.
113. Wustoni, S.; Combe, C.; Ohayon, D.; Akhtar, M. H.; McCulloch, I.; Inal, S., Membrane-Free Detection of Metal Cations with an Organic Electrochemical Transistor. *Adv. Funct. Mater.* **2019**, *29* (44), 1904403.

114. Strand, E. J.; Bihar, E.; Gleason, S. M.; Han, S.; Schreiber, S. W.; Renny, M. N.; Malliaras, G. G.; McLeod, R. R.; Whiting, G. L., Printed Organic Electrochemical Transistors for Detecting Nutrients in Whole Plant Sap. *Adv. Electron. Mater.* **2022**, 2100853.
115. Kubota, R.; Sasaki, Y.; Minamiki, T.; Minami, T., Chemical Sensing Platforms Based on Organic Thin-Film Transistors Functionalized with Artificial Receptors. *ACS Sens.* **2019**, 4 (10), 2571-2587.
116. Koklu, A.; Ohayon, D.; Wustoni, S.; Druet, V.; Saleh, A.; Inal, S., Organic Bioelectronic Devices for Metabolite Sensing. *Chem. Rev.* **2021**.
117. Vella, J. H.; Huang, L.; Eedugurala, N.; Mayer, K. S.; Ng, T. N.; Azoulay, J. D., Broadband infrared photodetection using a narrow bandgap conjugated polymer. *Sci. Adv.* **2021**, 7 (24), eabg2418.
118. Ocheje, M. U.; Goodman, R. B.; Lu, K.-T.; Wang, Y.; Galuska, L. A.; Soullard, L.; Cao, Z.; Zhang, S.; Yadiki, M.; Gu, X.; Chiu, Y.-C.; Rondeau-Gagné, S., Precise Control of Noncovalent Interactions in Semiconducting Polymers for High-Performance Organic Field-Effect Transistors. *Chem. Mater.* **2021**, 33 (21), 8267-8277.
119. Yang, J.; Zhao, Z.; Wang, S.; Guo, Y.; Liu, Y., Insight into High-Performance Conjugated Polymers for Organic Field-Effect Transistors. *Chem* **2018**, 4 (12), 2748-2785.
120. Chen, M.; Crispin, X.; Perzon, E.; Andersson, M. R.; Pullerits, T.; Andersson, M.; Inganäs, O.; Berggren, M., High carrier mobility in low band gap polymer-based field-effect transistors. *Appl. Phys. Lett.* **2005**, 87 (25), 252105.
121. Liu, C.; Xu, Y.; Noh, Y.-Y., Contact engineering in organic field-effect transistors. *Mater. Today* **2015**, 18 (2), 79-96.
122. Ito, Y.; Virkar, A. A.; Mannsfeld, S.; Oh, J. H.; Toney, M.; Locklin, J.; Bao, Z., Crystalline ultrasmooth self-assembled monolayers of alkylsilanes for organic field-effect transistors. *J. Am. Chem. Soc.* **2009**, 131 (26), 9396-404.
123. Tang, K.; Huang, L.; Lim, J.; Zaveri, T.; Azoulay, J. D.; Guo, S., Chemical Doping of Well-Dispersed P3HT Thin-Film Nanowire Networks. *ACS APpl. Polym. Mater.* **2019**, 1 (11), 2943-2950.
124. Huang, L.; Eedugurala, N.; Benasco, A.; Zhang, S.; Mayer, K. S.; Adams, D. J.; Fowler, B.; Lockart, M. M.; Saghayezhian, M.; Tahir, H.; King, E. R.; Morgan, S.; Bowman, M. K.; Gu, X.; Azoulay, J. D., Open-shell donor-acceptor conjugated polymers with high electrical conductivity. *Adv. Funct. Mater.* **2020**, 30 (24).
125. Friedlein, J. T.; McLeod, R. R.; Rivnay, J., Device physics of organic electrochemical transistors. *Org. Electron.* **2018**, 63, 398-414.
126. Zhou, G.; Chang, J.; Cui, S.; Pu, H.; Wen, Z.; Chen, J., Real-Time, Selective Detection of Pb²⁺ in Water Using a Reduced Graphene Oxide/Gold Nanoparticle Field-Effect Transistor Device. *ACS Appl. Mater. Interfaces* **2014**, 6 (21), 19235-19241.
127. Angione, M. D.; Cotrone, S.; Magliulo, M.; Mallardi, A.; Altamura, D.; Giannini, C.; Cioffi, N.; Sabbatini, L.; Fratini, E.; Baglioni, P.; Scamarcio, G.; Palazzo, G.; Torsi, L., Interfacial electronic effects in functional bilayers integrated into organic field-effect transistors. *Proc. Natl. Acad. Sci. U.S.A.* **2012**, 109 (17), 6429-34.
128. Qiao, B.; Leverick, G. M.; Zhao, W.; Flood, A. H.; Johnson, J. A.; Shao-Horn, Y., Supramolecular Regulation of Anions Enhances Conductivity and Transference Number of Lithium in Liquid Electrolytes. *J. Am. Chem. Soc.* **2018**, 140 (35), 10932-10936.

129. Yuvaraja, S.; Surya, S. G.; Chernikova, V.; Vijjapu, M. T.; Shekhah, O.; Bhatt, P. M.; Chandra, S.; Eddaoudi, M.; Salama, K. N., Realization of an ultrasensitive and highly selective OFET NO₂ sensor: the synergistic combination of PDVT-10 polymer and porphyrin-MOF. *ACS Appl. Mater. Interfaces* **2020**, *12* (16), 18748-18760.
130. Chen, H.; Guo, Y.; Yu, G.; Zhao, Y.; Zhang, J.; Gao, D.; Liu, H.; Liu, Y., *Adv. Mater.* **2012**, *24*, 4618.
131. Leenaers, P. J.; van Eersel, H.; Li, J.; Wienk, M. M.; Janssen, R. A. J., *Macromolecules* **2020**, *53* (18), 7749-7758.
132. Salzmann, I.; Heimel, G.; Oehzelt, M.; Winkler, S.; Koch, N., Molecular electrical doping of organic semiconductors: fundamental mechanisms and emerging dopant design rules. *Acc. Chem. Res.* **2016**, *49* (3), 370-8.
133. Lin, P.; Yan, F., Organic thin-film transistors for chemical and biological sensing. *Adv. Mater.* **2012**, *24*, 34.
134. Jang, M.; Kim, H.; Lee, S.; Kim, H. W.; Khedkar, J. K.; Rhee, Y. M.; Hwang, I.; Kim, K.; Oh, J. H., Highly sensitive and selective biosensors based on organic transistors functionalized with cucurbit[6]uril derivatives. *Adv. Funct. Mater.* **2015**, *25*, 4882.
135. Melitz, W.; Shen, J.; Kummel, A. C.; Lee, S., Kelvin probe force microscopy and its application. *Surf. Sci. Rep.* **2011**, *66* (1), 1-27.
136. Bobbert, P. A.; Sharma, A.; Mathijssen, S. G. J.; Kemerink, M.; De Leeuw, D. M., Operational Stability of Organic Field-Effect Transistors. *Adv. Mater.* **2012**, *24*, 1146.
137. Roberts, M. E.; Mannsfeld, S. C. B.; Queraltó, N.; Reese, C.; Locklin, J.; Knoll, W.; Bao, Z., Water-stable organic transistors and their application in chemical and biological sensors. *Proc. Natl. Acad. Sci. U.S.A.* **2008**, *105* (34), 12134.
138. Correll, D. L., The Role of Phosphorus in the Eutrophication of Receiving Waters: A Review. *J. Environ. Qual.* **1998**, *27*, 261.
139. Tyrrell, T., The relative influences of nitrogen and phosphorus on oceanic primary production. *Nature* **1999**, *400*, 525.
140. Raghothama, K. G., Phosphate Acquisition. *Annu. Rev. Plant Biol.* **1999**, *50* (1), 665-693.
141. Cordell, D.; Drangert, J.-O.; White, S., *Glob. Environ. Change* **2009**, *19*, 292.
142. Moe, S. M., Disorders involving calcium, phosphorus, and magnesium. *Prim. Care* **2008**, *35* (2), 215-37, v-vi.
143. Correll, D. L., *J. Environ. Qual.* **1998**, *27*, 261.
144. Carpenter, S. R.; Caraco, N. F.; Correll, D. L.; Howarth, R. W.; Sharpley, A. N.; Smith, V. H., Nonpoint pollution of surface waters with phosphorus and nitrogen. *Ecol. Appl.* **1998**, *8*, 559.
145. Smith, V. H., Eutrophication of freshwater and coastal marine ecosystems a global problem. *Environ. Sci. Pollut. Res.* **2003**, *10* (2), 126-139.
146. Hargrove, A. E.; Nieto, S.; Zhang, T.; Sessler, J. L.; Anslyn, E. V., Artificial Receptors for the Recognition of Phosphorylated Molecules. *Chem. Rev.* **2011**, *111*, 6603.
147. Duffy, G.; Regan, F., Recent developments in sensing methods for eutrophying nutrients with a focus on automation for environmental applications. *Analyst* **2017**, *142*, 4355.
148. Cuartero, M., Electrochemical sensors for in-situ measurement of ions in seawater. *Sens. Actuators B Chem.* **2021**, *334*, 129635.

149. Zhu, X.; Ma, J., Recent advances in the determination of phosphate in environmental water samples: insights from practical perspectives. *Trends Anal. Chem.* **2020**, *127*, 115908.
150. Warwick, C.; Guerreiro, A.; Soares, A., Sensing and analysis of soluble phosphates in environmental samples: a review. *Biosens. Bioelectron.* **2013**, *41*, 1-11.
151. Law al, A. T.; Adeloju, S. B., Progress and recent advances in phosphate sensors: a review. *Talanta* **2013**, *114*, 191-203.
152. Mahmud, M. A. P.; Ejeian, F.; Azadi, S.; Myers, M.; Pejicic, B.; Abbassi, R.; Razmjou, A.; Asadnia, M., *Chemosphere* **2020**, *259* (39).
153. Patey, M. D.; Rijkenberg, M. J. A.; Statham, P. J.; Stinchcombe, M. C.; Achterberg, E. P.; Mowlem, M., *Trends Anal. Chem.* **2008**, *27*, 169.
154. Williams, A. K.; Tropp, J.; Crater, E. R.; Eedugurala, N.; Azoulay, J. D., *ACS Appl. Polym. Mater.* **2019**, *1*, 309.
155. Cuartero, M.; Crespo, G. A., All-solid-state potentiometric sensors: a new wave for in situ aquatic research. *Curr. Opin. Electrochem.* **2018**, *10*, 98-106.
156. Langton, M. J.; Serpell, C. J.; Beer, P. D., *Angew. Chem.* **2016**, *55*, 1974.
157. Mulla, M. Y.; Tuccori, E.; Magliulo, M.; Lattanzi, G.; Palazzo, G.; Persaud, K.; Torsi, L., *Nat. Commun.* **2015**, *6*, 6010.
158. Torsi, L.; Magliulo, M.; Manoli, K.; Palazzo, G., *Chem. Soc. Rev.* **2013**, *42*, 8612.
159. Lange, U.; Mirsky, V. M., Chemiresistors based on conducting polymers: a review on measurement techniques. *Anal. Chim. Acta* **2011**, *687*, 105.
160. Cuartero, M.; Bakker, E., Environmental water analysis with membrane electrodes. *Curr. Opin. Electrochem.* **2017**, *3* (1), 97-105.
161. Wang, J.; Liang, R.; Qin, W., Molecularly imprinted polymer-based potentiometric sensors. *Trends Anal. Chem.* **2020**, *130*, 115980.
162. Rivnay, J.; Inal, S.; Salleo, A.; Owens, R. M.; Berggren, M.; Malliaras, G. G., Organic electrochemical transistors. *Nat. Rev. Mater.* **2018**, *3* (2), 17086.
163. Torricelli, F.; Adrahtas, D. Z.; Bao, Z.; Berggren, M.; Biscarini, F.; Bonfiglio, A.; Bortolotti, C. A.; Frisbie, C. D.; Macchia, E.; Malliaras, G. G.; McCulloch, I.; Moser, M.; Nguyen, T.-Q.; Owens, R. M.; Salleo, A.; Spanu, A.; Torsi, L., Electrolyte-gated transistors for enhanced performance bioelectronics. *Nat. Rev. Methods Primers* **2021**, *1* (1), 66.
164. Cai, J.; Sessler, J. L., *Chem. Soc. Rev.* **2014**, *43*, 6198.
165. Eytel, L. M.; Fargher, H. A.; Haley, M. M.; Johnson, D. W., The road to aryl CH \cdots anion binding was paved with good intentions: fundamental studies, host design, and historical perspectives in CH hydrogen bonding. *Chem. Commun.* **2019**, *55*, 5195.
166. Pal, S.; Ghosh, T. K.; Ghosh, R.; Mondal, S.; Ghosh, P., Recent advances in recognition, sensing and extraction of phosphates: 2015 onwards. *Coord. Chem. Rev.* **2020**, *405*, 213128.
167. Qiao, B.; Anderson, J. R.; Pink, M.; Flood, A. H., Size-matched recognition of large anions by cyanostar macrocycles is saved when solvent-bias is avoided. *Chem. Commun.* **2016**, *52* (56), 8683-6.
168. Zahran, E. M.; Fatila, E. M.; Chen, C.-H.; Flood, A. H.; Bachas, L. G., Cyanostar: C-H hydrogen bonding neutral carrier scaffold for anion-selective sensors. *Anal. Chem.* **2018**, *90* (3), 1925-1933.

169. Zeynaloo, E.; Zahran, E. M.; Fatila, E. M.; Flood, A. H.; Bachas, L. G., Anion-selective electrodes based on a CH-hydrogen bonding bis-macrocyclic ionophore with a clamshell architecture. *Anal. Chem.* **2021**, *93* (13), 5412-5419.
170. Boyle, C. J.; Upadhyaya, M.; Wang, P.; Renna, L. A.; Lu-Diaz, M.; Pyo Jeong, S.; Hight-Huf, N.; Korugic-Karasz, L.; Barnes, M. D.; Aksamija, Z.; Venkataraman, D., Tuning charge transport dynamics via clustering of doping in organic semiconductor thin films. *Nat. Commun.* **2019**, *10* (1), 2827.
171. Shannon, M. A.; Bohn, P. W.; Elimelech, M.; Georgiadis, J. G.; Marinas, B. J.; Mayes, A. M., Science and technology for water purification in the coming decades. *Nature* **2008**, *452* (7185), 301-10.
172. Gruber, N.; Galloway, J. N., An Earth-system perspective of the global nitrogen cycle. *Nature* **2008**, *451* (7176), 293-296.
173. Urbansky, E. T., Perchlorate as an environmental contaminant. *Environ. Sci. Pollut. Res.* **2002**, *9* (3), 187-92.
174. Angione, M. D.; Cotrone, S.; Magliulo, M.; Mallardi, A.; Altamura, D.; Giannini, C.; Cioffi, N.; Sabbatini, L.; Fratini, E.; Baglioni, P., Interfacial Electronic Effects in Functional Biolayers Integrated into Organic Field-Effect Transistors. *Proc. Natl. Acad. Sci. U. S. A.* **2012**, *109*, 6429.
175. Mao, S.; Pu, H.; Chang, J.; Sui, X.; Zhou, G.; Ren, R.; Chen, Y.; Chen, J., Ultrasensitive detection of orthophosphate ions with reduced graphene oxide/ferritin field-effect transistor sensors. *Environ. Sci. Nano* **2017**, *4* (4), 856-863.
176. Chen, X.; Pu, H.; Fu, Z.; Sui, X.; Chang, J.; Chen, J.; Mao, S., Real-time and selective detection of nitrates in water using graphene-based field-effect transistor sensors. *Environ. Sci. Nano* **2018**, *5* (8), 1990-1999.
177. Barhoumi, L.; Baraket, A.; Nooredeen, N. M.; Ali, M. B.; Abbas, M. N.; Bausells, J.; Errachid, A., Silicon nitride capacitive chemical sensor for phosphate ion detection based on copper phthalocyanine - acrylate-polymer. *Electroanalysis* **2017**, *29* (6), 1586-1595.
178. Racicot, J. M.; Mako, T. L.; Olivelli, A.; Levine, M., A paper-based device for ultrasensitive, colorimetric phosphate detection in seawater. *Sensors* **2020**, *20* (10).
179. Grand, M. M.; Clinton-Bailey, G. S.; Beaton, A. D.; Schaap, A. M.; Johengen, T. H.; Tamburri, M. N.; Connelly, D. P.; Mowlem, M. C.; Achterberg, E. P., A lab-on-chip phosphate analyzer for long-term in-situ monitoring at fixed observatories: optimization and performance evaluation in estuarine and oligotrophic coastal waters. *Front. Mar. Sci.* **2017**, *4*.
180. Bralić, M., Preparation of phosphate ion-selective membrane based on silver salts mixed with PTFE or carbon nanotubes. *Int. J. Electrochem. Sci.* **2018**, *13*, 1390-1399.
181. Kim, H. J.; Hummel, J. W.; Sudduth, K. A.; Birrell, S. J., Evaluation of phosphate ion-selective membranes and cobalt-based electrodes for soil nutrient sensing. *Trans. ASABE* **2007**, *50* (2), 415-425.
182. Jia, X.; Chen, D.; Bin, L.; Lu, H.; Zhang, R.; Zheng, Y., Highly selective and sensitive phosphate anion sensors based on AlGaN/GaN high electron mobility transistors functionalized by ion imprinted polymer. *Sci. Rep.* **2016**, *6*, 27728.
183. Zhou, G.; Jin, B.; Wang, Y.; Dong, Q.; Maity, A.; Chang, J.; Ren, R.; Pu, H.; Sui, X.; Mao, S.; Chen, J., Ultrasensitive sensors based on aluminum oxide-protected reduced

graphene oxide for phosphate ion detection in real water. *Mol. Syst. Des. Eng.* **2020**, *5* (5), 936-942.

184. Bhat, K. S.; Nakate, U. T.; Yoo, J. Y.; Wang, Y.; Mahmoudi, T.; Hahn, Y. B., Nozzle-jet-printed silver/graphene composite-based field-effect transistor sensor for phosphate ion detection. *ACS Omega* **2019**, *4* (5), 8373-8380.